NTNU

Norwegian University of
Science and Technology

Cyclic Behaviour of Water Saturated Dense Sand

Birgitte Misund Dahl
Marit Skaug Løyland

Civil and Environmental Engineering
Submission date: June 2017
Supervisor: Hans Petter Jostad, IBM
Co-supervisor: Gustav Grimstad, IBM

Norwegian University of Science and Technology
Department of Civil and Environmental Engineering

NORWEGIAN UNIVERSITY OF SCIENCE AND TECHNOLOGY
DEPARTMENT OF CIVIL AND ENVIRONMENTAL ENGINEERING

Report Title: **Cyclic Behaviour of Water Saturated Dense Sand**	Date: **08.06.1017**	
	Number of pages (incl. appendices): **178**	
	Master's thesis	x
Name: Birgitte Misund Dahl and Marit Skaug Løyland		
Professor in charge/supervisor: Hans Petter Jostad		
External professional contacts/supervisors: x		

Abstract:
Several monotonic and cyclic triaxial tests have been performed at NGI in association with the ongoing strategic project, SP9. The test material is dense saturated sand from the Siri offshore field in the North Sea, and this study includes interpretations of the tests within an elasto-plastic constitutive framework. Different drainage conditions have been evaluated, and characteristic behaviours have been established.

There have been observed deviation in the pore water pressure generation in the different cyclic triaxial tests. Sample preparation method affects the properties of the sand, and is most likely the reason for the deviations. Cycles from different tests with the same initial mean stress have been compared, and there is a striking resemblance of the response. This indicates that the material considers the mean stress condition as a state parameter, and is independent on how it got to the specific stress condition.

A monotonic and cyclic simulation of the SANISAND model limited to the triaxial stress space have been implemented in Excel. A verification of the model and a parameter study have been carried out. The response simulated by SANISAND has been compared with results from the triaxial tests performed on Siri sand. The SANISAND input parameters have been fitted to the monotonic tests, and then developed further for the cyclic simulations. This is done by evaluating the different SANISAND formulations and how the different parameters affect the simulations. One set of parameters has been applied in all cyclic simulations of the Siri sand. However, it has been observed in the results that due to some variation in stress condition and relative density of the tests, small modifications of the parameters are required to represent the behaviour of each test in an optimal manner.

This study indicates that the SANISAND model has some limitations. The representations of incremental plastic and volume strains are somewhat inaccurate, which result in inaccurate simulations of total shear and volume strains.

Despite the limitations, the model represents the behaviour of water saturated dense sand in an adequate manner. The model is relatively simple compared to the alternatives, and the user-friendly framework is advantageous.

Keywords:

1. Dense sand
2. Cyclic soil behaviour
3. Triaxial test
4. SANISAND

Birgitte Misund Dahl

Marit Skaug Løyland

MASTER DEGREE THESIS

Spring 2017
for

Birgitte Misund Dahl and Marit Skaug Løyland

Cyclic Behaviour of Water Saturated Dense Sand

Syklisk Oppførsel av Vannmettet, Fast Lagret Sand

BACKGROUND
Water saturated sand will during cyclic (repeated) undrained loading accumulate pore pressure and deformations. The pore pressure build-up will further reduce the effective stresses and thus reduce the stiffness and shear strength of the soil. During design of foundations for offshore structures, as for instance monopile or bucket foundations for offshore wind turbines (OWTs), in sand subjected to cyclic loading due to waves, wind and current, these effects need to be taken into account. One way to account for these effects is to carry out a large number of undrained cyclic laboratory tests and establish pore pressure and strain contour diagrams as described in several papers by Knut Andersen (NGI). These diagrams are then used by the soil model PDCAM (NGI) in finite element analyses of the foundation in order to calculate displacements, stiffnesses and capacity. In order to reduce the number of tests required to establish these diagrams, it is important to understand the behaviour of water saturated sand subjected to cyclic loading in more details. A laboratory test program on dense sand performed at NGI within a strategic research project, SP9, is one contribution to this process. A detailed interpretation of these test data is then the next step to better understand the behaviour of sand.

TASK
The aim of the present Master Degree Thesis is to interpret the available (monotonic and cyclic) tests within an elasto-plastic constitutive framework. As a part of this process the obtained results should be compared with results obtained with a model based on the framework of the SANISAND model. This means that the work consists of the following sub-tasks:

1) Interpretation of the laboratory tests performed at NGI in SP9. This includes making plots of plastic shear and volumetric strains, increments (change) in plastic shear and volumetric strains, dilatancy, i.e. ratio between plastic volumetric strain and shear strain increments, etc. as function of current shear stress ratio q/p'. As part of this process, it is necessary to smoothen the measured laboratory data. The results from these plots will be used to find characteristic behaviours as phase transformation line, hardening curves, dilatancy, etc.
2) Review the basic ingredients of the SANISAND constitutive model (limited to the triaxial stress space).
3) Make a tool in Excel that can simulate the undrained monotonic and cyclic behaviour of sand by the SANISAND formulation.

The main results from the work will be information that can be used to develop an improved SANISAND model for cyclic behaviour of water saturated dense sand.

Supervisor:
Hans Petter Jostad (NGI)

Co-supervisor:
Gustav Grimstad (NTNU)

Department of Civil and Environmental Engineering, NTNU
Date: 08.06.2017

Hans Petter Jostad

Supervisor

Preface

This master's thesis is written during the spring semester of 2017, as the final part of the master's programme in Geotechnical Engineering at the Norwegian University of Science and Technology (NTNU, Trondheim). It has been carried out as a collaboration between Birgitte M. Dahl and Marit S. Løyland, both graduate students at the aforementioned study programme. The thesis was proposed by the Norwegian Geotechnical Institute (NGI), and has been carried out in cooperation with them.

Trondheim, June 8, 2017

Birgitte Misund Dahl

Marit Skaug Løyland

Acknowledgements

We would like to extend a very special thank you to our supervisor Hans Petter Jostad for his insightful and constructive feedback on our work. We are very grateful for his invaluable support throughout the process of completing our thesis, and for the dedication he has shown towards our work.

We want to acknowledge the Norwegian Geotechnical Institute (NGI) who made this project possible by kindly providing us assistance and necessary data.

Thank you to all the members of the staff at the Geotechnical Division at NTNU for great assistance the last few years. Inputs from Gustav Grimstad have been well appreciated throughout the project.

We would also like to thank *Geogjengen 2017* for pleasant moments and great discussions. The positive environment in our office has been crucial to the completion of this study.

Finally, we would like to express our appreciation to our families and friends for personal support and for encouraging us throughout the process.

B.M.D. & M.S.L.

Abstract

Several monotonic and cyclic triaxial tests have been performed at NGI in association with the ongoing strategic project, SP9. The test material is dense saturated sand from the Siri offshore field in the North Sea, and this study includes interpretations of the tests within an elasto-plastic constitutive framework. Different drainage conditions have been evaluated, and characteristic behaviours have been established.

There have been observed deviation in the pore water pressure generation in the different cyclic triaxial tests. Sample preparation method affects the properties of the sand, and is most likely the reason for the deviations. Cycles from different tests with the same initial mean stress have been compared, and there is a striking resemblance of the response. This indicates that the material considers the mean stress condition as a state parameter, and is independent on how it got to the specific stress condition.

A monotonic and cyclic simulation of the SANISAND model limited to the triaxial stress space have been implemented in Excel. A verification of the model and a parameter study have been carried out. The response simulated by SANISAND has been compared with results from the triaxial tests performed on Siri sand. The SANISAND input parameters have been fitted to the monotonic tests, and then developed further for the cyclic simulations. This is done by evaluating the different SANISAND formulations and how the different parameters affect the simulations. One set of parameters has been applied in all cyclic simulations of the Siri sand. However, it has been observed in the results that due to some variation in stress condition and relative density of the tests, small modifications of the parameters are required to represent the behaviour of each test in an optimal manner.

This study indicates that the SANISAND model has some limitations. The representations of incremental plastic and volume strains are somewhat inaccurate, which result in inaccurate simulations of total shear and volume strains.

Despite the limitations, the model represents the behaviour of water saturated dense sand in an adequate manner. The model is relatively simple compared to the alternatives, and the user-friendly framework is advantageous.

Sammendrag

I forbindelse med et pågående strategisk forskningsprosjekt, SP9, har NGI utført flere statiske og sykliske treaksialforsøk. Testene er utført på fast lagret, vannmettet sand fra offshorefeltet Siri i Nordsjøen, og i denne studien er testresultatene tolket ved å anvende elastoplastisk teori. Ulike dreneringsbetingelser er vurdert, og karakteristisk oppførsel er funnet.

Det er observert variasjon i poretrykksgenerering i de ulike treaksialforsøkene. Forstyrrelse av prøvene påvirker egenskapene til sanden, og studien indikerer at dette mest sannsynlig er årsaken til avvikene. Sammenlikning av sykluser med samme middelspenning ved start viser likevel at det er en slående likhet i oppførselen til sanden. Dette indikerer at materialet ser på middelspenningstilstanden som en tilstandsparameter, og at oppførselen er uavhengig av hvordan sanden oppnådde den spesifikke spenningstilstanden.

Vurdering av SANISAND-modellen er begrenset til en treaksial spenningstilstand. En verifisering av modellen samt en parameterstudie er gjennomført. Responsen som er simulert av SANISAND har blitt sammenliknet med resultatene fra de treaksiale forsøkene gjennomført med Siri-sand. Modellparameterne til SANISAND er først tilpasset de statiske treaksialtestene før de er justert til å kunne beskrive syklisk materialoppførsel. Dette er gjort ved å vurdere de ulike SANISAND likningene, og hvordan de ulike parameterne påvirker simuleringen av Siri-sand. Ett sett med parametere er anvendt i simuleringen av alle de sykliske treaksialforsøkene. Resultatene indikerer behov for små justeringer i modellparameterne for hver enkelt test, grunnet små endringer i lagringstetthet og initialspenningstilstand.

Studien indikerer at SANISAND-modellen har noen begrensninger. Simuleringen av inkrementelle plastiske skjær- og volumtøyninger er noe unøyaktige, som fører til et feilaktig anslag av akkumulerte tøyninger.

Resultatene viser at modellen presenterer oppførselen av fast lagret, vannmettet sand på en tilstrekkelig måte. Modellen er brukervennlig, og relativt enkel å bruke sammenliknet med alternativene.

Contents

List of Figures

List of Tables

Acronyms

CAD$_c$ Anisotropic Consolidated Drained Compression triaxial test

CAD$_e$ Anisotropic Consolidated Drained Extension triaxial test

CAU$_c$ Anisotropic Consolidated Undrained Compression triaxial test

CAU$_e$ Anisotropic Consolidated Undrained Extension triaxial test

CAD$_{cy}$ Anisotropic Consolidated Drained Cyclic triaxial test

CAU$_{cy}$ Anisotropic Consolidated Undrained Cyclic triaxial test

CSL Critical State Line

CSSM Critical State Soil Mechanics

DD Dry Deposition

DSS Direct Simple Shear

MT Moist Tamping

NGI Norwegian Geotechnical Institute

NTNU Norwegian University of Science and Technology

PDCAM Partially Drained Accumulation Model

PWP Pore Water Pressure

SANISAND Simple Anisotropic Sand Constitutive Models

Symbols

$\boldsymbol{\alpha}$ stress ratio quantity (-)

$\boldsymbol{\gamma}$ shear strain (-)

$\boldsymbol{\varepsilon}_1, \boldsymbol{\varepsilon}_2, \boldsymbol{\varepsilon}_3$ principal strain (-)

$\boldsymbol{\varepsilon}_q$ deviatoric strain (-)

$\boldsymbol{\varepsilon}_q^e$ elastic deviatoric strain (-)

$\boldsymbol{\varepsilon}_q^p$ plastic deviatoric strain (-)

$\boldsymbol{\varepsilon}_v$ volumetric strain (-)

$\boldsymbol{\varepsilon}_v^e$ elastic volumetric strain (-)

$\boldsymbol{\varepsilon}_v^p$ plastic volumetric strain (-)

$\boldsymbol{\eta}$ stress ratio (-)

$\boldsymbol{\theta}$ lode angle (rad)

$\boldsymbol{\lambda}_c$ slope of critical state line (-)

$\boldsymbol{\nu}$ Poisson's ratio (-)

$\boldsymbol{\xi}$ material constant (-)

$\boldsymbol{\sigma}, \boldsymbol{\sigma}'$ total and effective stress (Pa)

$\boldsymbol{\sigma}_1, \boldsymbol{\sigma}'_1$ major in-plane principal total and effective stress (Pa)

$\boldsymbol{\sigma}_2, \boldsymbol{\sigma}'_2$ intermediate in-plane principal total and effective stress (Pa)

$\boldsymbol{\sigma}_3, \boldsymbol{\sigma}'_3$ minor in-plane principal total and effective stress (Pa)

$\boldsymbol{\sigma'_{ac}}$ axial consolidation stress (Pa)

$\boldsymbol{\sigma'_{rc}}$ radial consolidation stress (Pa)

$\boldsymbol{\tau_a}$ average shear stress (Pa)

$\boldsymbol{\tau_{cy}}$ cyclic shear stress (Pa)

$\boldsymbol{\phi}$ friction angle (rad)

$\mathbf{A}_0$ state parameter (-)

$\mathbf{A}_d$ function of the fabric dilatancy (-)

$\mathbf{c}_z$ pace of evolution of z (-)

$\mathbf{D}_r$ relative density (-)

d dilatancy (-)

e void ratio (-)

$\mathbf{e}_0$ void ratio at $p_c = 0$ (-)

$\mathbf{e}_c$ critical void ratio (-)

G elastic shear modulus (Pa)

$\mathbf{G}_0$ dimensionless material constant (-)

$\mathbf{G_{max}}$ measured maximum elastic shear modulus (Pa)

H plastic hardening modulus (-)

h function of the state variables (-)

$\mathbf{h}_0$ scalar parameter (-)

K elastic bulk modulus (Pa)

M critical stress ratio (-)

$\mathbf{M}_c$ critical stress ratio in compression (-)

$\mathbf{M}_e$ critical stress rartio in extension (-)

$\mathbf{M}^b$ bounding stress ratio (-)

$\mathbf{M}^d$ dilatancy stress ratio (-)

$\mathbf{N}$ cycle (-)

$\mathbf{m}$ stress ratio quantity (-)

$\mathbf{n}^b$ positive material constant (-)

$\mathbf{n}^d$ positive material constant (-)

$\boldsymbol{p}, \boldsymbol{p}'$ total and effective mean stress (Pa)

$\mathbf{p_{atm}}$ atmospheric pressure (Pa)

$\mathbf{p}_c$ critical mean stress (Pa)

$\mathbf{q}$ deviatoric stress (Pa)

$\mathbf{q}_c$ critical deviatoric stress (Pa)

$\mathbf{z}$ fabric-dilatancy internal variable (-)

$\mathbf{z_{max}}$ maximum value z can attain (-)

Chapter 1

Introduction

1.1 Background

During design of foundations of offshore structures, one need to account for cyclic loading effects. When water saturated sand is subjected to cyclic loading, the sand accumulates either pore water pressure or deformation, or both. In general, this pore water pressure build-up reduces the effective stresses and thus reduces the stiffness and shear strength of the soil. In some cases, a negative pore water pressure is built up, and the effective stresses are then increased.

One approach to represent the change in soil properties as a result of cyclic loading is to establish pore water pressure and strain contour diagrams, as described in Andersen (2015). A large number of undrained cyclic laboratory tests have to be performed to establish these diagrams. The diagrams are then applied to the Partially Drained Accumulation Model (PDCAM) in a finite element analysis in order to assess displacements, stiffness and capacity of foundations (Jostad et al., 2015).

In order to reduce the number of tests required to establish these diagrams, it is important to understand the behaviour of water saturated sand subjected to cyclic loading in more details. To improve the understanding of the cyclic effects on sand, the Norwegian Geotechnical Institute (NGI) has an ongoing laboratory test programme in association with a strategic research project, SP9. The test programme is performed on dense saturated sand from the field Siri in the North Sea. A detailed interpretation of these test data is desirable to get a better understanding of the behaviour of sand.

1.2 Problem Formulation

This master's thesis will concentrate on interpretation of the triaxial test data to evaluate a material model simulating cyclic behaviour of soil, and the Simple ANIsotropic SAND (SANISAND) constitutive model will be the main focus. The problem formulations are stated as follows:

1. Interpret monotonic and cyclic triaxial tests within an elasto-plastic constitutive framework, how does the response from the triaxial tests on Siri sand behave?

2. How does a model based on the framework of SANISAND compare to the results from the triaxial tests?

1.3 Published Work

Critical state soil mechanics (Schofield and Wroth, 1968) is a framework that can be used to study soil behaviour, and can capture the stress-strain response well for sands under monotonic loading conditions. When the need to describe the cyclic response from soil arose, the isotropic hardening plasticity framework in the critical state soil mechanics had limitations. This was related to the representation of response such as the pore water pressure development under cyclic undrained loading.

Manzari and Dafalias' (1997) main objective was to develop a simple and easy understandable constitutive model which was able to describe the monotonic and cyclic behaviour of sand. This was an early version of the SANISAND model. The model aimed to use the same parameters for one sand, independent of stress condition and density. A shortcoming of the model introduced by Manzari and Dafalias (1997) was that it did not account for fabric change effects. The stress path loops stabilised early, while sand exposed to undrained loading often generates pore water pressure resulting in the effective mean stress, p', approaching zero. This is an important factor as failure due to liquefaction in loose sand may occur when the effective mean stress reaches zero. The model also struggled to describe the dilatant behaviour of dense sand. Dafalias and Manzari (2004) implemented a fabric-dilatancy internal variable in the SANISAND model to account for this effect.

The SANISAND model has been studied and evaluated after it was introduced by Manzari and Dafalias (1997). Cheng et al. (2013) implemented the 2004-version of the SANISAND model as a user defined model in FLAC^{3D}. Experimental data of triaxial compression tests

were compared with the simulation results to verify the model validations. Barrero et al. (2015) also implemented the SANISAND model in FLAC for a nonlinear dynamic analysis of a tailings dam. The SANISAND model can capture liquefaction due to cyclic loading. Advanced material models can reduce the engineering effort in evaluation of a complex soil system. The results from the dam analysis showed tolerable performance also after shaking.

Wichtmann (2016) processed a huge amount of laboratory data to inspect the constitutive models; hypoplasticity, ISA and SANISAND. The conclusion was that each model had its own strengths and weaknesses. An evaluation of SANISAND input parameters are included in the article.

1.4 Objectives

The aim of this master's thesis is to interpret monotonic and cyclic triaxial tests performed on dense saturated sand within an elasto-plastic constitutive framework. The results from the interpretations will be compared with simulations obtained with a model based on the framework of the SANISAND constitutive models.

The main objectives are:

1. Interpret monotonic and cyclic triaxial tests performed at NGI in connection with the strategic project, SP9.

2. Evaluate the SANISAND constitutive model for sand in the triaxial stress space.

3. Evaluate limitations of the model with respect to the Siri sand.

1.5 Limitations

This thesis concentrates on the SANISAND material model, and how the model represents the response of the Siri sand. It is limited to focus on the triaxial stress space of the material model.

A considerable amount of triaxial test data have been available during the work of this thesis. The available triaxial test data have a limited range of relative densities and consolidation stresses. The SANISAND model has therefore not been verified for other ranges of relative densities and consolidation stresses.

1.6 Scientific Approach

A literature survey has been carried out to increase the understanding of cyclic loading and the response of sand exposed to this. In addition, a review of plasticity sand models has been performed.

To interpret monotonic and cyclic triaxial tests, a MATLAB script has been utilised to reduce the noise in the raw data, and several Excel spreadsheets have been created to process the filtered data. Different plots have been created in Excel to find characteristic behaviours such as phase transformation line, hardening curve, dilatancy and effect of change in fabric.

The SANISAND formulation has been implement in Excel to simulate the undrained and drained, monotonic and cyclic behaviour of sand. The model has been verified and a parameter study is performed. The model has been compared to the laboratory data by the use of different plots in Excel to find a set of model parameters for the Siri sand. The SANISAND formulations are dissected in order to evaluate different input parameters and potential limitations.

1.7 Outline of the Thesis

The remaining chapters of this thesis are structured as follows:

Chapter 2 gives an introduction to cyclic loading characteristics and cyclic behaviour of sand.

Chapter 3 gives a brief review of elasto-plasticity, critical state soil mechanics and the bounding surface plasticity model, theories that SANISAND is based on.

Chapter 4 gives an introduction to the SANISAND model, together with a verification and parameter study of the model.

Chapter 5 gives an introduction to how triaxial tests on sand are performed.

Chapter 6 presents the results from triaxial tests for monotonic and cyclic loading.

Chapter 7 presents the implementation of the SANISAND constitutive model.

Chapter 8 gives a discussion of the triaxial test results and the simulations by the SANISAND model.

Chapter 9 gives a summary and final conclusions of the work carried out in this thesis. Recommendations for further work are suggested.

Chapter 2

Cyclic Loading

Cyclic loading effects are important in design of foundations of offshore structures, structures along the coast and on land. There are several factors that may cause cyclic loading, illustrated in Figure 2.1 It may be caused by wind, wave and ice loads for onshore and offshore wind power structure and coastal structures, traffic due to high-speed trains, and repeated filling and emptying processes in tanks and silos. Other factors that introduce cyclic loads into the soil are construction processes, for example by vibration of sheet piles, mechanical compaction by vibration or earthquakes.

According to Andersen (2015) there are several different design issues for cyclically loaded foundations, these are: ensuring sufficient capacity and tolerable cyclic displacements, providing equivalent soil spring stiffness and damping for dynamic soil-structure or earthquake analyses, or to assess the long term permanent displacements, and soil reactions.

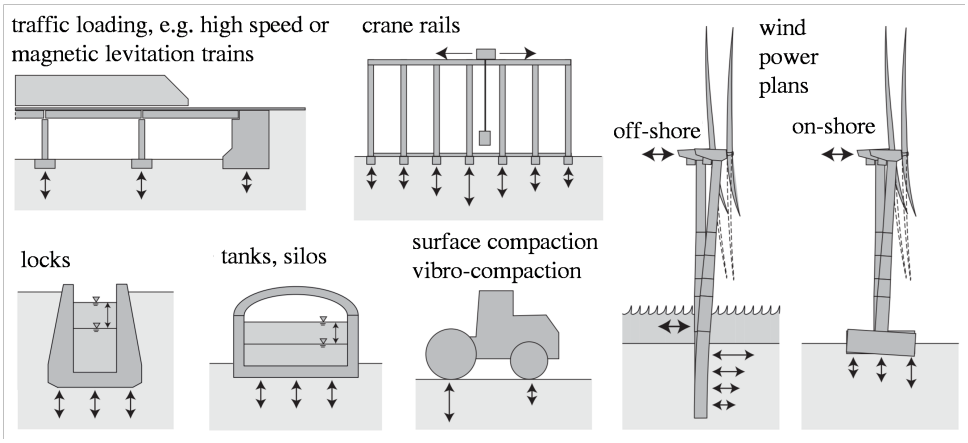

Figure 2.1: Illustration of sources of cyclic loading (Wichtmann, 2016)

2.1 Characteristics of Cyclic Loading

The characteristics of cyclic loading are depending on its origin, and the cyclic loading varies in amplitude, period and duration. The time history of cyclic loading may be irregular with a cyclic amplitude changing from one wave to the next, and the average load component may also change during a storm. Cyclic loading from traffic and earthquakes have a cyclic load period around 1 s, whereas wave loading has a cyclic load period of 10–20 s (Andersen, 2009). In many cases different sources generate cyclic loading simultaneously, for instance wave and wind loads on an offshore wind power structure. Resonance of structures may also generate additional cyclic loading on the soil as a reaction to the primary source (Andersen, 2015).

The stress condition in soils subjected to cyclic loading is often complex. Figure 2.2 illustrates how the stress condition below a foundation subjected to cyclic loading may change along a potential failure surface. It is depending on the characteristics of the load, the soil properties and the type of foundation. The stress condition in the soil is described by different tests, Direct Simple Shear (DSS) and triaxial compression/extension test, along the failure surface, as presented in the figure. The different tests represent different combinations of average shear stress, τ_a, and cyclic shear stress, τ_{cy}, due to the cyclic loading.

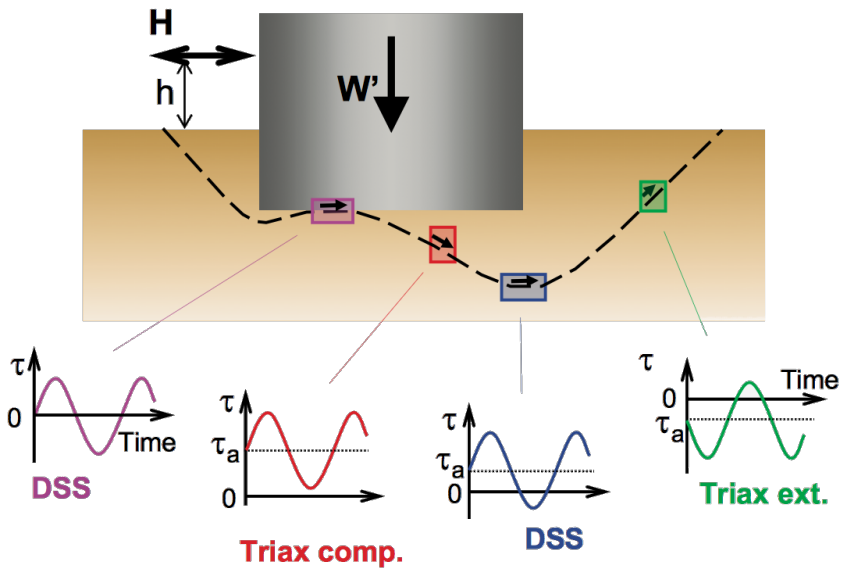

Figure 2.2: A typical stress condition below a foundation subjected to cyclic loading (Andersen, 2015)

A simple expression of the average shear stress, τ_a, is given in Equation 2.1.

$$\tau_a = \tau_0 + \Delta\tau_a \tag{2.1}$$

Where τ_0 is the initial shear stress in the soil prior to installation of any structures and $\Delta\tau_a$ is the additional shear stress due to the submerged weight of the structure and any average environmental loads. The soil is consolidated under the initial shear stress, and the stress acts under drained conditions. The average shear stress contribution acts under drained conditions after the soil is consolidated. For sand, this will happen relatively fast.

The cyclic shear stress, τ_{cy}, appears due to cyclic loading. As mentioned above, the cyclic loads may vary in amplitude, period and duration which also applies for the cyclic shear stress. The cyclic shear stress may vary from one cycle to the next. Figure 2.3 illustrates how the shear stresses, τ, and shear strains, γ, are defined according to Andersen (2015). The development of shear strains are not depending on the maximum shear stress alone, but the combination of cyclic and average shear stress.

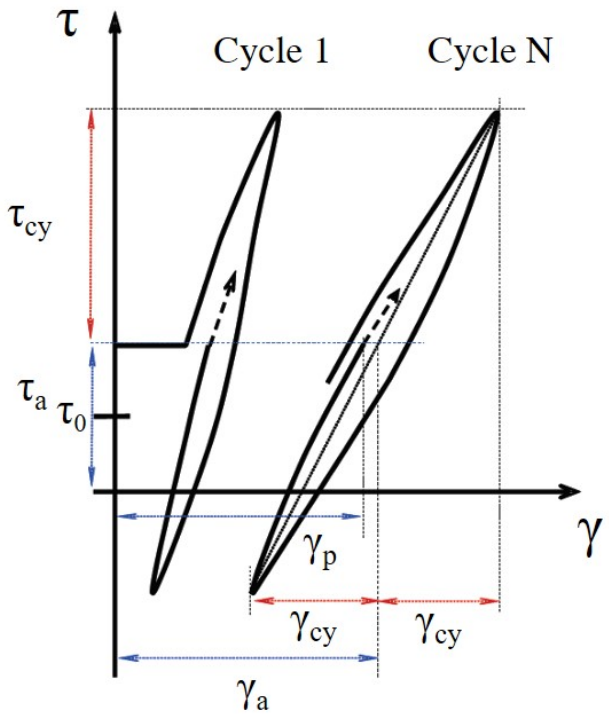

Figure 2.3: Definition of shear stresses and shear strains (Andersen, 2015)

2.2 Soil Subjected to Cyclic Loading

When sand is subjected to cyclic loading, the soil structure is gradually broken down and it causes a tendency of volumetric reduction in the soil. If the soil is saturated and the water in the pores is unable to drain away, i.e. *undrained* condition, volumetric changes are prevented by the low volumetric compressibility of the water. The normal stresses that were carried by the soil will be transferred to the pore water, and the effective stresses in the soil will decrease accordingly. As the effective stresses decrease, the soil becomes weaker and more deformable (Andersen, 2009).

Figure 2.4 illustrates the effective stress paths of a soil subjected to monotonic and cyclic loading. The discontinuous line corresponds to an effective stress path due to monotonic loading, and the path hits the failure envelope at a maximum shear stress, softens and follows the failure envelope. The continuous lines correspond to an effective stress path due to cyclic loading, where a constant average shear stress, τ_a, is applied, in addition to a cyclic shear stress, τ_{cy}, smaller than the maximum shear stress in the monotonic path. The first cycle forms a loop that ends up to the left of the starting point, with a decreased effective stress, σ'. The difference in effective stresses corresponds to a developed pore water pressure, u_p. When additional load is applied, the build-up of pore water pressure increases, and the cycle hits the failure envelope. The dense sand dilates as the path follows the failure envelope due to its strong dilative properties. For the following cycles, the stress path reaches and follows the failure envelope repeatedly during a large part of each cycle and forms a butterfly shape. The soil structure is gradually broken down, and larger strains are required to mobilise negative pore water pressure (Andersen, 2015).

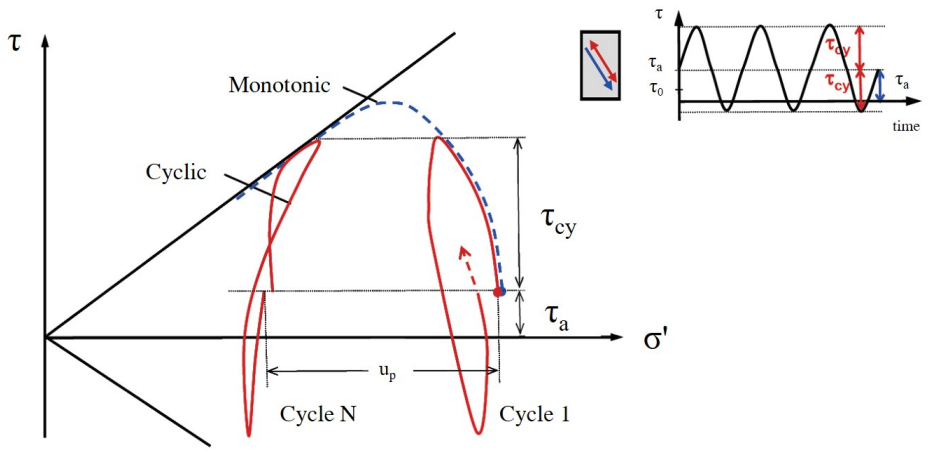

Figure 2.4: Monotonic and cyclic stress paths (Andersen, 2015)

The accumulation of pore water pressure with time for an undrained condition is illustrated in Figure 2.5. The cyclic loading generates a permanent pore water pressure component, u_p, and a cyclic pore water pressure component, u_{cy}. The increased pore water pressure reduces the effective stresses, resulting in an increased permanent shear strain and cyclic shear strain amplitude with time.

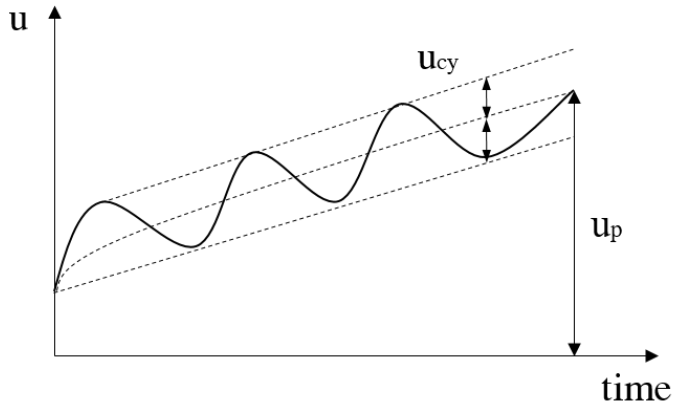

Figure 2.5: Pore water pressure development with time (Andersen, 2015)

2.2.1 Dilatancy and Change in Fabric

Dilatancy and change in fabric are two important parameters describing the behaviour of sand due to cyclic loading. Dilatancy describes the volume change when a granular material is subjected to shear deformation. The sand dilates when it is subjected to shear stress because grains are interlocking. The particles start to climb over each other as they do not have the freedom to move around one another. If the material is initially in a loose state it may contract instead of dilate when shear stress is applied. A specimen is characterised as contractive if it tends to decrease in volume when the shear stress is increased, and dilative if it tends to increase in volume when the shear stress is increased (Casagrande and Hirschfeld, 1962). The dilatancy behaviour is characterised by the phase transformation line. The phase transformation line describes the change from a contractive to a dilative behaviour (Lade and Ibsen, 1997).

Fabric change describes a change in grain structure. During compression of a dense sand, it will first have a tendency to contract, before it dilates. When it dilates, the fabric changes. The fabric is defined as the sand particle contact-normal orientation distribution (Nasser, 1980). The change in fabric makes the sand start to contract when a reversal load

is applied. The particle contact plane orientations are biased toward dilation in forward shearing and then becomes biased toward contraction in reverse shearing. The same fabric change effects will appear during dilation in reversed shearing, but in reverse sense. This behaviour repeats for further cycles (Nemat-Nasser and Tobita, 1982).

The concept of fabric change is illustrated in Figure 2.6, where L_1 and L_2 refer to the major and minor principal stresses respectively. The loading direction influences how the grain structure changes, and the figure illustrates two situations that have identical void ratios prior to loading. The grain structure expands when L_1 is in the vertical direction, the void ratio increases and the the sand dilates. When L_1 is in the horizontal direction, the grain structure contracts, and the void ratio decreases. This is why the sand starts to contract when the load is reversed during cyclic loading.

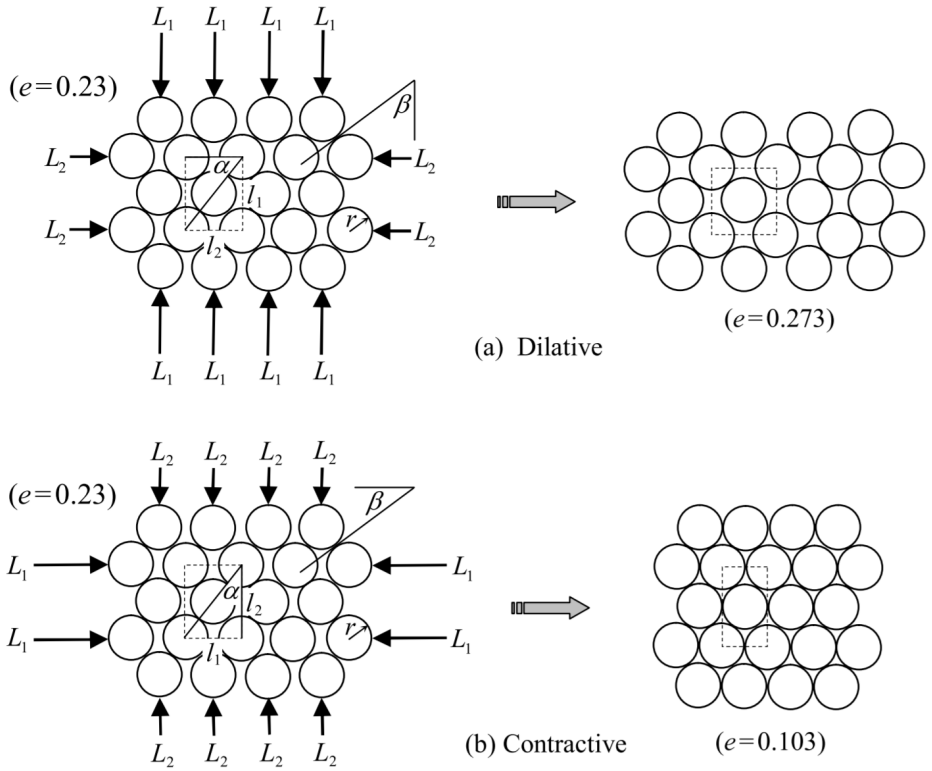

Figure 2.6: Impact of loading direction (a) dilative; (b) contractive (Li and Dafalias, 2011)

Chapter 3

Material Models

Different models are used to describe the behaviour of soils. The behaviour of soil is complex, and no constitutive model is able to describe a soil under all conditions. This chapter will give a brief introduction to elasto-plasticity, critical state soil mechanics and the bounding surface plasticity model which form the basis of the SANISAND constitutive model described in Chapter 4.

3.1 Elastic-Plastic Model for Soil

Elastic-plastic material models are based on the principle that total strains can be separated into elastic strains, ε^e, and plastic strains, ε^p, see Equation 3.1 (Irgens, 2008).

$$\varepsilon = \varepsilon^e + \varepsilon^p \tag{3.1}$$

The elastic strains are reversible, there is no permanent deformation or change in geometry. The plastic strains are irrecoverable, and permanent deformations will occur.

3.1.1 Elasticity

In an elastic model there is a one-to-one relationship between stress and strain. The relationship may be linear or non-linear, and may be described with a material law. An example of a linear material law is Hooke's law (Hooke, 1675), which states that the stress increment is proportional to the strain increment with an elastic modulus, E, Equation 3.2.

$$d\varepsilon^e = \frac{d\sigma}{E} \tag{3.2}$$

The linear relation of Hooke's law states that all elastic strains are reversible.

The isotropic elastic stiffness can be described in different ways. It can be described with the constants E and ν. Sometimes it can be more advantageous to use the elastic constants G and K. The shear modulus, G, in Equation 3.3 is associated to the stiffness related to change in shape and the bulk modulus, K, in Equation 3.4 controls the stiffness related to the relative change in volume.

$$G = \frac{\Delta\tau}{\Delta\gamma} = \frac{E}{2(1+\nu)} \tag{3.3}$$

$$K = \frac{\Delta p'}{\Delta\varepsilon_v} = \frac{E}{3(1-2\nu)} \tag{3.4}$$

The benefit of using G and K is great when elasticity of soil is considered (Wood, 1990). When undrained deformation is described, the volume is constant, and the deformation is pure distortion of soil, the shape of the soil is changed, but the size is still the same.

3.1.2 Plasticity

In elastic materials the mechanism of deformation depends on the stress increment. For plastic materials, the mechanism of plastic deformations depends on the stress. When trying to apply a load above the failure limit, the material will yield and plastic strains will develop. When reversing a plastic deformation there will be dissipation of plastic work, in contrast to reversing of elastic deformations. The elastic work of reversing a deformation equals the elastic work of initiating a deformation such that the total elastic work is zero.

The yield criteria can be defined as a limiting surface in the stress space. For stress increments inside the limiting surface, $F < 0$, the strains are elastic, for $F = 0$, on the yield surface, the material is yielding plastic deformation and may also cause elastic strains. $F > 0$ is impossible.

What happens when the load is increased to a stress level above the failure limit is described by the plastic flow rule, Equation 3.5.

$$d\varepsilon^p = d\lambda \left\{ \frac{\partial Q}{\partial \sigma} \right\} \tag{3.5}$$

Where Q is the plastic potential and $d\lambda$ is the plastic multiplier. For $Q = F$ the flow rule is associative and the plastic flow is perpendicular to the yield surface. For $Q \neq F$ the flow rule is non-associative.

3.1.3 Elasto-Plasticity

There are several ways of idealising an elastic-plastic material. Figure 3.1 illustrates different elasto-plastic models.

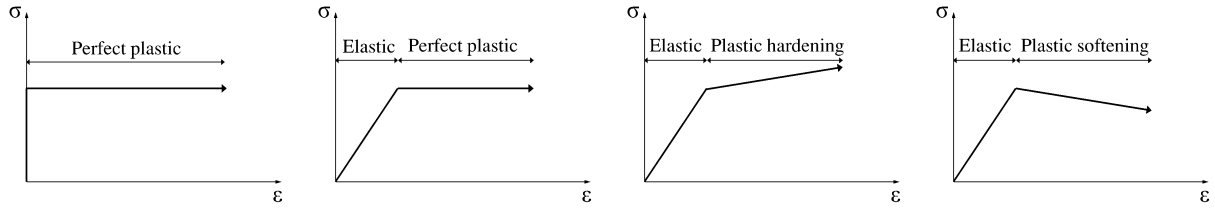

(a) Rigid perfectly plastic (b) Elastic perfectly plastic (c) Elastic-plastic hardening (d) Elastic-plastic softening

Figure 3.1: Idealisation of elasto-plastic behaviour

The linear elastic perfectly plastic model (Figure 3.1b) is the simplest elasto-plastic model. There is no hardening or softening of the material. When the stress is below the failure line elastic strains will develop, and when the stress is on the failure line plastic strains will develop. Loading above the failure line is not possible. Unloading will give an elastic response. Figure 3.1a illustrates a model which only includes the plastic component, and Figure 3.1c and Figure 3.1d illustrates plastic hardening and softening respectively.

3.2 Critical State Soil Mechanics

If a sample of granular soil is continuously sheared it will end up in a critical state. Wood (1990) defined the critical state as a state where large shear strains may be applied without any change in effective stresses or volume. The framework is based in the $p' - q$ and $p' - e$ space, where q is the deviatoric stress, p' is the effective mean stress and e is the void ratio.

Critical State Soil Mechanics (CSSM) states that if you shear a sand in drained condition it will end up at a constant critical void ratio, independent of the initial void ratio. In this state, called a critical state, shear distortion occurs without any further changes in mean effective stress, deviatoric stress or void ratio. Shearing of a dense sand at a constant normal effective stress causes an initial contraction, followed by an expansion where the void ratio increases, and ends up at a constant void ratio at large displacements, the critical void ratio. On the other hand, shearing of a loose sand at the same effective stress level results in a decrease in void ratio as the soil is compacted until the same constant void ratio, the critical void ratio. This is illustrated in Figure 3.2 on page 14.

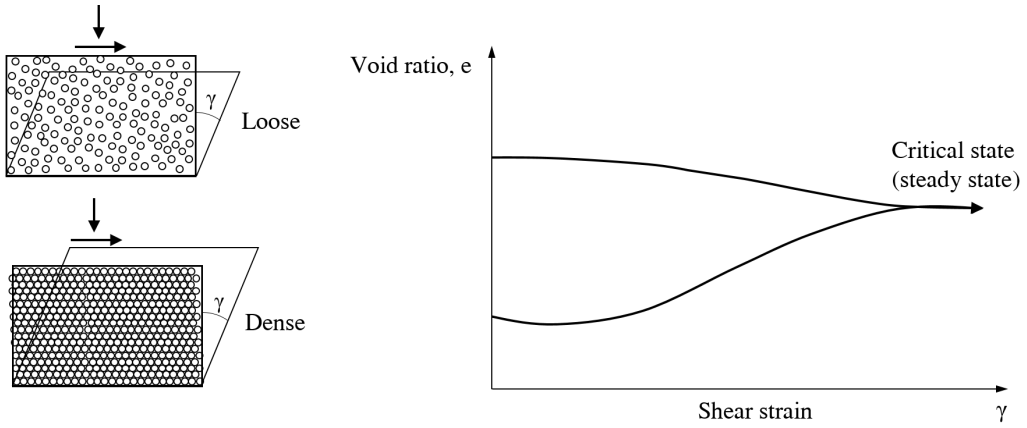

Figure 3.2: Shearing of a loose and dense sample towards a critical state. Adapted from Nordal (2016).

The critical void ratio is depending on the normal effective stress, where an increase in stress results in a decrease in critical void ratio (Casagrande, 1979). A Critical State Line (CSL) describes the combination of effective stress and critical void ratio at which shearing of soil may continue indefinitely. This is illustrated in Figure 3.3. For any initial conditions where the void ratio is above the CSL, the void ratio will decrease during shearing, and for void ratios below CSL, the void ratio will increase during shearing when the volume is allowed to change. The critical state line defines the failure state of the soil. For undrained conditions, there is no change in void ratio and the soil follows a path to the left or right in relation to the CSL.

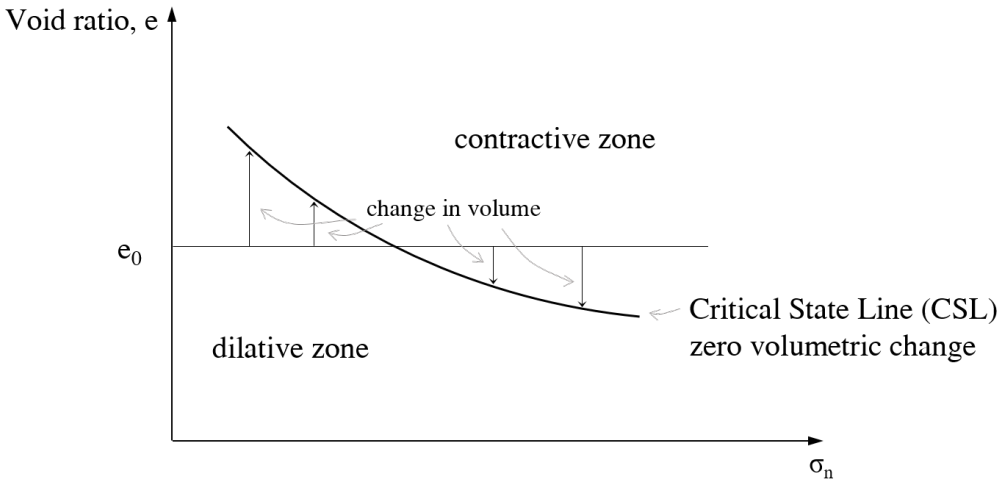

Figure 3.3: Illustration of Critical State Line

The model is based on the following equations obtained from Wood (1990). The deviatoric stress and mean stress is defined by the principal stresses, σ_1, σ_2 and σ_3, in Equation 3.6.

$$q = \sigma_1 - \sigma_3; \qquad p = \frac{1}{3}(\sigma_1 + 2\sigma_3) \tag{3.6}$$

The incremental strains are, like in the elasto-plastic model, the sum of the incremental elastic strains and incremental plastic strains. The incremental elastic and plastic strains are given in Equation 3.7 and 3.8 respectively.

$$d\boldsymbol{\varepsilon}^e = \begin{bmatrix} d\varepsilon_p^e \\ d\varepsilon_q^e \end{bmatrix} = \begin{bmatrix} \frac{1}{K} & 0 \\ 0 & \frac{1}{3G} \end{bmatrix} \begin{bmatrix} dp' \\ dq \end{bmatrix} = \boldsymbol{D}^{-1} d\boldsymbol{\sigma} \tag{3.7}$$

$$d\boldsymbol{\varepsilon}^p = \begin{bmatrix} d\varepsilon_p^p \\ d\varepsilon_q^p \end{bmatrix} = d\lambda \begin{bmatrix} \frac{\partial F}{\partial p'} \\ \frac{\partial F}{\partial q} \end{bmatrix} = d\lambda \begin{bmatrix} M^2\left(2p' - p_0'\right) \\ 2q \end{bmatrix} \tag{3.8}$$

K and G are the bulk and shear modulus respectively. M is the critical stress ratio and λ is a soil constant. CSSM use an elliptic yield surface, Equation 3.9, and is shown in Figure 3.4.

$$F = q^2 - M^2\left[p'\left(p_0' - p'\right)\right] = 0 \tag{3.9}$$

Where p_0' is the isotropic preconsolidation stress. The critical stress ratio, M, is related to the friction angle, ϕ, with the Coulomb criterion $M = 6\sin\phi/(3 \pm \sin\phi)$ where minus (-) is used for triaxial compression and plus (+) is used for triaxial extension. The M-line is considered as a residual strength limit for large strains. The elliptic yield line allows stress points above the M-line for small stresses, but after shearing, the material will arrive at a critical state which coincide with this M-line.

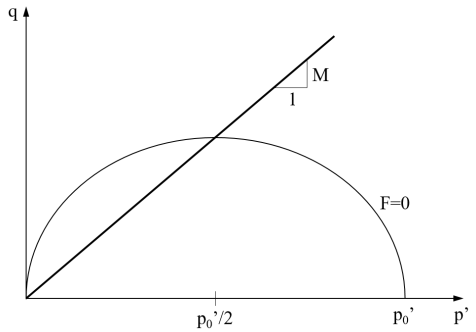

Figure 3.4: Critical state soil mechanics yield surface

3.3 Bounding Surface Plasticity Model

The concept of a bounding surface in the stress space was first introduced for metals by Dafalias and Popov (1975). The model has later been extended to other materials such as soils (Bardet, 1986; Dafalias, 1986).

The bounding surface limits plastic deformations to occur only for stress states on or within the bounding surface. For any stress state below or on the bounding surface, a mapping rule associates the stress state with a corresponding stress point on the bounding surface. The distance between the actual stress point and the corresponding stress point is used to specify the plastic modulus at the actual point in terms of a bounding plastic modulus at the corresponding stress state (Dafalias, 1986). The bounding surface evolves as the soil is deformed, and is therefore not identical to a critical state.

Different shapes of the bounding surface have been described in the literature, a straight line is used in the SANISAND model (Dafalias and Manzari, 2004). Khalili et al. (2005) describe a bounding surface determined from the undrained response of soil at its loosest state. Figure 3.5 illustrates the loading surface and bounding surface for a first time loading. The distance between the stress point, σ', on the loading surface and the stress point $\bar{\sigma}$ on the bounding surface defines a decreasing function of the plastic modulus (Tennakoon et al., 2015).

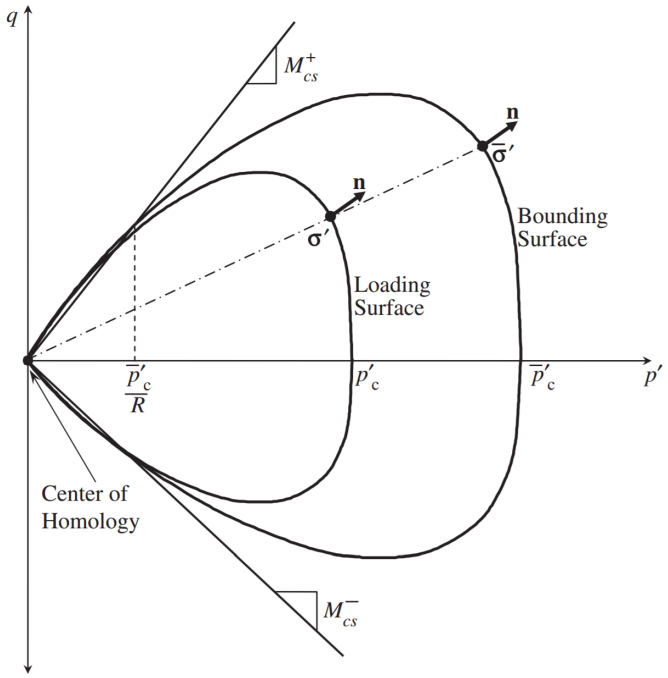

Figure 3.5: Loading surface and bounding surface (Khalili et al., 2005)

Chapter 4

SANISAND Constitutive Model

SANISAND is the name used for a family of Simple ANIsotropic SAND constitutive models (Taiebat and Dafalias, 2007). SANISAND is developed to realistically simulate the stress-strain behaviour of sands under monotonic and cyclic, drained and undrained loading conditions. Manzari and Dafalias (1997) introduced a critical state two-surface plasticity model for sands, a model in the triaxial $p' - q$ space based on the critical state soil mechanics framework and the bounding surface plasticity model. The model is meant to be simple and easy to understand, and can easily be modified to account for aspects of material response. In this thesis a SANISAND model which is extended to account for the effect of fabric changes during loading will be presented (Dafalias and Manzari, 2004).

The SANISAND model is based on the assumption that only changes of stress ratio ($\eta = q/p'$) can cause plastic deformation. Increased stress with a constant stress ratio is assumed to only cause elastic deformations, assuming there is no crushing of grains. A stress increment is applied, and thus the model is not able to simulate softening behaviour.

The model will be described in the triaxial stress space, before the generalisation to the multiaxial stress space will be briefly introduced. A validation and a parameter study of the model will then be presented.

4.1 Triaxial Formulation

The SANISAND equations are formulated in the triaxial stress space, with all stress components considered as effective stresses. All equations are obtained from (Dafalias and Manzari, 2004) if not else is specified. The principal stresses and strains are defined in the axisymmetric triaxial space as σ'_1, $\sigma'_2 = \sigma'_3$ and ε_1, $\varepsilon_2 = \varepsilon_3$.

The deviatoric stress, q, and mean stress , p, are defined as in Equation 4.1. Deviatoric strain, ε_q, and volumetric strain, ε_v, are defined as in Equation 4.2.

$$q = \sigma_1 - \sigma_3; \qquad p = \frac{1}{3}(\sigma_1 + 2\sigma_3) \tag{4.1}$$

$$\varepsilon_q = \frac{2}{3}(\varepsilon_1 - \varepsilon_3); \qquad \varepsilon_v = \varepsilon_1 + 2\varepsilon_3 \tag{4.2}$$

The strains are divided into an elastic and a plastic part. The incremental stress-strain relations for the elastic and plastic parts are given in Equation 4.3 and 4.4 respectively.

$$d\varepsilon_q^e = \frac{dq}{3G}; \qquad d\varepsilon_v^e = \frac{dp}{K} \tag{4.3}$$

$$d\varepsilon_q^p = \frac{d\eta}{H}; \qquad d\varepsilon_v^p = d\left|d\varepsilon_q^p\right| \tag{4.4}$$

Where $\eta = q/p'$ is the stress ratio, G is the elastic shear modulus, K is the elastic bulk modulus, H is the plastic hardening modulus, and d is the dilatancy parameter.

The elastic moduli G and K, given in Equation 4.5 and 4.6, are defined according to Richart et al. (1970) and Li and Dafalias (2000) and are functions of the mean stress, p, and the void ratio, e.

$$G = G_0 p_{\text{atm}} \frac{(2.97 - e)^2}{1 + e} \left(\frac{p}{p_{\text{atm}}}\right)^{1/2} \tag{4.5}$$

$$K = \frac{2(1+\nu)}{3(1-2\nu)} G \tag{4.6}$$

G_0 is a dimensionless material constant, ν is the Poisson's ratio and p_{atm} is the atmospheric pressure.

Incremental plastic shear strains occur only when $d\eta \neq 0$ (Equation 4.4). Consequently a stress-ratio defined yield surface is proposed in Equation 4.7. It also represents a wedge shown by the shaded area in Figure 4.1. The bisecting line has a slope α and the opening of the wedge has a value of $2mp$. When η has a value inside the wedge, only elastic strains will occur. A stress ratio, η, on the wedge will induce plastic strains.

$$f = |\eta - \alpha| - m = 0 \tag{4.7}$$

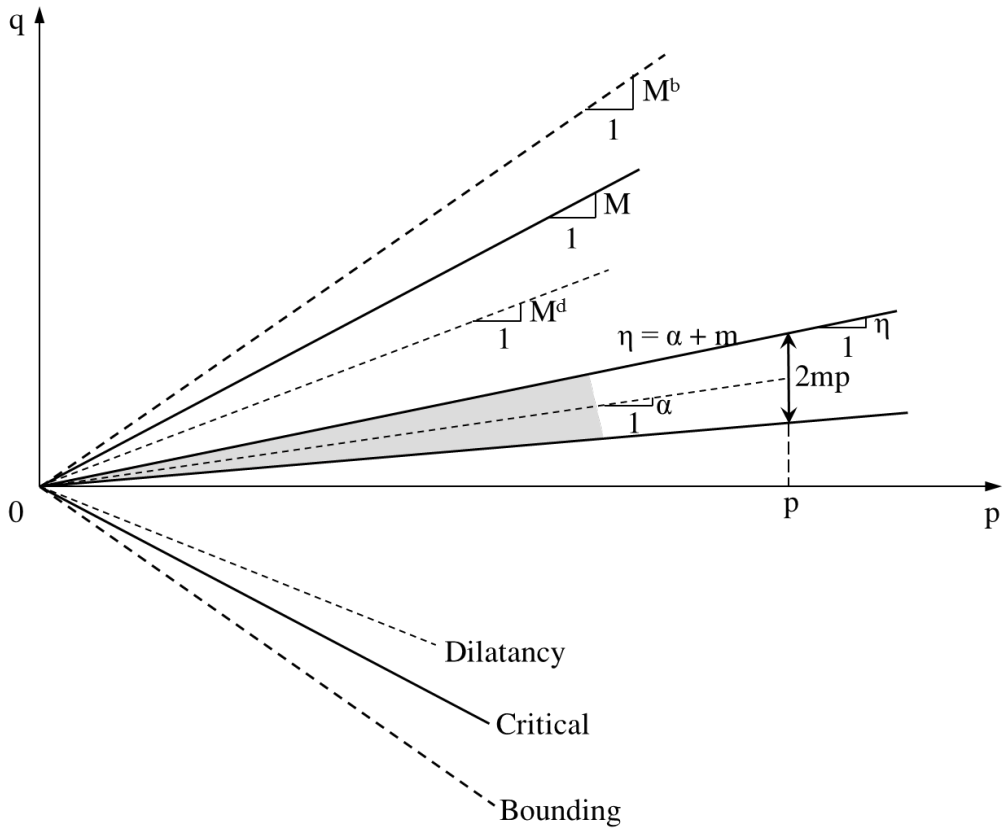

Figure 4.1: Schematic of the yield, critical, dilatancy and bounding lines in $p' - q$ space (Dafalias and Manzari, 2004)

The stress ratio, η, will increase under monotonic drained triaxial compression loading, but is bounded by the bounding stress ratio, M^b, illustrated as a discontinuous line in Figure 4.1. The bounding stress ratio varies with the material state and is related to the hardening modulus, H, Equation 4.8. The amplitude of H depends on the distance from the current stress ratio to the bounding line.

$$H = h\left(M^b - \eta\right) \tag{4.8}$$

Where h is a function of the state variables, and varies with b_0. The equations of h and b_0 are shown in Equation 4.9.

$$h = \frac{b_0}{|\eta - \eta_{\text{in}}|}; \qquad b_0 = G_0 h_0 \left(1 - c_h e\right) \left(\frac{p}{p_{\text{atm}}}\right)^{-1/2} \tag{4.9}$$

η_{in} is the initial stress ratio at the initiation of a loading process, and is updated when the loading is reversed, according to Dafalias (1986), and h_0 and c_h are scalar parameters.

The dilatancy parameter, d, given in Equation 4.10, is proportional to the difference of current stress ratio, η, from dilatancy stress ratio, M^d. The dilatancy stress ratio, M^d, is shown as a dashed line in Figure 4.1 and is also called the phase transformation line.

$$d = A_d \left(M^d - \eta \right) \tag{4.10}$$

Where A_d is a function of the state. A contractant behaviour is obtained when $d > 0$, and for $d < 0$ there is a dilatant behaviour of the material.

SANISAND is a material model based on the critical state soil mechanics framework. The critical state stress ratio, M, is defined from the critical deviatoric stress, q_c, and the critical mean stress, p_c, and is shown as a continuous straight line in Figure 4.1. From Section 3.2 about Critical State Soil Mechanics, the critical state line is different in compression and extension, to account for this a c-parameter is introduced in the model as the relation between M in compression and extension. While M is related to the friction angle, the critical void ratio, e_c, and the critical mean stress, p_c, vary depending on the soil and for the range of pressure considered. A relation between e_c and p_c is suggested by Wang and Li (1998) in Equation 4.11.

$$e_c = e_0 - \lambda_c \left(\frac{p_c}{p_{\text{atm}}} \right)^{\xi} \tag{4.11}$$

Where e_0 is the initial void ratio at $p_c = 0$, and λ_c and ξ are constants.

Li and Dafalias (2000) introduced an exponential variation of the bounding and dilatancy line, given in Equation 4.12 and Equation 4.13. The bounding and dilatancy lines vary with the material state, and the lines are defined in such a way that when $e = e_c$ and $p = p_c$ then $M^b = M^d = M$.

$$M^b = M \exp(-n^b \Psi) \tag{4.12}$$

$$M^d = M \exp(n^d \Psi) \tag{4.13}$$

Where n^b and n^d are positive material constants, and Ψ is called the state parameter by Been and Jefferies (1985), and is defined in Equation 4.14.

$$\Psi = e - e_c \tag{4.14}$$

This version of the SANISAND model is extended to account for the effect of fabric change on dilatancy. The fabric-dilatancy internal variable, z, is introduced. The z will influence the dilatancy, d, to give a more realistic interpretation of the soil behaviour under cyclic loading. Initially the $z = 0$, and Equation 4.15 gives the development in z. For a contractant behaviour there is no development in z, $dz = 0$ because $\langle -d\varepsilon_v^p \rangle = 0$, and for a dilatant behaviour a negative z will develop in compression and a positive z will develop during dilation in triaxial extension.

$$dz = -c_z \langle -d\varepsilon_v^p \rangle (sz_{\max} + z) \tag{4.15}$$

$z_{\max}$ is the maximum value z can attain and c_z controls the speed of the change in z. The parameter A_d of the dilatancy is a function of z given in Equation 4.16.

$$A_d = A_0 (1 + \langle sz \rangle) \tag{4.16}$$

The Macaulay brackets, $\langle\rangle$, are used to describe a ramp function, $\langle sz \rangle = sz$ for $sz > 0$ and $\langle sz \rangle = 0$ for $sz \leq 0$. The parameter, s, defines the direction of loading, and is +1 for triaxial compression and -1 for triaxial extension.

4.2 Multiaxial Generalisation

The model is generalised to a multiaxial/generalised stress space by the work of Manzari and Dafalias (1997). In the multiaxial generalisation the yield surface was independent of the third stress invariant. The generalisation by Dafalias and Manzari (2004) introduces a dependency for the plastic deviatoric strain rate direction to facilitate a more realistic stress-strain simulation. Table 4.1 on page 22 shows the triaxial equations and the corresponding multiaxial constitutive equations. The input material constants are also listed in the table.

Table 4.1: Triaxial and corresponding multiaxial constitutive equations with associated model constants (Dafalias and Manzari, 2004)

Triaxial equations	**Multiaxial equations**	**Constants**
Critical state line		
—	$e_c = e_0 - \lambda_c (p_c / p_{\text{atm}})^{\xi}$	e_0, λ_c, ξ
Elastic deviatoric strain increment		
$d\varepsilon_q^e = dq/3G$	$d\boldsymbol{e}^e = d\boldsymbol{s}/2G$	—
—	$G = G_0 p_{\text{atm}} \left[(2.97-e)^2/(1+e)\right] \left(p/p_{\text{atm}}\right)^{1/2}$	G_0
Elastic volumetric strain increment		
—	$d\varepsilon_v^e = dp/K$	
	$K = 2(1+\nu)G/3(1-2\nu)$	ν
Yield surface		
$f = \lvert\eta - \alpha\rvert - m = 0$	$f = \left[(\boldsymbol{s} - p\boldsymbol{\alpha}) : (\boldsymbol{s} - p\boldsymbol{\alpha})\right]^{1/2} - \sqrt{2/3}pm = 0$	m
Plastic deviatoric strain increment		
$d\varepsilon_v^p = d\eta / H$	$d\boldsymbol{e}^p \langle L \rangle \boldsymbol{R}'$	
$H = h(M^b - \eta)$	$K_p = (2/3) p h (\boldsymbol{\alpha}_\theta^b - \boldsymbol{\alpha}) : \boldsymbol{n}$	
$M^b = M \exp(-n^b \boldsymbol{\Psi})$	$\boldsymbol{\alpha}_\theta^b = \sqrt{2/3}[g(\theta, c) M \exp(-n^b \Psi) - m]\boldsymbol{n}$	M, c, n^b
$h = b_0 / \lvert\eta - \eta_{\text{in}}\rvert$	$h = b_0 / (\boldsymbol{\alpha} - \boldsymbol{\alpha}_{\text{in}}) : \boldsymbol{n}$	
—	$b_0 = G_0 h_0 (1 - c_h e)(p/p_{\text{atm}})^{-1/2}$	h_0, c_h
Plastic volumetric strain increment		
$d\varepsilon_v^p = d\lvert\varepsilon_q^p\rvert$	$d\varepsilon_v^p = \langle L \rangle D$	
$d = A_d (M^d - \eta)$	$D = A_d (\boldsymbol{\alpha}_\theta^b - \boldsymbol{\alpha}) : \boldsymbol{n}$	
$M^d = M \exp(-n^d \boldsymbol{\Psi})$	$\boldsymbol{\alpha}_\theta^d = \sqrt{2/3}[g(\theta, c) M \exp(-n^d \Psi) - m]\boldsymbol{n}$	n^d
$A_d = A_0 (1 + \langle sz \rangle)$	$A_d = A_0 (1 + \langle \boldsymbol{z} : \boldsymbol{n} \rangle)$	A_0
Fabric-dilatancy tensor update		
$dz = -c_z \langle -d\varepsilon_v^p \rangle (s z_{\max} + z)$	$d\boldsymbol{z} = -c_z \langle -d\varepsilon_v^p \rangle (z_{\max} \boldsymbol{n} + \boldsymbol{z})$	$c_z, z_{\max}$
Back-stress ratio tensor update		
$d\alpha = d\eta$	$d\boldsymbol{\alpha} = \langle L \rangle (2/3) h (\boldsymbol{\alpha}_\theta^b - \boldsymbol{\alpha})$	

4.3 Parameter Study

To verify the SANISAND model presented in this thesis, a comparison with the simulation of Toyoura sand in Dafalias and Manzari (2004) is performed. Dafalias and Manzari (2004) introduces a set of input parameters for the Toyoura sand, given in Table 4.2, and illustrates how the model represents the behaviour of the sand by several plots of stress paths and strains.

Table 4.2: SANISAND parameters for Toyoura sand (Dafalias and Manzari, 2004)

Input parameters		**Value**
Elasticity	G_0	125
	ν	0.05
Critical state	M	1.25
	c	0.712
	λ_c	0.019
	e_0	0.934
	ξ	0.7
Yield surface	m	0.01
Plastic modulus	h_0	7.05
	c_h	0.968
	n^b	1.1
Dilatancy	A_0	0.704
	n^d	3.5
Fabric dilatancy	$z_{\max}$	5
	c_z	600

The Toyoura sand is simulated as an undrained isotropic consolidated triaxial test. The test is consolidated to $\sigma_{ac} = \sigma_{rc} = 250$ kPa and $q = \pm 114.2$ kPa is applied. A comparison of the $p' - q$ plot and $\varepsilon_a - q$ plot of the simulation with $z_{\max} = 0$ is given in Figure 4.2 on page 24. The same simulation including the effect of fabric change on the dilatancy, with a $z_{\max} = 5$, is shown in Figure 4.3 on page 24. The figures at the top (in black) are taken from the article, while the figures below (in red) are the simulations from the model presented in this thesis. The comparisons of the models display a stress path that coincide well. The behaviour of the models are very similar, and the representations are satisfying. However, a small change in axial strains is noticed. The model from Dafalias and Manzari (2004) differs from the model in this thesis as it includes an elastic core of 1 % by defining $m = 0.01$. The relative density, hence the value of the void ratio, e, is not given in the article, and the applied initial void ratio is found by trial and error, and set to $e = 0.734$.

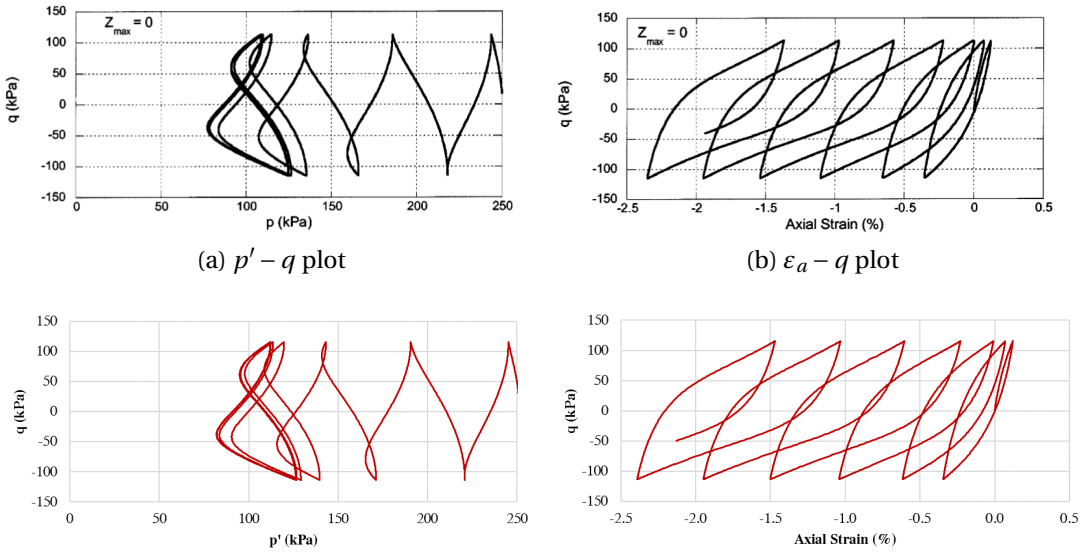

(a) $p' - q$ plot (b) $\varepsilon_a - q$ plot

(c) $p' - q$ plot (d) $\varepsilon_a - q$ plot

Figure 4.2: Verification of model, $z_{\max} = 0$

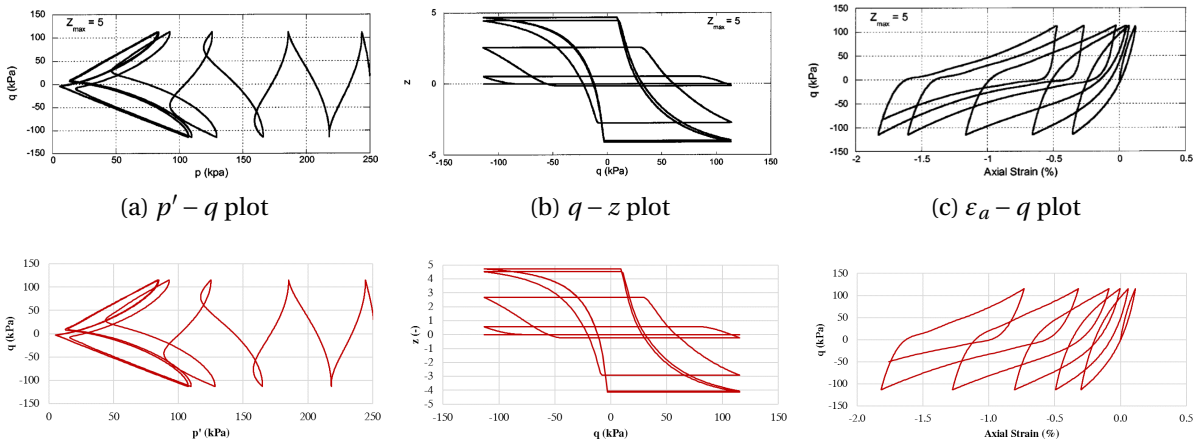

(a) $p' - q$ plot (b) $q - z$ plot (c) $\varepsilon_a - q$ plot

(d) $p' - q$ plot (e) $q - z$ plot (f) $\varepsilon_a - q$ plot

Figure 4.3: Verification of model, $z_{\max} = 5$

4.3.1 Isotropic versus Anisotropic Consolidation

The example from Dafalias and Manzari (2004) is isotropic consolidated, a simulation with anisotropic consolidation is performed to verify the validity of the model. All simulations are consolidated with a radial consolidation stress of 90 kPa, while the axial consolidation stress is varied from 125 kPa to 200 kPa. The results are shown in Figure 4.4.

The model is able to represent an anisotropic consolidated triaxial test, and the load is imposed as a change in deviatoric stress, q. When the anisotropy in consolidation is large, $\sigma_{ac} \gg \sigma_{rc}$, the simulation barely hits the failure line in extension and the butterfly shape is less prominent.

The accumulation of axial strains depends on the anisotropy in the consolidation. When the anisotropy in the consolidation is large, with a significantly larger axial consolidation stress than radial consolidation stress, the simulation generates large positive axial strains. This is reasonable as the radial consolidation stress is too small to resist expansion of the sample in the radial direction. A simulation, where the radial consolidation stress is significantly larger than the axial consolidation stress, will generate large negative axial strains. The amplitude in the strain cycles are observed to be approximately the same, which differs from what is expected from a cyclic triaxial test where the amplitude of the strain cycles will increase with numbers of cycles. This is a weakness in the SANISAND simulations.

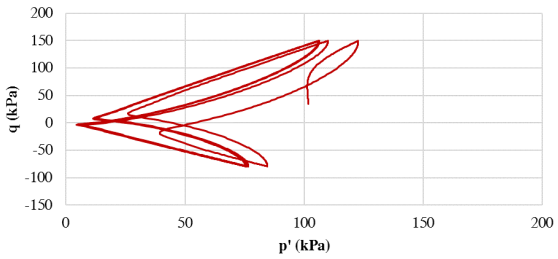

(a) $\sigma_{ac} = 125$ kPa, $\sigma_{rc} = 90$ kPa

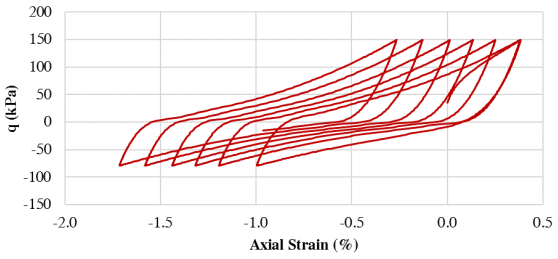

(b) $\sigma_{ac} = 125$ kPa, $\sigma_{rc} = 90$ kPa

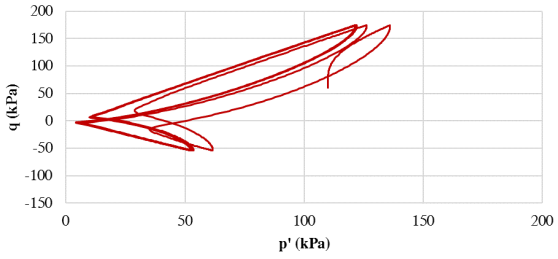

(c) $\sigma_{ac} = 150$ kPa, $\sigma_{rc} = 90$ kPa

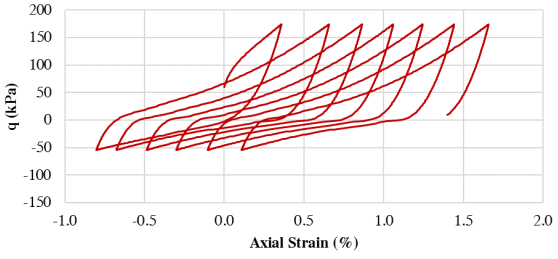

(d) $\sigma_{ac} = 150$ kPa, $\sigma_{rc} = 90$ kPa

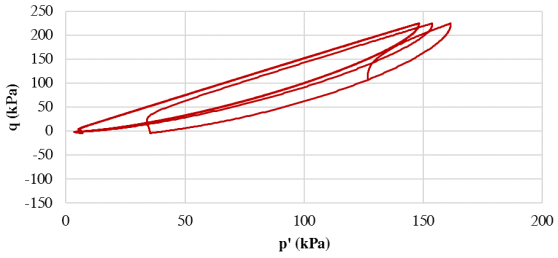

(e) $\sigma_{ac} = 200$ kPa, $\sigma_{rc} = 90$ kPa

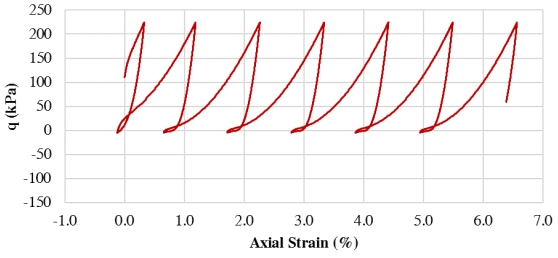

(f) $\sigma_{ac} = 200$ kPa, $\sigma_{rc} = 90$ kPa

Figure 4.4: Effect of change in consolidation pressure

4.3.2 Effect of Change in Relative Density

The model is able to represent different densities. A parameter study showing the simulations for different relative densities is given in Figure 4.5. The density is regulated with the void ratio, e, in the SANISAND model. The corresponding e for each relative density for the Toyoura sand is found in Zhang et al. (2013). For denser sand the model generates less pore water pressure for each cycle and also less accumulated strain per cycle compared with lower densities. For low relative densities, the model fails after a few cycles due to problems with the iterations. The problems in the iteration are due to large negative increments in the mean stress, $\mathrm{d}p'$, which eventually result in a negative value of p'.

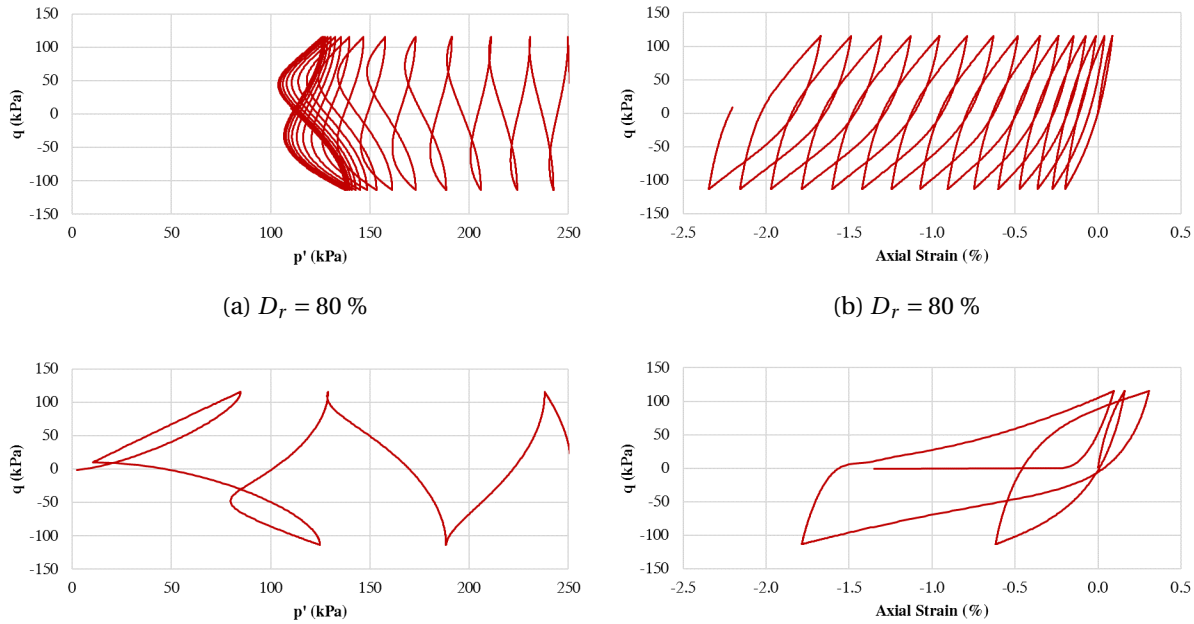

(a) $D_r = 80$ %

(b) $D_r = 80$ %

(c) $D_r = 40$ %

(d) $D_r = 40$ %

Figure 4.5: Effect of change in relative density

4.3.3 Loading Condition

To verify that the model is able to simulate different loading conditions, different stresses have been applied. Figure 4.6 illustrates how the model behaves when the applied change in deviatoric stress, q, is ±50 kPa and ±250 kPa. 20 cycles are applied for q = ±50 kPa, while 6 cycles are applied for q = ±250 kPa. The figures show that the model represents the different loading conditions reasonably. The case with decreased loading generates less pore water pressure per cycle and it takes more cycles to reach failure, compared to the case with larger loading. While less load results in smaller axial strains, greater load results in larger axial strains. This agrees with the response from the laboratory tests presented in Chapter 6.

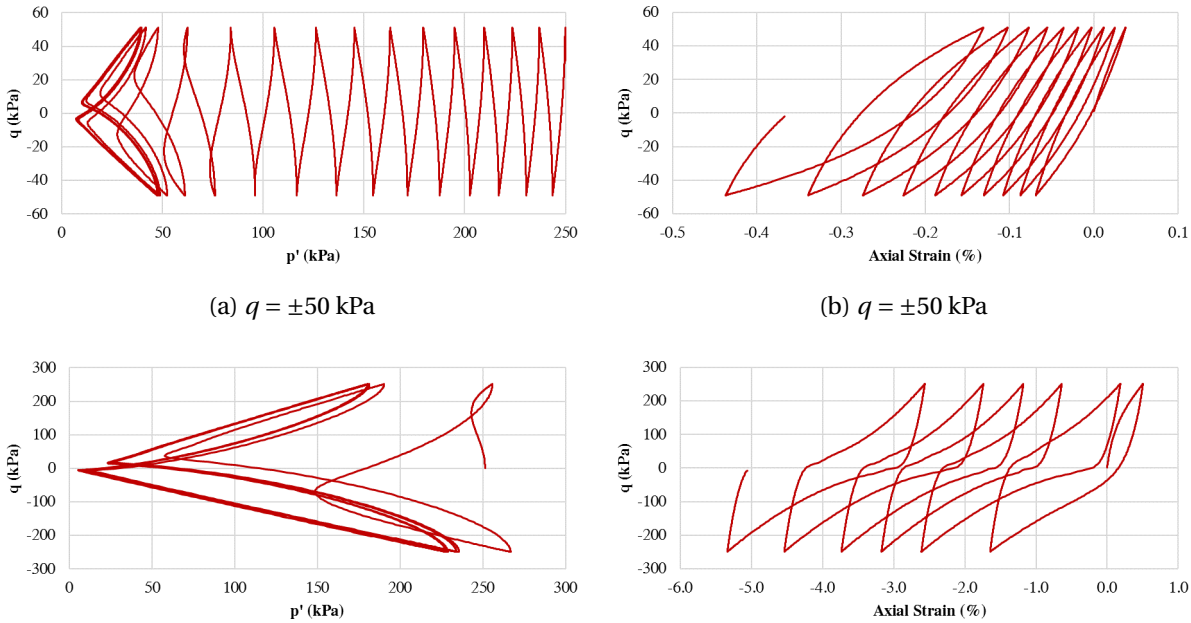

(a) q = ±50 kPa

(b) q = ±50 kPa

(c) q = ±250 kPa

(d) q = ±250 kPa

Figure 4.6: Different loading conditions

4.3.4 SANISAND Model Simulating Drained Response

The implementation of the SANISAND model is modified to account for drained response by allowing volume change. Figure 4.7 illustrates the stress path, the shear strain and the volume strain development for the drained implementation of the SANISAND model with the parameters listed in Table 4.2 on page 23. In the drained SANISAND model, the pore water pressure is allowed to dissipate and no pore water pressure is generated. Due to this, the stress path is identical for each cycle as observed in Figure 4.7a. In the undrained SANISAND model the pore water pressure builds up because the sand wants to contract. In the drained model, the volume is not prevented from changing, and the volume strains accumulate as presented in Figure 4.7c.

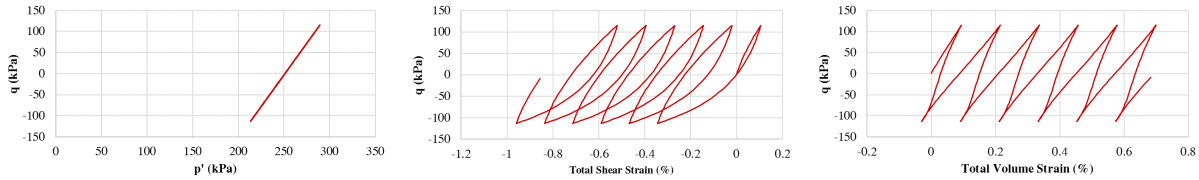

(a) p'-q plot (b) $\varepsilon_q - q$ plot (c) $\varepsilon_{vol} - q$ plot

Figure 4.7: Drained simulation of the SANISAND model

In addition to the test above, the simulation is run with an isotropic material. The isotropic material is simulated by applying identical parameters in compression and extension, by setting $c = 1$. A constant cyclic shear stress, q, is applied, and this results in a decrease in volume. The change in volume occurs because the mobilisation of strength is larger in extension compared to compression. In extension, the stress path moves closer to the strength envelope.

Chapter 5

Triaxial Test on Sand

The triaxial test is the most popular method to provide estimates of shear strength and pore water pressure parameters, as well as information of the stress-strain behaviour of a soil under controlled laboratory conditions. The main test principle is to apply a three-dimensional stress condition on the specimen, which corresponds as close as possible to the *in situ* stress conditions. The test results enable determination of both total and effective strength parameters, pore water pressure parameters and deformation properties of the soil (Sandven, 2011).

The triaxial test may be carried out as an active or passive test which correspond to compression or extension, respectively. The triaxial stress condition is described with the principal stresses, σ_1, σ_2 and σ_3. σ_1 is the major in-plane principal stress, σ_2 is the intermediate in-plane principal stress and σ_3 is the minor in-plane principal stress. In the active triaxial compression test, $\sigma_2 = \sigma_3$ in the horizontal direction, and σ_1 is in the vertical direction. In the passive triaxial extension test, $\sigma_1 = \sigma_2$ in the horizontal direction, and σ_3 corresponds to the vertical stress.

The triaxial test may be conducted in various ways, either drained or undrained, consolidated or unconsolidated, and the consolidation may be isotropic or anisotropic. The loading condition is either monotonic or cyclic, and there are several sample preparation methods. The behaviour of saturated sands is depending on the initial grain structure of the sand, the void ratio, and the mean effective stress level.

5.1 Drainage Conditions

An advantage of the triaxial test is the possibility to control the drainage conditions. During a triaxial test, an external total stress change is applied on the sample. The soil sample responds by an internal reaction in the grain skeleton and in the pore water. The drainage condition represents whether this change in pore water pressure is allowed to dissipate or not. The different drainage conditions are listed below (Sandven, 2011).

- For an *undrained condition* the dissipation of the excess pore water pressure is prevented, and there cannot be any volume change.
- For a *fully drained condition* any excess pore water pressure is permitted to dissipate, and there is no excess pore water pressure built up in the soil. This makes the effective stresses equal the total stresses.
- There are different ways of doing a triaxial test with a *partly drained condition*. For a standard partly drained test an excess pore water pressure develops during loading and unloading because the dissipation is going on at the same time as pore water pressure increase. Excess pore water pressure and volumetric strains are developed at the same time. A partly drained test in this thesis refers to a test where packages of 19-20 undrained cycles are applied with drainage in between each package.

5.2 Sample Preparation

During laboratory testing of sand, the sample preparation method plays an important part on how the test manages to represent the response of the sand. It is virtually impossible to obtain an undisturbed sample of sand in the laboratory, because the fabric of the sand in the field is not usually known (Mitchell et al., 1976). A sample prepared by two different methods conducting the same density may behave quite differently. The reason for the differences is associated with the change in fabric of the samples for the different sample preparation methods (Sze and Yang, 2013).

Figure 5.1 illustrates two different sample preparation methods. Figure 5.1 (a) and (b) show the procedures of Moist Tamping (MT) and Dry Deposition (DD) respectively. For the MT method, the sand is mixed with water to a specific water content and placed in the triaxial cylinder in layers. Each layer is tamped to a desired density, and the method tries to attain a uniform sample. Different initial densities are achievable with this method. For the DD

method, the sand is dried in the oven and placed in the triaxial cylinder by a funnel. The funnel tip is always located at a minimal height above the surface of the sand, to give the lowest possible density. When the cylinder is filled, it is tapped by a rubber rod to achieve a higher density. A sample prepared by the DD method has a more anisotropic microstructure compared to the MT method (Yang et al., 2008). The MT method results in a more random orientation of the grains and contact normals, and the chosen sample preparation method should be as close to the *in situ* condition as possible (Wichtmann, 2016).

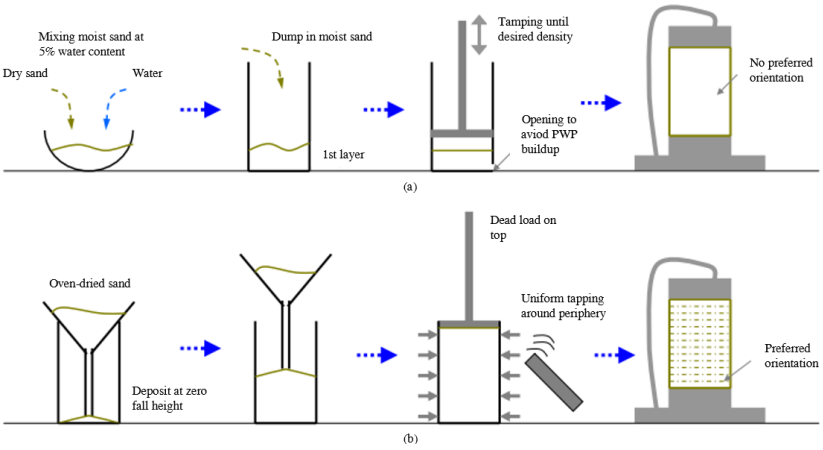

Figure 5.1: Schematic illustration of the (a) MT and (b) DD method (Sze and Yang, 2013)

5.2.1 Deformation Patterns

Laboratory tests have shown that soils subjected to cyclic loading may result in different deformation patterns depending on how the sample is prepared, how the test is conducted and the properties of the soil. The soil will not necessarily reach failure, but may in some cases reach a state of equilibrium before failure. Moist tamping and dry deposition will result in different failure modes (Sze and Yang, 2013).

Liquefaction and cyclic mobility are two basic phenomena that have been observed in saturated sand when subjected to cyclic loading (Castro, 1975). Liquefaction develops only in loose sand, while cyclic mobility may develop in both loose and dense sand. Liquefaction occurs when a saturated sand looses a large percentage of its shear resistance as the pore water pressure increases, and flows like a liquid. Cyclic mobility occurs when a saturated sand has a progressive reduction of effective stresses due to the cyclic loading. Cyclic mobility, in contrast to liquefaction, results in limited soil deformation without liquid-like flow.

5.3 Data Filtering

The raw data from the triaxial tests are filtered using the *filtfilt* function in MATLAB. The purpose of the filtering is to reduce high-frequency fluctuations in data. *Filtfilt* is a function in MATLAB that performs a zero-phase digital filtering by processing the data in forward direction through the filter, then reversing the filtered sequence and run it back through the filter (MathWorks, 2017). An all-zero filter is used. Figure 5.2 illustrates how the numerator coefficients of the filter affect the result. It is particularly due to the derivatives that filtration of the raw-data is necessary. The differences are small for the first cycles, but increase as the effect of the dilatancy increases.

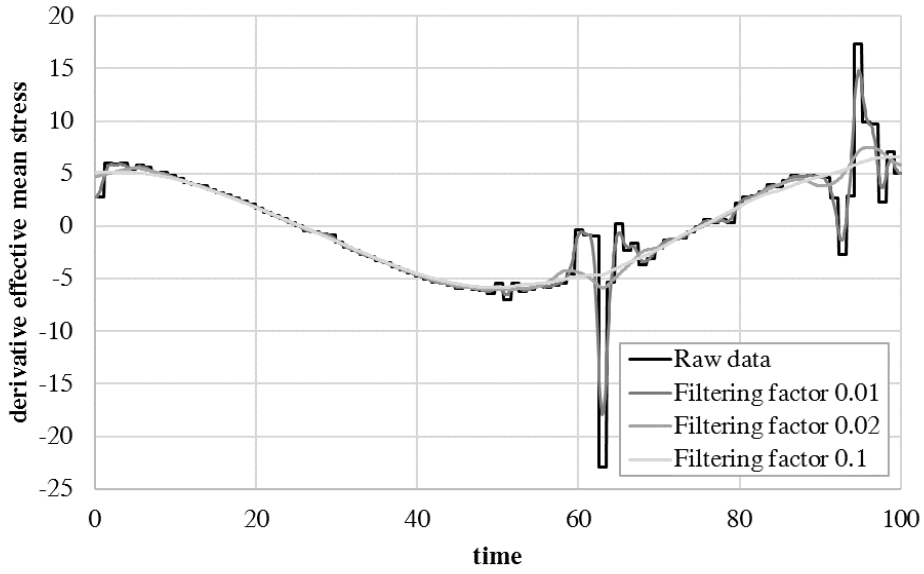

Figure 5.2: The effect of the different filtering factors

Chapter 6

Results from Triaxial Tests

NGI has carried out several monotonic and cyclic triaxial tests in association with the ongoing strategic project, SP9, at their lab in Oslo. The tests are performed with dense saturated sand from the Siri offshore field in the North Sea. Figure 6.1 presents the grain size distribution of the Siri sand, along with other typical North Sea sands. In the triaxial test, the specimens are reconstituted to the desired relative density by the moist tamping method according to NGI standard procedures. The samples are compacted at a water content of 3 % in six layers of equal height of 18 mm in a split aluminium compaction mould. The average minimum and maximum void ratios of the tests are $e_{min} = 0.502$ and $e_{max} = 0.787$. Data from 19 tests have been interpreted, of which 10 are monotonic and 9 are cyclic.

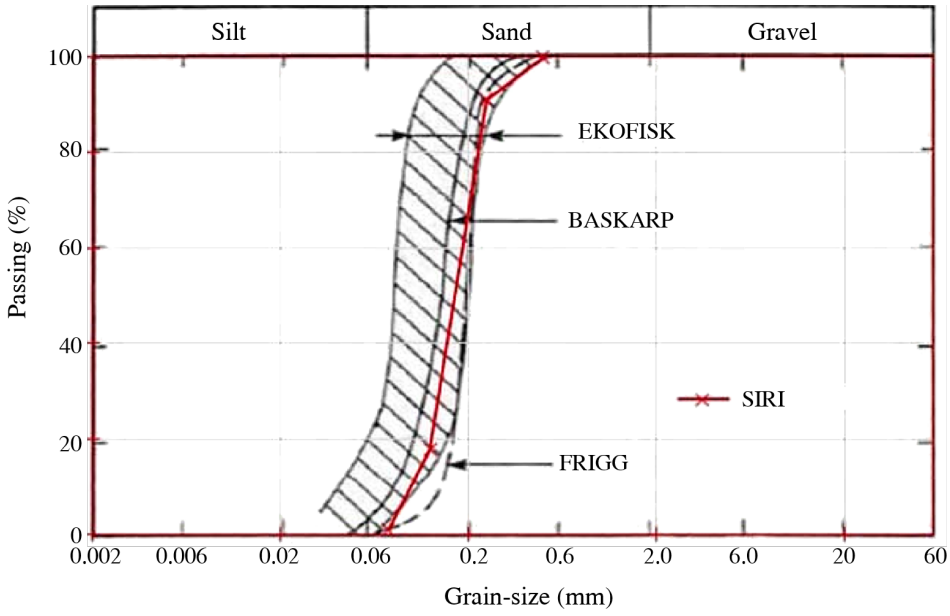

Figure 6.1: Grain size distribution of Siri sand (Carotenuto and Suzuki, 2016)

The monotonic triaxial tests are carried out with sand at a relative density of 60 % and 80 % in both compression and extension. Half of the tests are performed drained and the other half are performed undrained. Most of the samples are consolidated to an axial consolidation stress of $\sigma'_{ac} = 200$ kPa and a radial consolidation stress of $\sigma'_{rc} = 90$ kPa, except two tests which are consolidated to $\sigma'_{ac} = 100$ kPa and $\sigma'_{rc} = 45$ kPa.

The cyclic triaxial tests are carried out with sand at a relative density of 80 %. The tests have different drainage conditions, of which three tests have step partial drainage, two have fully drainage and four are undrained. All samples are consolidated to an axial consolidation stress of $\sigma'_{ac} = 200$ kPa and a radial consolidation stress of $\sigma'_{rc} = 90$ kPa. The tests are run with an average shear stress of $\tau_a = 55$ kPa, with no change in average shear stress, $\Delta\tau_a = 0$ kPa, and a cyclic shear stress of $\tau_{cy} = 100$ kPa. For the cyclic samples, drained preshearing of $\tau_{cy} = 0.06 \cdot \sigma'_{ac}$ for 400 cycles is performed.

Table 6.1 gives a summary of the 19 tests that are considered. It includes type of tests, consolidation stresses, index properties, other remarks and references to corresponding appendices. The triaxial data are filtered in MATLAB with a numerator coefficient of 0.02, and the filtered data are processed in Microsoft Excel. The cyclic results show an unrealistic discontinuity from one cycle to the next due to the filtering.

The results are interpreted within an elasto-plastic framework and are presented in six different plots, as listed below. The results will be discussed in Chapter 8.

- $p' - q$ plot
- dilatancy $-\eta$ plot
- $\varepsilon_q^p - \eta$ plot
- $d\varepsilon_q^p - \eta$ plot
- $\varepsilon_{vol}^p - \eta$ plot
- $d\varepsilon_{vol}^p - \eta$ plot

The incremental strains are normalised with respect to the increment in stress ratio, $d\eta$. The stress paths of the tests are studied from the $p' - q$ plots, and the dilatancy$-\eta$ plots display the sand's tendency of contraction and dilatancy. The plots of incremental plastic shear and volume strains are included for evaluation of the hardening and dilatancy trends respectively, and the total plastic shear and volume strains are included to show the accumulation of strains.

Table 6.1: Summary of tests

Test no.		Type of test	Consolidation stress			Relative density, D_r (%)	G_{max} (MPa)	Void ratio, e (-)	Remarks	Appendix
			σ'_a (kPa)	σ'_r (kPa)	τ'_0 (kPa)					
Monotonic tests	1	CADc	199.2	88.7	55.3	80.0		0.57		A.1
	2	CAUc	201.9	90.5	55.7	80.0		0.57		A.1
	3	CADe	200.3	90.8	54.8	79.0		0.57		A.1
	4	CAUe	200.1	90.9	54.6	77.5		0.57		A.1
	5	CADc	201.6	91.0	55.3	59.8		0.63		A.2
	6	CAUc	200.1	90.4	54.9	59.8		0.63		A.2
	7	CADe	200.7	90.9	54.9	59.3		0.63		A.2
	8	CAUe	199.8	91.0	54.4	59.9		0.63		A.2
	9	CADc	101.6	46.3	27.7	79.1		0.57		A.3
	10	CAUc	100.6	45.1	27.8	78.1		0.57		A.3
Cyclic tests	11	CAUcy	199.9	90	55.0	80.0	142.6	0.57	Standard undrained test τ_{cy} = 80 kPa	B.1
	12	CAUcy	200.0	90	55.0	77.9	118.9	0.57	Standard undrained test τ_{cy} = 100 kPa	B.2
	12b	CAUcy	200.0	90	55.0	80.0		0.57	Repetition of Test 12	B.2
	13	CAUcy	200.0	90	55.0	78.3	146.3	0.57	20 cycles undrained and then full drainage, for 15 time. Then undrained shearing to failure	B.3
	14	CAUcy	200.0	90	55.0	76.1	135.1	0.58	40 cycles undrained and then dissipate 50 % of pore water pressure, for 15 time. Then undrained shearing to failure	B.4
	15	CAUcy	200.0	90	55.0	80.5	135.2	0.57	20 cycles undrained and then dissipate 50 % of pore water pressure, for 15 time. Then undrained shearing to failure	B.5
	16	CADcy	195.8	89.8	53.0	80.0		0.57	Standard drained test	B.6
	17	CAUcy	174.6	65.6	54.5	80.0		0.57	The test is consolidated to 200 kPa, then unloaded to 175 kPa prior to start	B.7
	18	CADcy	200.0	90.0	55.0	80.0		0.57	Standard drained test $\tau_{cy} = 80kPa$	B.8

6.1 Results from Monotonic Loading

This section presents the results from all monotonic triaxial tests. Larger versions of the figures are attached in the appendices, reference in Table 6.1.

The results are interpreted within an elasto-plastic framework and the following parameters are used:

- $G_0 = 250$
- $\nu = 0.05$
- $e = 0.57$ for $D_r = 80$ % and $e = 0.63$ for $D_r = 60$ %
- $p_{\text{atm}} = 100$ kPa

Test 1, 2, 3 and 4

Test 1 is a drained triaxial compression test. Test 2 is an undrained triaxial compression test. Test 3 is a drained triaxial extension test. Test 4 is an undrained triaxial extension test. The relative density of the tests are 80 %. The tests are plotted together in Figure 6.2.

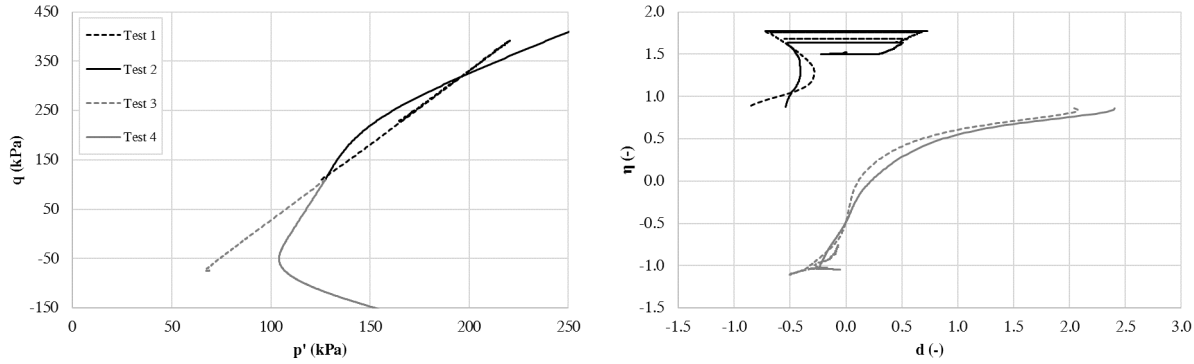

(a) $p' - q$ plot

(b) dilatancy$-\eta$ plot

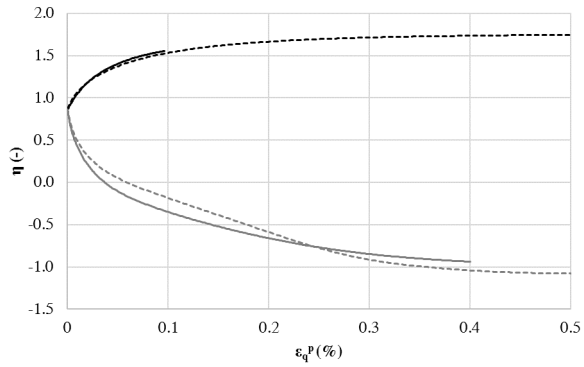

(c) $\varepsilon_q^p - \eta$ plot

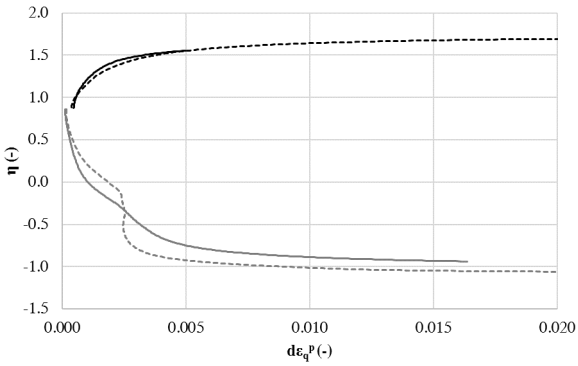

(d) $d\varepsilon_q^p - \eta$ plot

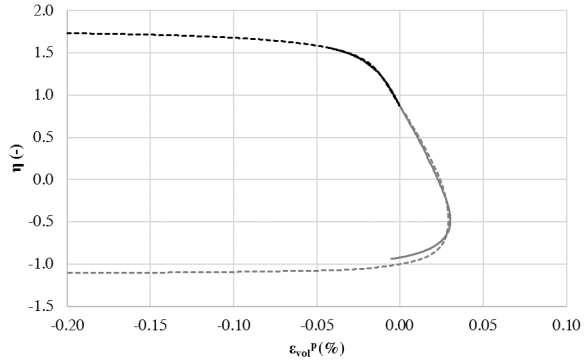

(e) $\varepsilon_{vol}^p - \eta$ plot

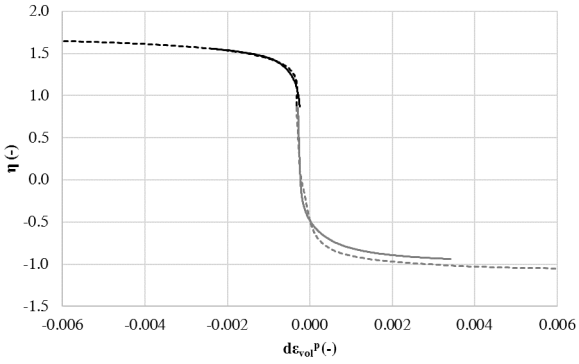

(f) $d\varepsilon_{vol}^p - \eta$ plot

Figure 6.2: Triaxial test results for Test 1, 2, 3 and 4

Test 5, 6, 7 and 8

Test 5 is a drained triaxial compression test. Test 6 is an undrained triaxial compression test. Test 7 is a drained triaxial extension test. Test 8 is an undrained triaxial extension test. The relative density of the tests are 60 %. The tests are plotted together in Figure 6.3.

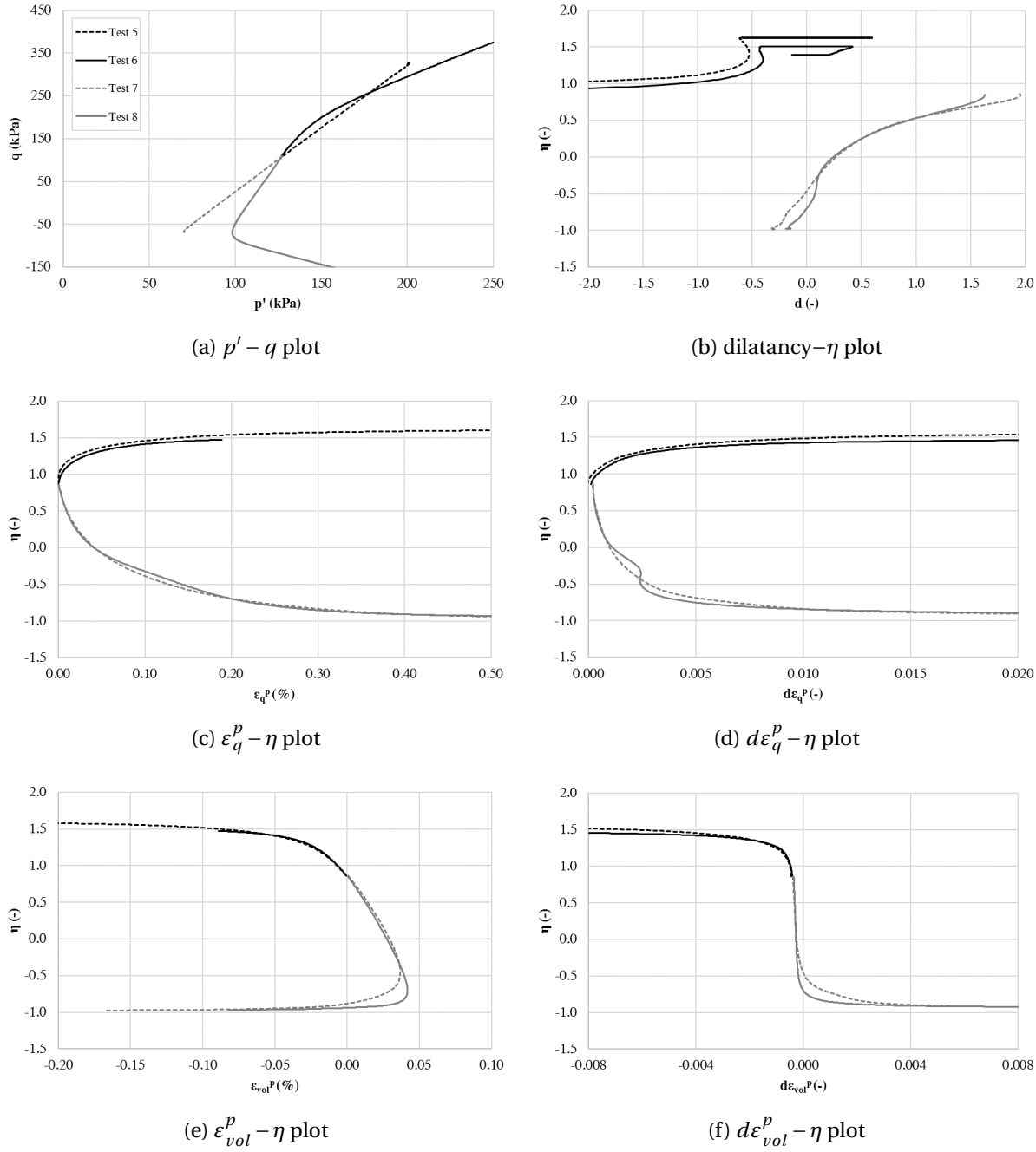

(a) $p' - q$ plot

(b) dilatancy$-\eta$ plot

(c) $\varepsilon_q^p - \eta$ plot

(d) $d\varepsilon_q^p - \eta$ plot

(e) $\varepsilon_{vol}^p - \eta$ plot

(f) $d\varepsilon_{vol}^p - \eta$ plot

Figure 6.3: Triaxial test results for Test 5, 6, 7 and 8

Test 9 and 10

Test 9 is a drained triaxial compression test. Test 10 is an undrained triaxial compression test. The tests are consolidated to σ_{ac} = 100 kPa and σ_{rc} = 45 kPa. The tests are plotted together in Figure 6.4.

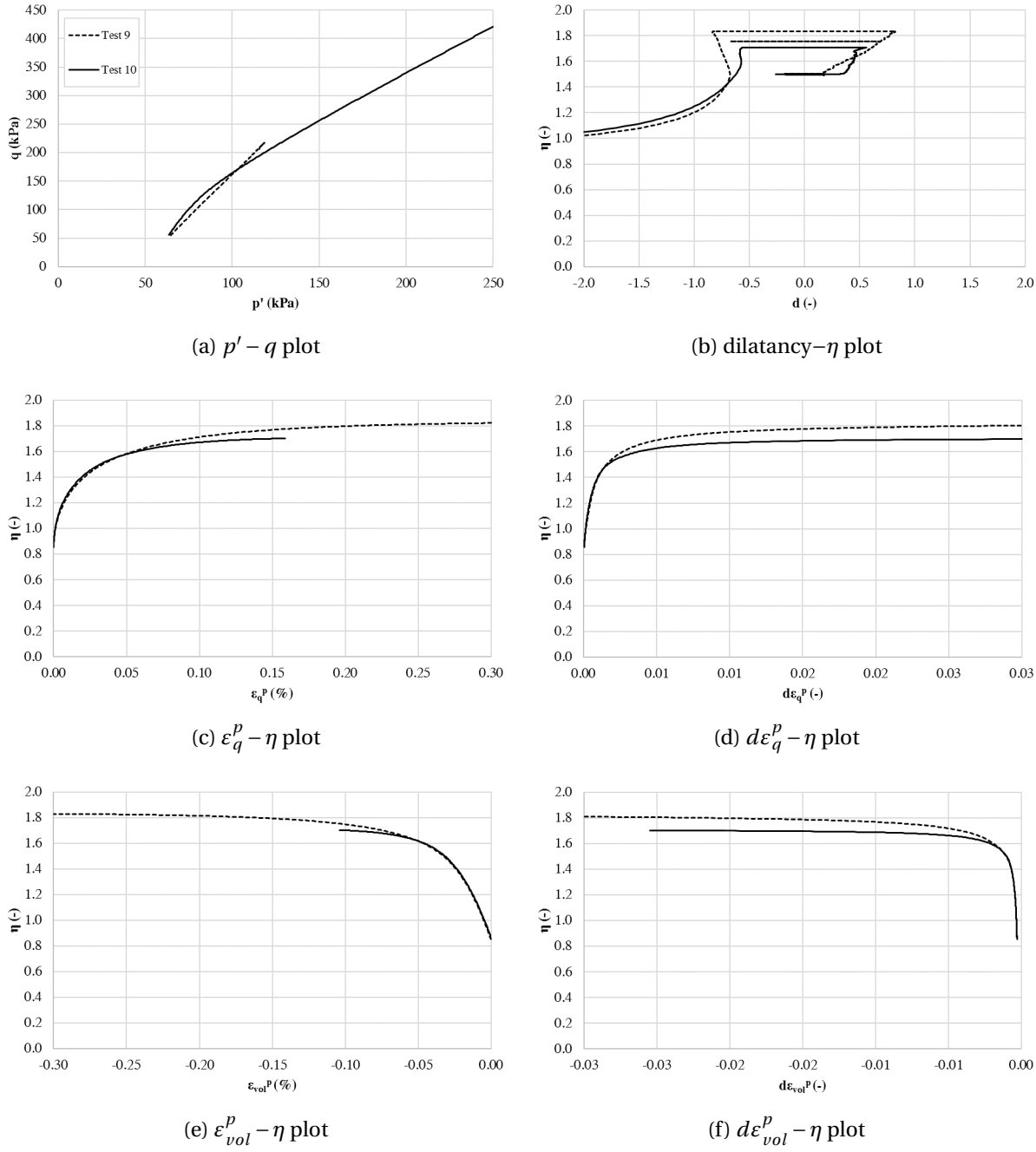

(a) $p' - q$ plot

(b) dilatancy$-\eta$ plot

(c) $\varepsilon_q^p - \eta$ plot

(d) $d\varepsilon_q^p - \eta$ plot

(e) $\varepsilon_{vol}^p - \eta$ plot

(f) $d\varepsilon_{vol}^p - \eta$ plot

Figure 6.4: Triaxial test results for Test 9 and 10

6.2 Results from Cyclic Loading

This section presents the results from all cyclic triaxial tests. The first cycle is marked as a dark line, and the cycles becomes gradually lighter throughout the cycles. Several extreme values appear at the point of stress reversal, these can be neglected. Larger versions of the figures are attached in the appendices, reference in Table 6.1.

The results are interpreted within an elasto-plastic framework and the following parameters are used:

- $G_0 = 250$
- $\nu = 0.05$
- $e = 0.57$
- $p_{\text{atm}} = 100$ kPa

Test 11

Test 11 is a standard undrained cyclic triaxial test. The loading amplitude is τ_{cy} = 80 kPa. Figure 6.5 shows the first 30 cycles.

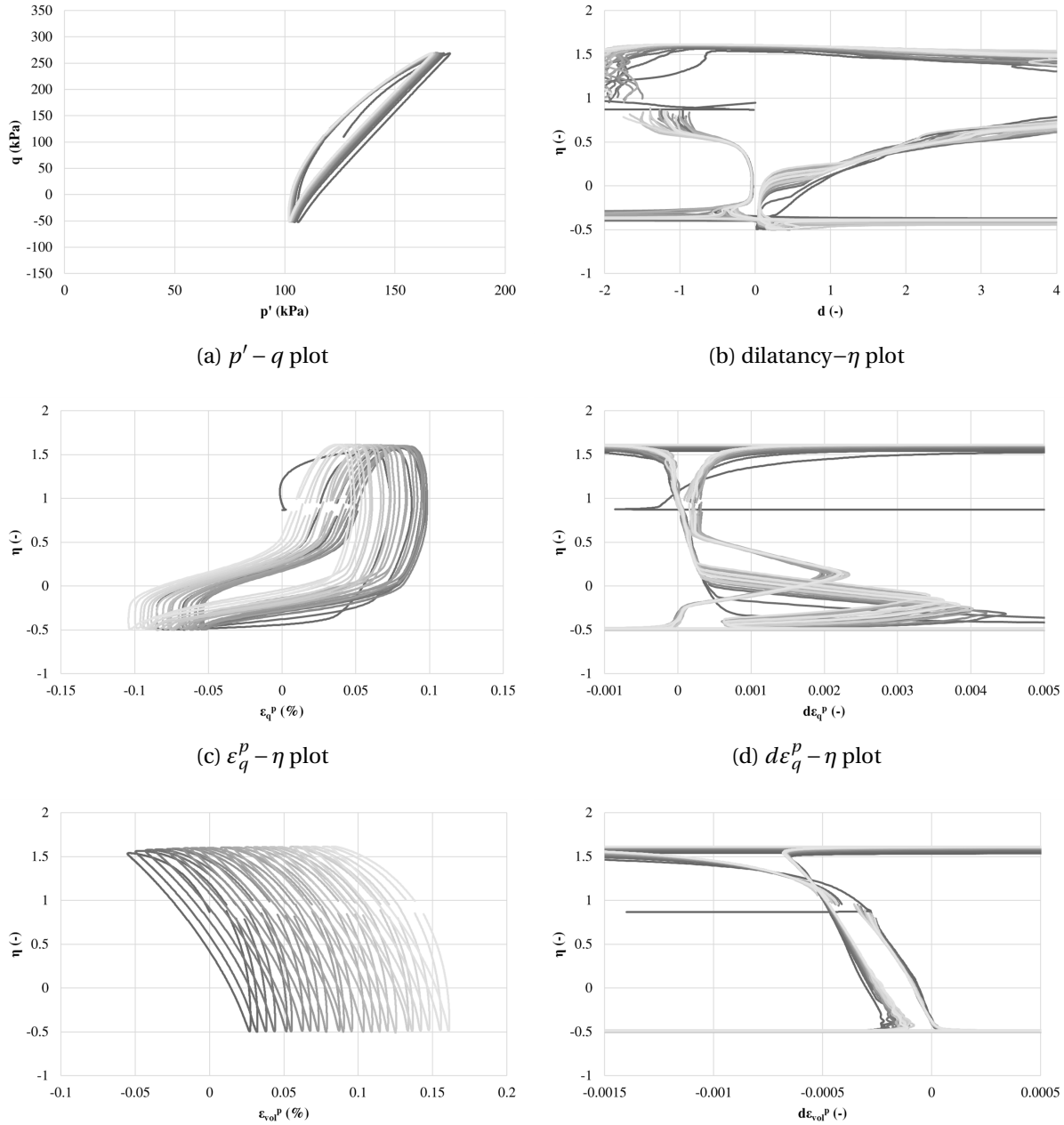

(a) $p' - q$ plot

(b) dilatancy$-\eta$ plot

(c) $\varepsilon_q^p - \eta$ plot

(d) $d\varepsilon_q^p - \eta$ plot

(e) $\varepsilon_{vol}^p - \eta$ plot

(f) $d\varepsilon_{vol}^p - \eta$ plot

Figure 6.5: Cyclic triaxial test results for Test 11

Test 12

Test 12 is a standard undrained cyclic triaxial test. Figure 6.6 shows the first 60 cycles of the test.

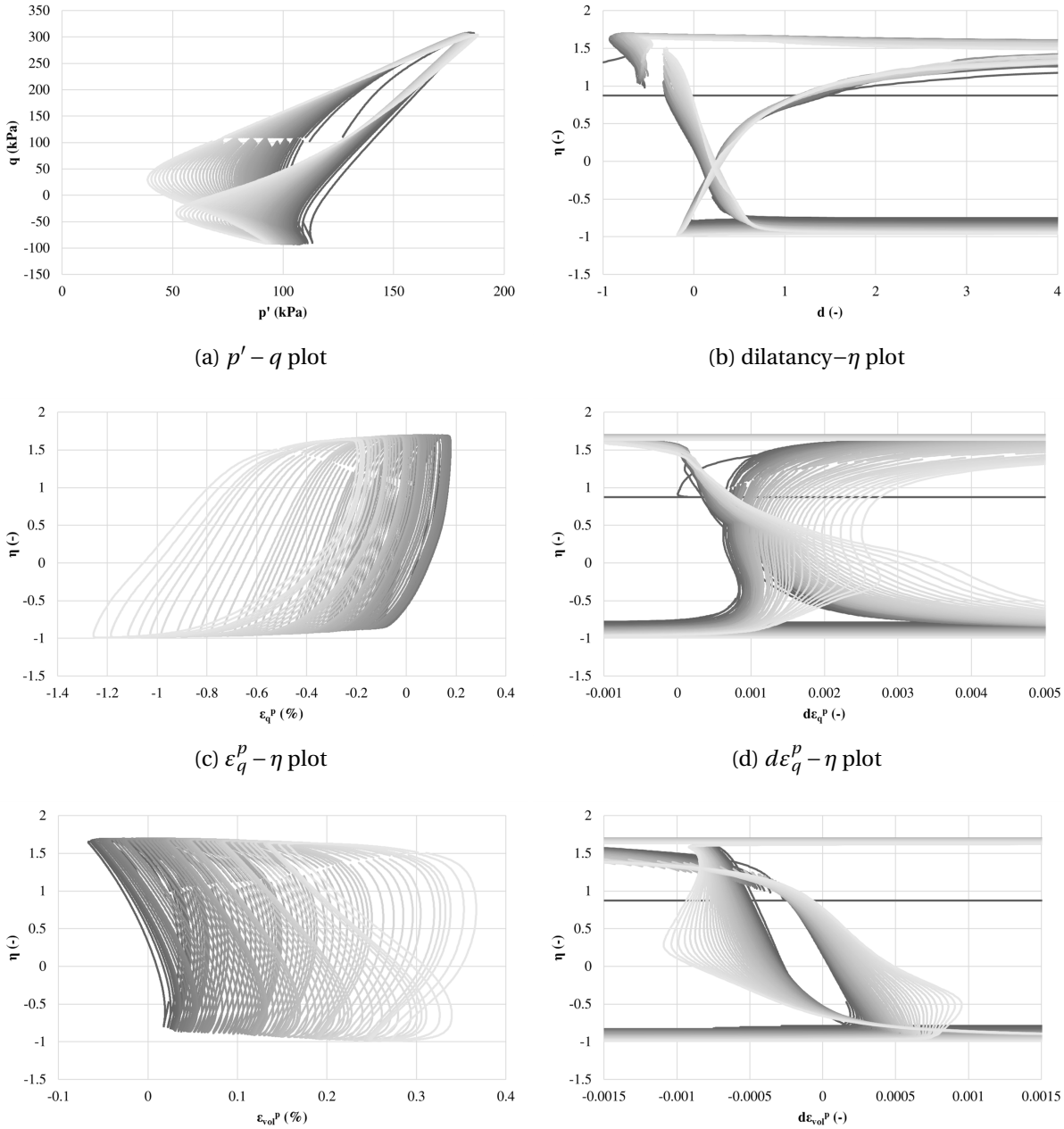

(a) $p' - q$ plot

(b) dilatancy$-\eta$ plot

(c) $\varepsilon_q^p - \eta$ plot

(d) $d\varepsilon_q^p - \eta$ plot

(e) $\varepsilon_{vol}^p - \eta$ plot

(f) $d\varepsilon_{vol}^p - \eta$ plot

Figure 6.6: Cyclic triaxial test results for Test 12

Test 12b

Test 12b is a standard undrained cyclic triaxial test and is a repetition of Test 12. Figure 6.7 shows the first 30 cycles of the test in addition to cycle 40, 50 and 60.

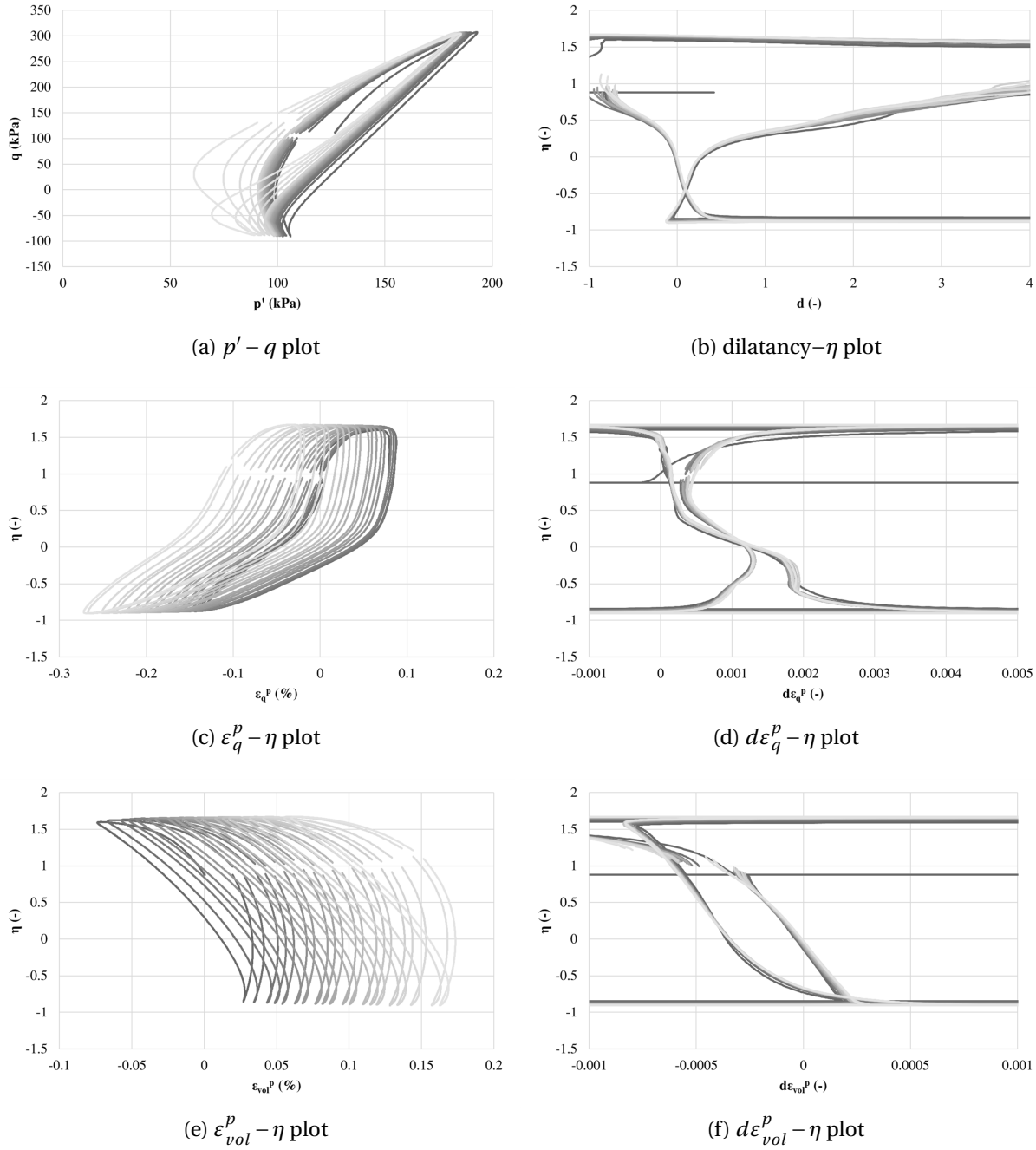

(a) $p' - q$ plot

(b) dilatancy$-\eta$ plot

(c) $\varepsilon_q^p - \eta$ plot

(d) $d\varepsilon_q^p - \eta$ plot

(e) $\varepsilon_{vol}^p - \eta$ plot

(f) $d\varepsilon_{vol}^p - \eta$ plot

Figure 6.7: Cyclic triaxial test results for Test 12b

Test 13

Test 13 is a partly drained cyclic triaxial test. Figure 6.8 shows the first package of 20 undrained cycles before drainage is applied.

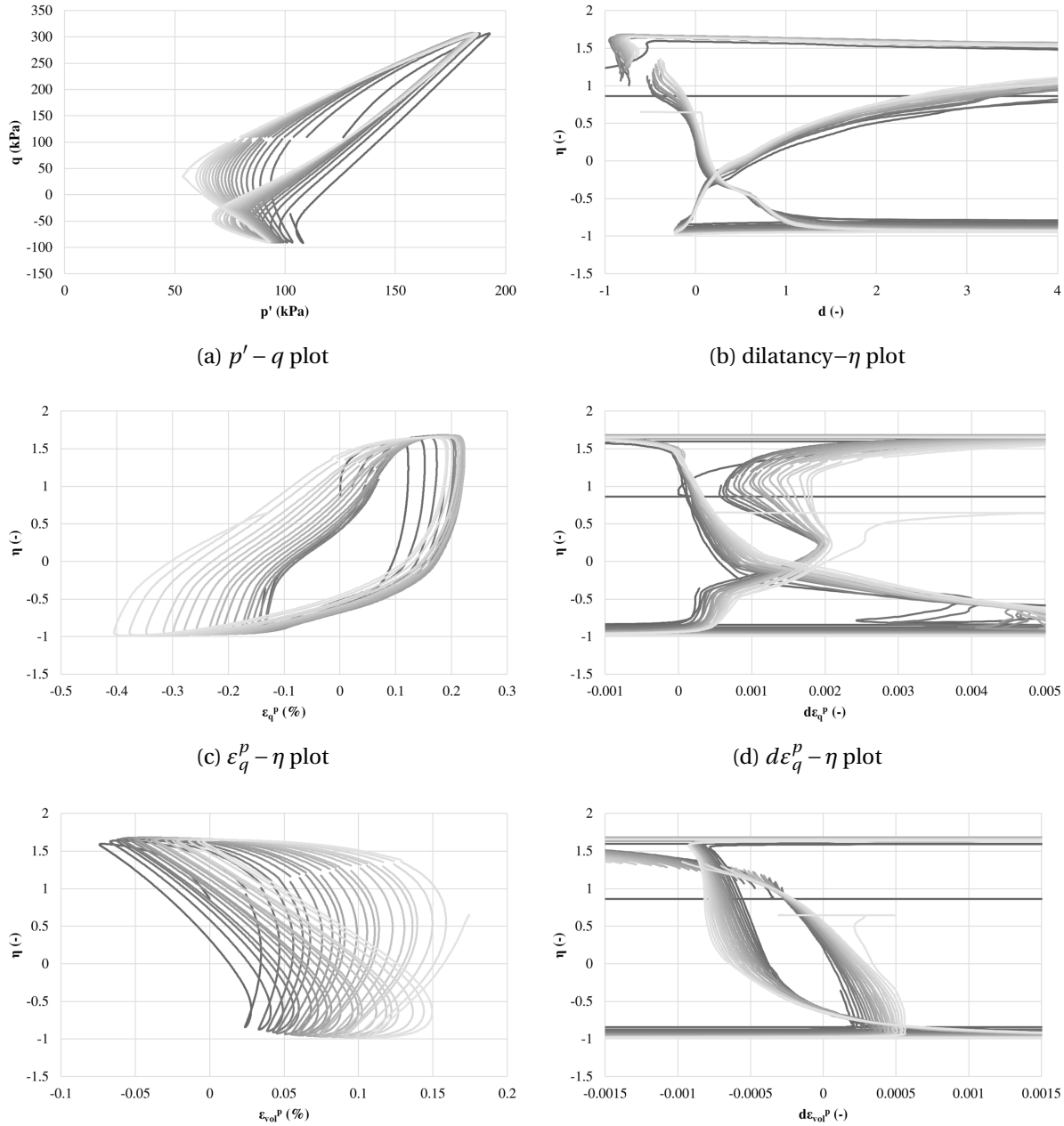

(a) $p' - q$ plot

(b) dilatancy$-\eta$ plot

(c) $\varepsilon_q^p - \eta$ plot

(d) $d\varepsilon_q^p - \eta$ plot

(e) $\varepsilon_{vol}^p - \eta$ plot

(f) $d\varepsilon_{vol}^p - \eta$ plot

Figure 6.8: Cyclic triaxial test results for Test 13

Test 14

Test 14 is a partly drained cyclic triaxial test. Figure 6.9 shows the first package of 40 undrained cycles before drainage is applied.

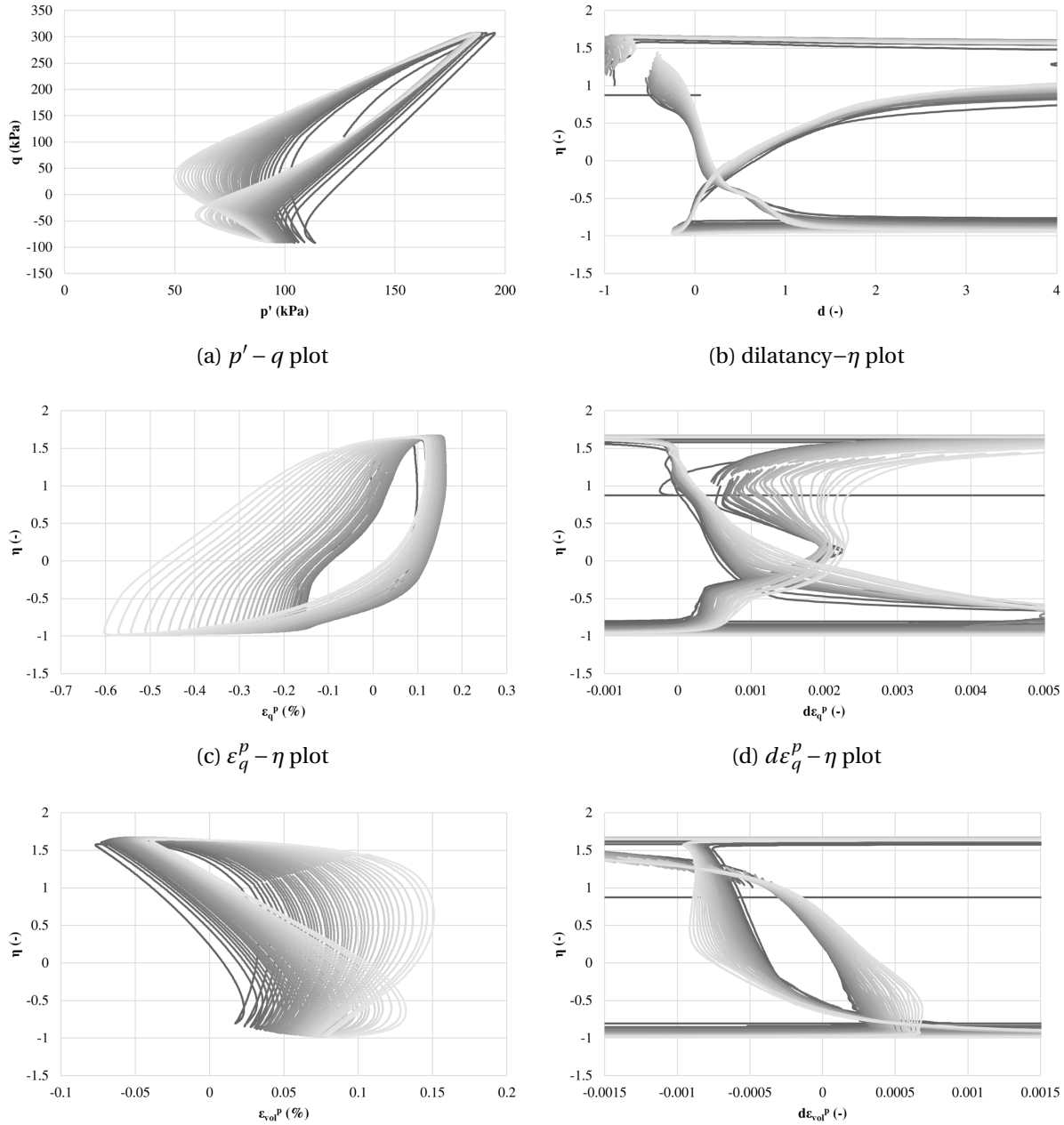

(a) $p' - q$ plot

(b) dilatancy$-\eta$ plot

(c) $\varepsilon_q^p - \eta$ plot

(d) $d\varepsilon_q^p - \eta$ plot

(e) $\varepsilon_{vol}^p - \eta$ plot

(f) $d\varepsilon_{vol}^p - \eta$ plot

Figure 6.9: Cyclic triaxial test results for Test 14

Test 15

Test 15 is a partly drained cyclic triaxial test. Figure 6.10 shows the first package of 20 undrained cycles before drainage is applied.

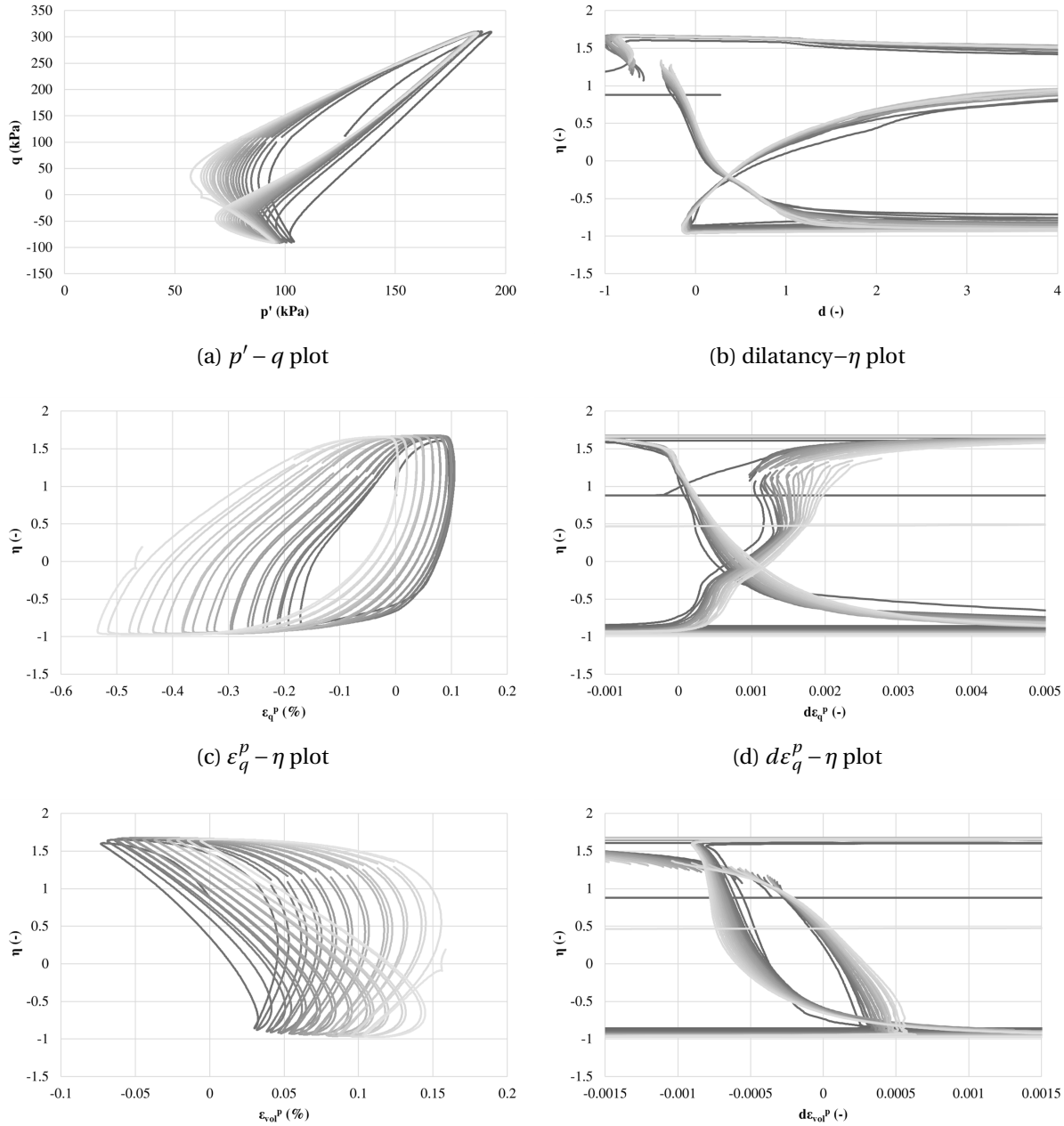

(a) $p' - q$ plot

(b) dilatancy$-\eta$ plot

(c) $\varepsilon_q^p - \eta$ plot

(d) $d\varepsilon_q^p - \eta$ plot

(e) $\varepsilon_{vol}^p - \eta$ plot

(f) $d\varepsilon_{vol}^p - \eta$ plot

Figure 6.10: Cyclic triaxial test results for Test 15

Test 16

Test 16 is a standard drained cyclic triaxial test. Figure 6.11 shows the first 12 cycles in addition to cycle 100 and 600.

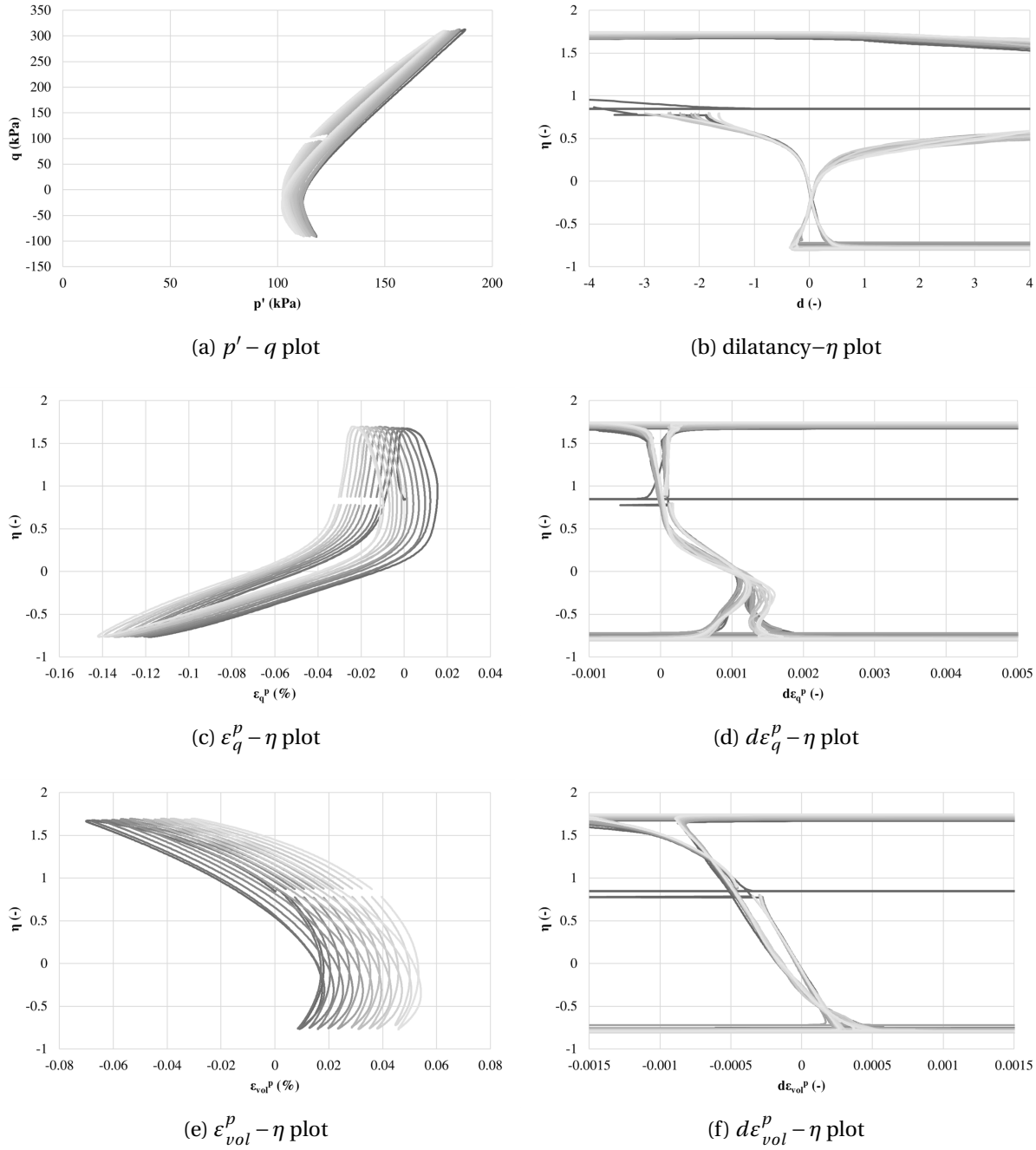

(a) $p' - q$ plot

(b) dilatancy$-\eta$ plot

(c) $\varepsilon_q^p - \eta$ plot

(d) $d\varepsilon_q^p - \eta$ plot

(e) $\varepsilon_{vol}^p - \eta$ plot

(f) $d\varepsilon_{vol}^p - \eta$ plot

Figure 6.11: Cyclic triaxial test results for Test 16

Test 17

Test 17 is a standard undrained cyclic triaxial test. This test is consolidated to σ_{ac} = 200 kPa then unloaded to σ_{ac} = 170 kPa before the test is run. Figure 6.12 shows the first 60 cycles.

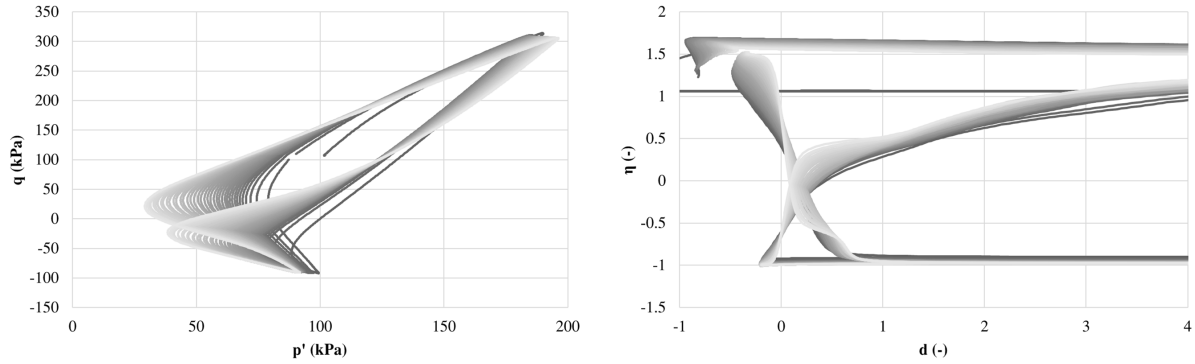

(a) $p' - q$ plot

(b) dilatancy$-\eta$ plot

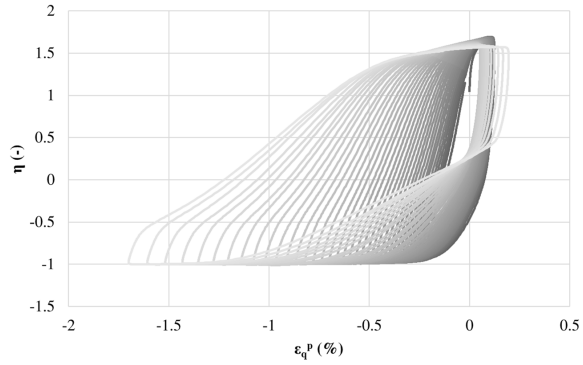

(c) $\varepsilon_q^p - \eta$ plot

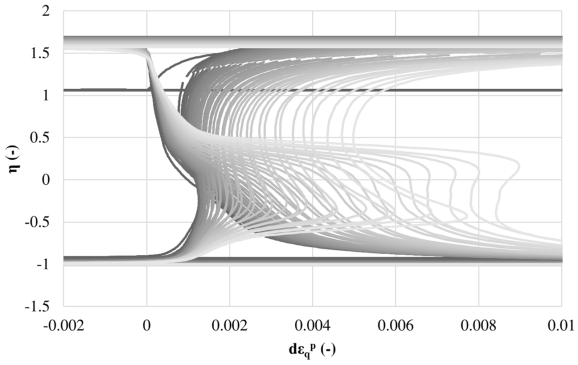

(d) $d\varepsilon_q^p - \eta$ plot

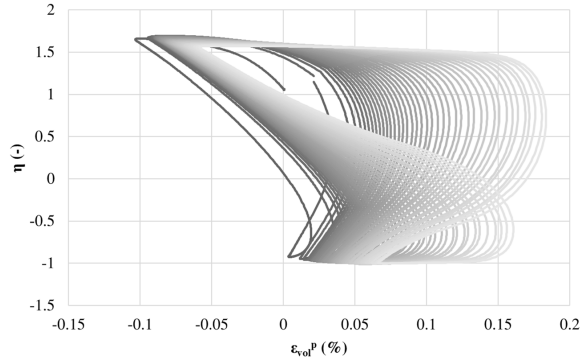

(e) $\varepsilon_{vol}^p - \eta$ plot

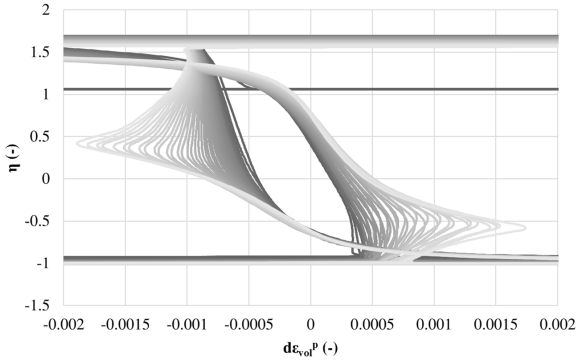

(f) $d\varepsilon_{vol}^p - \eta$ plot

Figure 6.12: Cyclic triaxial test results for Test 17

Test 18

Test 18 is a standard drained cyclic triaxial test. The test has a loading amplitude of τ_{cy} = 85 kPa. Figure 6.13 shows the first 20 cycles in addition to cycle 100 and 600.

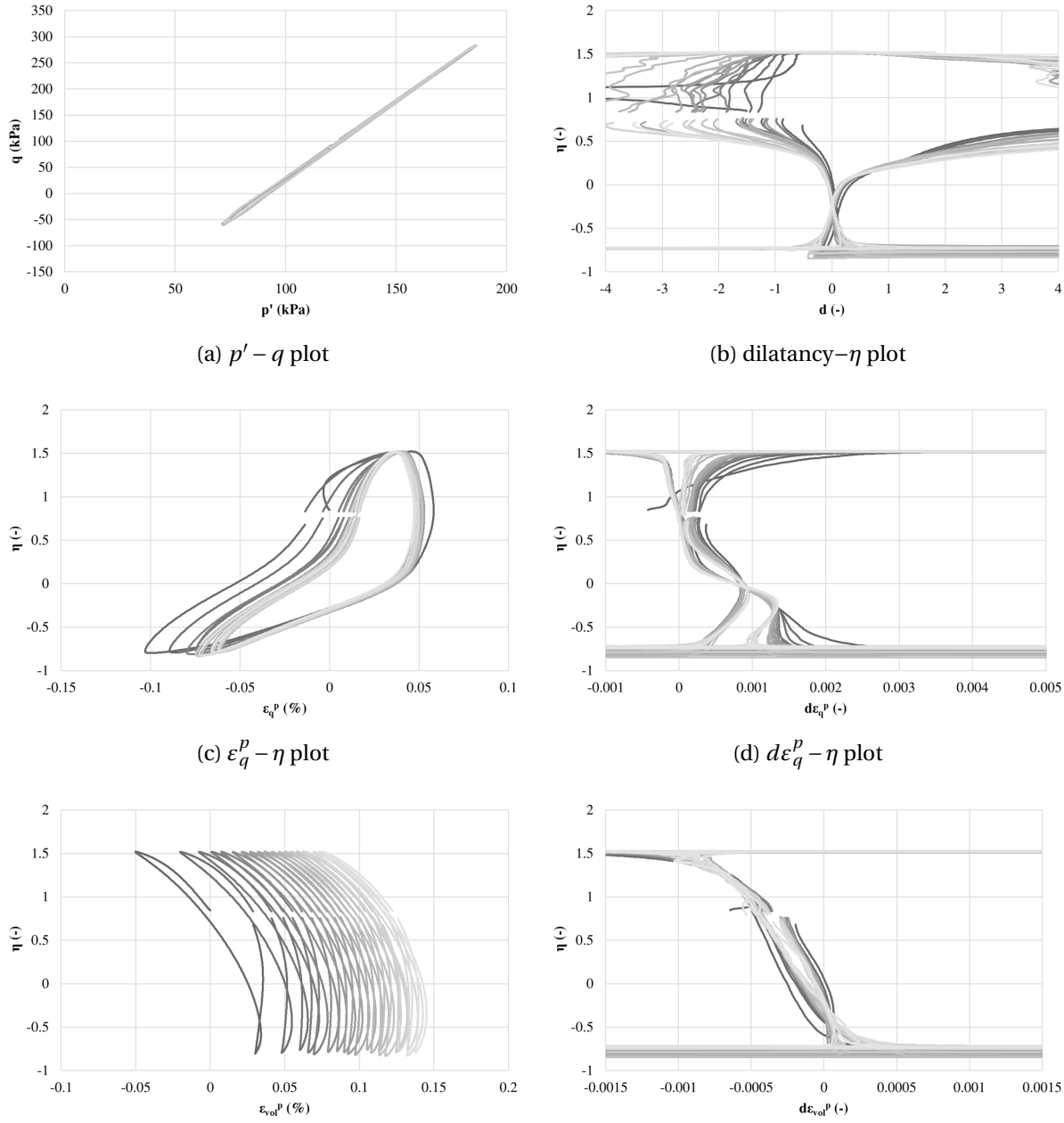

(a) $p' - q$ plot

(b) dilatancy$-\eta$ plot

(c) $\varepsilon_q^p - \eta$ plot

(d) $d\varepsilon_q^p - \eta$ plot

(e) $\varepsilon_{vol}^p - \eta$ plot

(f) $d\varepsilon_{vol}^p - \eta$ plot

Figure 6.13: Cyclic triaxial test results for Test 18

Chapter 7

Implementation of the SANISAND Constitutive Model

The SANISAND constitutive model have been implemented in Microsoft Excel to simulate the monotonic and cyclic behaviour of sand. It consists of a number of different input parameters as described in Chapter 4. The user specifies the stress state, loading condition and number of cycles, along with the parameters listed in Table 4.1 on page 22. The model is based on the formulation presented in Dafalias and Manzari (2004), and the implementation is constructed in such a way that all constants listed in Table 4.1 may have different values in extension and compression.

This chapter introduces how the SANISAND constitutive model simulates the monotonic and cyclic behaviour of the Siri sand. The simulations are presented together with the results from the triaxial tests introduced in Chapter 6, and are always marked as red lines. The results from the monotonic SANISAND simulation are first presented together with the monotonic triaxial data. The results from the cyclic SANISAND simulation are then presented together with the cyclic triaxial data. The main results from the work will be information that can be used to develop an improved SANISAND model for cyclic behaviour of water saturated dense sand. The results will be discussed in Chapter 8

7.1 SANISAND Simulation of Monotonic Loading

The input parameters applied to the different monotonic tests are listed in Table C.1 in Appendix C. The SANISAND model is simulating both drained and undrained response by preventing volume change for the undrained simulation, and allowing volume change in the

drained simulation. Figure 7.1 presents the simulation of Test 1-4 for drained and undrained response in both compression and extension. The results from the simulations of the tests are attached in Appendix C.

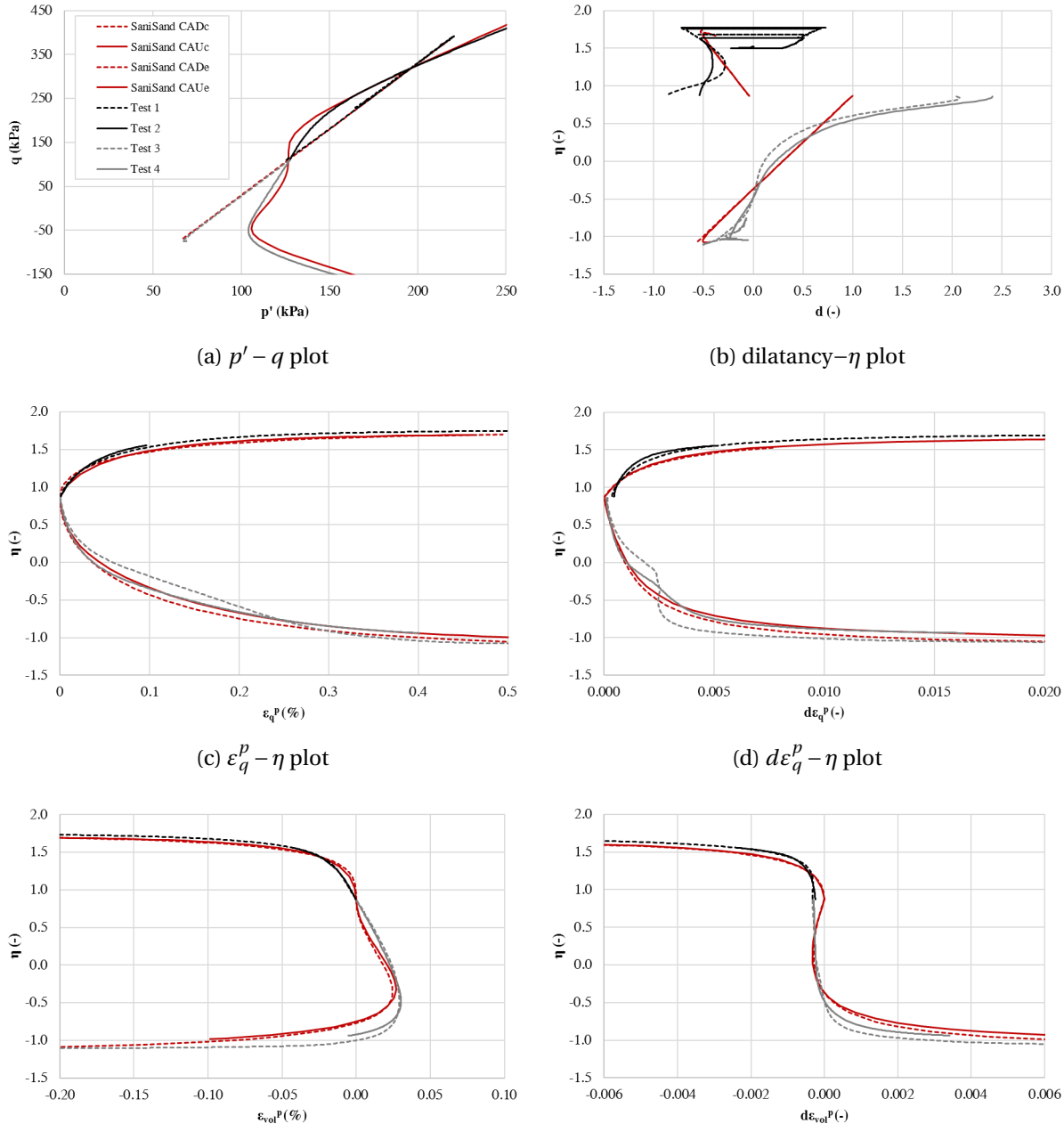

(a) $p' - q$ plot

(b) dilatancy$-\eta$ plot

(c) $\varepsilon_q^p - \eta$ plot

(d) $d\varepsilon_q^p - \eta$ plot

(e) $\varepsilon_{vol}^p - \eta$ plot

(f) $d\varepsilon_{vol}^p - \eta$ plot

Figure 7.1: SANISAND simulation and triaxial test results for Test 1, 2, 3 and 4

7.2 SANISAND Simulation of Cyclic Loading

This section presents the cyclic SANISAND simulations together with the cyclic triaxial test results. The input parameters applied to the SANISAND model are listed in Table 7.1.

The main focus has been to simulate the undrained cyclic response of the Siri sand by choosing a suitable set of input parameters. The simulation of the undrained cyclic SANISAND model is attached in Appendix D.1.

The model is modified to account for drained response by allowing volume change. The SANISAND input parameters for the undrained simulation of the cyclic response are applied to the drained simulation, with exception of the fabric dilatancy parameter, c_z. The input parameter $c_z = 25$ for the drained simulation, and the applied load is $q = \pm 170$ kPa compared to $q = \pm 200$ kPa for the undrained simulation. The simulation of the drained cyclic SANISAND model is attached in Appendix D.2.

Table 7.1: Summary of SANISAND parameters

Input parameters		**Compression**	**Extension**
Elasticity	G_0	250	250
	ν	0.05	0.05
Critical state	M	1.49	0.90
	c	-	-
	λ_c	0.013	0.013
	e_0	0.71	0.71
	ξ	0.67	0.67
Yield surface	m	0.0	0.0
Plastic modulus	h_0	8.00	8.00
	c_h	1.20	1.10
	n^b	6.00	6.00
Dilatancy	A_0	0.6	0.5
	n^d	8.00	3.00
Fabric dilatancy	$z_{\max}$	3.0	3.0
	c_z	100	100

7.2.1 SANISAND Model Simulating Undrained Cyclic Response

The SANISAND model simulating undrained cyclic response is presented in Figure 7.3 together with Test 13.

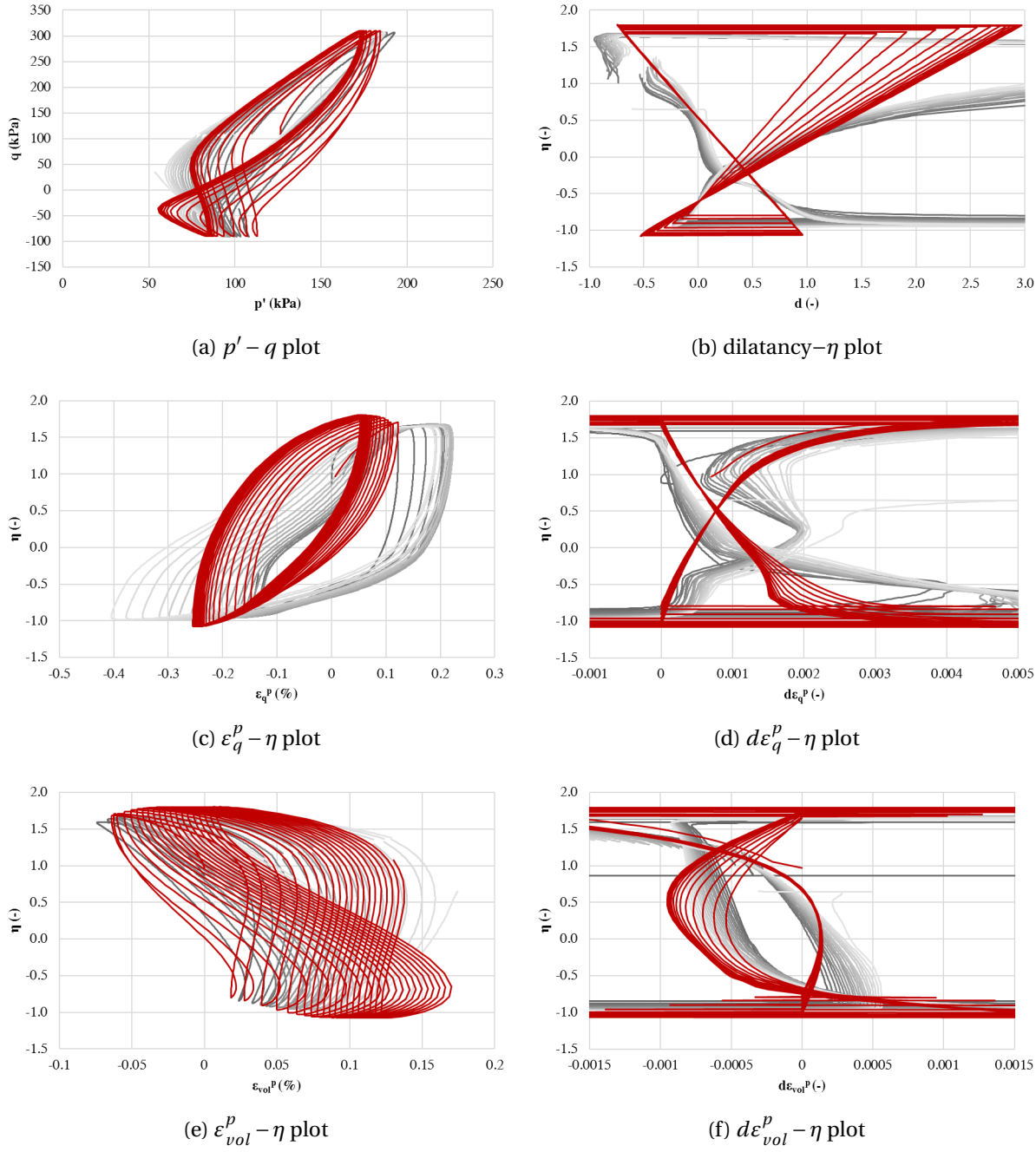

(a) $p' - q$ plot

(b) dilatancy$-\eta$ plot

(c) $\varepsilon_q^p - \eta$ plot

(d) $d\varepsilon_q^p - \eta$ plot

(e) $\varepsilon_{vol}^p - \eta$ plot

(f) $d\varepsilon_{vol}^p - \eta$ plot

Figure 7.2: Undrained SANISAND simulation together with Test 13

7.2.2 SANISAND Model Simulating Drained Cyclic Response

The SANISAND model simulating drained cyclic response is presented in Figure 7.3 together with Test 18.

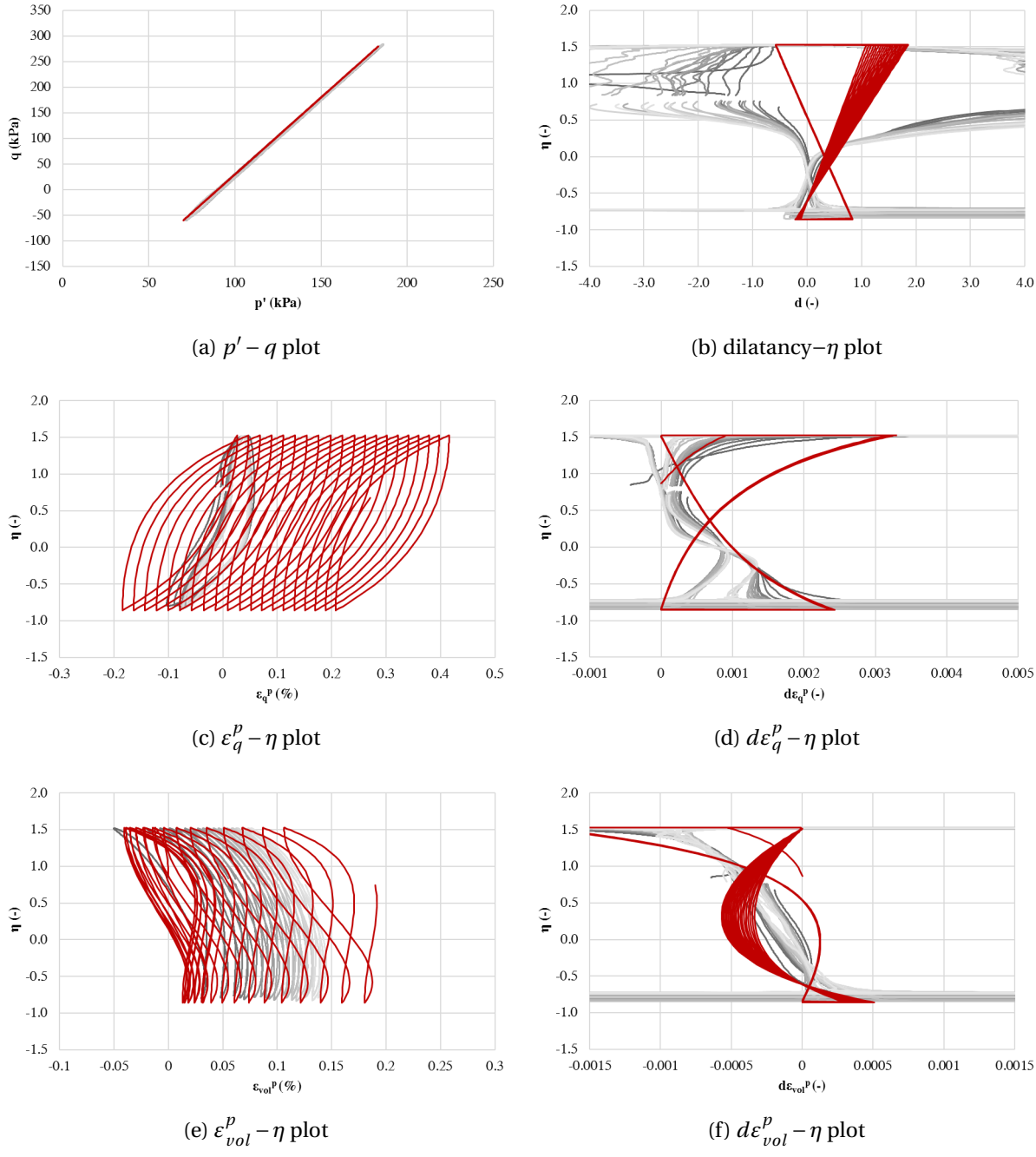

(a) $p' - q$ plot

(b) dilatancy$-\eta$ plot

(c) $\varepsilon_q^p - \eta$ plot

(d) $d\varepsilon_q^p - \eta$ plot

(e) $\varepsilon_{vol}^p - \eta$ plot

(f) $d\varepsilon_{vol}^p - \eta$ plot

Figure 7.3: Drained SANISAND simulation together with Test 18

Chapter 8

Discussion

In this chapter, the results from the laboratory tests and the implementation of the SANISAND model will be discussed. The discussion of monotonic loading is first presented, and is followed by cyclic loading. To evaluate how the cyclic SANISAND model predicts cyclic response of sand, soil response under monotonic loading is used as reference. The parameters are first calibrated with the monotonic tests, and then a modification to the cyclic model is performed.

8.1 Monotonic Loading

The monotonic triaxial tests show the same trends in stress paths, dilatancy and strains independent of relative densities and stress conditions. The stress paths, illustrated by the $p' - q$ plots, behave as expected. Test 1-4 with $D_r = 80$ % have a phase transformation line around $\eta = -0.5$, and Test 5-8 with $D_r = 60$ % have a phase transformation line which varies from $\eta = -0.75$ to $\eta = -0.5$.

The tests show decreasing plastic volume strains in the compression tests and increasing in the main part of the extension tests. The plastic shear strains increase in compression and extension as the sample is sheared. The incremental shear strains appear to be similar in the different tests, thus the hardening is comparable. The plastic incremental shear strains display a z form in extension, which implies that the hardening is constant for these stress ratios. The representations of the total plastic shear strains seem reasonable, thus the incremental strains are acceptable.

8.1.1 SANISAND Material Model

The monotonic SANISAND model simulates the behaviour of the Siri sand in an adequate manner for a chosen set of parameters. The input parameters are primarily chosen by curve fitting, striving for a simulation that represents the behaviour in an optimal manner.

It is desirable to establish one unique set of parameters in compression and one set of parameters in extension independent of stress condition. To obtain these sets of parameters, the input parameters listed in Table 4.2 on page 23 are initially chosen.

Table C.1 on page 131 in Appendix C presents a summary of the established parameters for the monotonic SANISAND model. The elasticity parameters and the yield surface parameter have the same values in compression and extension, because one type of material is simulated. The Poisson's ratio, $\nu = 0.05$, is chosen to have the same value as in the article written by Dafalias and Manzari (2004). It is decided to keep an unrealistic low value of ν as it predicts the stiffness in a satisfying manner. The material constant, G_0, is increased to agree with the $G_{\max}$ measurements from the laboratory tests, and is found to be $G_0 = 250$. In the critical state parameters the critical state stress ratio, M, differs from compression to extension, and the values are chosen based on the Coulomb criterion.

A deviation between parameters in compression and extension mainly appears in the plastic modulus and dilatancy parameters. These values are chosen based on curve fitting. The results show that the model simulates the response well with one unique set of parameters for drained and undrained behaviour in both compression and extension. The model is only able to simulate a linear trend in dilatancy behaviour, but it has been emphasised in this thesis that it should describe the phase transformation line correctly. This has been successful by varying the material constant n^d in compression and extension.

8.1.2 $D_r = 80$ % versus $D_r = 60$ %

A comparison of Test 1-4 with $D_r = 80$ % and Test 5-8 with $D_r = 60$ % is presented in Figure 8.1. The stress paths are shown in Figure 8.1a, and the figure indicates similar trends for both relative densities. Figure 8.1b presents how the dilatancy develops during the tests. It is expected that the tests with $D_r = 60$ % behave softer and thus show less dilatancy compared to the tests with $D_r = 80$ %. The figure indicates a greater dilatancy for $D_r = 60$ %. A possible explanation of this is that the grains have chosen a slightly different orientation during preparation of the sample, resulting in a slightly different sand. The sand is highly sensitive to the sample preparation method, as pointed out in Section 5.2.

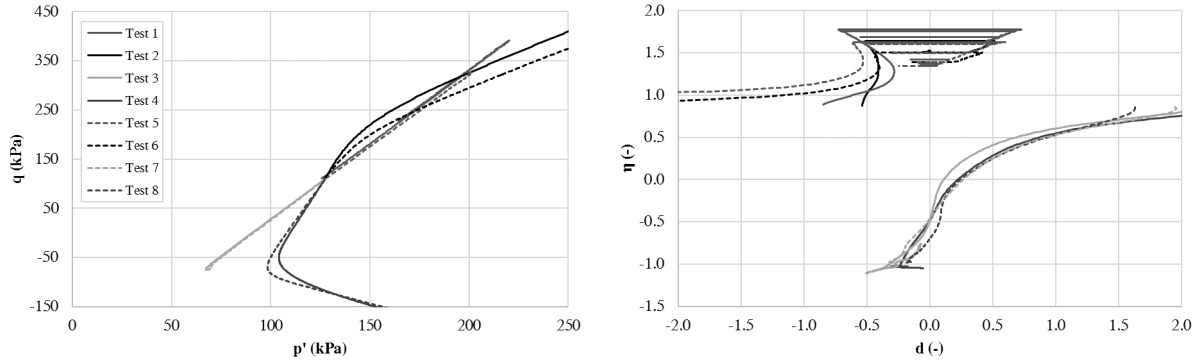

(a) $p' - q$ plot (b) $d - \eta$ plot

Figure 8.1: Comparison of $D_r = 80$ % and $D_r = 60$ %

The input parameters for the simulations of tests with $D_r = 80$ % and $D_r = 60$ % are very similar. The input values from $D_r = 80$ % are chosen as a starting point, but some of the parameters are changed to improve the simulation for $D_r = 60$ %. The most obvious difference in the input parameters is the initial void ratio which is calculated from the triaxial test data. In addition, the constants h_0 and n^d are changed, and the new constants are found by trial and error. The simulations together with the tests are attached in Appendix C.

An evaluation of which value of the material constant, G_0, that is appropriate as input for $D_r = 60$ % has been carried out. This is done based on the assumption that $G_0 = 250$ for the tests performed with $D_r = 80$ %. Figure 8.2 presents a plot of the plastic shear strain versus the deviatoric stress for $D_r = 60$ % with different G_0 input values together with $D_r = 80$ % and $G_0 = 250$. A large input value results in a high elastic shear stiffness and neglected elastic strains, which is not preferable. It is expected that the two relative density conditions behave similar, and a G_0 input value of 250 is therefore chosen based on Figure 8.2.

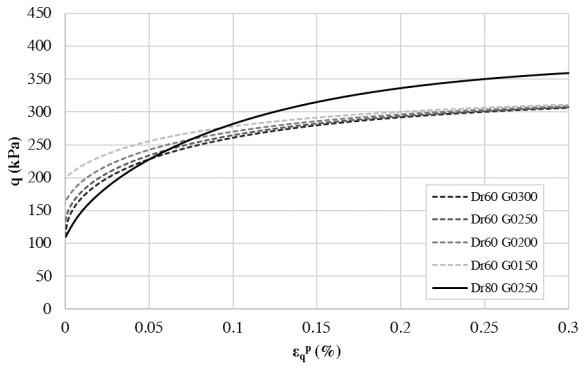

Figure 8.2: Evaluation of the input value, G_0

8.1.3 σ'_{ac} = 200 kPa versus σ'_{ac} = 100 kPa

The responses of Test 1-2 with σ'_{ac} = 200 kPa and Test 9-10 with σ'_{ac} = 100 kPa are presented in Figure 8.3. Figure 8.3a displays the stress paths and Figure 8.3b displays the total plastic shear strain versus the stress ratio. The stress paths have different starting points as it is consolidated to different stress conditions, but the trends are similar. Figure 8.3b indicates that Test 9-10 with σ'_{ac} = 100 kPa have a higher shear stiffness compared to Test 1-2 with σ'_{ac} = 200 kPa.

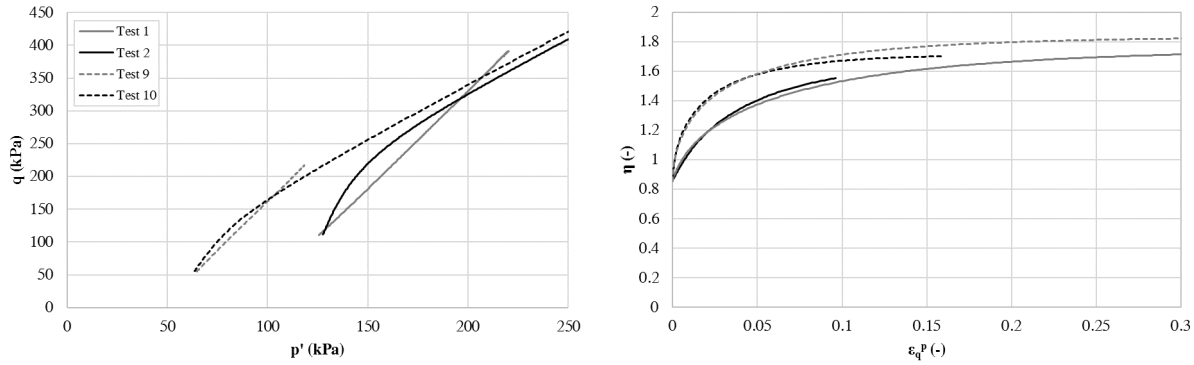

(a) p'-q plot

(b) $\varepsilon_q^p - \eta$ plot

Figure 8.3: Comparison of σ'_{ac} = 200 kPa and σ'_{ac} = 100 kPa

It is desirable to have one unique set of SANISAND input parameters independent of the stress condition, thus the input parameters for Test 1-2 with σ'_{ac} = 200 kPa are applied to the simulation of Test 9-10 with σ'_{ac} = 100 kPa. The SANISAND simulation fits well for both stress conditions, presented in Appendix C. When the SANISAND simulation of Test 9-10 with σ'_{ac} = 100 kPa is compared with the triaxial data, it may however be noticed that SANISAND simulates a sand with a lower plastic shear stiffness than the actual sand.

The hardening modulus, H, is back calculated from the triaxial data by using Equation 4.4 on page 18 and is presented together with the hardening modulus from the SANISAND formulation, Equation 4.8 on page 19, in Figure 8.4. Figure 8.4a and Figure 8.4b present the hardening modulus for drained and undrained tests respectively. The figures display a greater hardening for Test 9-10 with σ'_{ac} = 100 kPa compared with Test 1-2 with σ'_{ac} = 200 kPa for both undrained and drained triaxial tests. The SANISAND simulations display the same trends, but the difference between σ'_{ac} = 200 kPa and σ'_{ac} = 100 kPa is not as significant as in the triaxial tests. The SANISAND formulation represents a sand that is too soft for tests with σ'_{ac} = 100 kPa, and the SANISAND model does not represent the behaviour of tests with σ'_{ac} = 100 kPa as nicely as tests with σ'_{ac} = 200 kPa.

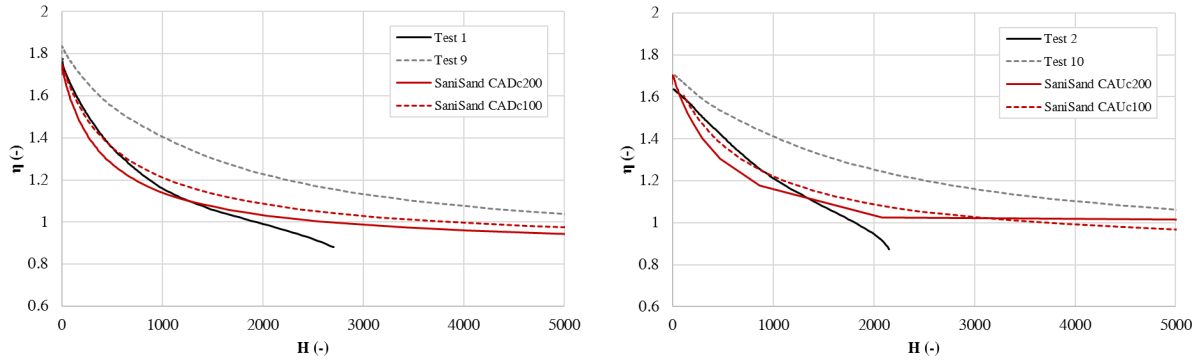

(a) $H-\eta$ plot for CADc tests

(b) $H-\eta$ plot for CAUc tests

Figure 8.4: Comparison of the hardening modulus for $\sigma'_{ac} = 200$ kPa and $\sigma'_{ac} = 100$ kPa

Together with the back calculation of the hardening modulus, an evaluation of how the different parameters change as a function of the mean effective stress is performed. It is found that the bounding stress ratio, M^b, the dilatancy stress ratio, M^d, and the dilatancy, d, are not changing with the mean stress, while the hardening parameter, b_0, has some stress dependency.

8.1.4 Introducing Cyclic Triaxial Data

The cyclic triaxial data are introduced and compared with monotonic triaxial tests and monotonic SANISAND simulations in Figure 8.5 on page 62. Stress paths, dilatancy and incremental shear strains are evaluated for a couple of drained and undrained cycles from Test 18 and Test 13, respectively. The drained and undrained tests are presented separately. Cycle number 1 and 600 are presented for the drained cyclic test, and cycle number 1 and 20 are presented for the undrained cyclic test. The same trends are seen in the monotonic and cyclic triaxial tests. The stress paths coincide well for the represented parts and the phase transformation lines are similar in both cases. The incremental shear strains and dilatancy show similar trends, but due to noise in the cyclic data it is hard to compare the dilatancy.

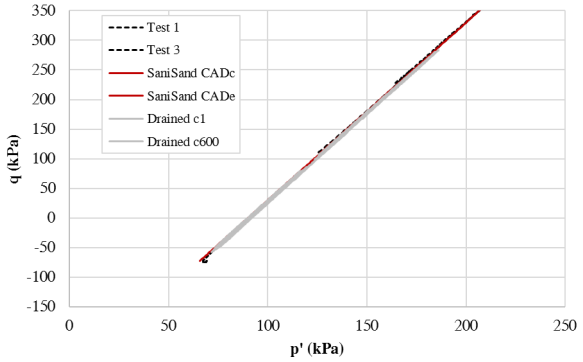

(a) $p' - q$ plot, drained

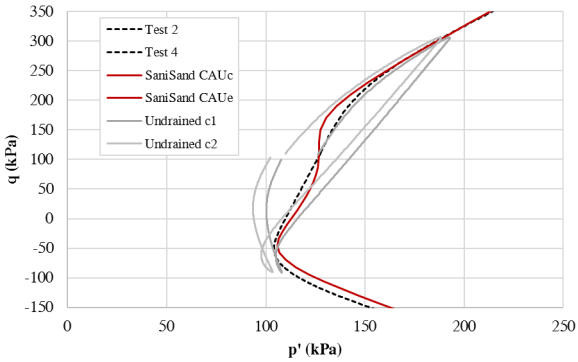

(b) $p' - q$ plot, undrained

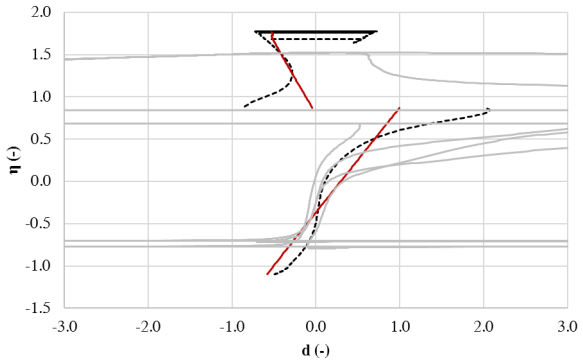

(c) d-η plot, drained

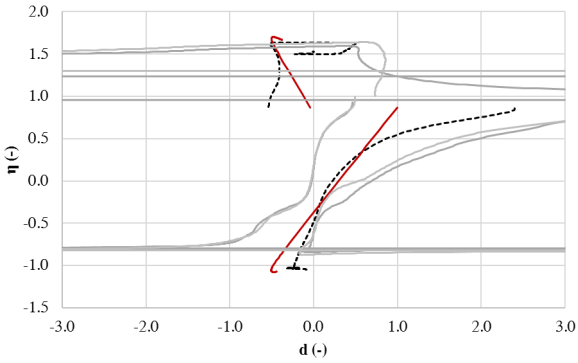

(d) d-η plot, undrained

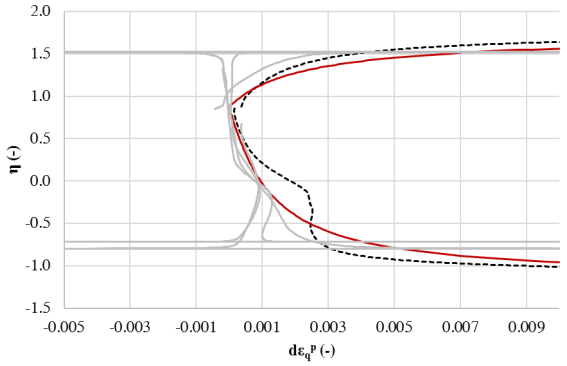

(e) $d\varepsilon_q^p - \eta$ plot, drained

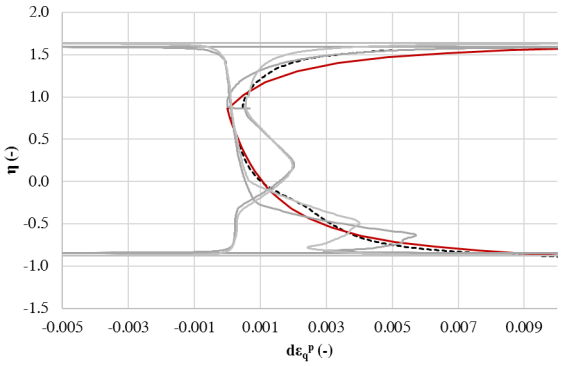

(f) $d\varepsilon_q^p - \eta$ plot, undrained

Figure 8.5: Monotonic triaxial and SANISAND results together with cyclic triaxial results

8.2 Cyclic Loading

Nine cyclic triaxial tests are run. Four of the tests are standard undrained cyclic triaxial tests, three of the tests are partly drained cyclic triaxial tests and two of the tests are standard drained cyclic triaxial tests. The tests with the same cyclic amplitude show the same trends in stress path, dilatancy and strains. Similar to the results from the monotonic tests discussed in Section 8.1, the stress paths behave as expected. Also the phase transformation line is approximately the same for all undrained tests with same cyclic amplitude which is expected because the density and load are equal for all samples.

Test 11 is a standard undrained cyclic triaxial test which differs from the other tests because it has a cyclic amplitude of $\tau_{cy} = 80$ kPa. It has not achieved the same butterfly-shape as the other tests, which indicates that the stress path is not close to the failure line in extension. This means that the material is only contracting in the extension part of the triaxial test, which also shown by the dilatancy-η plot where the line never crosses the phase transformation line.

Test 12 is a standard undrained cyclic triaxial test, consolidated to $\sigma_{ac} = 200$ kPa and $\sigma_{rc} = 90$ kPa. Test 12b is a repetition of Test 12 and will be discussed in Section 8.2.2. Test 17 is also a standard undrained cyclic triaxial test which is consolidated to $\sigma_{ac} = 200$ kPa and $\sigma_{rc} = 90$ kPa, but unlike Test 12 the sample is unloaded to $\sigma_{ac} = 170$ kPa before the test is run.

What happens to the sand properties after partial drainage is also of interest. Test 13, 14 and 15 have partial drainage. The three tests are standard undrained tests before drainage of the pore water is applied. Test 13 includes packages of 19-20 cycles with full drainage in between, while Test 14 and 15 include packages of 19-20 cycles with dissipation of 50% of the pore water pressure after each package. Test 13 has 20 undrained cycles before the applied drainage, Test 14 has 41 undrained cycles, and Test 15 has 21 undrained cycles.

Test 16 is a standard drained cyclic triaxial test. It is consolidated to $\sigma_a = 200$ kPa and $\sigma_h = 90$ kPa. The stress path does not behave as expected from a standard drained test because the sample generates pore water pressure during a cycle. The reason for this is unknown, and the results are looked upon as unreliable. Test 18 is also a standard drained cyclic triaxial test, but the cyclic amplitude $\tau_{cy} = 85$ kPa. The test behaves as expected and is used as a reference test when evaluating the drained SANISAND model.

8.2.1 Spread in Data

All undrained and partly drained cyclic tests started with at least 20 undrained cycles. It is expected for the behaviour of the sand to be identical, but it is observed deviations in pore water pressure generation among the first 20 cycles in the different tests. This can be seen in Figure 8.6, where the generated pore pressure is the difference between p'_{initial} for the first cycle and the p'_{initial} for the cycle of interest. There is no obvious reason for the deviation in the data, all the tests are prepared by the same method, they are anisotropically consolidated to the same stress state, and loaded with the same cyclic amplitude, $\tau_{\text{cy}} = 100$ kPa. The build-in relative density ranges from 75 % to 80 % and the G_{max} measurements vary from 118 kPa to 148 kPa, but there is no distinct correlation. It is possible that the grains have chosen a slight different orientation during preparation of the sample resulting in slightly deviation in behaviour. In order to further understand and interpret the variability in pore water pressure, the tests should be repeated by the same person to minimise the effect of sample preparation method.

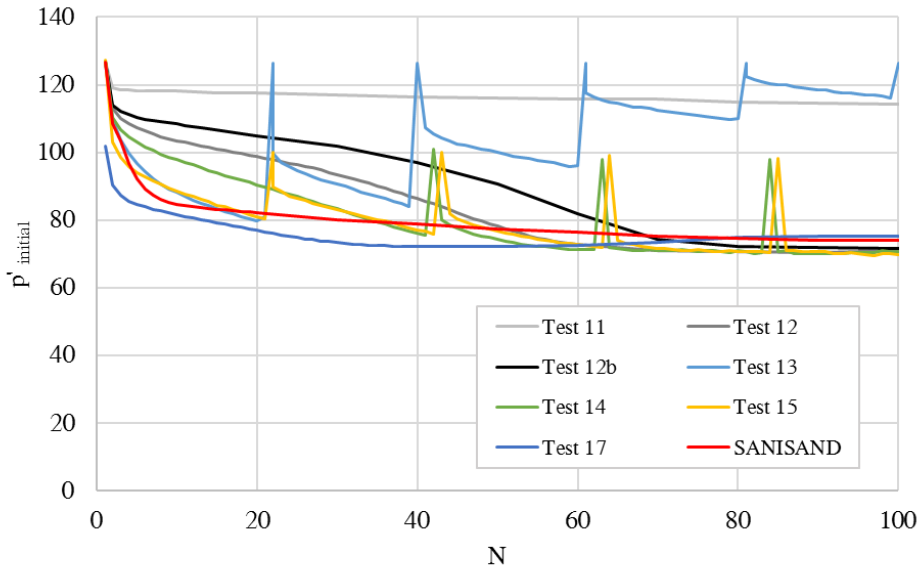

Figure 8.6: p'_{initial} versus number of cycles, N

The deviation in developed pore water pressure results in a variation of accumulated strains. The tests with slower generation of pore water pressure also accumulate plastic shear and volumetric strains in a rate slower than the tests with faster pore water pressure generation.

8.2.2 Repetition of Test 12

Test 12 is a standard undrained cyclic triaxial test. The dilative response of the test deviates from the other tests, so it was decided to repeat the test. Observed response from Test 12, marked as a grey line, and the repeated test, Test 12b, marked as a black line, is compared in Figure 8.7 where Cycle 1 and Cycle 20 for both tests are plotted. It is observed a more dilative response in the repeated test, and this agrees with the other monotonic and cyclic tests.

The repeated test generates pore water pressure in a slower rate than the original test, as can be seen in Figure 8.6. There are no differences in how the samples are prepared or run, still it is observed a different response in the repeated test. As discussed in Section 8.2.1 a reason for the deviation might be that the sample preparation methods used cannot guarantee the same sand properties even if the samples have approximately the same relative density.

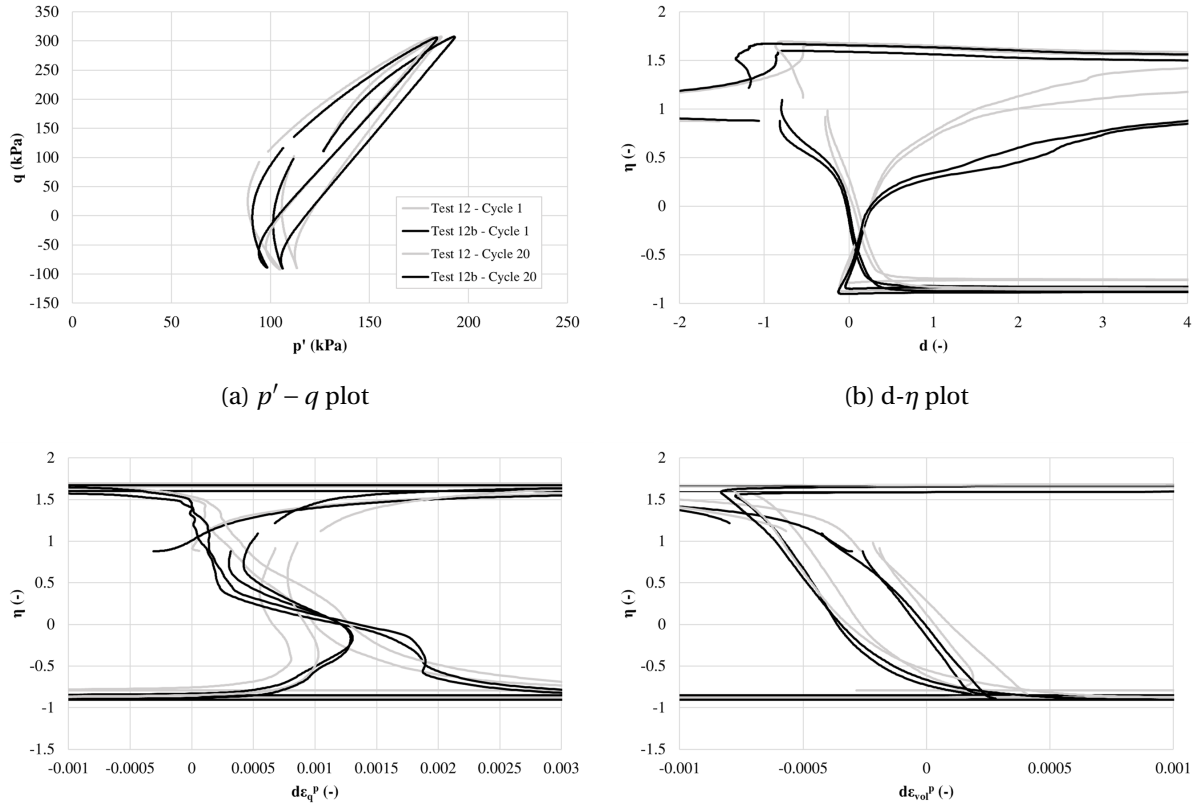

(a) $p' - q$ plot

(b) d-η plot

(c) $d\varepsilon_q^p - \eta$ plot

(d) $d\varepsilon_{vol}^p - \eta$ plot

Figure 8.7: Cycle 1 and 20 from Test 12 and 12b

8.2.3 Effect of Partly Drainage

Three of the tests, Test 13, Test 14 and Test 15, are partly drained cyclic triaxial tests. The tests include packages of undrained cycles, often with 19-20 undrained cycles in each package. Dissipation of the pore water is allowed after each package. 100 % of the pore water pressure is dissipated after each package in Test 13, and 50 % of the pore water pressure is dissipated after each package in Test 14 and 15. In Test 14 and 15, the undrained packages are applied until the samples fail after approximately 140 cycles. After 300 cycles in Test 13 there is no more pore water to dissipate, and the test is run undrained for 400 more cycles. The pore water dissipation for the first 100 cycles is illustrated in the plot of accumulated pore water pressure in Figure 8.6 on page 64.

Package 1 and 2 for Test 13 are plotted in Figure 8.8. The response of the soil is similar. The $p' - q$ plot shows the same tendencies in the stress paths, more pore water pressure is generated in the first cycle of the test, and after drainage. The phase transformation line is almost identical for the cycles in the first and the second package, and shows that the dilative behaviour of the soil is not affected by the drainage.

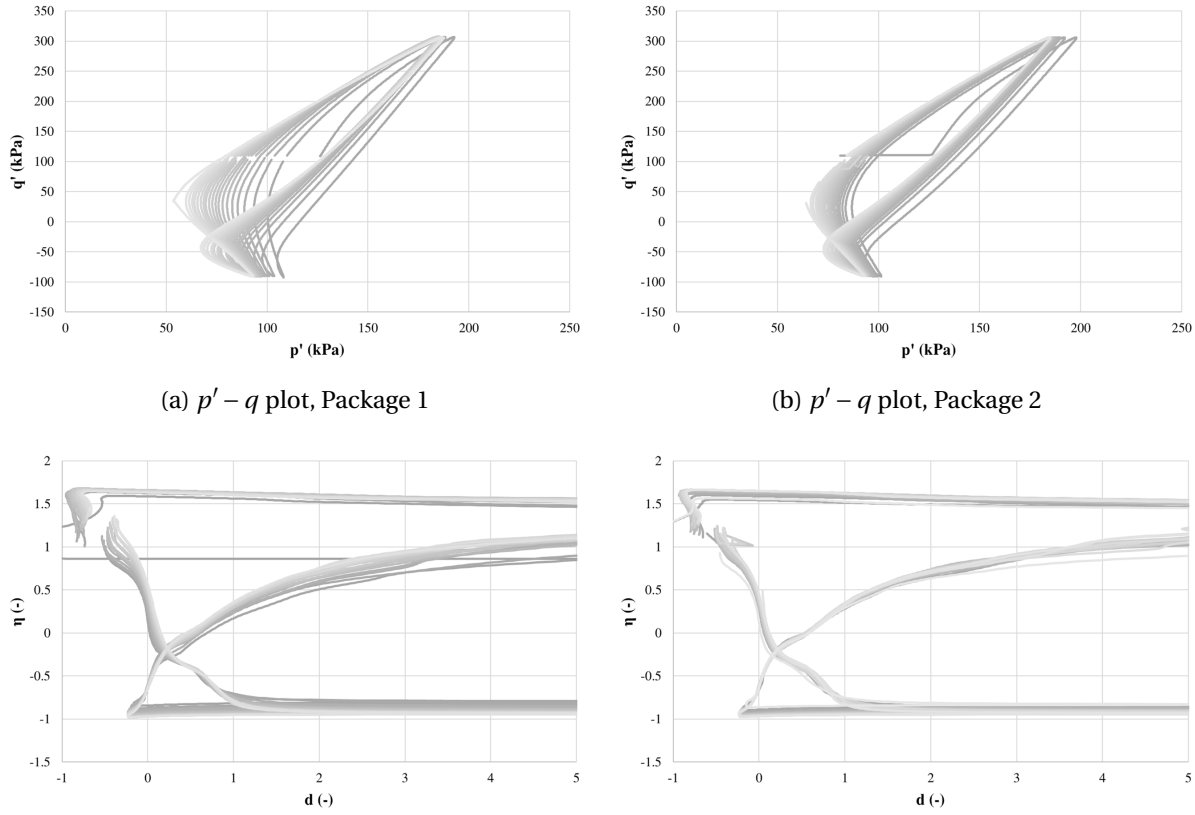

(a) $p' - q$ plot, Package 1

(b) $p' - q$ plot, Package 2

(c) $d - \eta$ plot, Package 1

(d) $d - \eta$ plot, Package 2

Figure 8.8: Partly drained cyclic triaxial test, package 1 and 2

8.2.4 Mean Stress Condition as a State Parameter

The material looks at the mean stress condition as a state parameter. How the material got to the specific stress condition does not seem to have an impact on the behaviour of the material. Different cycles with a similar p'_{initial} are compared, and the material behaves similar in the different tests performed. Two examples are given in Figure 8.9 and 8.10 on page 68-69. Cycles from continuously undrained tests are marked as continuous lines, and cycles from the partly drained tests after drainage are marked as discontinuous lines. In Figure 8.9 all tests are represented with a cycle from the undrained part of the triaxial tests, Test 13 is in addition presented with a cycle after the first drainage. Despite deviation in pore water pressure generation, the different tests behave very similar when considering cycles starting at the same p'.

The phase transformation line is the same for all tests in Figure 8.9, but Test 12 has a behaviour that is less dilative compared to the other tests seen in Figure 8.9b. The $p' - q$ plot verifies the less dilative behaviour as the butterfly-shape is not as prominent as in the other tests.

When studying the tests exposed to dissipation of water, the material behaviour does not seem to have changed after the drainage. In Figure 8.10, Test 14 and Test 15 have been exposed to dissipation of pore water pressure twice. The responses are similar to the tests run continuously undrained. There is deviation in the $\varepsilon_q^p - \eta$ plot in Figure 8.10c, where the amplitude of the plastic shear strain is different. Test 14 and Test 15 with partial drainage are extremes, Test 15 with the smallest amplitude and Test 14 with the greatest amplitude. The same can also be seen in the $d\varepsilon_q^p - \eta$ plot in Figure 8.10d. The difference in incremental strain and the amplitude for the two partly drained tests imply that there is no direct correlation between the dissipation of pore water pressure and change in incremental strains. However, the strains are small and the deviation is not prominent.

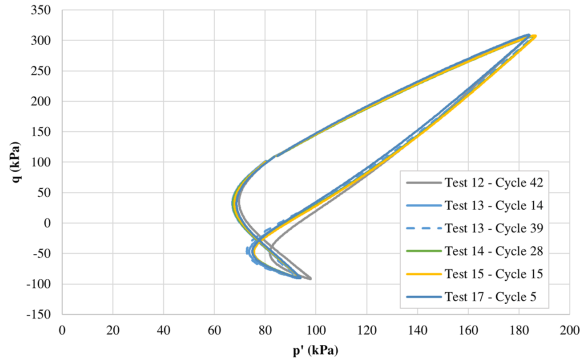

(a) $p' - q$ plot

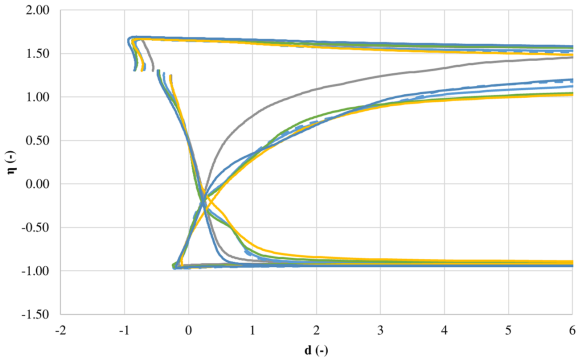

(b) $d - \eta$ plot

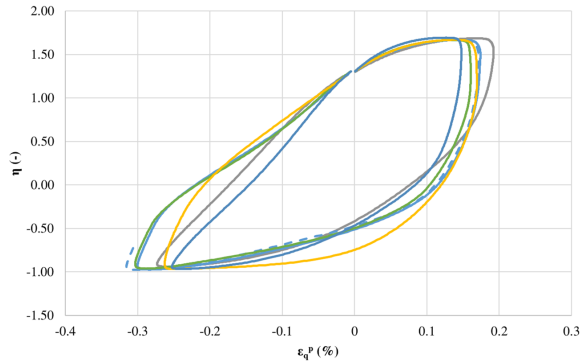

(c) $\varepsilon_q^p - \eta$ plot

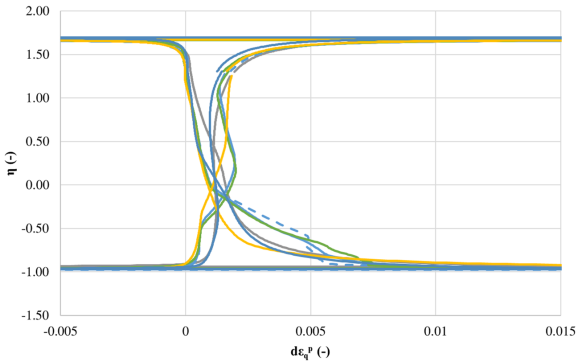

(d) $d\varepsilon_q^p - \eta$ plot

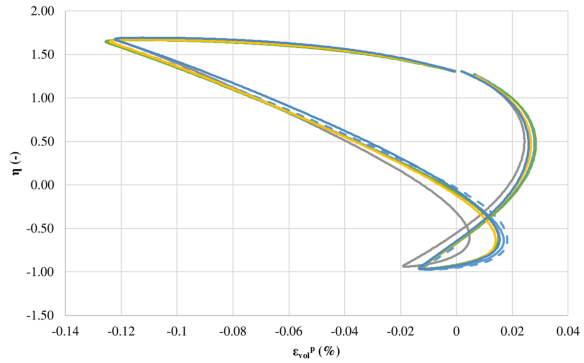

(e) $\varepsilon_{vol}^p - \eta$ plot

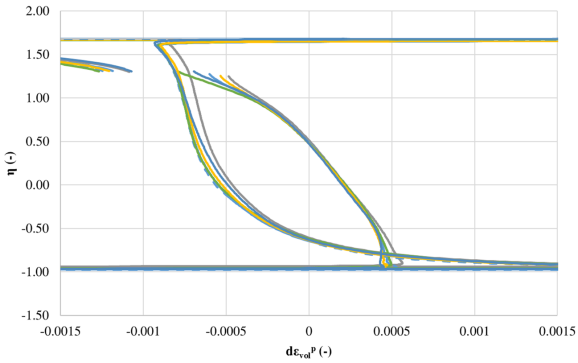

(f) $d\varepsilon_{vol}^p - \eta$ plot

Figure 8.9: Comparison of cycles from various tests starting at $p' = 84$ kPa

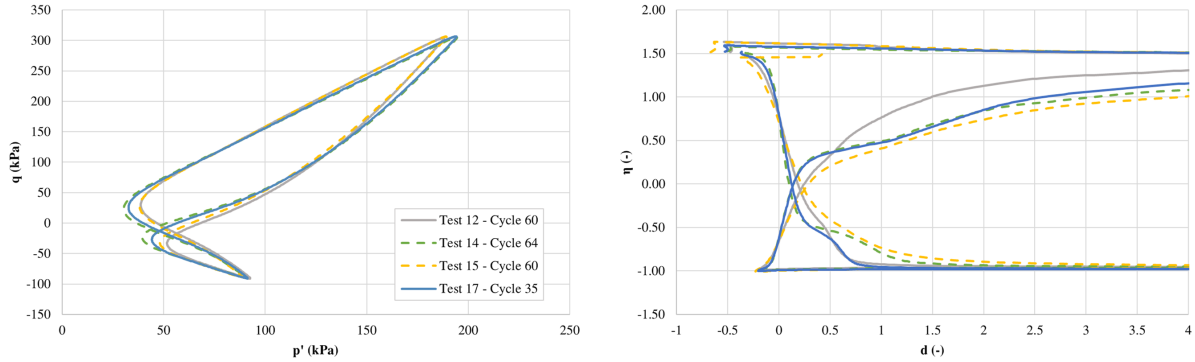

(a) $p' - q$ plot

(b) $d - \eta$ plot

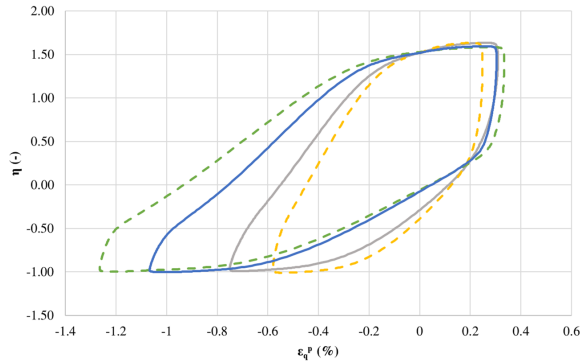

(c) $\varepsilon_q^p - \eta$ plot

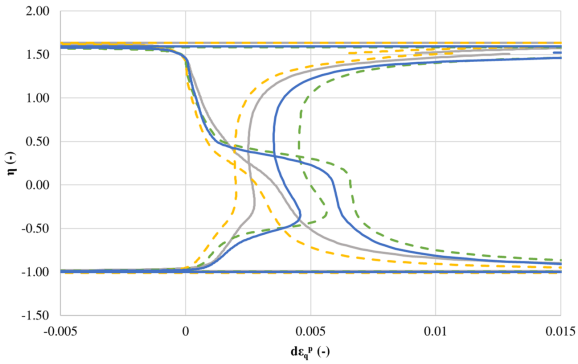

(d) $d\varepsilon_q^p - \eta$ plot

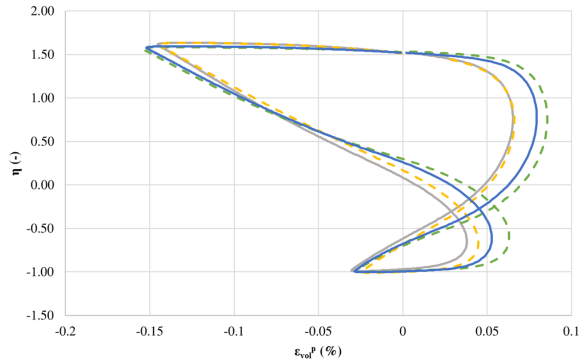

(e) $\varepsilon_{vol}^p - \eta$ plot

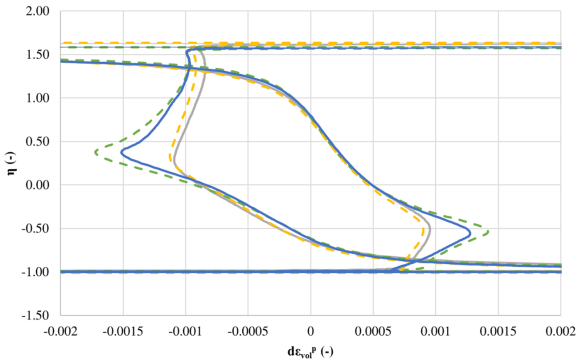

(f) $d\varepsilon_{vol}^p - \eta$ plot

Figure 8.10: Comparison of cycles from various tests starting at $p' = 72$ kPa

8.2.5 SANISAND Material Model

The behaviour of the sand presented from the cyclic triaxial tests are simulated by the cyclic SANISAND material model. The SANISAND model accounting for fabric changes (Dafalias and Manzari, 2004) is utilised, but to represent the behaviour of the Siri sand in an optimal manner, the input parameters are separated into one set for compression and one set for extension.

Dividing the parameters into one set for compression and one set for extension works well in the triaxial formulation of the model. The compression and extension parts are well defined with the s which is +1 in compression and -1 in extension. In the multiaxial generalisation of the model the direction of the loading is complex. Dafalias and Manzari (2004) defines a lode angle, θ, that varies from 0 to $\pi/3$ as the loading changes from triaxial compression to extension. In their model, the lode angle is used to interpolate the critical stress ratio, M, for a given θ between its values in compression, M_c, and extension, M_e. A similar solution should be possible to implement for the other parameters.

The input parameters for the cyclic SANISAND model are listed in Table 7.1 on page 53. One unique set of parameters is applied in the cyclic simulations of the Siri sand, but there are several combinations of parameters that simulate the sand in an adequate manner. E.g. the stress dependency in the critical state parameters are marginal, thus different combinations of the parameters result in the same product.

When selecting SANISAND parameters for the cyclic simulation of the Siri sand the values from the monotonic SANISAND model are taken as a starting point. The parameters are adjusted to fit Test 13. It is emphasised to reproduce the phase transformation line, and also to simulate the correct hardening response. By concentrating on this, the representation of the stress path is not optimal, observed in Figure 7.2a on page 54. Choosing a different set of parameters would simulate the stress path in a more correct manner, but this would affect the other components. The SANISAND simulation underestimates the contractive behaviour during reversing of the load because the hardening goes towards infinite. The elasto-plastic framework does not capture the behaviour at load reversing accurately.

The elasticity parameters, the critical state parameters and the yield surface parameter are identical in the cyclic and monotonic SANISAND model. These parameters have the same values in compression and extension, with the exception of the critical state stress ratio, M. The dilatancy and hardening parameters have been fitted with the data from the cyclic triaxial tests as explained in Section 8.2.6 and 8.2.7.

8.2.6 Dilatancy Parameters

The simulation of the dilatancy from the cyclic SANISAND model together with the calculated dilatancy from Test 13 are illustrated in Figure 8.11. The model predicts the dilatancy behaviour fairly well, the trends are represented and the phase transformation lines coincide.

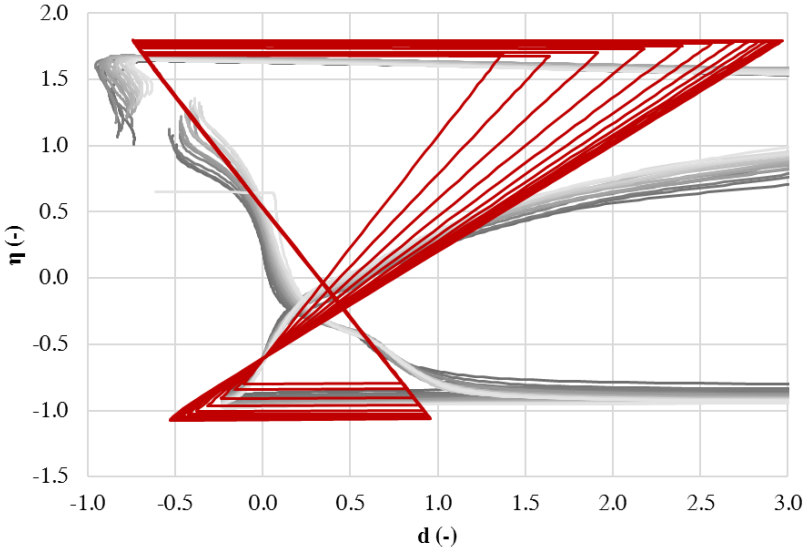

Figure 8.11: SANISAND representation of the dilatancy

The dilatancy behaviour in the SANISAND model is affected by several input parameters. These are the state parameters A_0 and n^d, in addition to the fabric-dilatancy parameters c_z and $z_{\max}$ which are introduced in the cyclic SANISAND model.

The magnitude of the dilatancy is directly correlated to the parameter A_d as presented in Equation 4.10 on page 20. The value of A_d is depending on the parameter A_0 and z, see Equation 4.16 on page 21. SANISAND includes fabric change by introducing a dilatancy internal variable z that changes depending on the incremental plastic volume strain, and the fabric-dilatancy parameters c_z and $z_{\max}$. The fabric-dilatancy parameters c_z and $z_{\max}$ are introduced because during stress increment reversal during cyclic loading, the pore water pressure is increased and p' correspondingly decrease, following a dilative tendency response. This is seen from the butterfly $p' - q$ orbits in the triaxial test results. $z_{\max}$ is a material constant, and ranges from 3 to 5 for most sands. c_z is also a material constant and a greater c_z results in a greater change in z, which leads to a faster stabilisation of the cycles. A $z_{\max}$ of 3.0 and a c_z of 100 for both compression and extension fits well to simulate our tests.

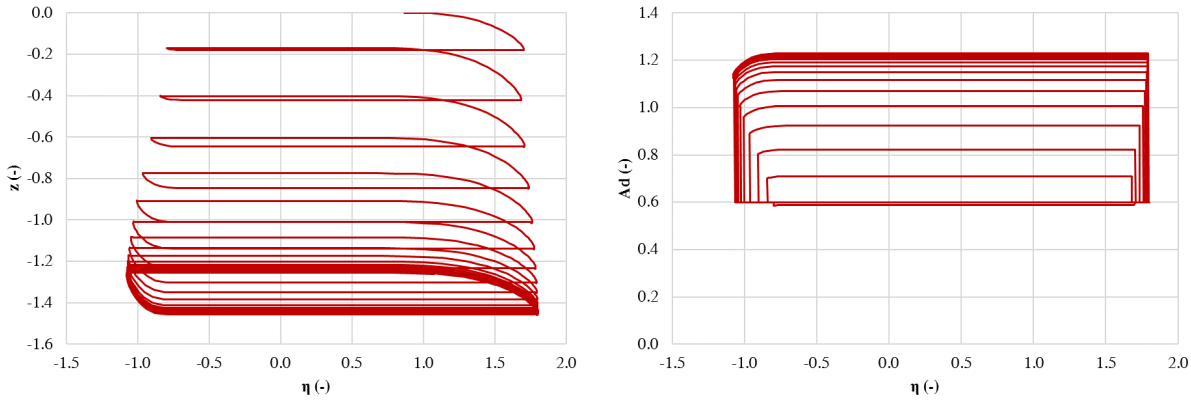

(a) η - z plot

(b) η - A_d plot

Figure 8.12: Dilatancy parameters

Figure 8.12 illustrates how A_0 and z change as a function of the stress ratio, η. Due to the anisotropic consolidation, z is always negative in our tests. The sand dilates for a large part of the compression phase, which results in a negative dz. In extension, dz changes to a slightly positive value due to some dilation, but this results in a negative z for the whole test. The development of z is illustrated in Figure 8.12a. As a consequence of the negative z, the Macauley brackets in Equation 4.10 on page 20 gives a value of zero in compression, thus A_d equals A_0 in compression. The A_d value in extension increases due to the decreasing z for each cycle, as illustrated in Figure 8.12b. The A_0 input parameter is slightly larger in compression compared to extension. This results in a very similar A_d in compression and extension for the first cycle. Due to the change in A_d in extension, the stress path changes more for this part. For the chosen A_0 input value in compression and extension, A_d is larger in extension compared to compression. This implies that the sand has a greater increase in dilatancy in extension compared to compression. This is one of the reasons why the model has some problems in describing our sand. The model implies that the sand dilates more than what the triaxial data displays in extension.

The last dilatancy input parameter is the material constant n^d which affects the phase transformation line, as opposed to A_0. When n^d is increased in compression, the dilatancy stress ratio M^d decreases and the phase transformation line moves closer to the x-axis when the state is denser than critical. This occurs in extension when n^d is decreased. n^d is chosen to correctly describe the phase transformation line.

8.2.7 Plastic Modulus Parameters

The SANISAND simulation of the hardening of the Siri sand is illustrated in Figure 8.13a by the incremental plastic shear strains. As seen from the figure, the model is only able to partly describe the behaviour. The shape of the incremental plastic shear strains are well described, except the last part of each cycle. In the cyclic triaxial test on the Siri sand, the incremental plastic shear strains increase throughout the cycles, in contrast to the SANISAND simulation which has an insignificant increase. As a consequence of this, SANISAND poorly describes the total plastic shear strains. The SANISAND model represents a sand that is too stiff compared to the Siri sand, as can be seen Figure 8.13b. Wichtmann (2016) discovered the same tendency in his study of the SANISAND model. The SANISAND formulations do not manage to simulate total strains in a correct manner. The SANISAND model predicts a constant amplitude in total strains for the chosen input parameters, but the triaxial test results display an increasing amplitude throughout the cycles.

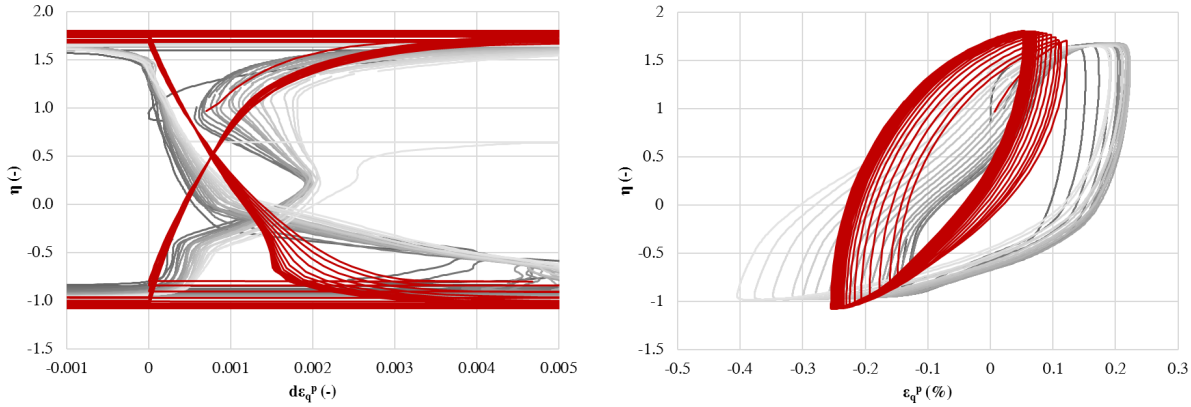

(a) Incremental plastic shear strains

(b) Total plastic shear strains

Figure 8.13: SANISAND representation of the plastic shear strains

The simulation of the hardening in the SANISAND model is controlled by three plastic modulus input parameters, h_0, c_h and n^b. In addition, the stress ratio at initiation of a loading process, η_{in}, influences the representation of the hardening. The plastic modulus parameters h_0 and c_h are included in the equation of b_0 as described in Equation 4.9 on page 19. An increase in b_0 results in an increase in the hardening, H. An increase in b_0 is caused by an increase in h_0 and a decrease in c_h. The last plastic modulus parameter, n^b, is included in the equation of the bounding stress ratio, M^b, see Equation 4.12 on page 20. The hardening increases if n^b is increased.

To get a deeper understanding of how the different parameters in the SANISAND formulations affect the representation of the Siri sand, a comparison with the triaxial tests is carried out. The SANISAND formulations are applied to the triaxial data to back calculate the parameters h, b_0 and h_0 with the other input values as listed in Table 7.1 on page 53. Figure 8.14 displays the back calculation of the hardening parameter h from the triaxial data together with the development of h in the SANISAND model. The development of h in the triaxial data and the SANISAND model seem to have similar trends, but they do not coincide accurately. The deviation in h explains the difference in incremental shear strains as pointed out above.

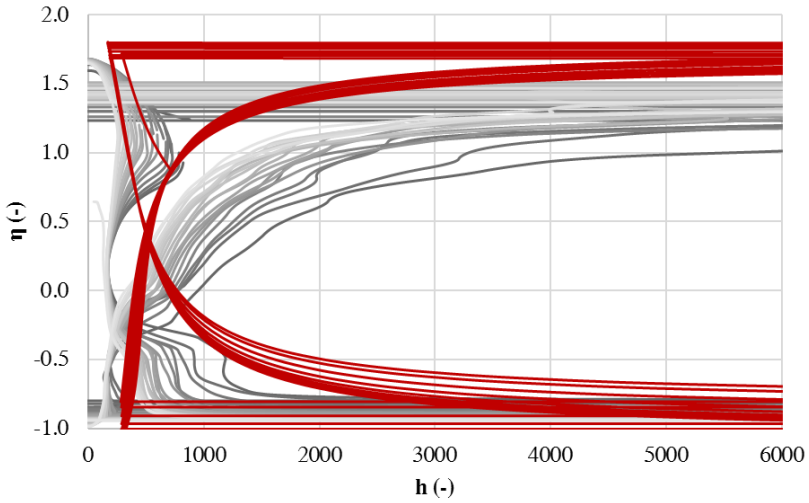

Figure 8.14: Comparison of h from the SANISAND formulation and triaxial test data

The parameter h_0 is a constant input parameter in the SANISAND model. However, when the triaxial data is back calculated, the tests show a decreasing h_0 throughout the cycles. Figure 8.15 illustrates how the parameters h and h_0 develop for a specific stress ratio for the first 20 cycles of Test 13 and Test 15 and first 40 cycles of Test 12, Test 14 and Test 17. h and h_0 are selected with $\eta = 0.5$ in extension, as this is the stress ratio that shows the most decrease in h and h_0. The trend of h in Figure 8.15a and h_0 in Figure 8.15b are equal, which implies that the stress dependency in Equation 4.9 on page 19 does not make any contribution.

To improve the prediction of the hardening of the sand, an equation of the hardening parameter, h_0, should be implemented. The function should decrease throughout the cycles, and this would also give a better representation of the incremental and total shear strains. One suggestion is to look at the possibility to implement it as a function of the fabric change, similar to the dilatancy.

The different tests are performed with the same approach with similar relative density, thus it was expected that the tests would behave in a similar manner. The tests deviate to a significantly degree, see Figure 8.15. This implies that the sand has changed some of its properties during the preparation of the tests, which has resulted in a small change in behaviour. It may therefore be necessary to use different input parameters for different tests when the SANISAND model is applied.

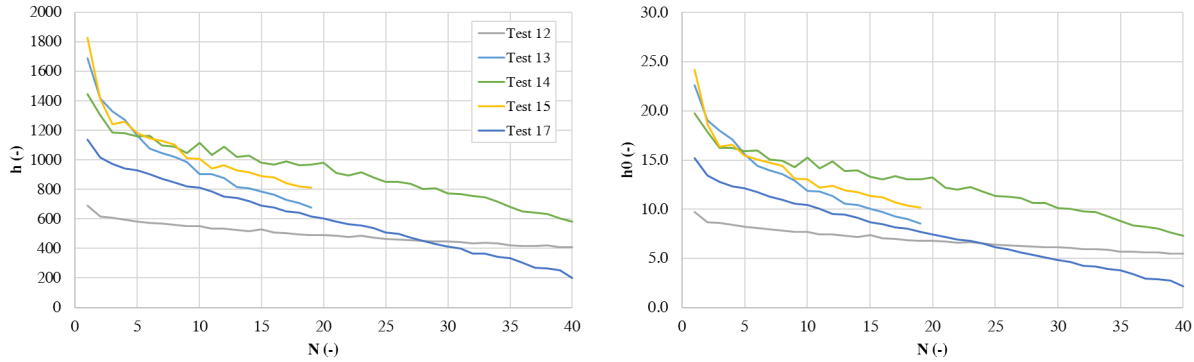

(a) $N-h$ plot (b) $N-h_0$ plot

Figure 8.15: Back calculation of h and h_0 from different tests

In SANISAND the η_{in} is given as the initial η for each cycle. When fitting parameters to the data from the triaxial tests, it was found that the SANISAND model was simulating a too stiff response for the first cycle. By reducing the first η_{in} in the simulation to $0.1 \cdot \eta_{\text{start}}$ the representation improved significantly, this is illustrated in Figure 8.16.

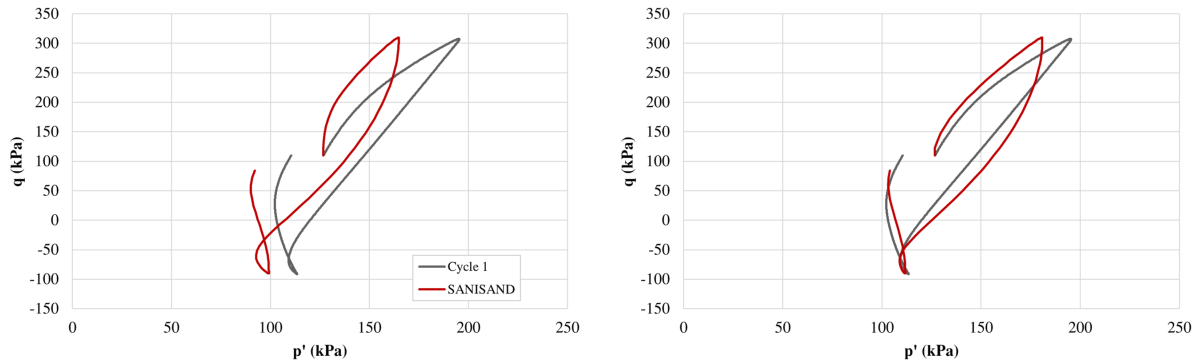

(a) $\eta_{\text{initial}} = 0.99 \cdot \eta$ (b) $\eta_{\text{initial}} = 0.1 \cdot \eta$

Figure 8.16: Evaluation of η_{initial}

8.2.8 SANISAND Model Simulating Drained Response

The undrained response of the Siri sand is the main focus of this master thesis, but it is also desirable to simulate the drained response of the sand. This is done by modifying the implementation of the model to allow volume change. In the SANISAND model simulating drained response, the pore water pressure is allowed to dissipate and no pore water pressure is generated. This can be seen in the stress path in Figure 7.3a on page 55, as it is identical for each cycle.

The undrained input parameters are applied to the drained simulation, except c_z. The value of c_z is decreased compared to the undrained simulation to make the cycles stabilise in a slower rate. The simulation predicts the behaviour of the sand to some extent. To improve the representation, some of the parameters should be modified. The phase transformation line does not coincide with the triaxial tests and the total and incremental shear strains are not correctly represented.

Chapter 9

Conclusions and Recommendations for Further Work

9.1 Summary and Conclusions

Several monotonic and cyclic triaxial tests have been performed at NGI in association with the ongoing strategic project, SP9. The tests have been performed with dense saturated sand from the Siri offshore field in the North Sea, and the aim have been to interpret the triaxial test results within an elasto-plastic constitutive framework. The laboratory data has been filtered in MATLAB and the interpretations have been performed in Excel. Different drainage conditions have been evaluated, and characteristic behaviours have been established.

The interpretations of the tests within an elasto-plastic framework describe a response as expected. However, there have been observed deviation in the pore water pressure generation in the different cyclic triaxial tests. Sample preparation method affects the properties of the sand, and is most likely the reason for the deviations. Cycles with the same initial mean stress from different tests have been compared, and there is a striking resemblance of the response. This indicates that the material considers the mean stress condition as a state parameter, and is independent on how it got to the specific stress condition.

A monotonic and cyclic simulation of the SANISAND model limited to the triaxial stress space have been implemented in Excel. A verification of the model and a parameter study have been carried out. It has been desirable to compare the response simulated by SANISAND to the triaxial test results, and a set of input parameters for the SANISAND model were required. The SANISAND input parameters were initially fitted by trial and error to the monotonic tests with the Toyoura sand parameters as a starting point. The parameters obtained

for the monotonic model were then adapted to the cyclic simulations. By evaluating the different SANISAND formulations and how the different parameters affect the simulations, the parameters were improved for the cyclic SANISAND model. The SANISAND model simulates the triaxial test results in a suitable manner with the applied input parameters.

One set of parameters has been applied in all cyclic simulations of the Siri sand. However, it has been observed that due to some variation in stress condition and relative density of the tests, small modifications of the parameters are required to represent the behaviour of each test in an optimal manner. It was also found that several combinations of input parameters would simulate the sand in a satisfying manner.

This study indicates that the SANISAND model has some limitations. The representations of incremental plastic and volume strains are inaccurate, which result in inaccurate simulations of total shear and volume strains. An equation of the hardening parameter, h_0, should be implemented as a function which decreases throughout the cycles. The intention is to obtain a better representation of the hardening of the sand, in addition to the incremental shear strains. One suggestion is to look at the possibility to implement it as a function of the fabric change, similar to the dilatancy.

Despite the limitations, the model represents the behaviour of water saturated dense sand in an adequate manner. The model is relatively simple compared to the alternatives, and the user-friendly framework is advantageous.

9.2 Recommendations for Further Work

The SANISAND model accounting for fabric change effects is a relatively new material model. Model parameters for the Toyoura sand have been well studied by Dafalias and Manzari (2004). When it comes to other types of sand there is not much information on model parameters. A further study of the material model and parameters fitted to different types of sand should be performed to validate the model.

The model has some limitations. The cyclic undrained triaxial tests show a tendency of decreased hardening. To capture this tendency in the model, it is suggested to implement an equation for h_0.

The model parameters for Siri sand should only be used as a proposed set of parameters, and should be studied further before implementation in design projects. For further validation of the model parameters, more tests should be performed. The cyclic triaxial tests have a density of D_r = 80 % and all tests are run anisotropically consolidated. To make sure

the parameters simulates the Siri sand, tests of different densities should be performed, also an isotropically consolidated test should be run. Tests with different τ_{cy} exhibit different behaviour, and it is therefore recommend to run cyclic tests with higher loading amplitudes.

During the first 20 undrained cycles in the laboratory tests, there is a deviation in the pore water pressure generation. A repetition of some of the tests may be useful to understand the behaviour of the sand and to see if there is some correlation between how the sample is prepared and the response. It would also be advantageous to develop a standardised sample preparation method that guarantees the sand samples to have the same properties.

Bibliography

Andersen, K. H. (2009). Bearing capacity under cyclic loading—offshore, along the coast, and on land. *Canadian Geotechnical Journal*, 46(5):513–535.

Andersen, K. H. (2015). Cyclic soil parameters for offshore foundation design. *Frontiers in Offshore Geotechnics III*, 5.

Bardet, J. P. (1986). Bounding surface plasticity model for sands. *Journal of Engineering Mechanics*, 112(11):1198–1217.

Barrero, A. R., Manzari, M. T., and Lizcano, A. (2015). Application of an advanced constitutive model in nonlinear dynamic analysis of tailings dam. In *Proceedings of the Sixty Eighth Canadian Geotechnical Conference*.

Been, K. and Jefferies, M. G. (1985). A state parameter for sands. *Géotechnique*, 35(2):99–112.

Carotenuto, P. and Suzuki, Y. (2016). WP3 - Technical Note - Summary 2016. Technical report, NGI.

Casagrande, A. (1979). *Liquefaction and cyclic deformation of sands: a critical review*. Pierce Hall.

Casagrande, A. and Hirschfeld, R. C. (1962). Investigation of stress-deformation and strength characteristics of compacted clays. Technical report, DTIC Document.

Castro, G. (1975). Liquefaction and cyclic mobility of saturated sands. *Journal of the Geotechnical Engineering Division*, 101(6):551–569.

Cheng, Z., Dafalias, Y. F., and Manzari, M. T. (2013). Application of sanisand dafalias-manzari model in flac3d. *Continuum and Distinct Element Numerical Modeling in Geomechanics*, 09(03).

Dafalias, Y. F. (1986). Bounding surface plasticity. i: Mathematical foundation and hypoplasticity. *Journal of Engineering Mechanics*, 112(9):966–987.

Dafalias, Y. F. and Manzari, M. T. (2004). Simple plasticity sand model accounting for fabric change effects. *Journal of Engineering Mechanics*, 130(6):622–634.

Dafalias, Y. F. and Popov, E. P. (1975). A model of nonlinearly hardening materials for complex loading. *Acta Mechanica*, 21(3):173–192.

Hooke, R. (1675). *A description of helioscopes, and some other instruments*. London.

Irgens, F. (2008). *Continuum mechanics*. Springer Science & Business Media.

Jostad, H., Grimstad, G., Andersen, K., and Sivasithamparam, N. (2015). A fe procedure for calculation of cyclic behaviour of offshore foundations under partly drained conditions. *Frontiers in Offshore Geotechnics III*, pages 153–172.

Khalili, N., Habte, M. A., and Valliappan, S. (2005). A bounding surface plasticity model for cyclic loading of granular soils. *International Journal for Numerical Methods in Engineering*, 63(14):1939–1960.

Lade, P. and Ibsen, L. (1997). A study of the phase transformation and the characteristic lines of sand behaviour. In *Proc. Int. Symp. on Deformation and Progressive Failure in Geomechanics, Nagoya*, pages 353–359.

Li, X. S. and Dafalias, Y. F. (2000). Dilatancy for cohesionless soils. *Géotechnique*, 50(4):449–460.

Li, X. S. and Dafalias, Y. F. (2011). Anisotropic critical state theory: role of fabric. *Journal of Engineering Mechanics*, 138(3):263–275.

Manzari, M. T. and Dafalias, Y. F. (1997). A critical state two-surface plasticity model for sands. *Géotechnique*, 47(2):255–272.

MathWorks (2017). *Signal Processing Toolbox™, User's Guide*. MathWorks.

Mitchell, J. K., Soga, K., et al. (1976). *Fundamentals of soil behavior*. John Wiley & Sons Hoboken, NJ.

Nasser, S. N. (1980). On behavior of granular materials in simple shear. *Soils and Foundations*, 20(3):59–73.

Nemat-Nasser, S. and Tobita, Y. (1982). Influence of fabric on liquefaction and densification potential of cohesionless sand. *Mechanics of Materials*, 1(1):43–62.

Nordal, S. (2016). *Geotechnical Engineering Advanced Course, Lecture notes and background material*. Norwegian University of Science and Technology Geotechnical Division, Trondheim.

Richart, F. E., Hall, J. R., and Woods, R. D. (1970). *Vibrations of Soils and Foundations*. Prentice Hall.

Sandven, R. (2011). Tba 4110 geotechnics, field and lab investigations. *NTNU Geothecnical Division, Trondheim*.

Schofield, A. N. and Wroth, C. P. (1968). *Critical State Soil Mechanics*. McGraw-Hill.

Sze, H. Y. and Yang, J. (2013). Failure modes of sand in undrained cyclic loading: Impact of sample preparation. *Journal of geotechnical and geoenvironmental engineering*, 140(1):152–169.

Taiebat, M. and Dafalias, Y. F. (2007). Sanisand: Simple anisotropic sand plasticity model. *International journal for numerical and analytical methods in geomechanics*, 32:915–948.

Tennakoon, N., Indraratna, B., Nimbalkar, S., and Sloan, S. W. (2015). Application of bounding surface plasticity concept for clay-fouled ballast under drained loading. *Computers and Geotechnics*, 70:96 – 105.

Wang, Y. and Li, X. S. (1998). Linear representation of steady-state line for sand. *Journal of Geotechnical and Geoenvironmental Engineering, ASCE*, 123(7):1215–1217.

Wichtmann, T. (2016). Soil behaviour under cyclic loading-experimental observations, constitutive description and applications. habilitation. *Karlsruhe Institute for Technology, Institute of Soil Mechanics and Rock Mechanics*, 181.

Wood, D. M. (1990). *Soil Behaviour and Critical State Soil Mechanics*. Cambridge University Press, Cambridge.

Yang, Z., Lit, X., and Yang, J. (2008). Quantifying and modelling fabric anisotropy of granular soils. *Géotechnique*.

Zhang, F., Ye, B., and Ye, G. (2013). *A Unified Description of Toyoura Sand*, pages 663–674. Springer Berlin Heidelberg, Berlin, Heidelberg.

Appendices

List of Figures in Appendices

List of Tables in Appendices

Appendix A

Results from Monotonic Triaxial Tests

A.1 Test 1, 2, 3, 4

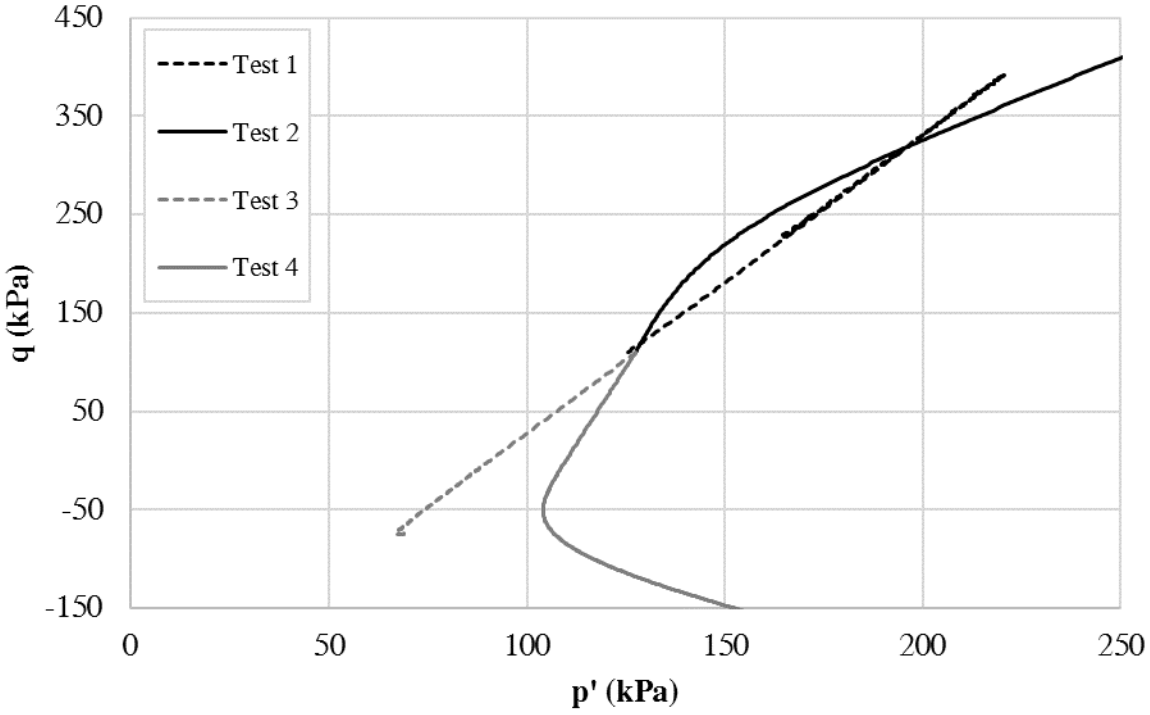

Figure A.1: $p' - q$ plot

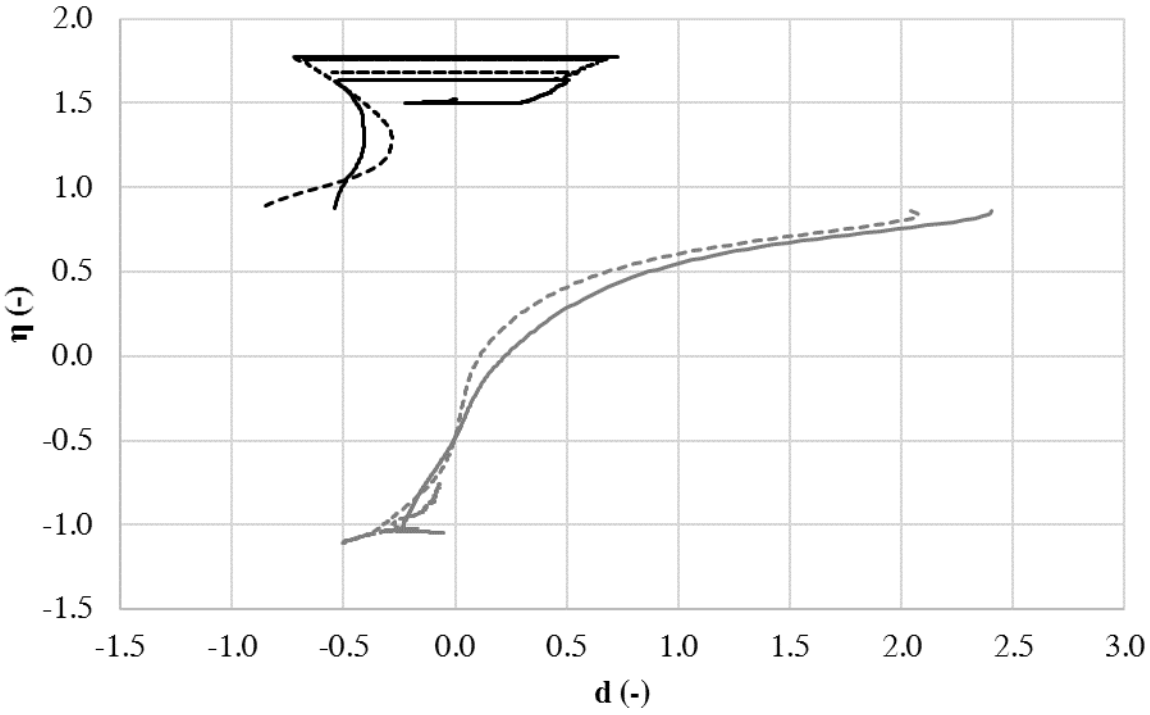

Figure A.2: $d - \eta$ plot

A.2 Test 5, 6, 7, 8

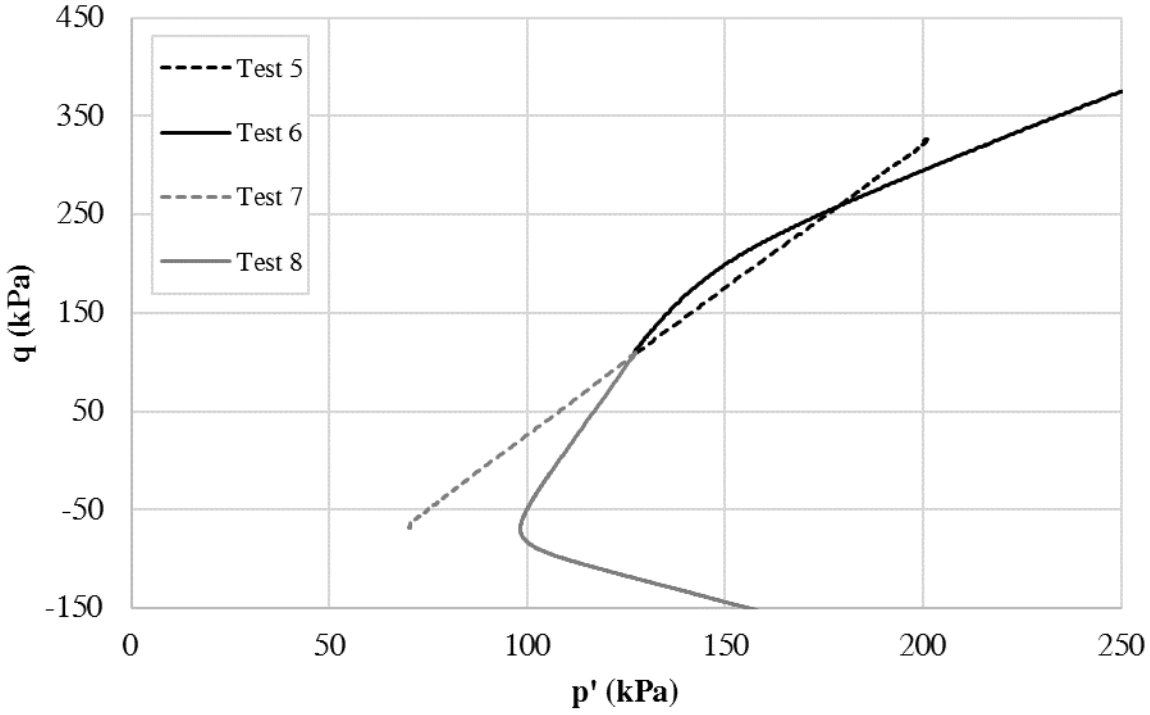

Figure A.7: $p' - q$ plot

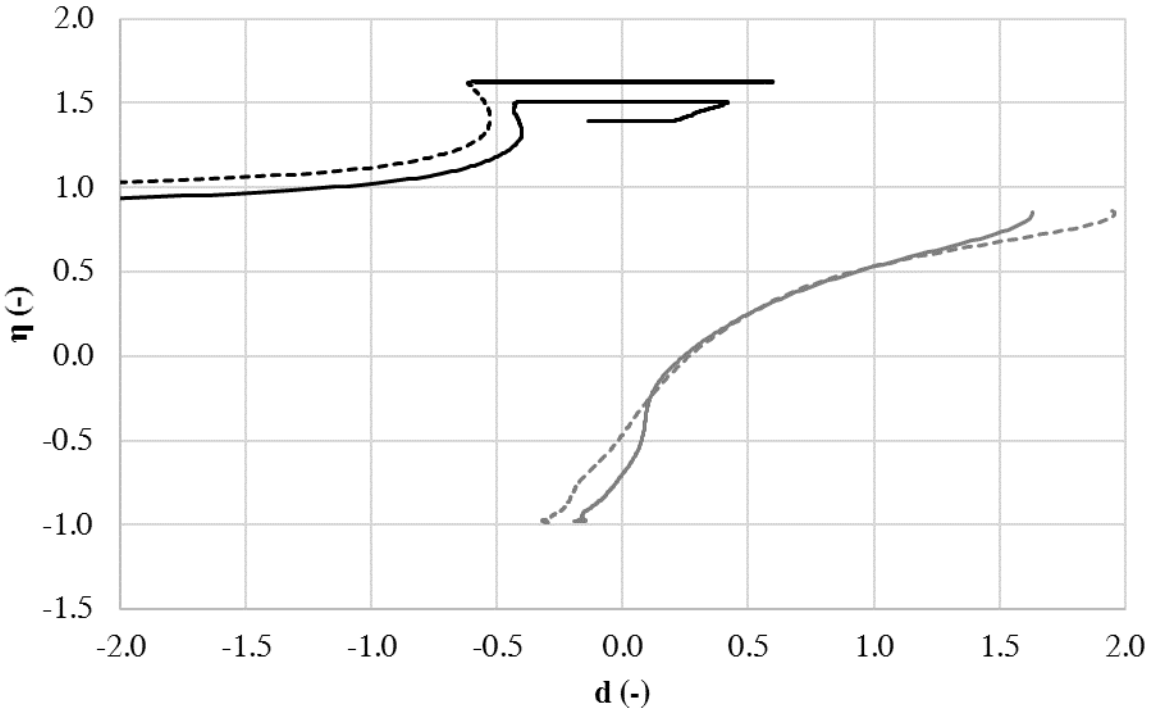

Figure A.8: $d - \eta$ plot

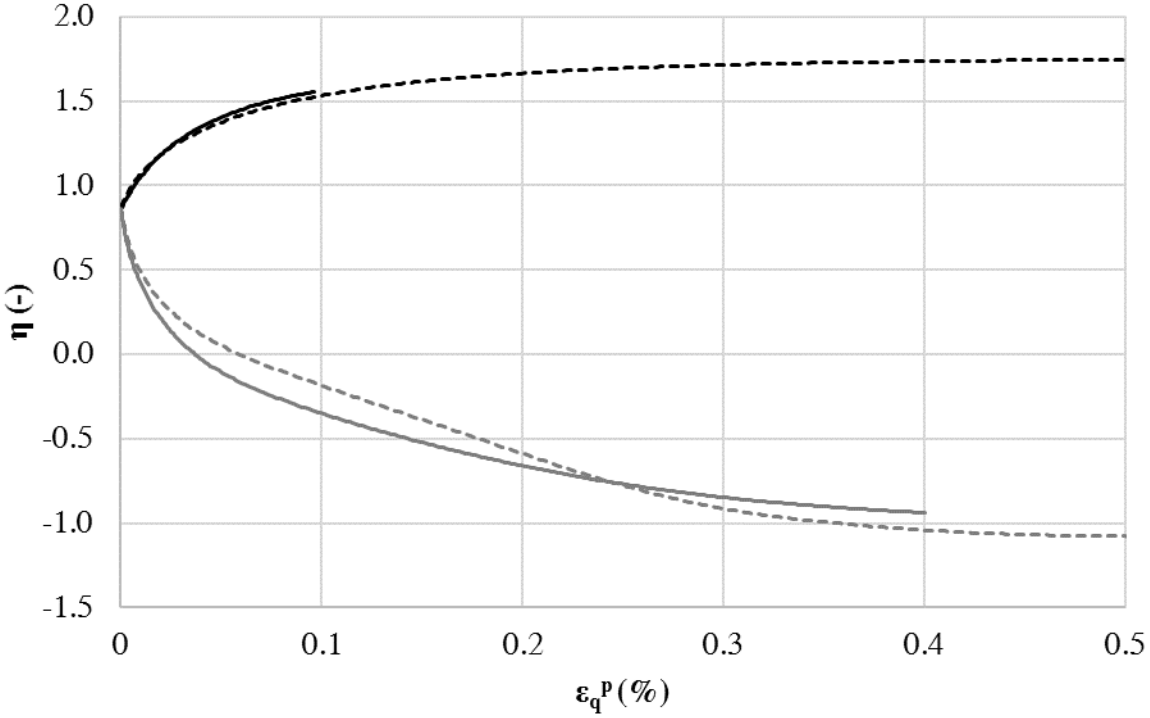

Figure A.3: $\varepsilon_q^p - \eta$ plot

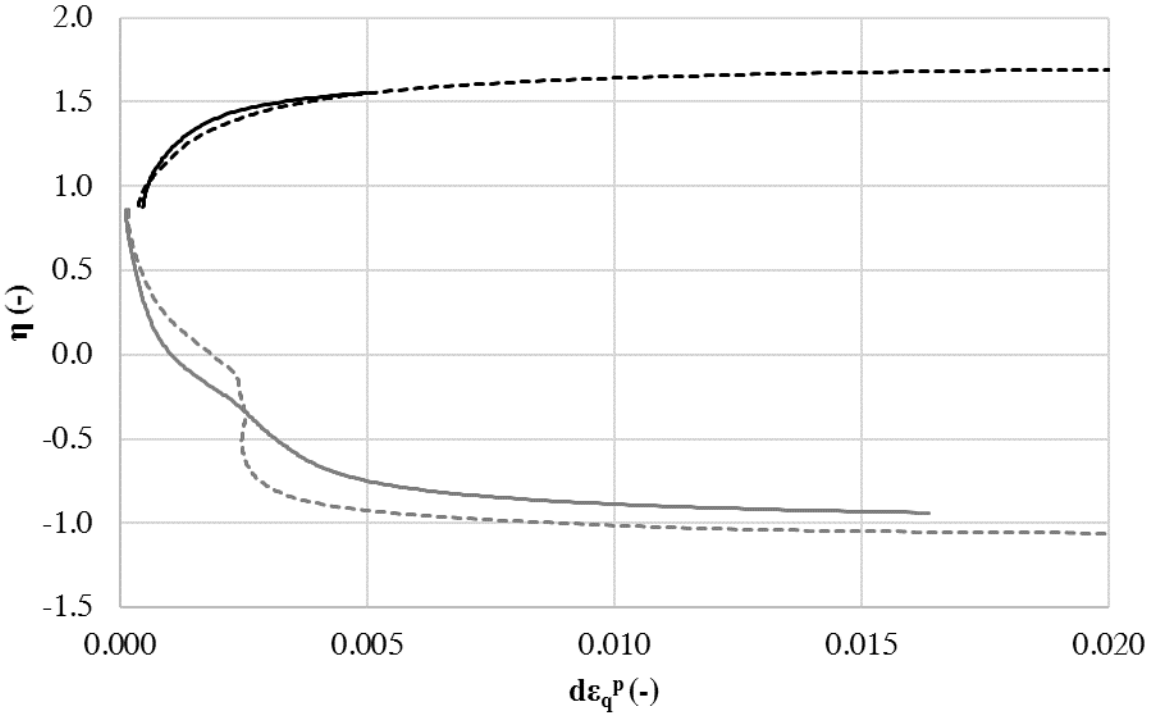

Figure A.4: $d\varepsilon_q^p - \eta$ plot

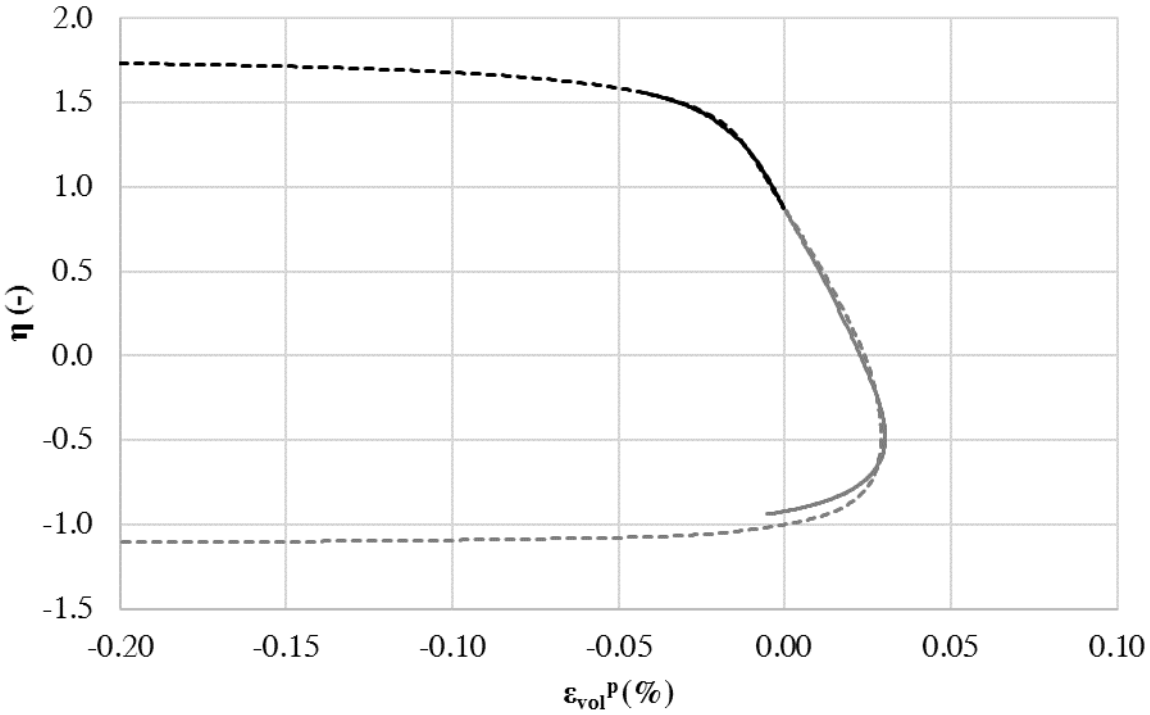

Figure A.5: $\varepsilon^p_{vol} - \eta$ plot

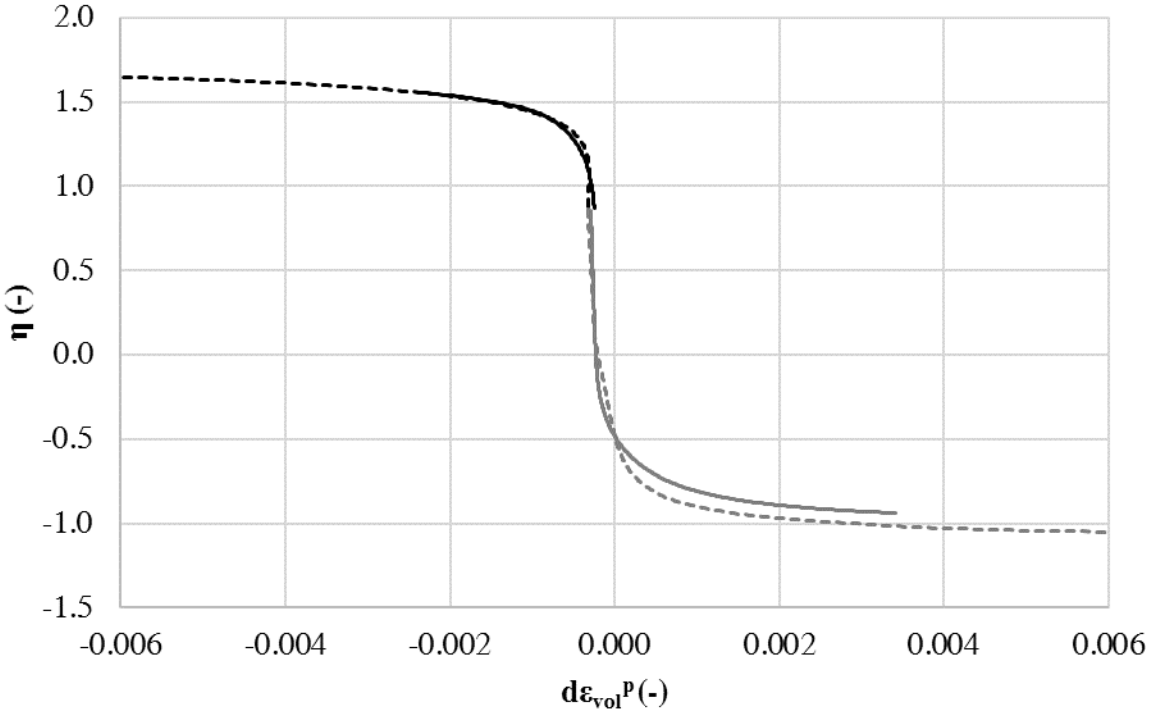

Figure A.6: $d\varepsilon^p_{vol} - \eta$ plot

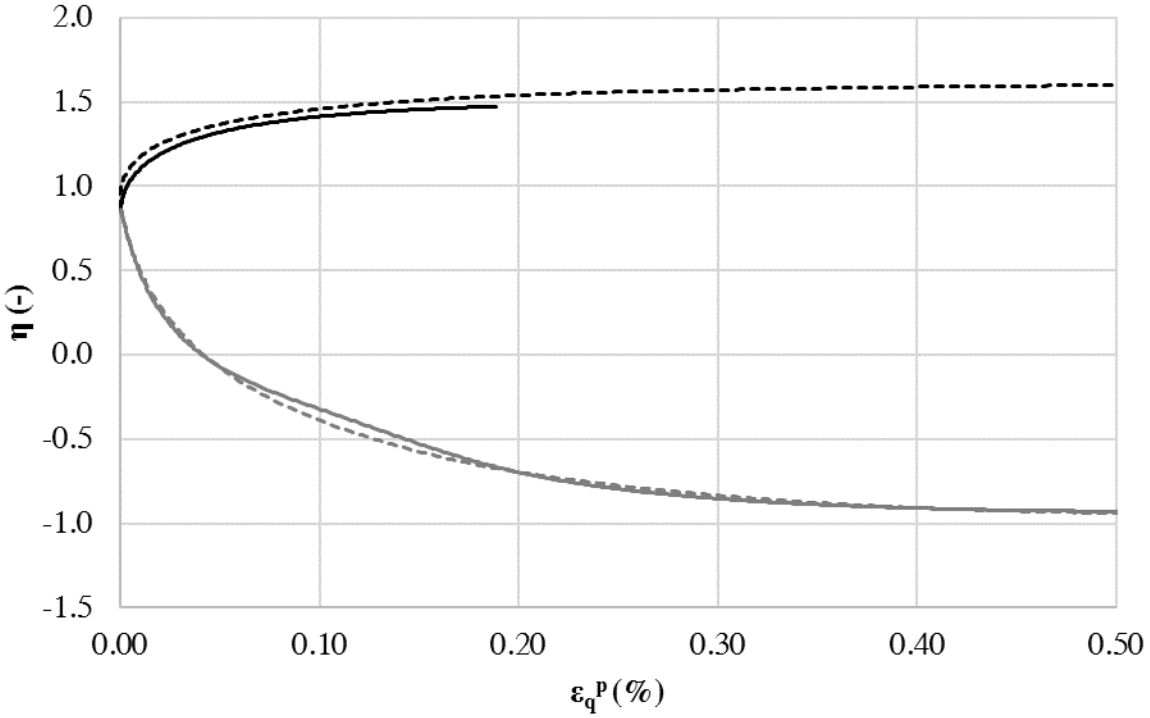

Figure A.9: $\varepsilon_q^p - \eta$ plot

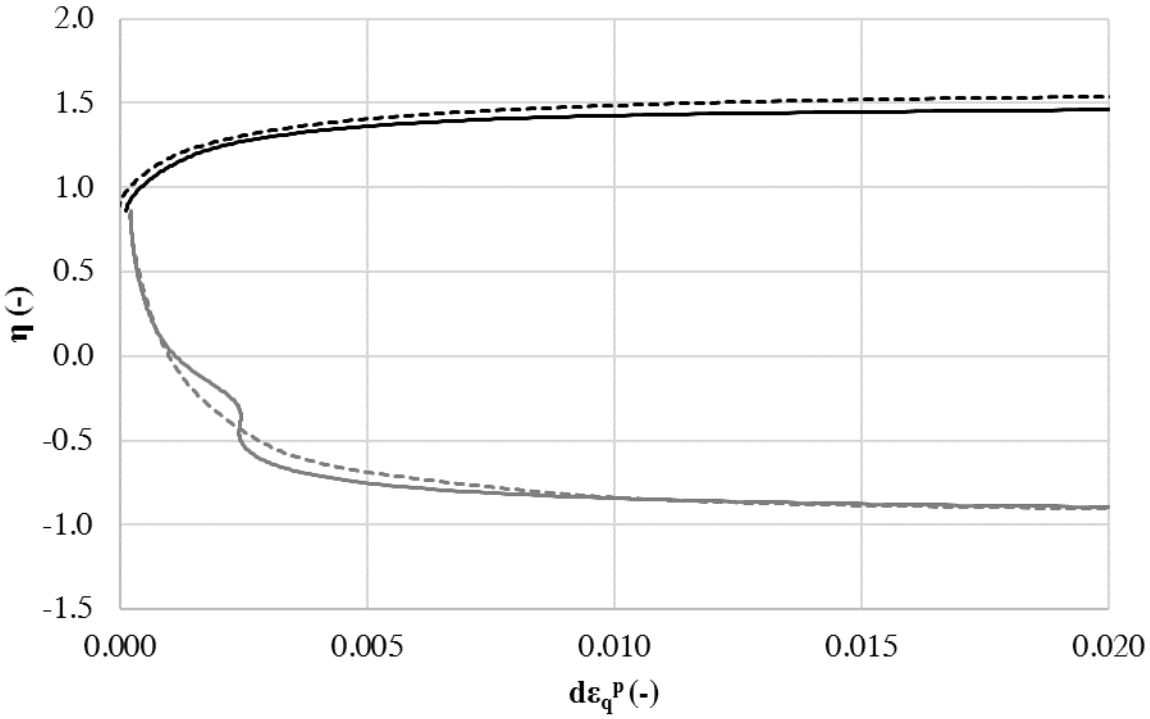

Figure A.10: $d\varepsilon_q^p - \eta$ plot

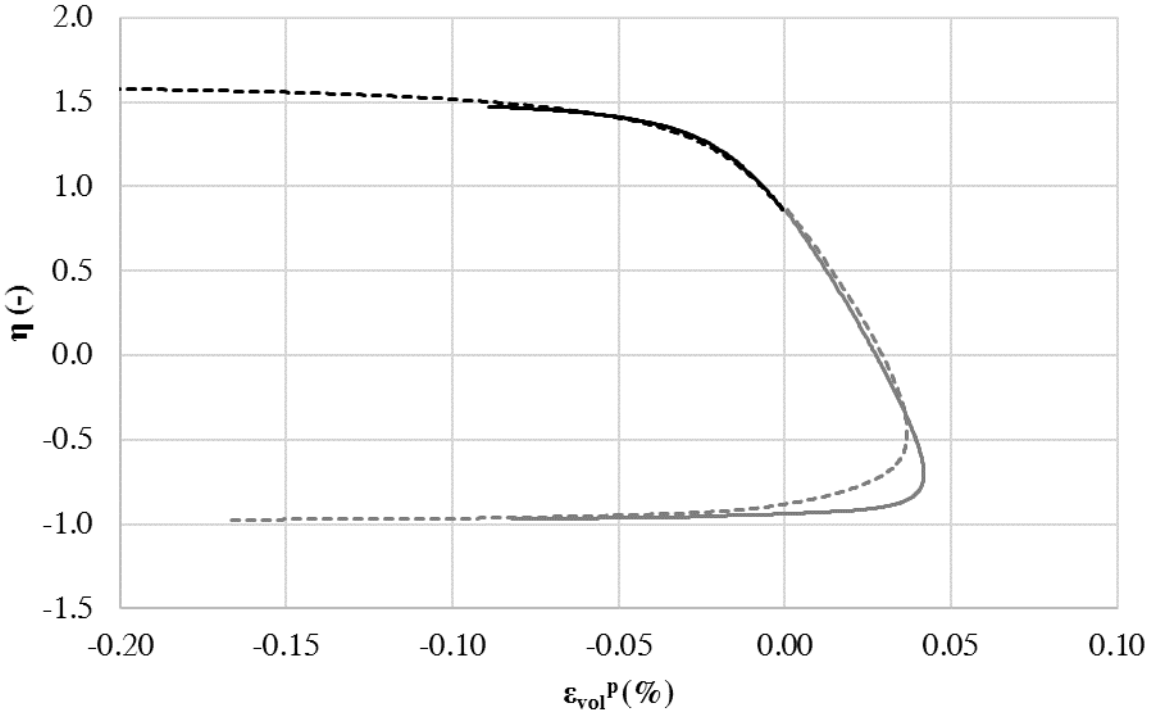

Figure A.11: $\varepsilon^p_{vol} - \eta$ plot

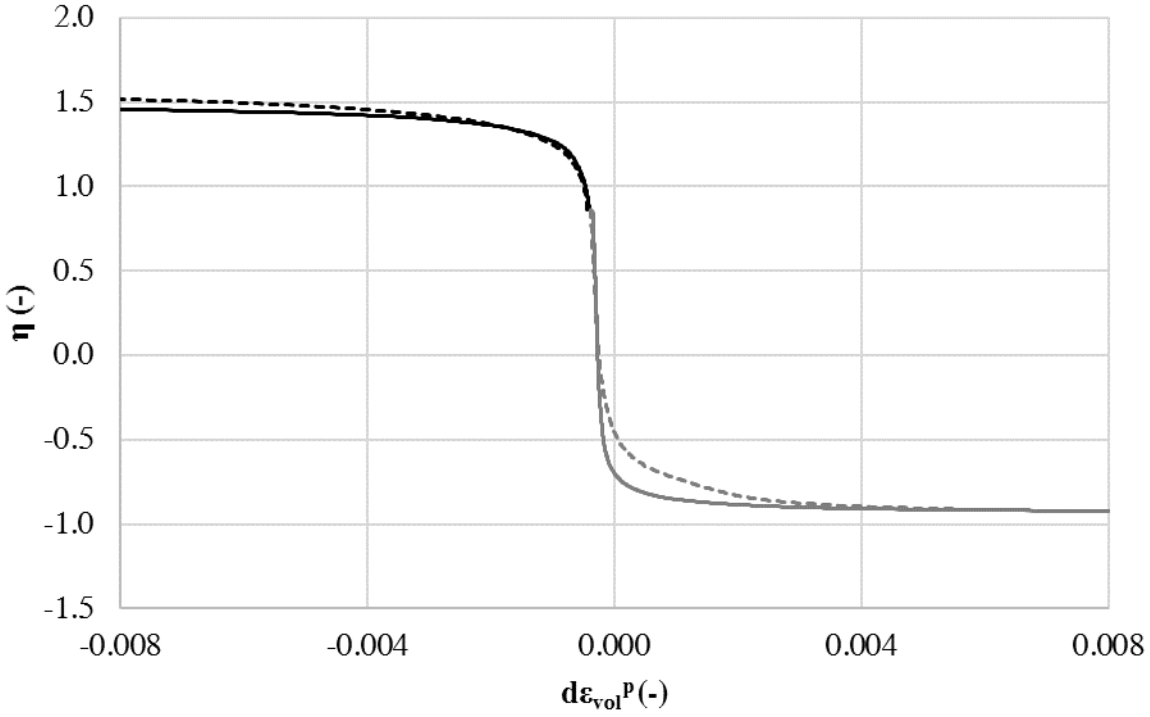

Figure A.12: $d\varepsilon^p_{vol} - \eta$ plot

A.3 Test 9, 10

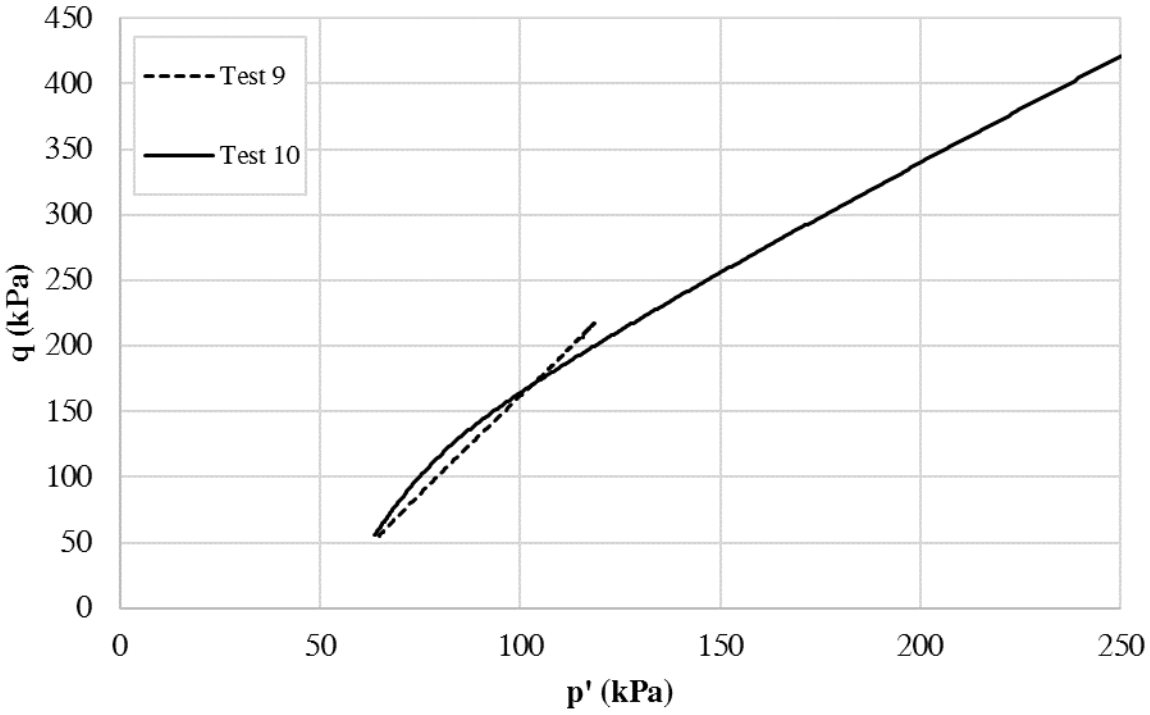

Figure A.13: $p' - q$ plot

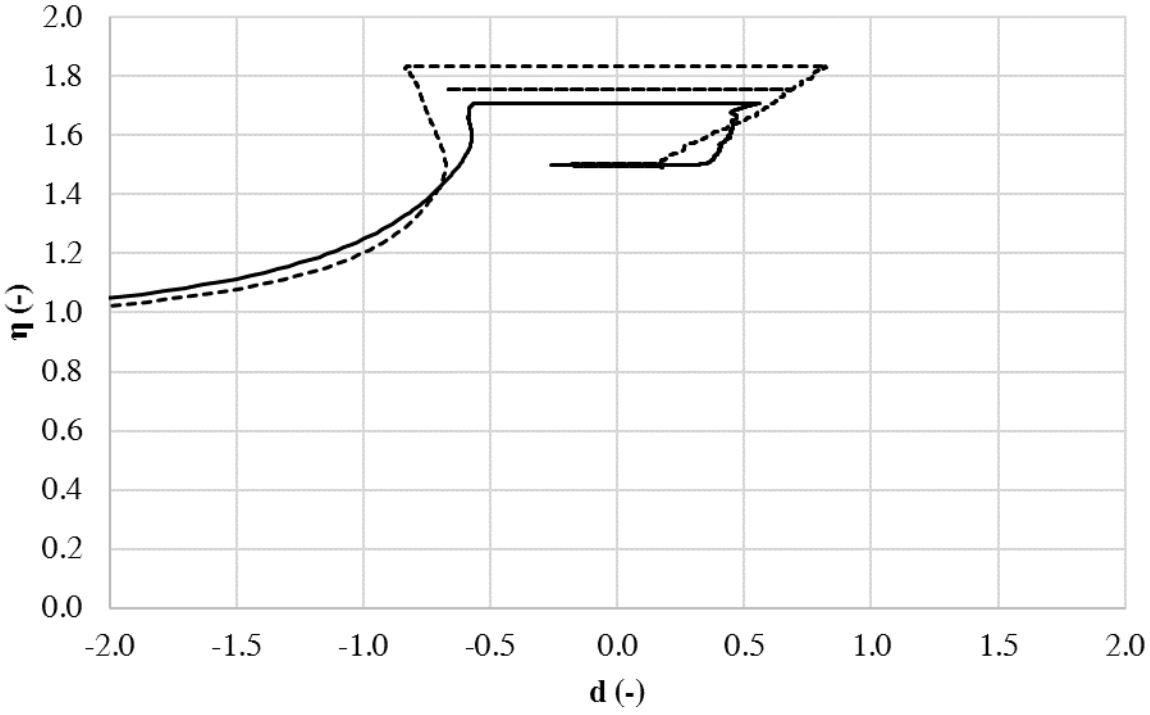

Figure A.14: $d - \eta$ plot

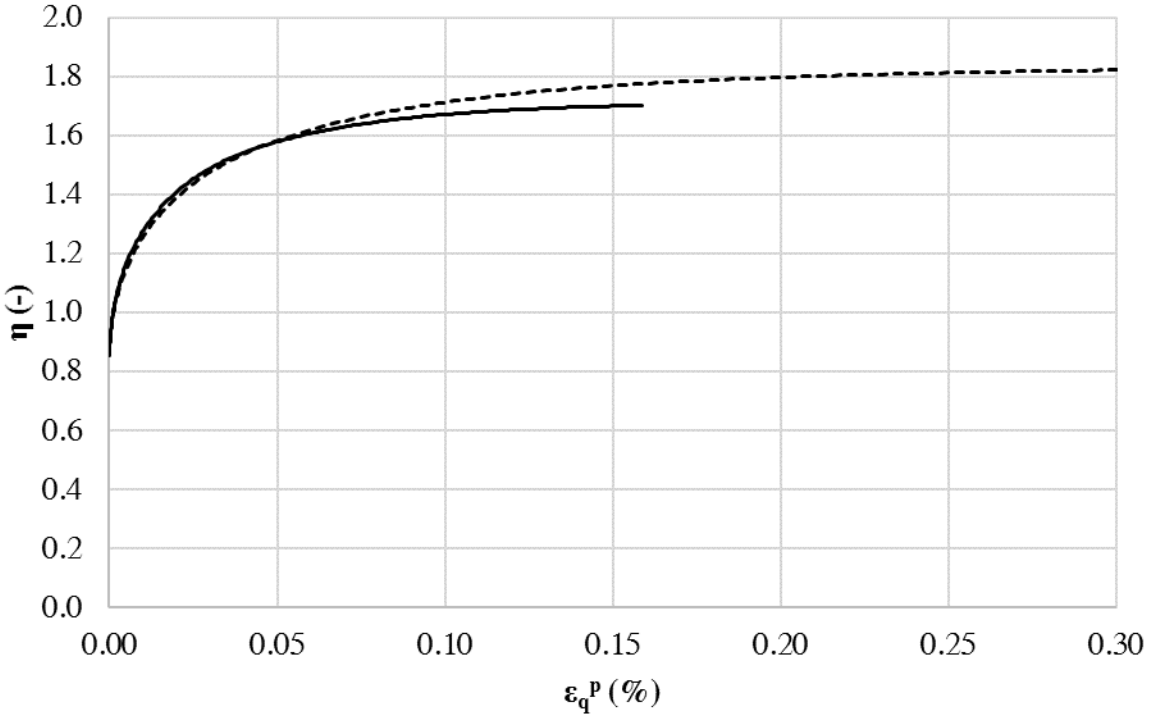

Figure A.15: $\varepsilon_q^p - \eta$ plot

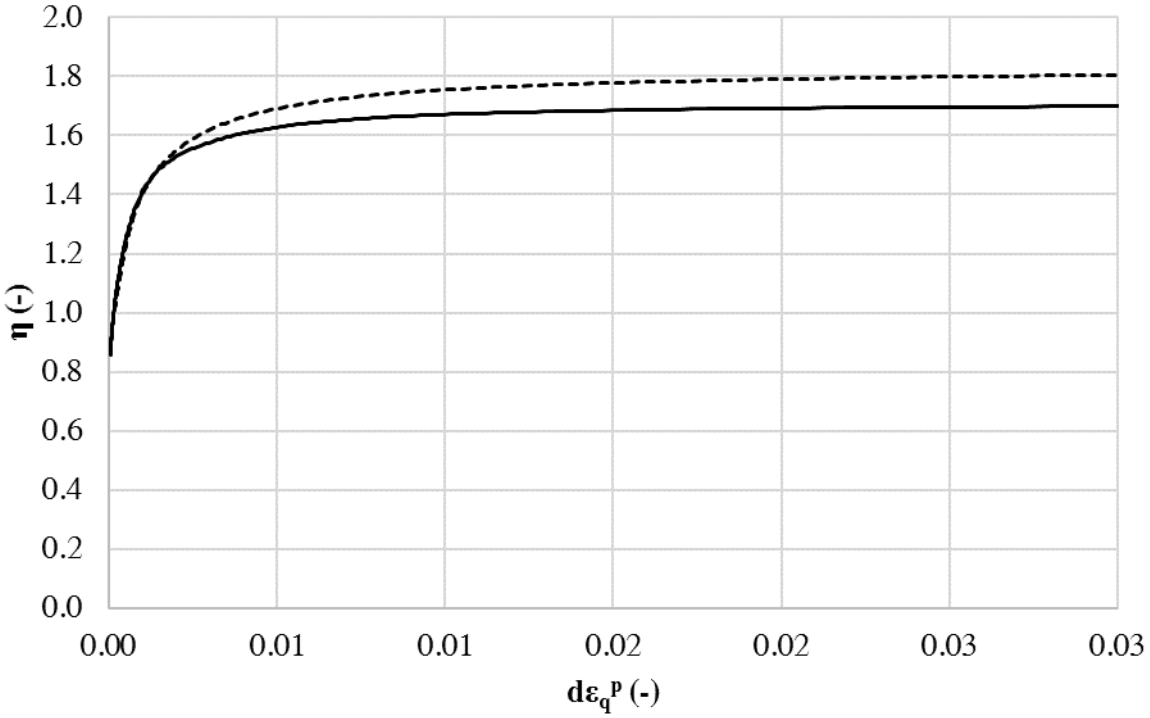

Figure A.16: $d\varepsilon_q^p - \eta$ plot

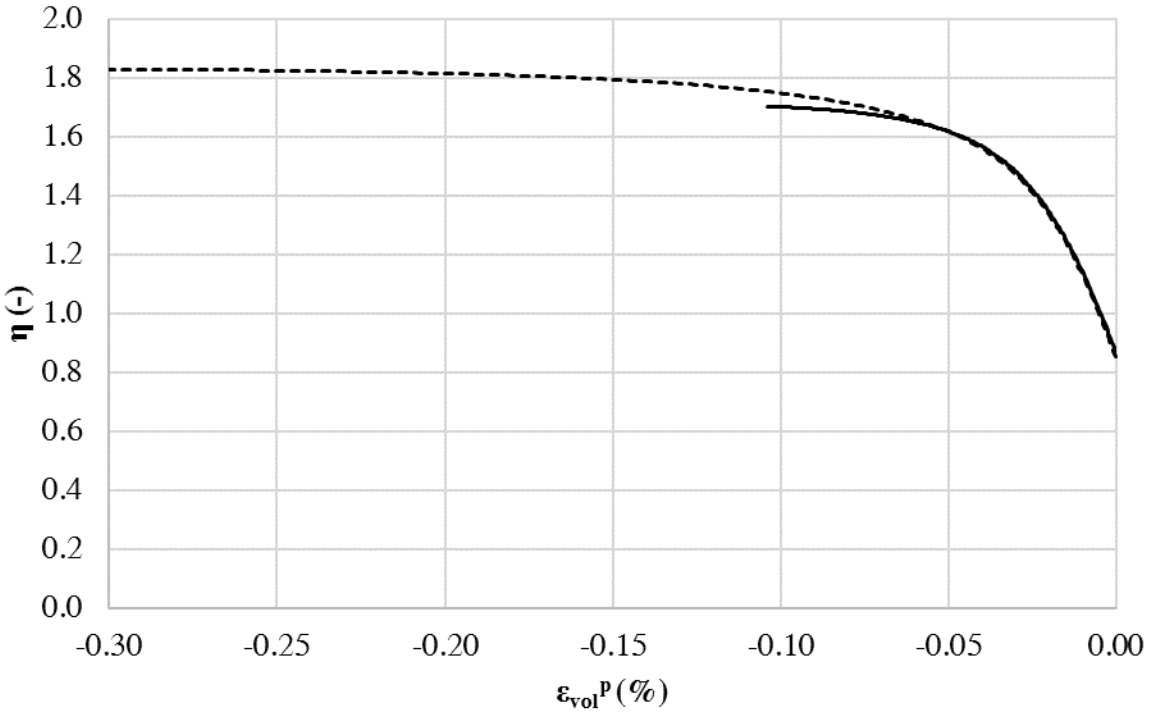

Figure A.17: $\varepsilon^p_{vol} - \eta$ plot

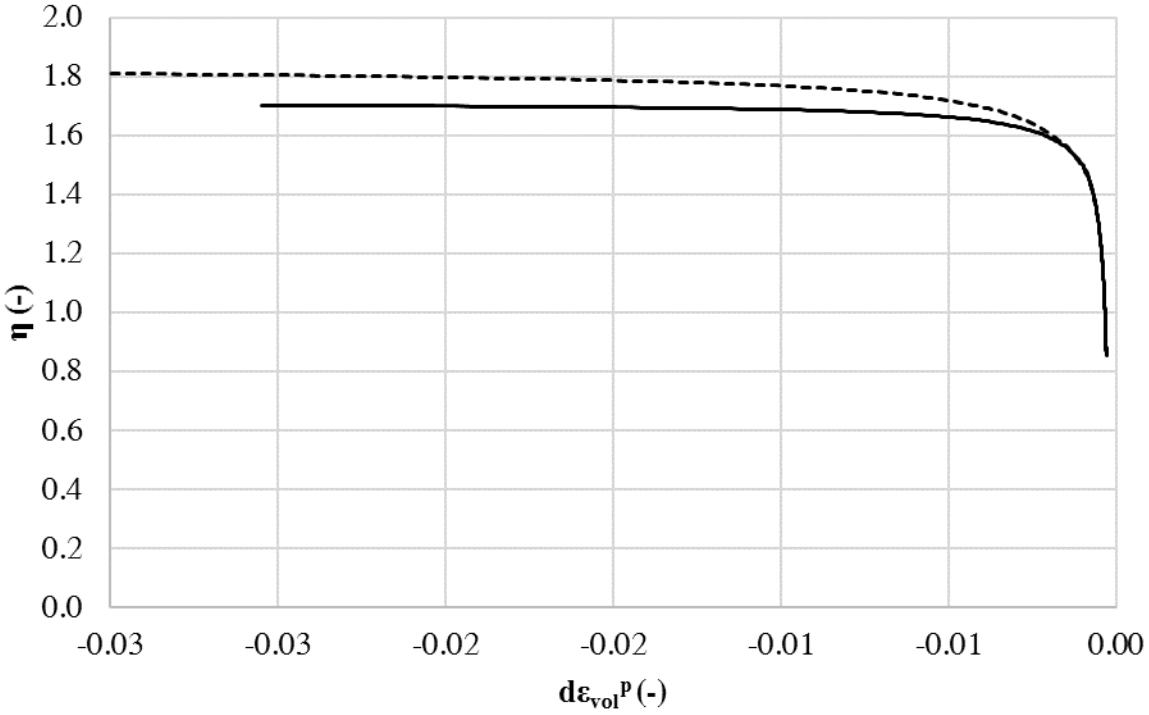

Figure A.18: $d\varepsilon^p_{vol} - \eta$ plot

Appendix B

Results from Cyclic Triaxial Tests

B.1 Test 11

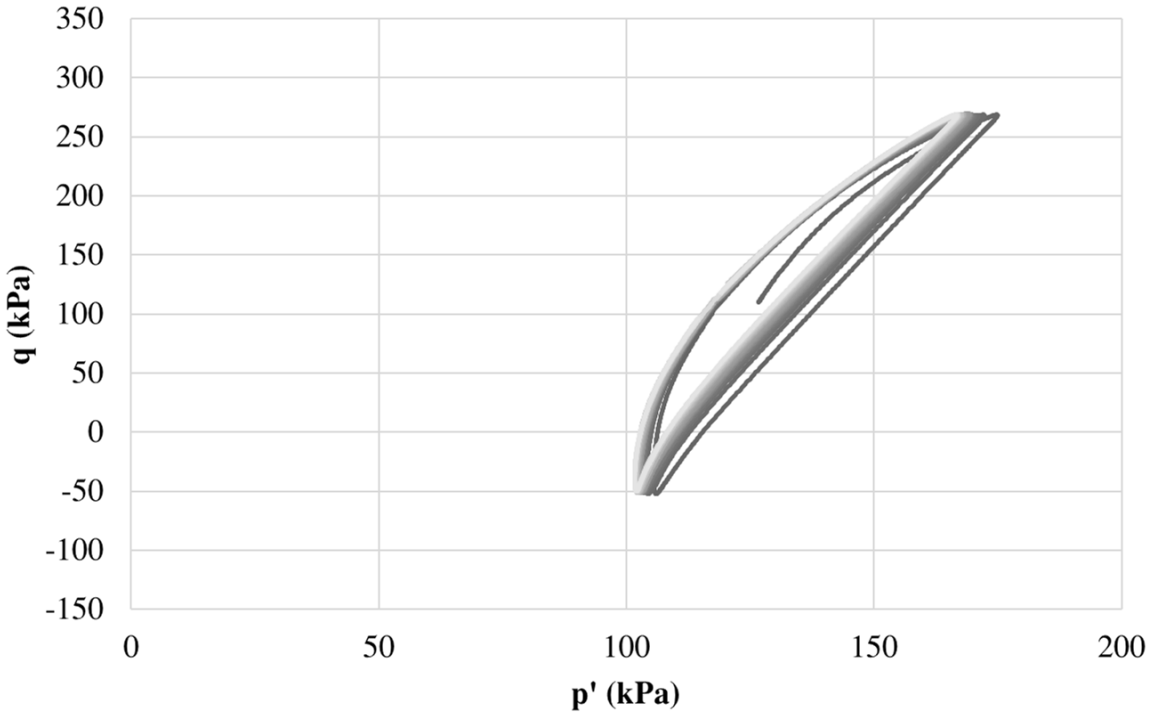

Figure B.1: $p' - q$ plot

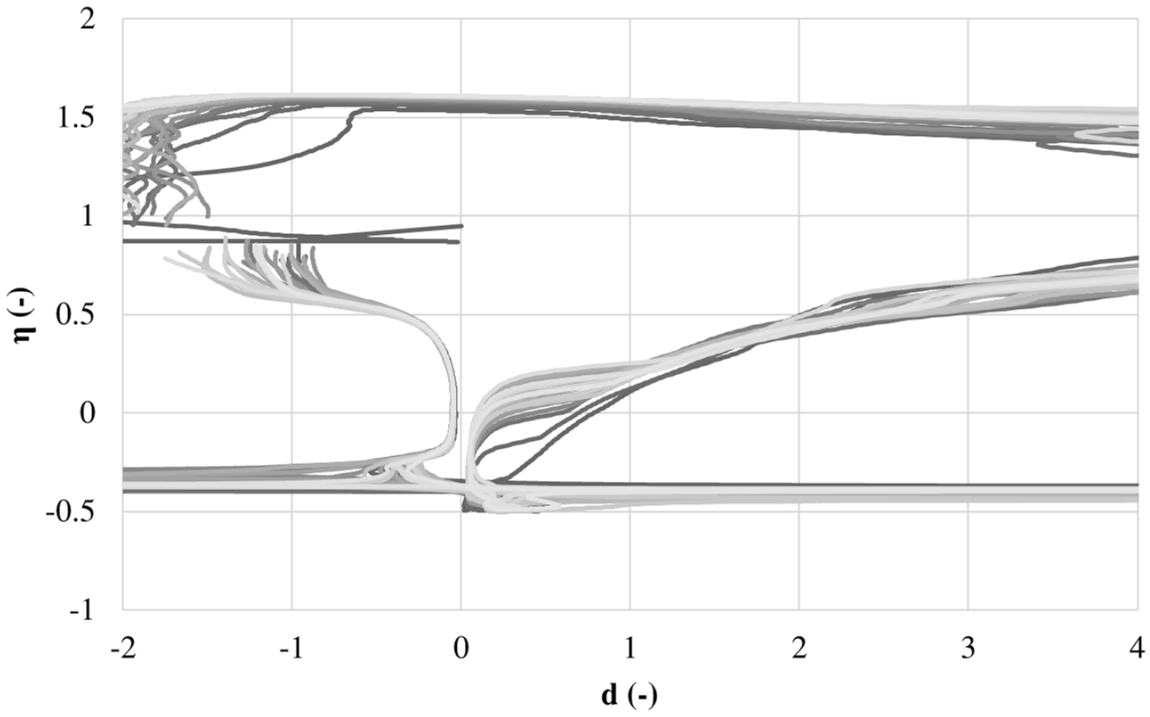

Figure B.2: $d - \eta$ plot

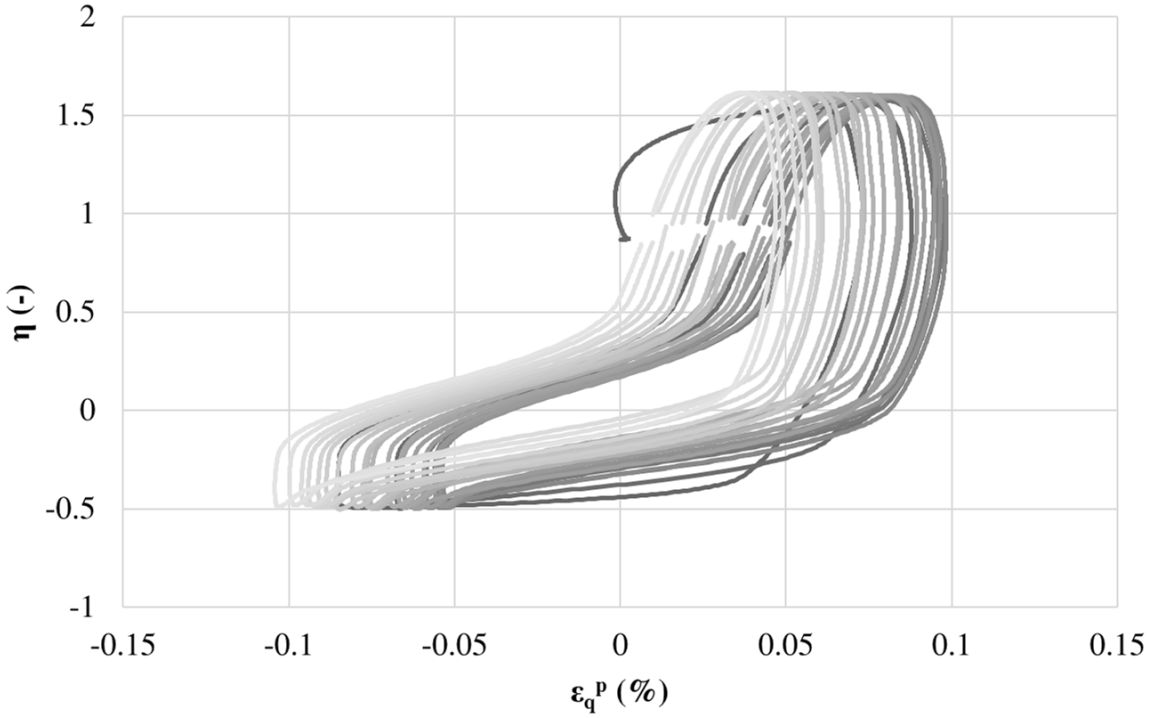

Figure B.3: $\varepsilon_q^p - \eta$ plot

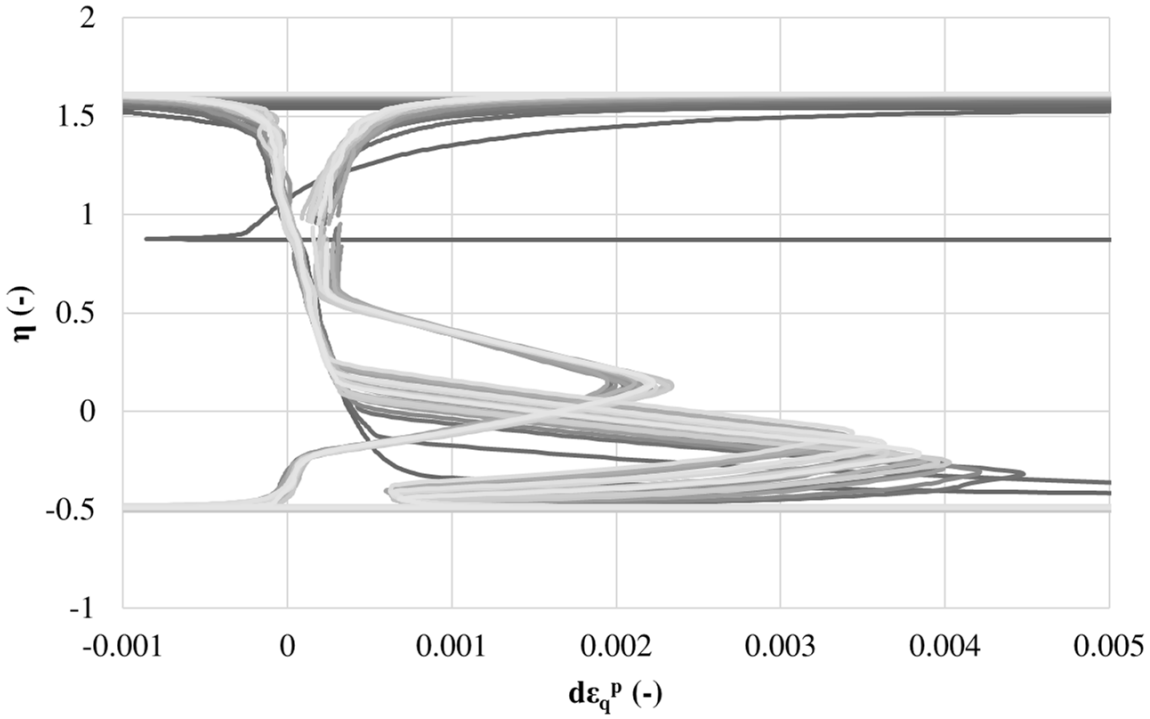

Figure B.4: $d\varepsilon_q^p - \eta$ plot

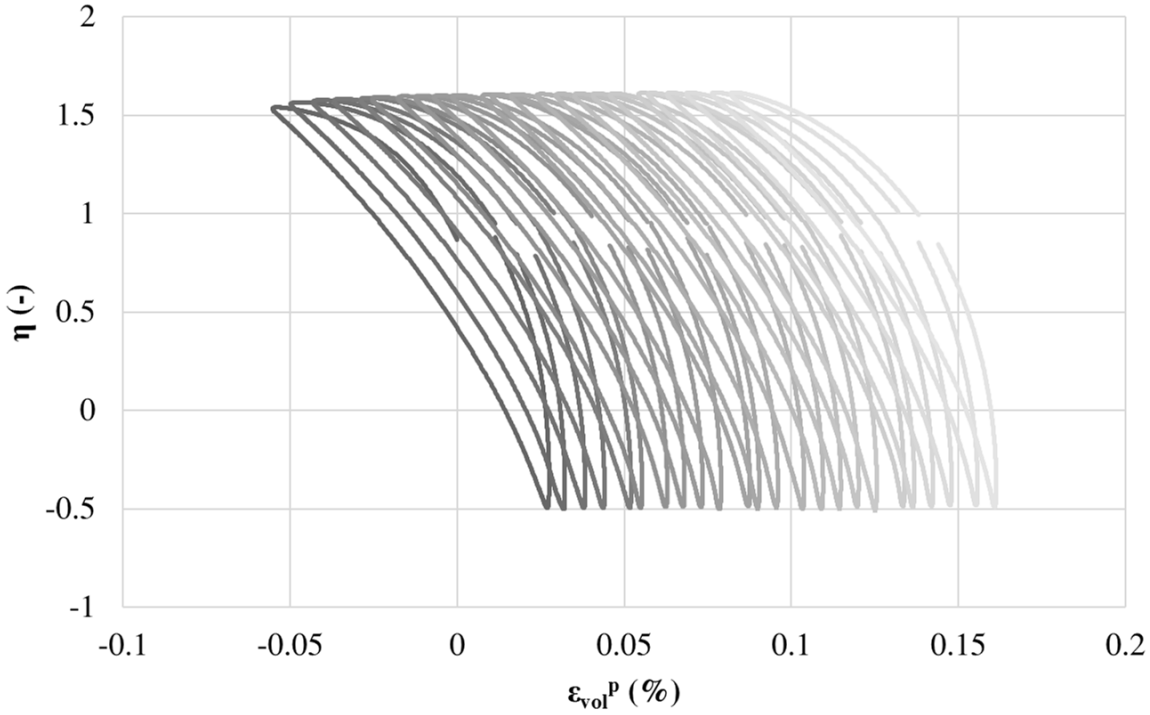

Figure B.5: $\varepsilon^p_{vol} - \eta$ plot

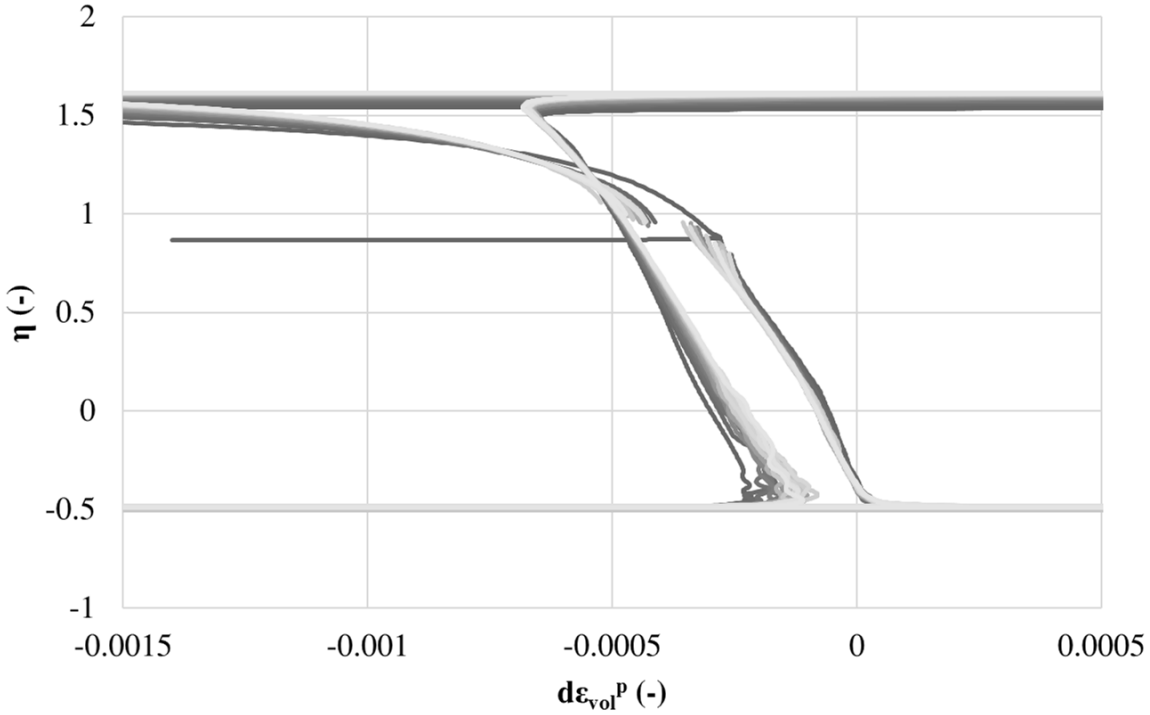

Figure B.6: $d\varepsilon^p_{vol} - \eta$ plot

B.2 Test 12

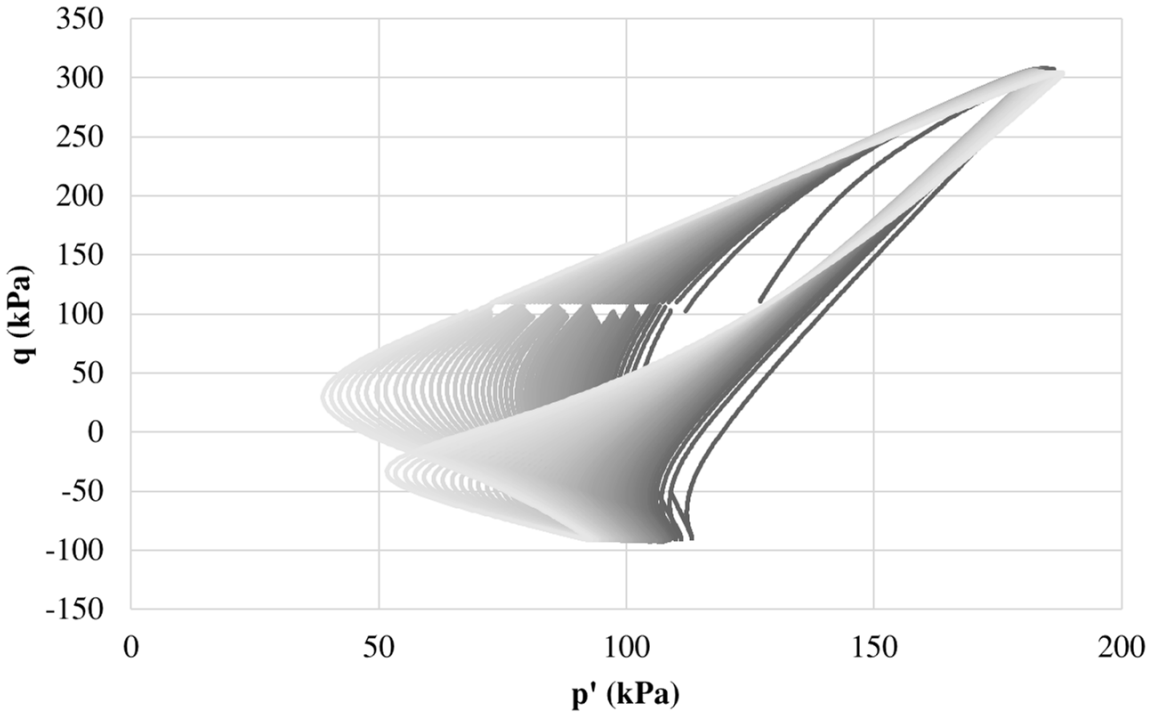

Figure B.7: $p' - q$ plot

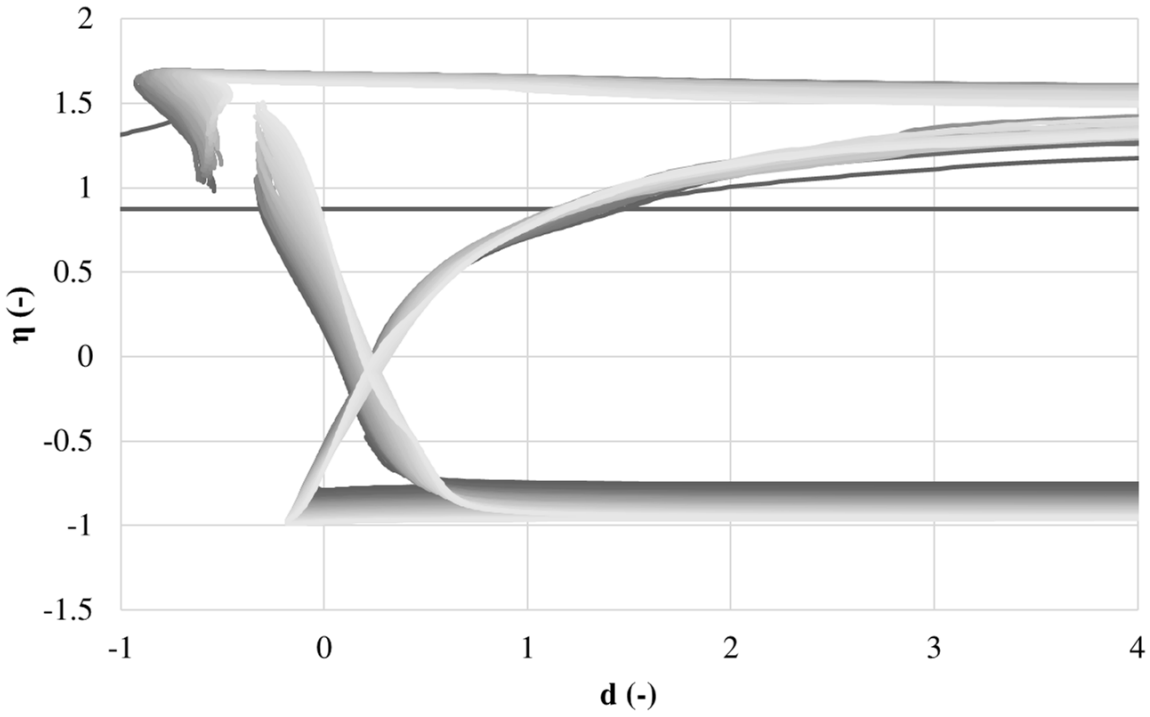

Figure B.8: $d - \eta$ plot

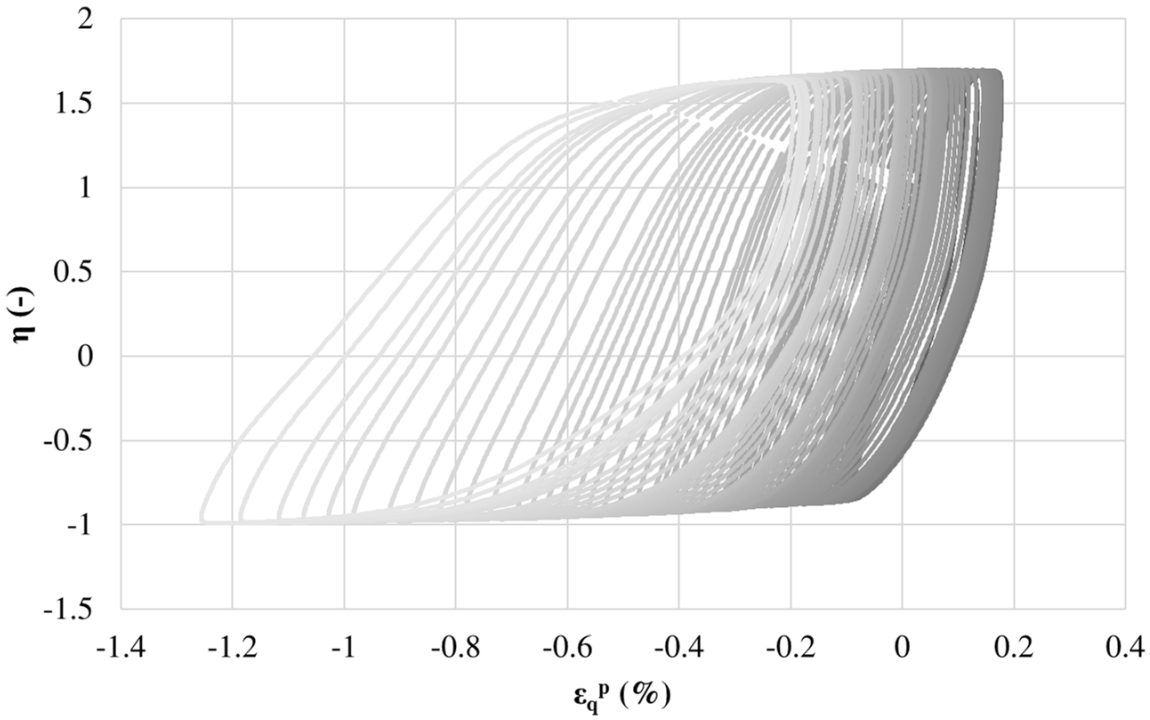

Figure B.9: $\varepsilon_q^p - \eta$ plot

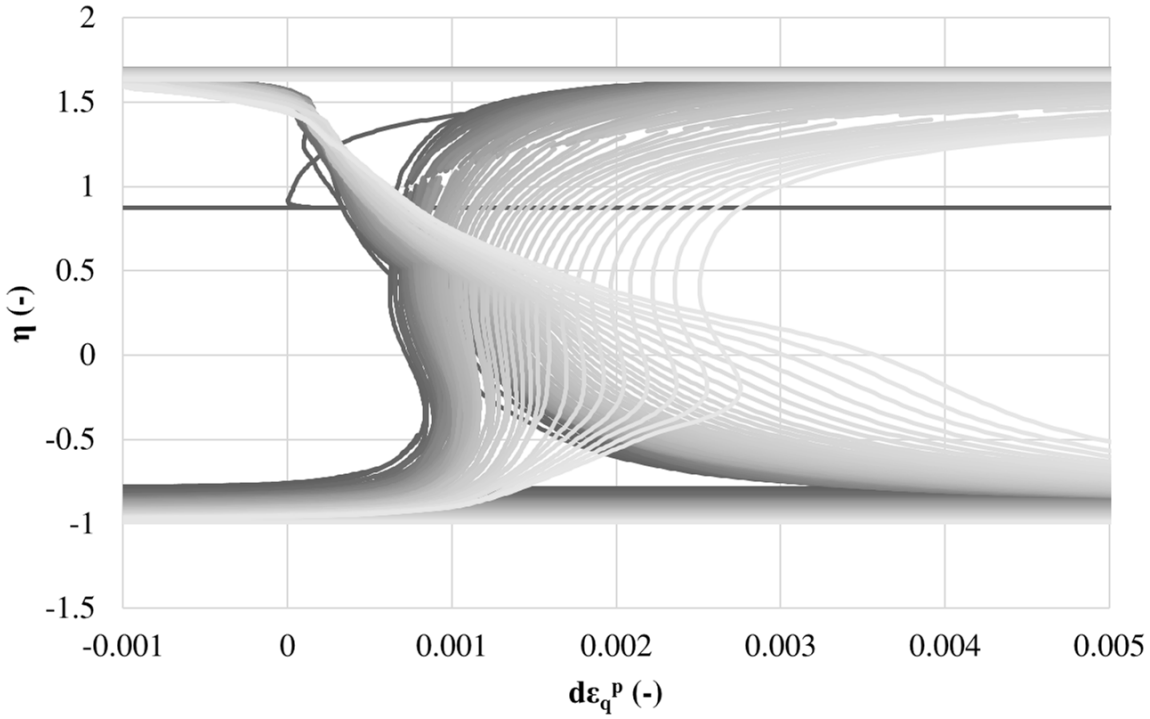

Figure B.10: $d\varepsilon_q^p - \eta$ plot

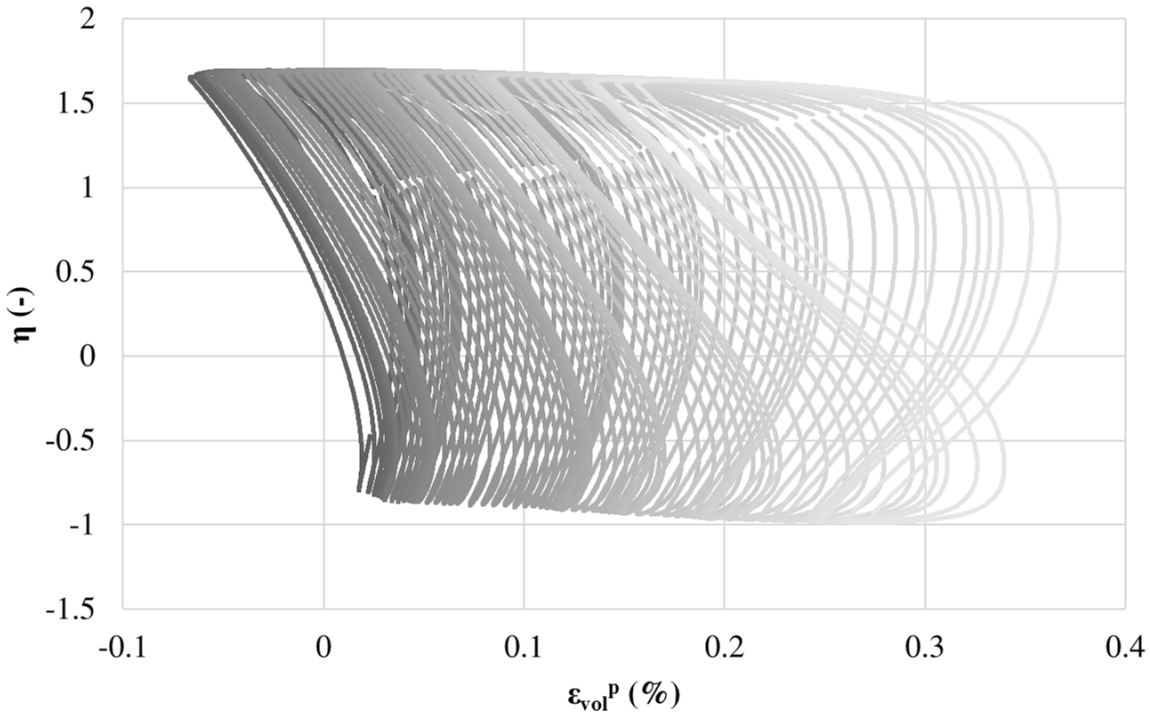

Figure B.11: $\varepsilon^p_{vol} - \eta$ plot

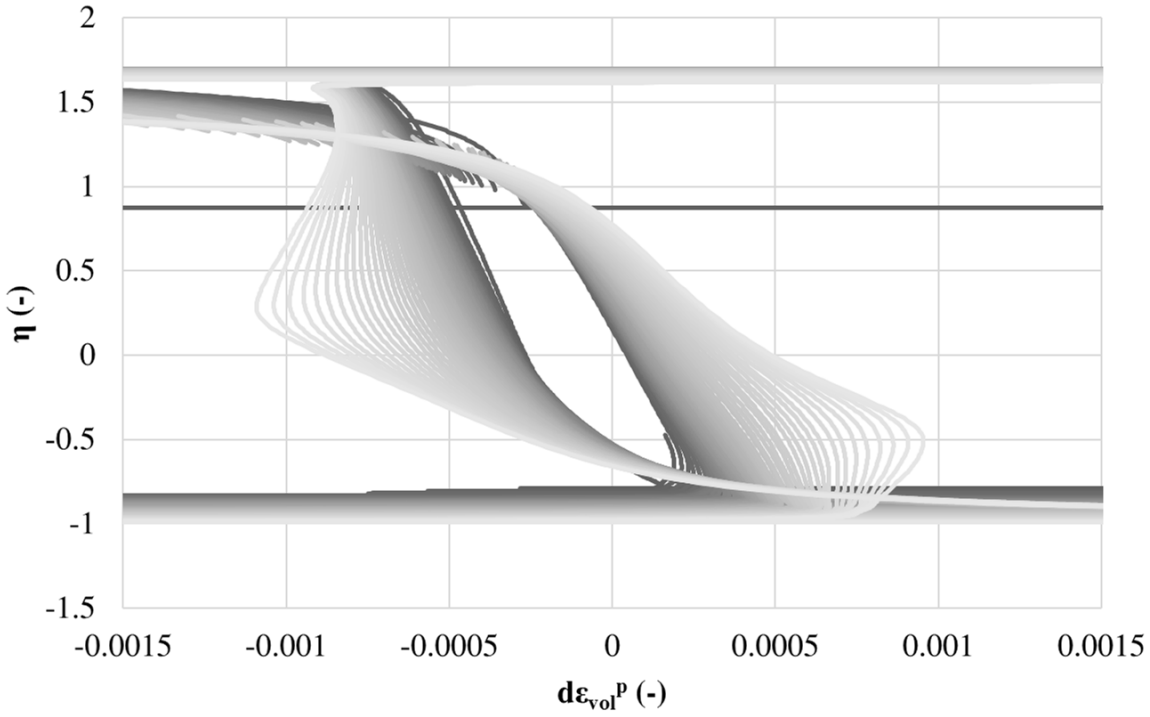

Figure B.12: $d\varepsilon^p_{vol} - \eta$ plot

Test 12b

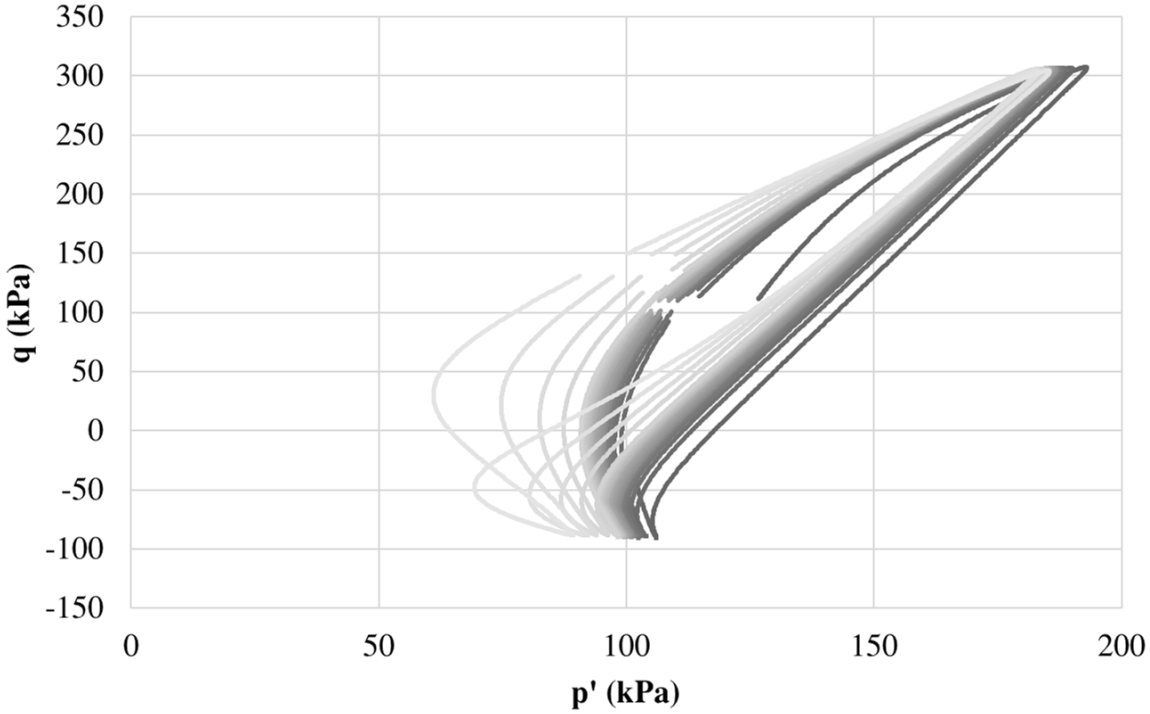

Figure B.13: $p' - q$ plot

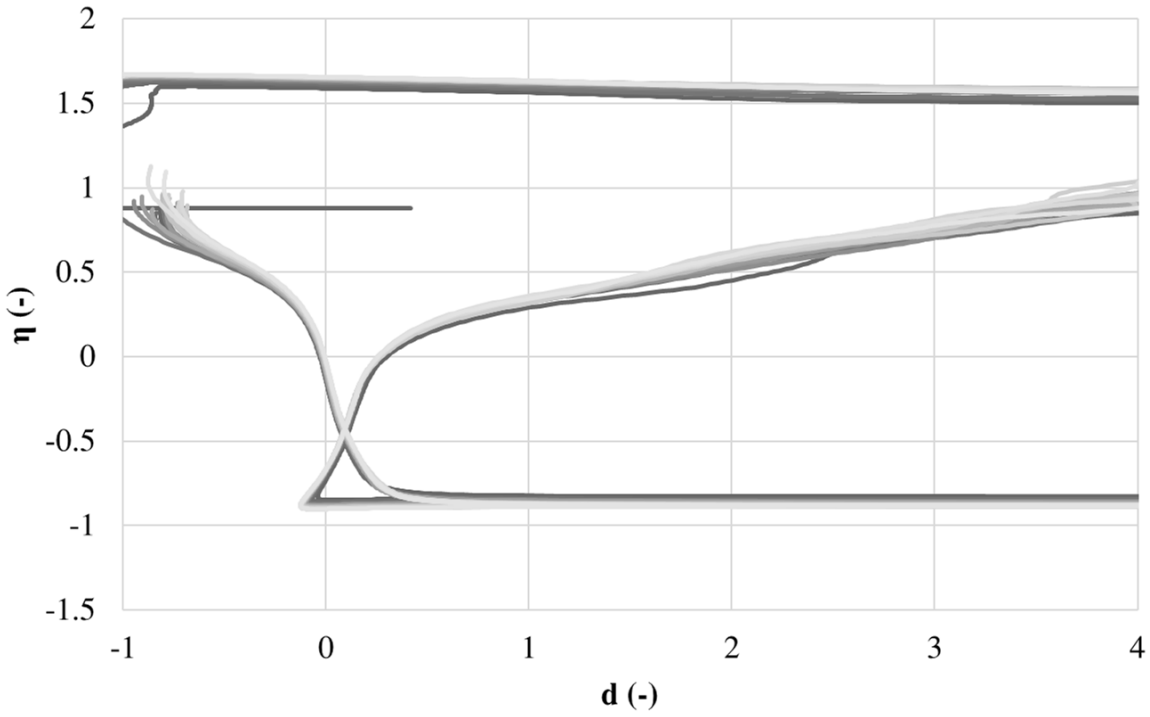

Figure B.14: $d - \eta$ plot

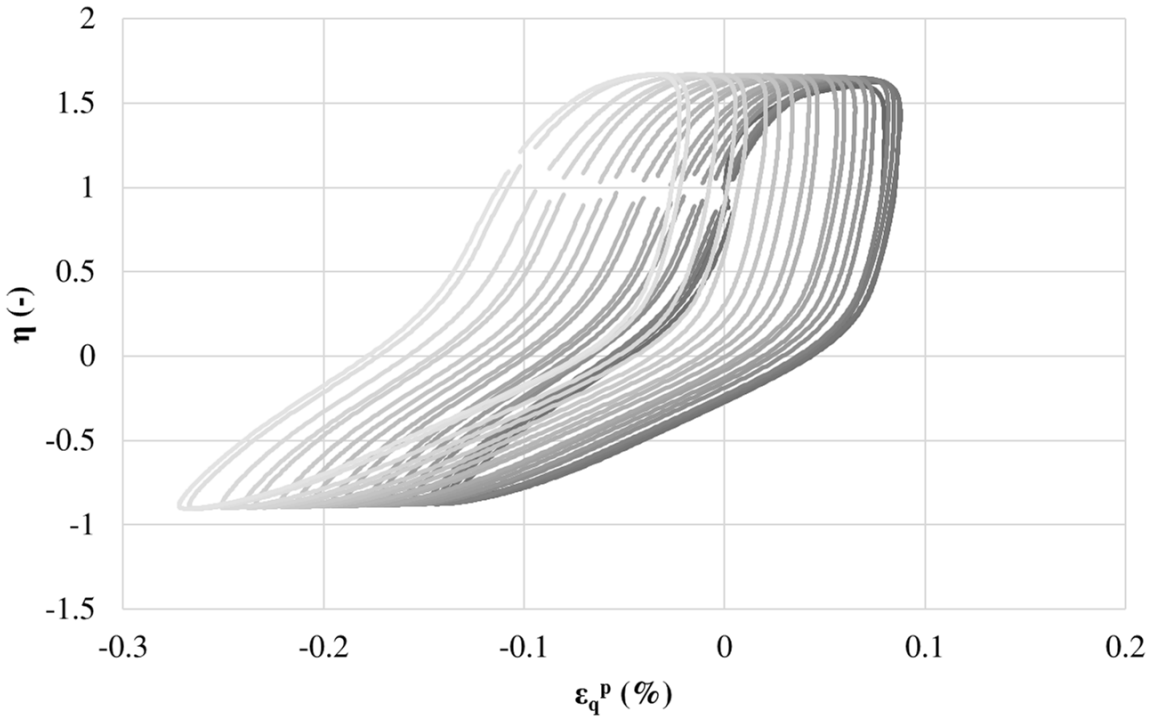

Figure B.15: $\varepsilon_q^p - \eta$ plot

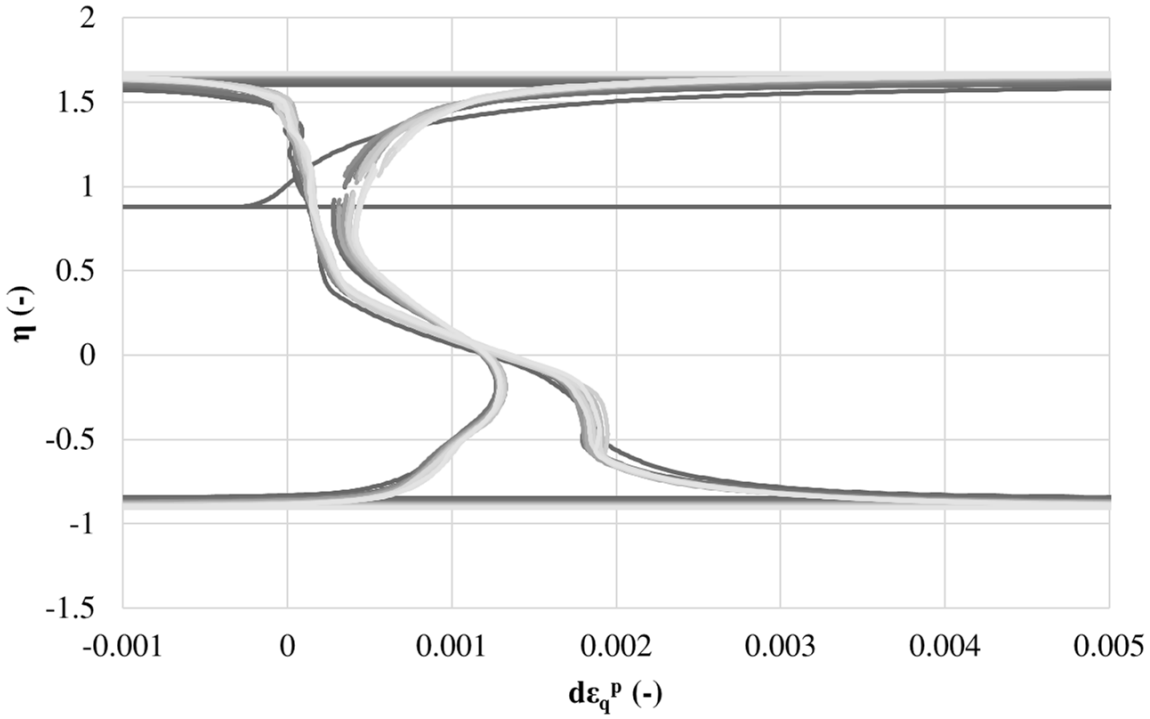

Figure B.16: $d\varepsilon_q^p - \eta$ plot

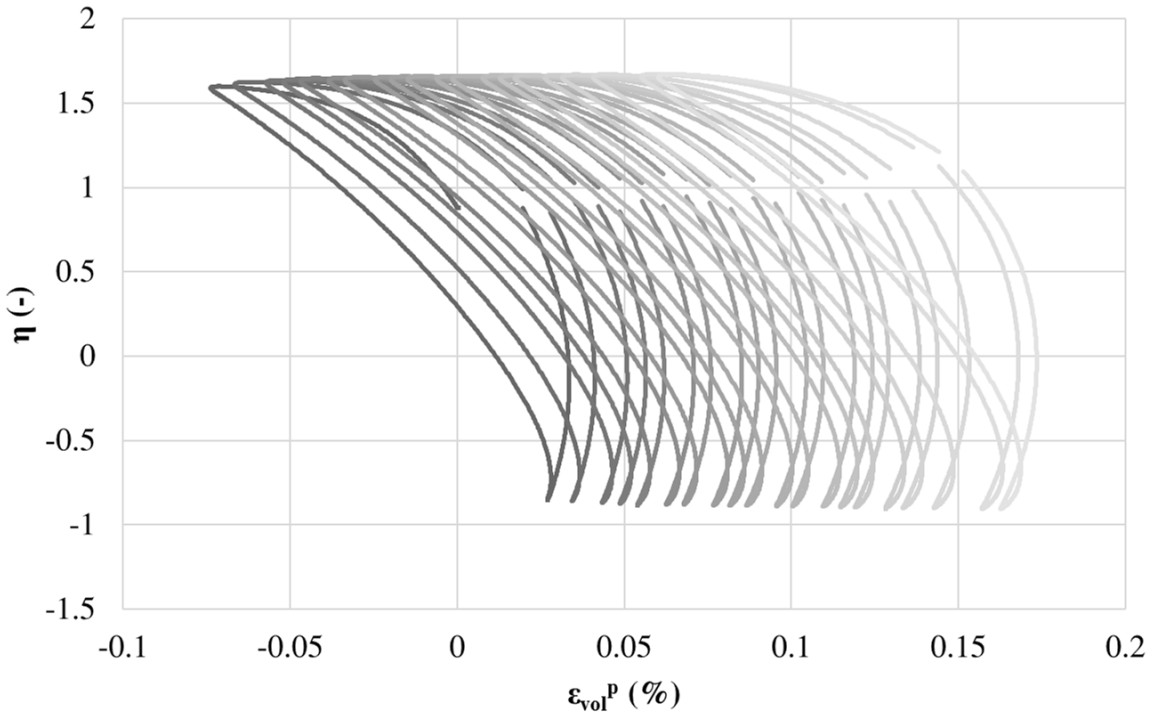

Figure B.17: $\varepsilon^p_{vol} - \eta$ plot

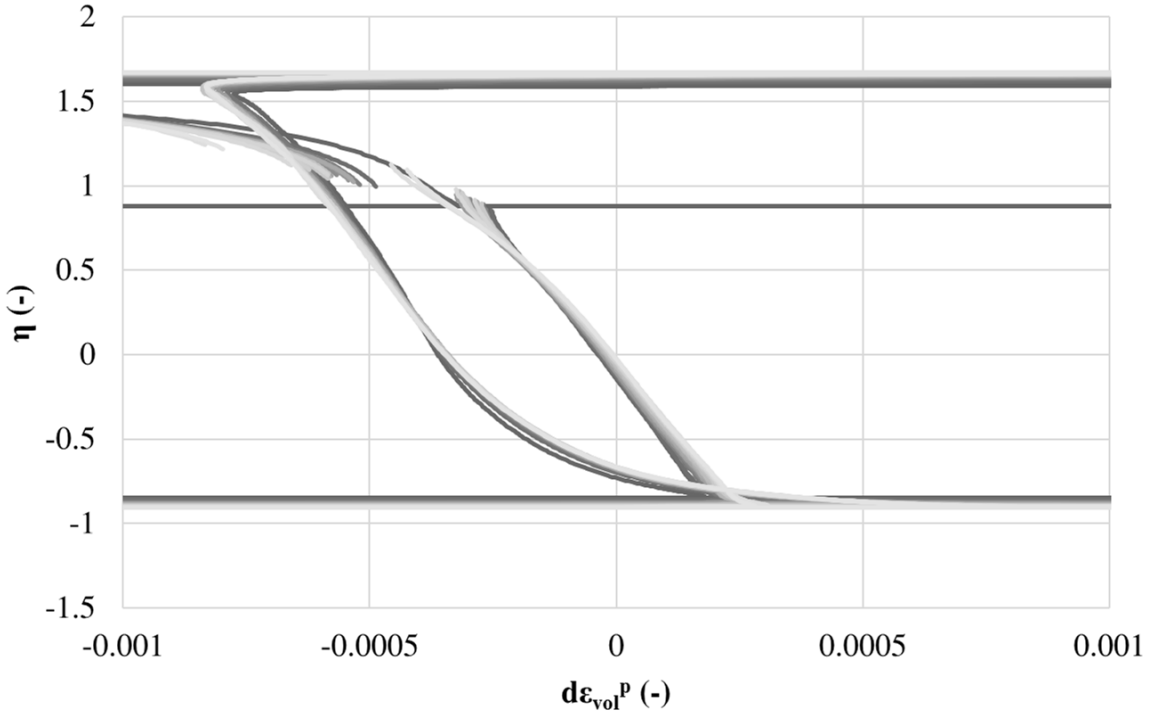

Figure B.18: $d\varepsilon^p_{vol} - \eta$ plot

B.3 Test 13

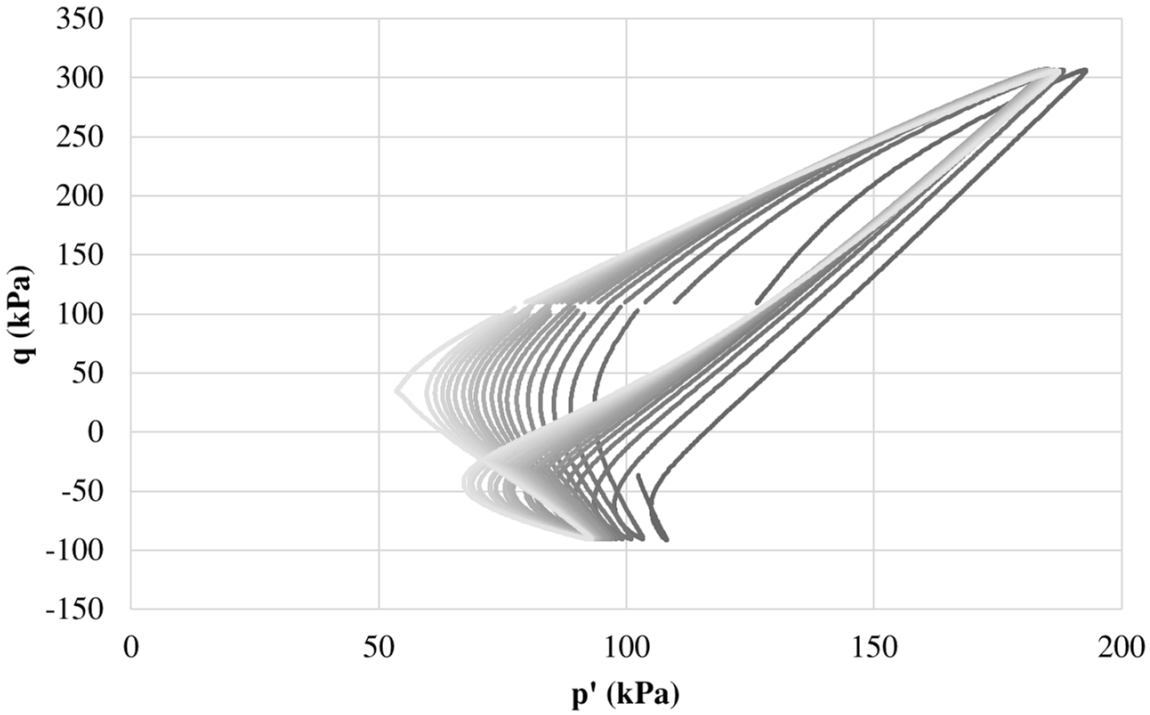

Figure B.19: $p' - q$ plot

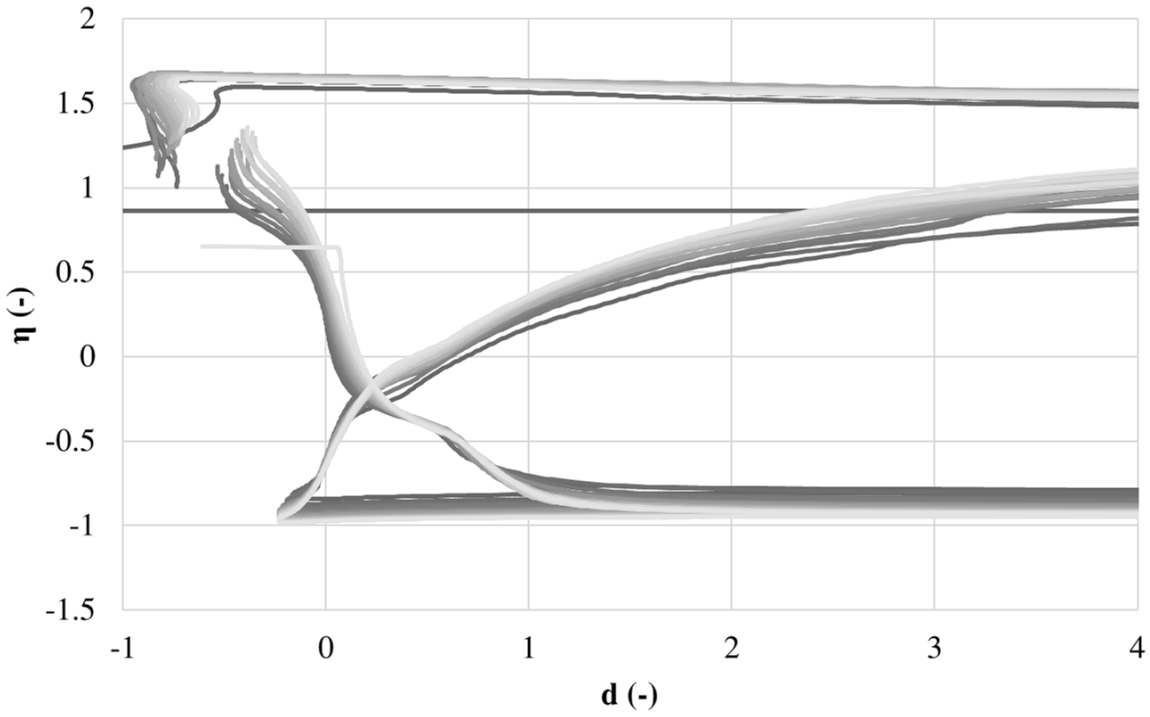

Figure B.20: $d - \eta$ plot

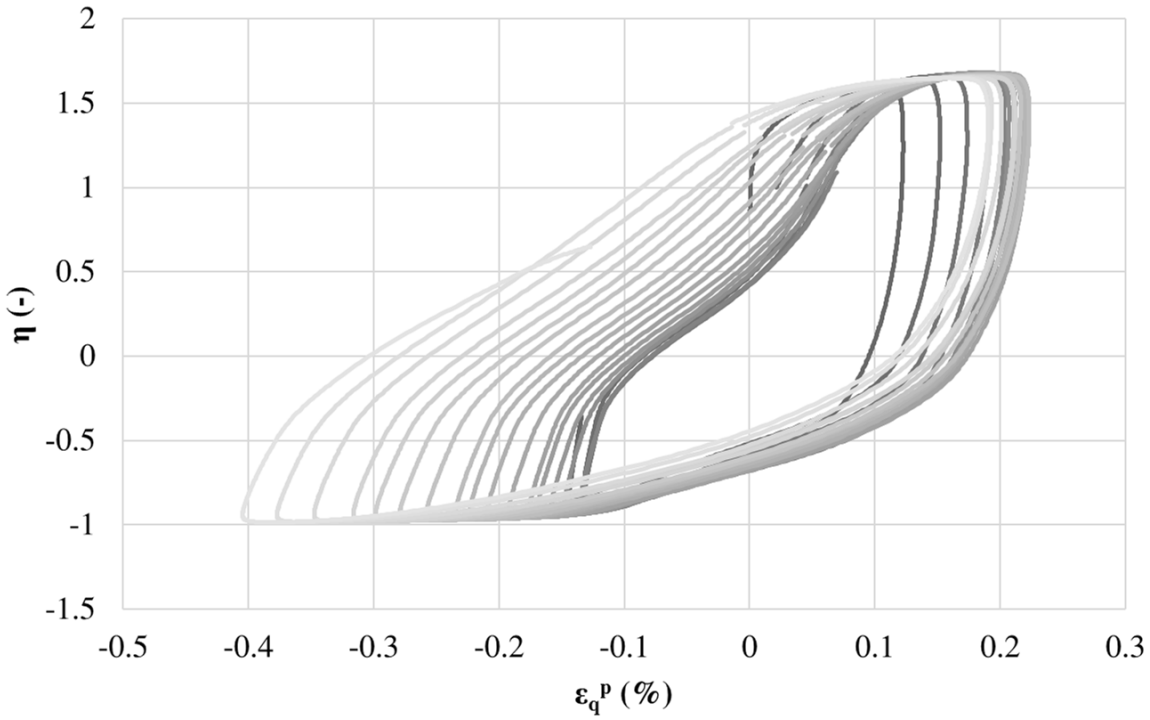

Figure B.21: $\varepsilon_q^p - \eta$ plot

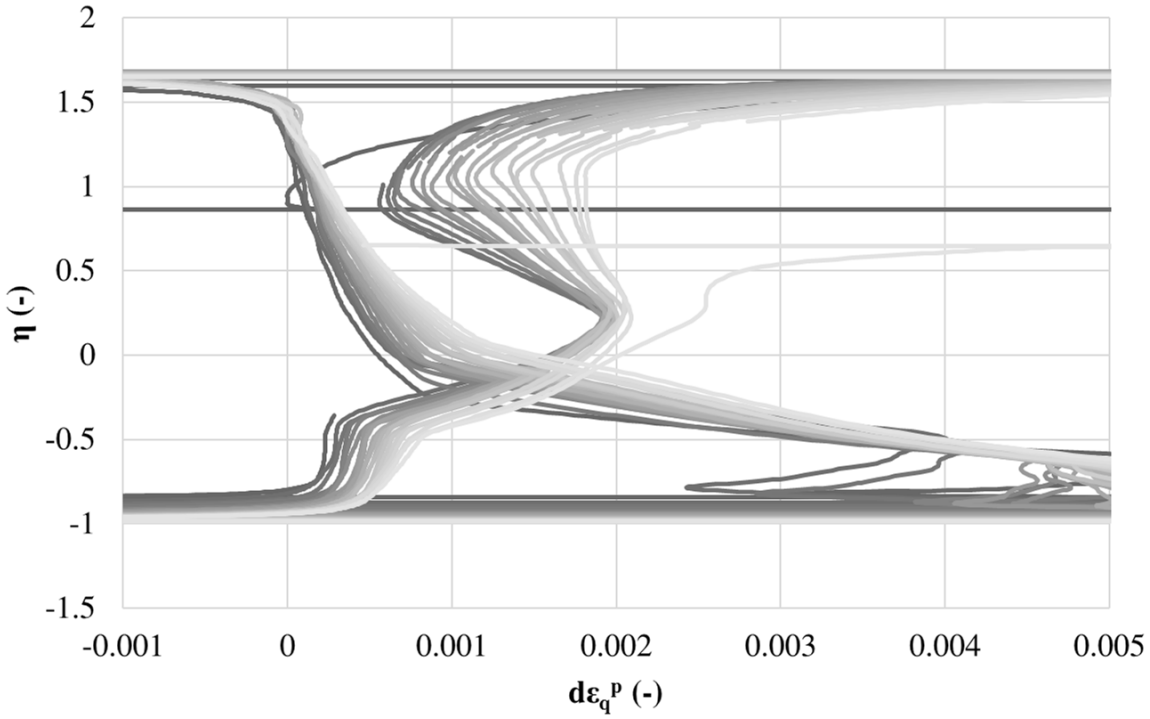

Figure B.22: $d\varepsilon_q^p - \eta$ plot

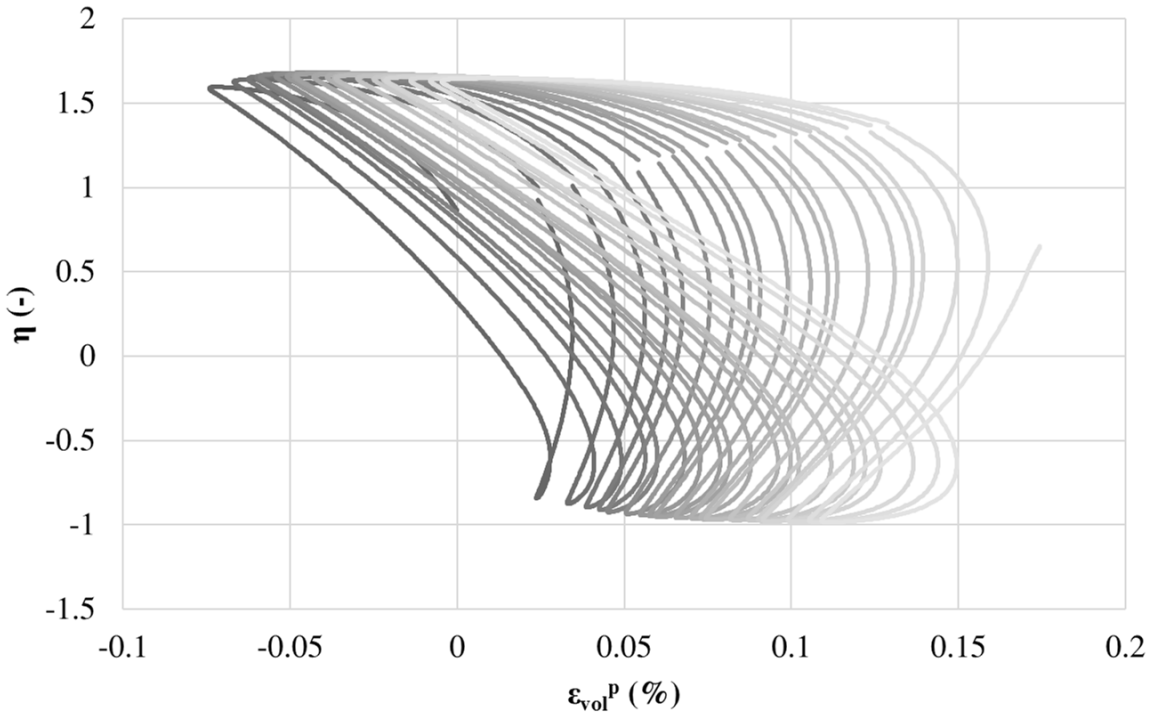

Figure B.23: $\varepsilon^p_{vol} - \eta$ plot

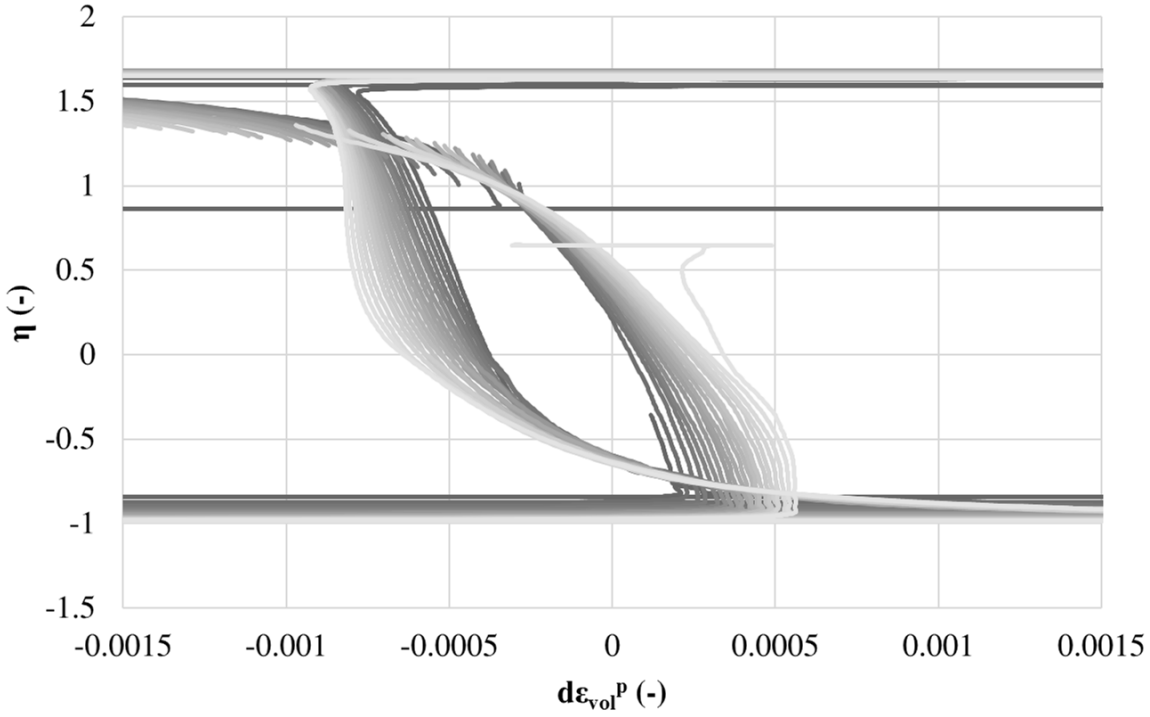

Figure B.24: $d\varepsilon^p_{vol} - \eta$ plot

B.4 Test 14

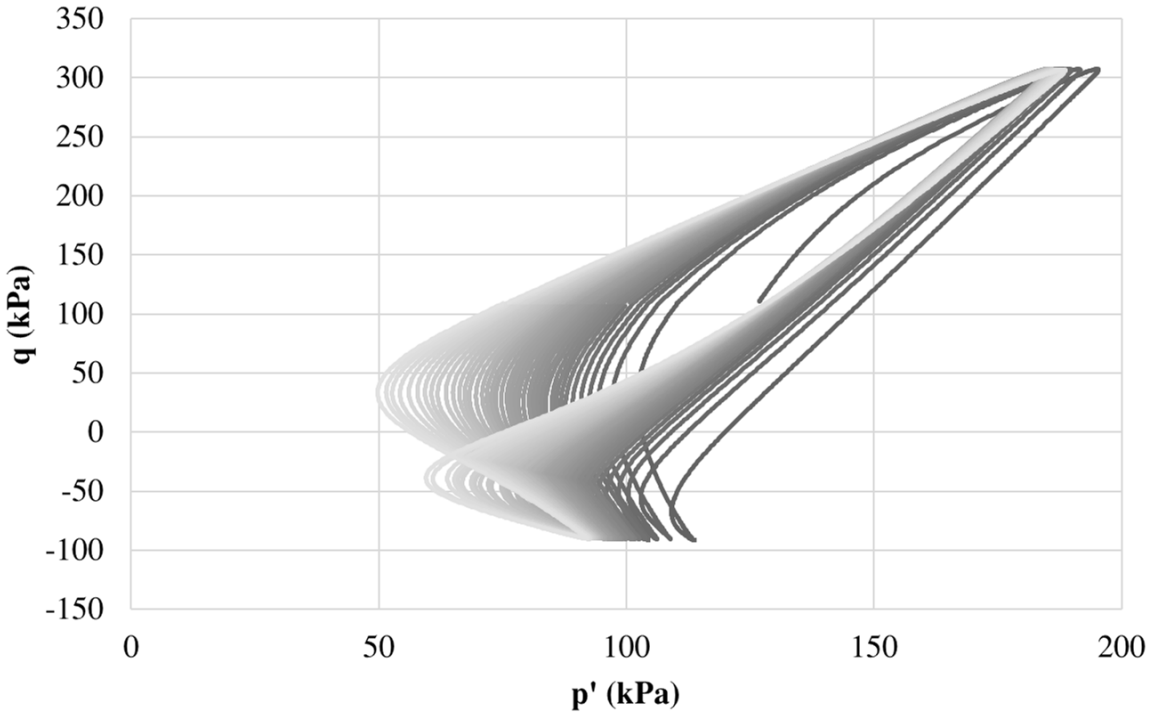

Figure B.25: $p' - q$ plot

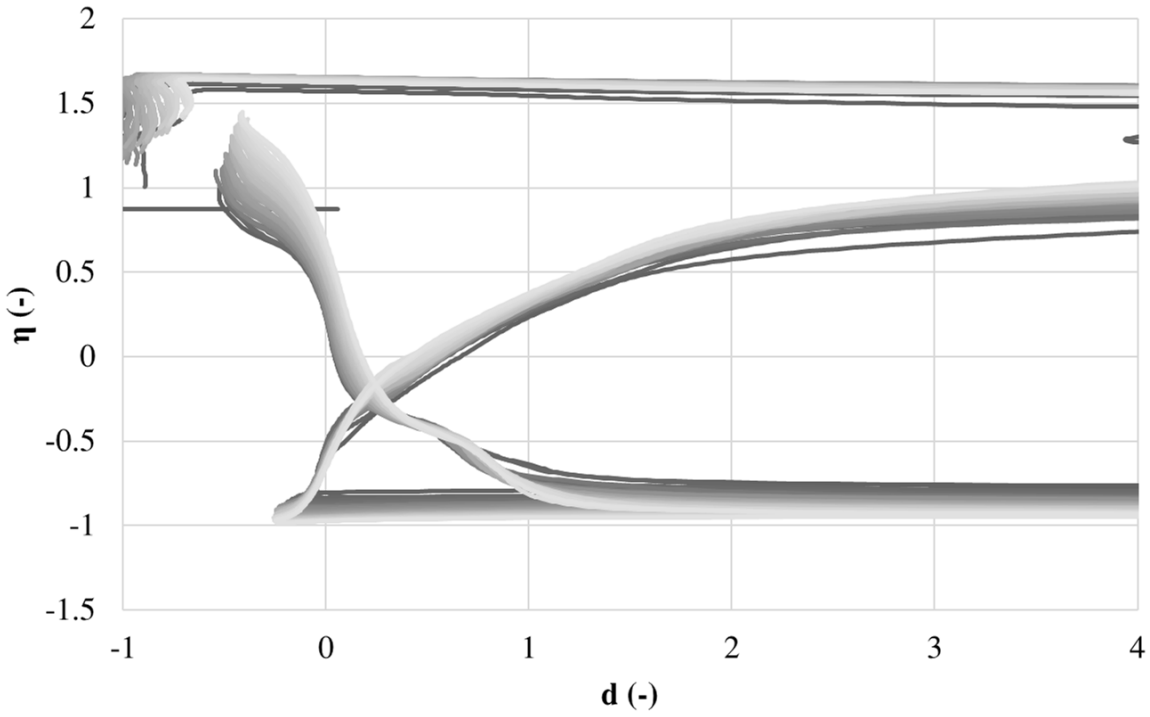

Figure B.26: $d - \eta$ plot

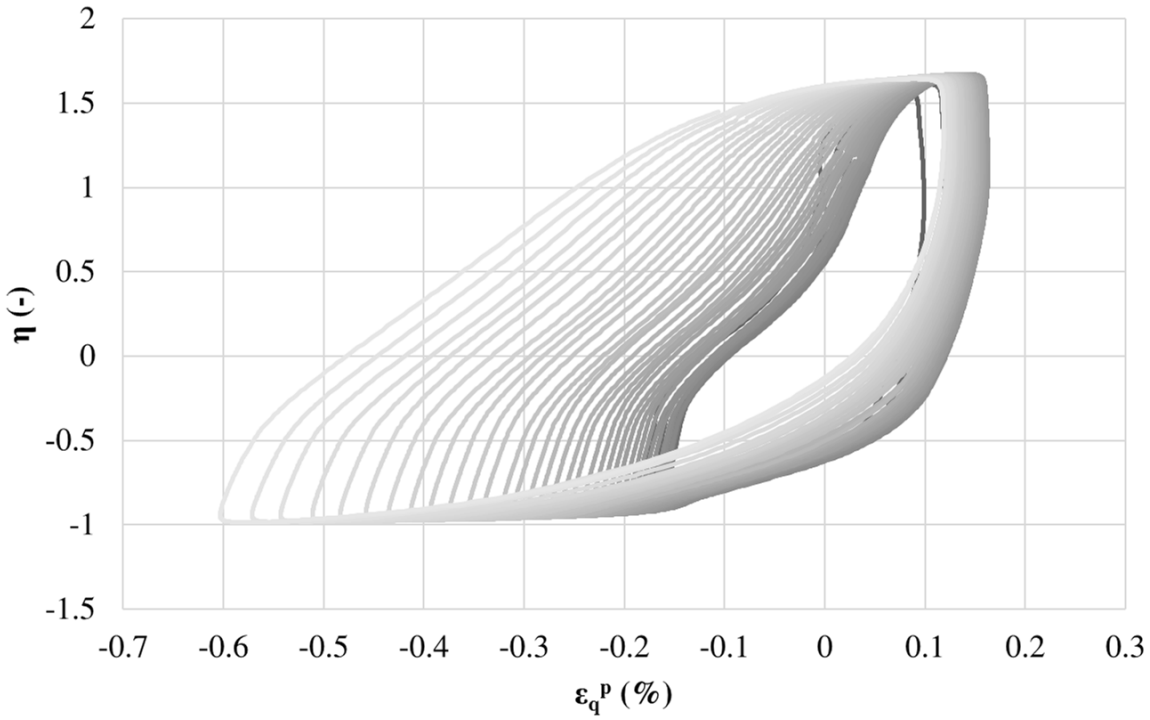

Figure B.27: $\varepsilon_q^p - \eta$ plot

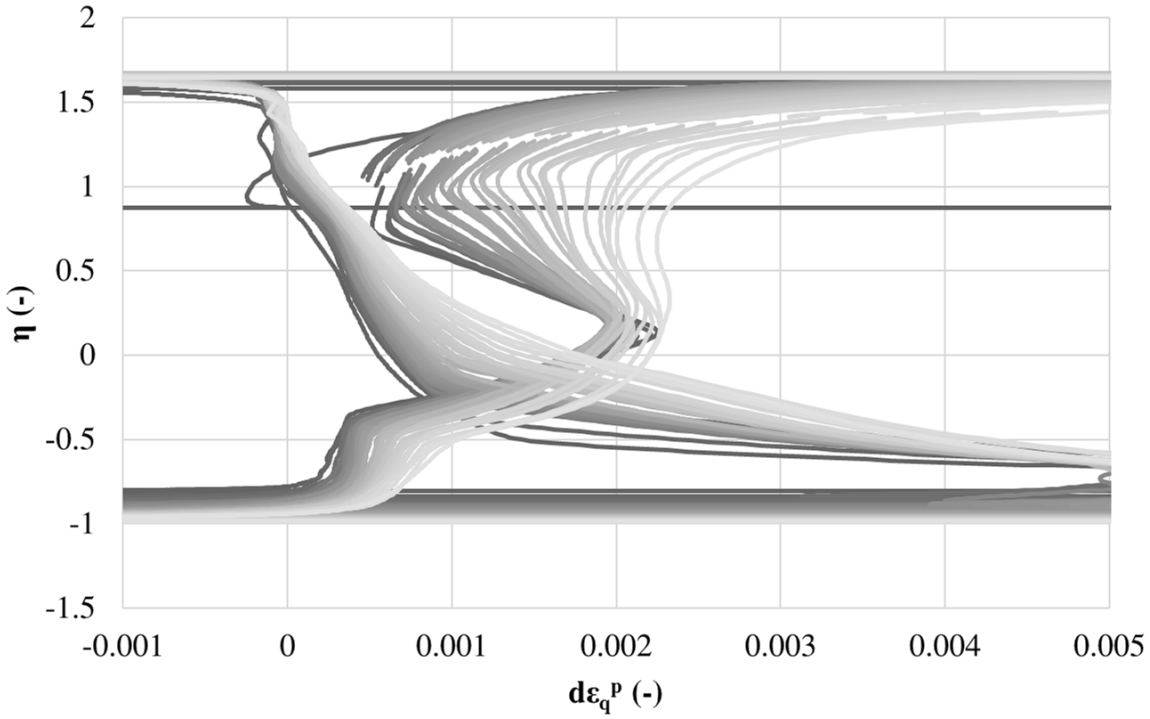

Figure B.28: $d\varepsilon_q^p - \eta$ plot

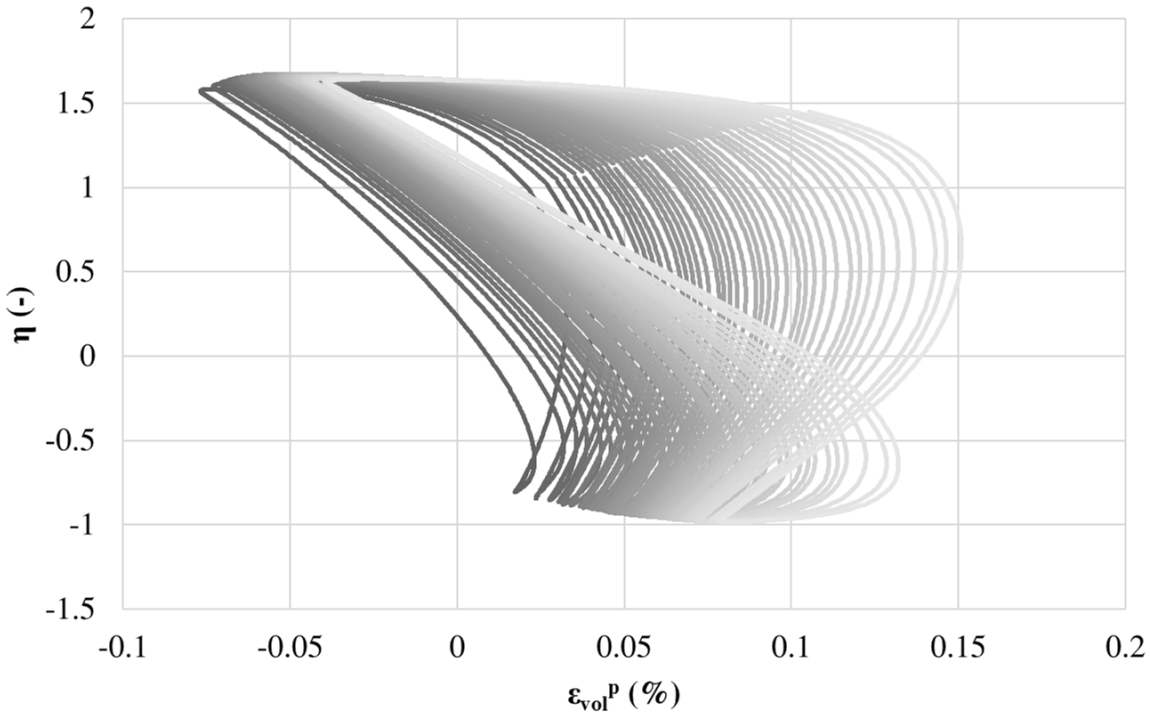

Figure B.29: $\varepsilon^p_{vol} - \eta$ plot

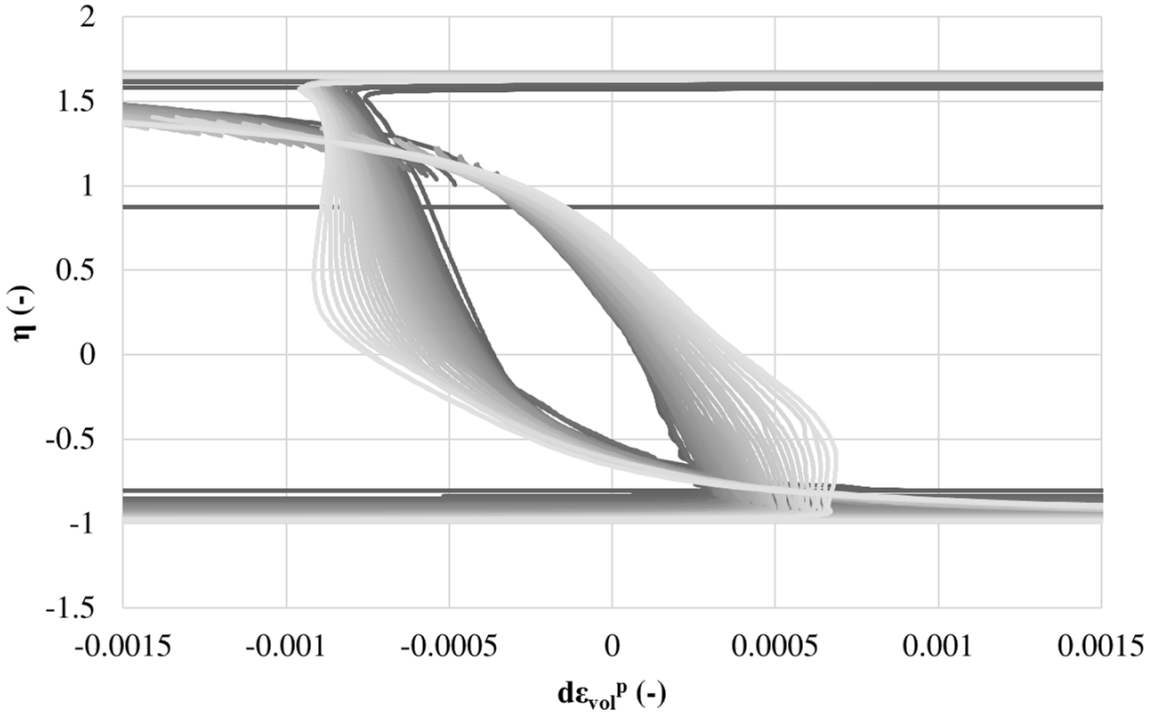

Figure B.30: $d\varepsilon^p_{vol} - \eta$ plot

B.5 Test 15

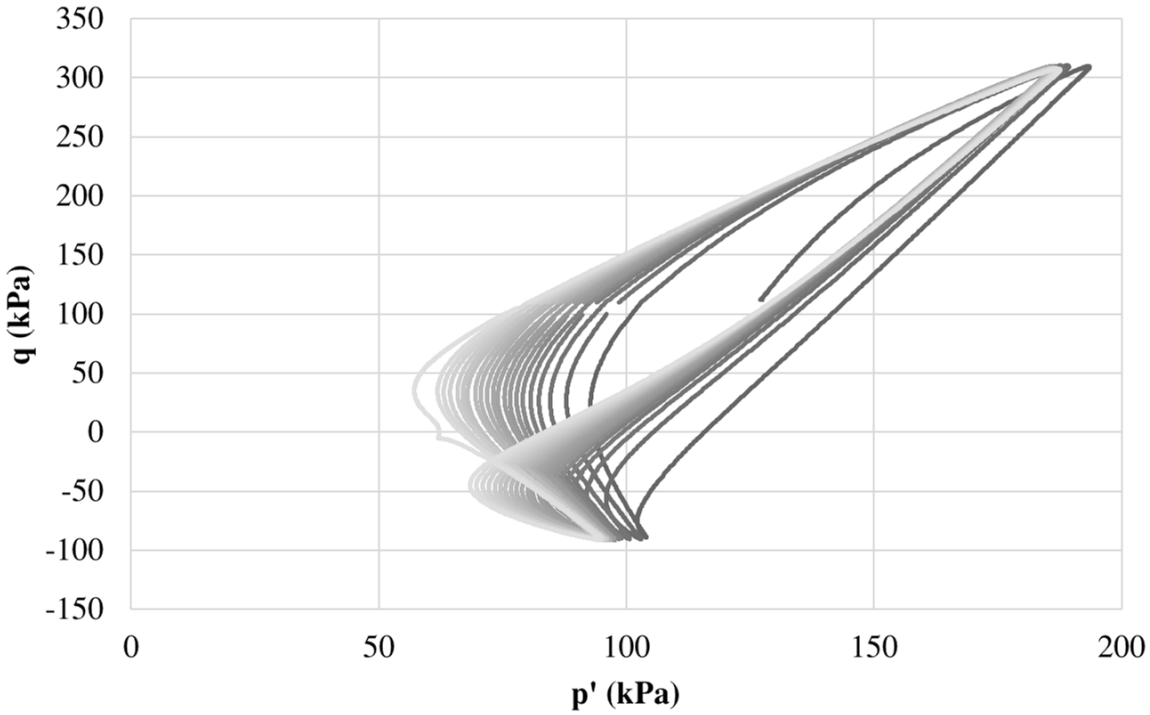

Figure B.31: $p' - q$ plot

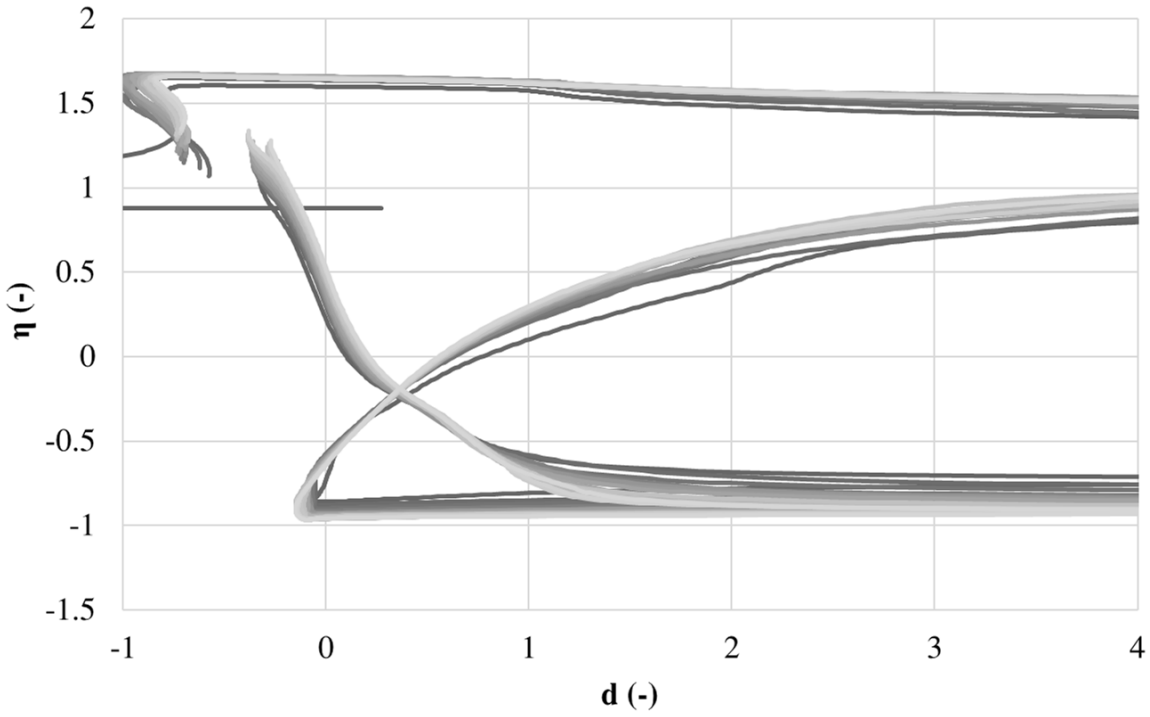

Figure B.32: $d - \eta$ plot

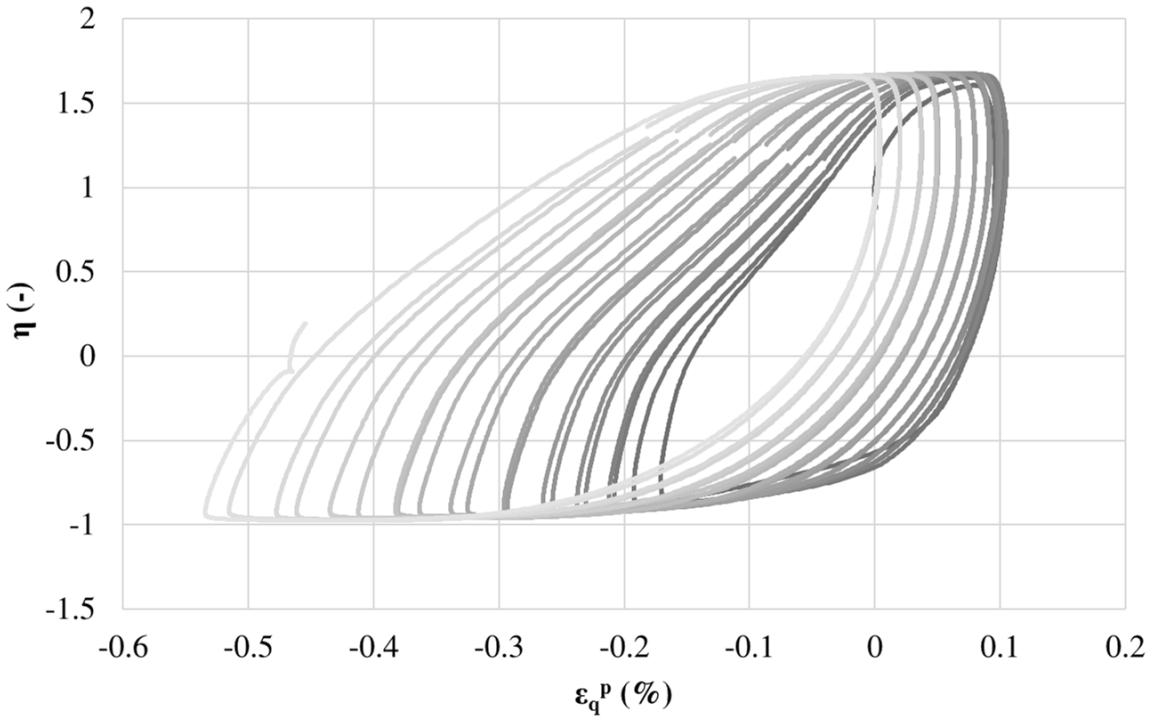

Figure B.33: $\varepsilon_q^p - \eta$ plot

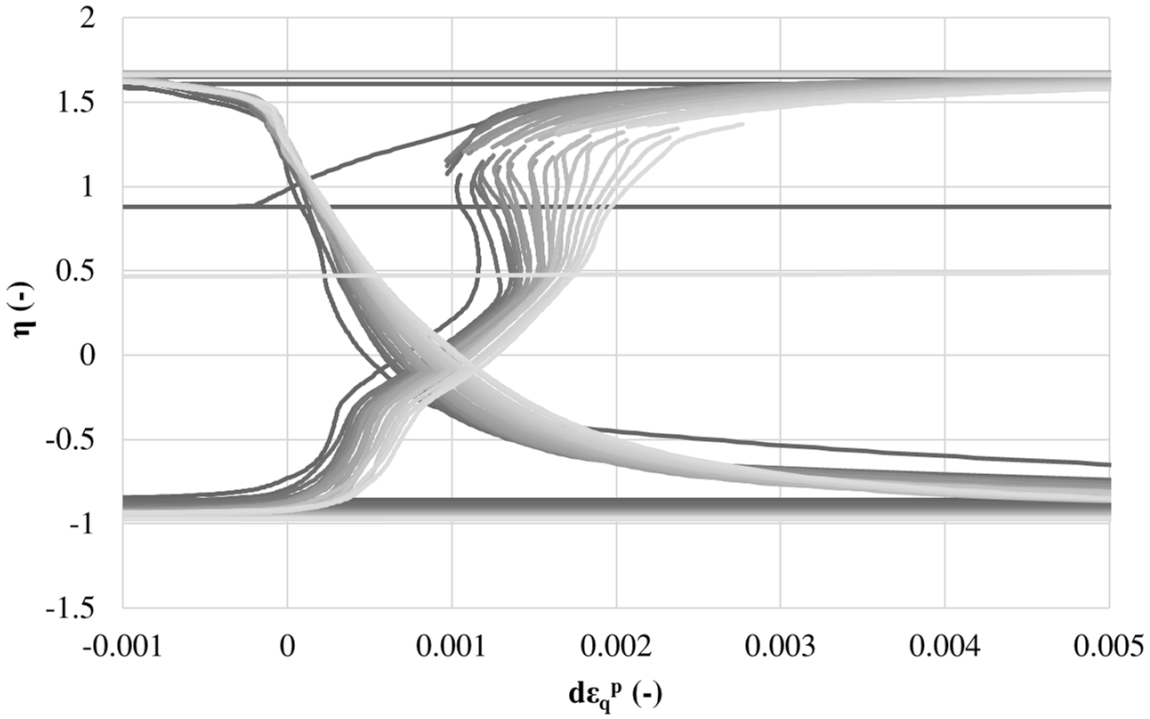

Figure B.34: $d\varepsilon_q^p - \eta$ plot

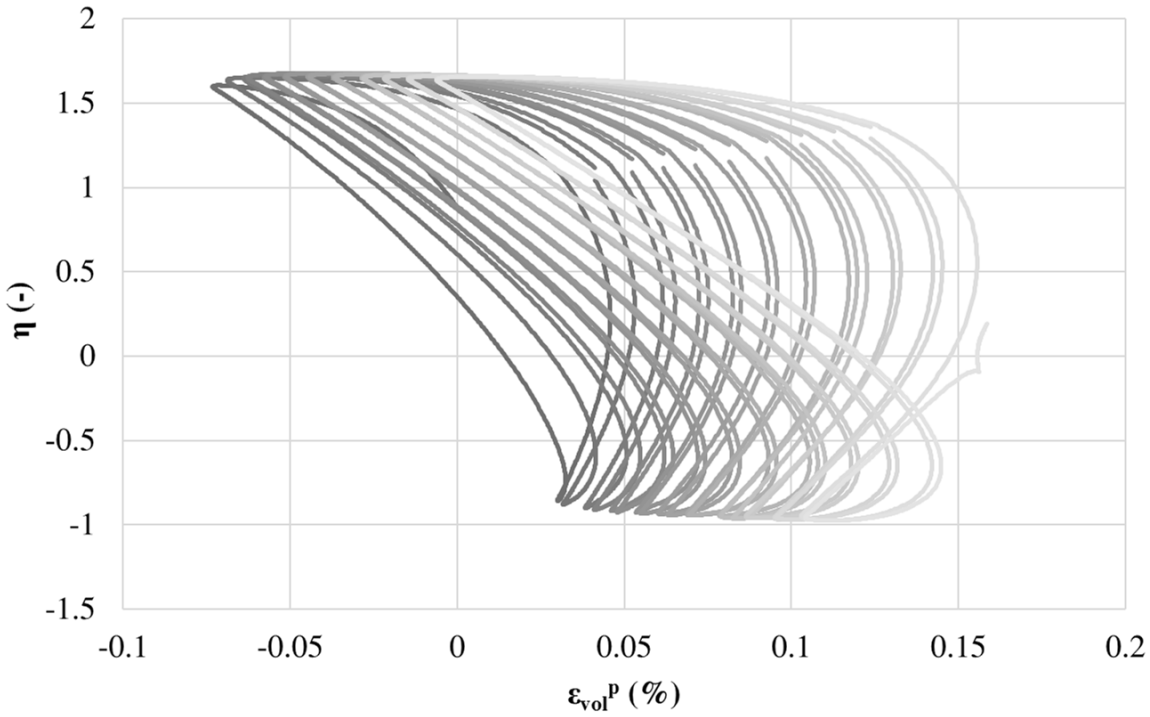

Figure B.35: $\varepsilon^p_{vol} - \eta$ plot

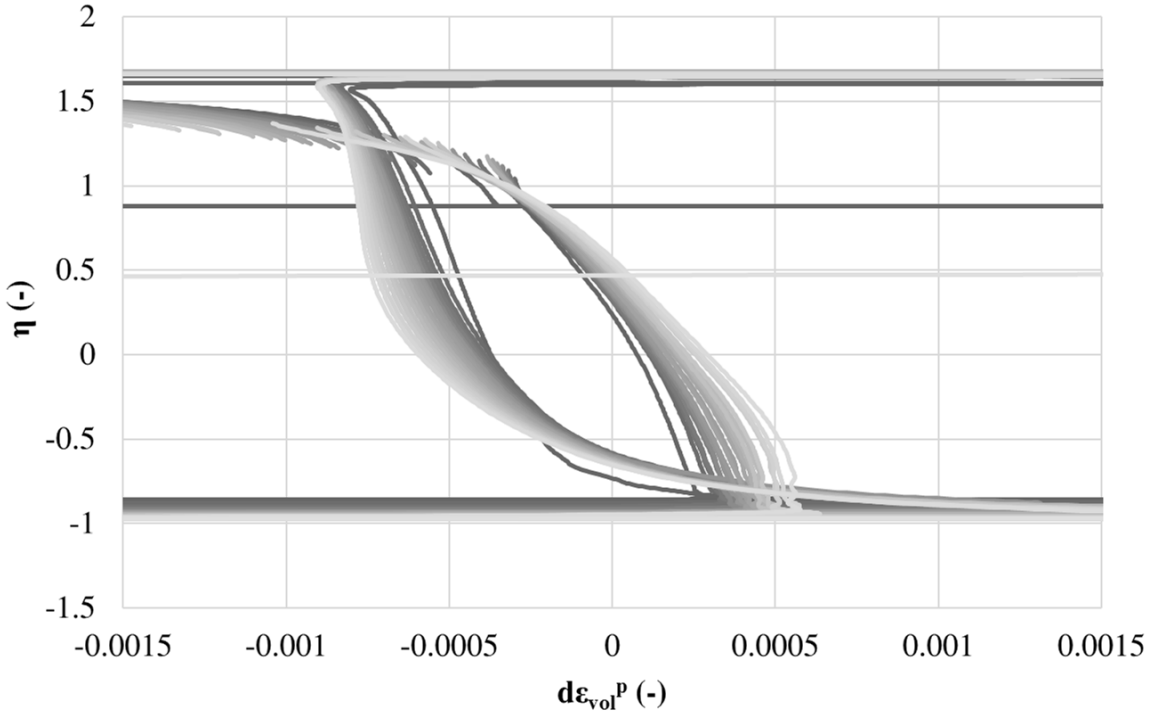

Figure B.36: $d\varepsilon^p_{vol} - \eta$ plot

B.6 Test 16

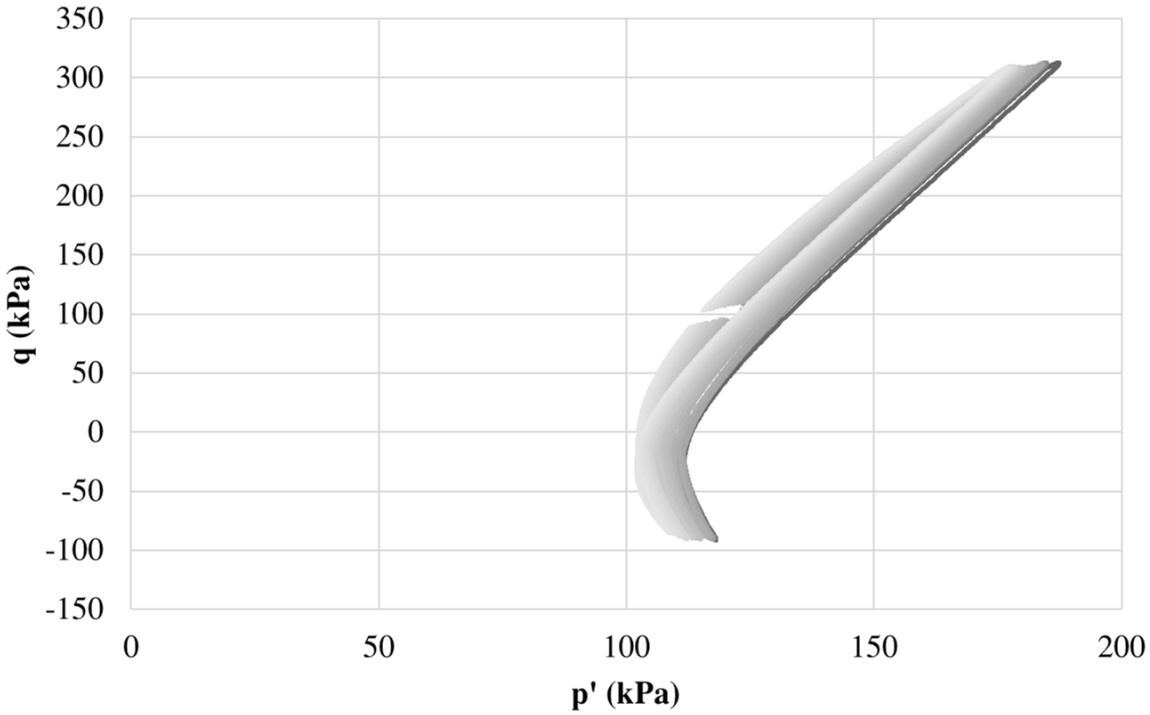

Figure B.37: $p' - q$ plot

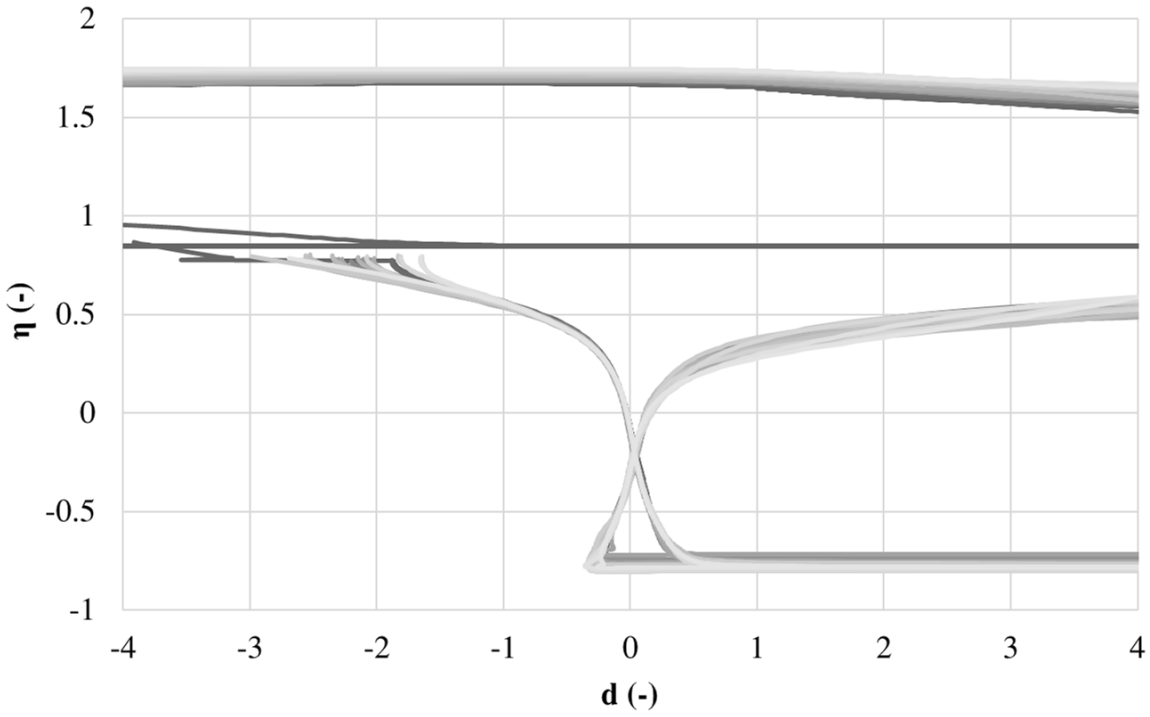

Figure B.38: $d - \eta$ plot

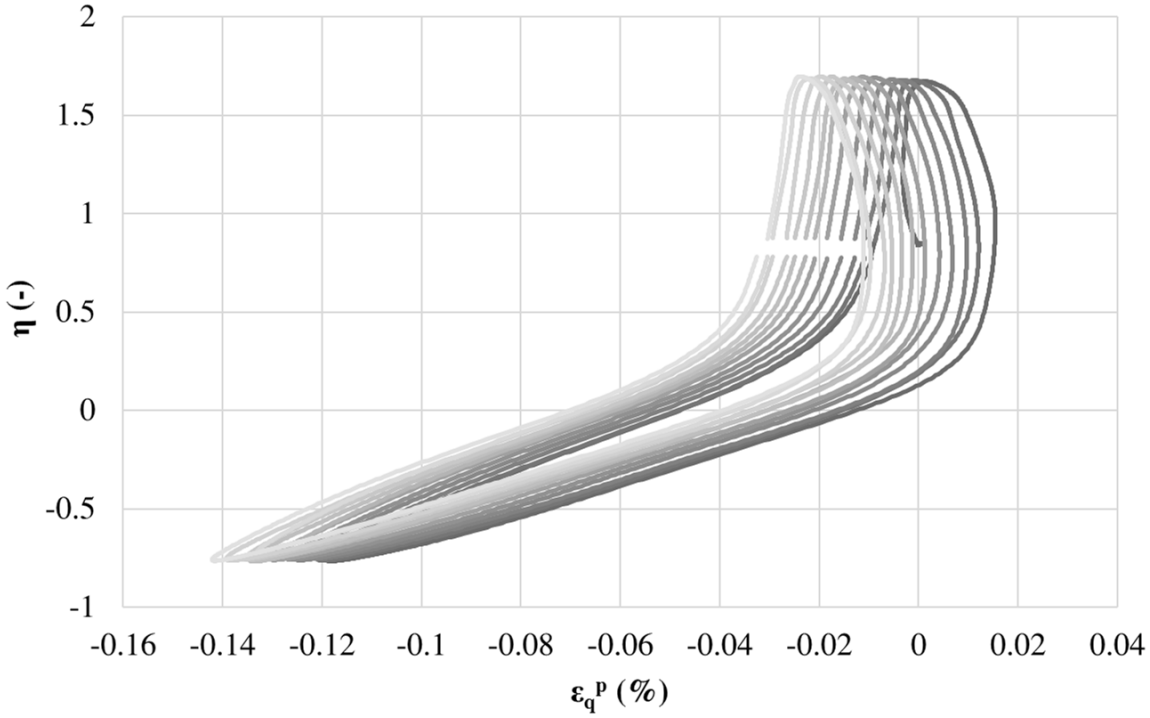

Figure B.39: $\varepsilon_q^p - \eta$ plot

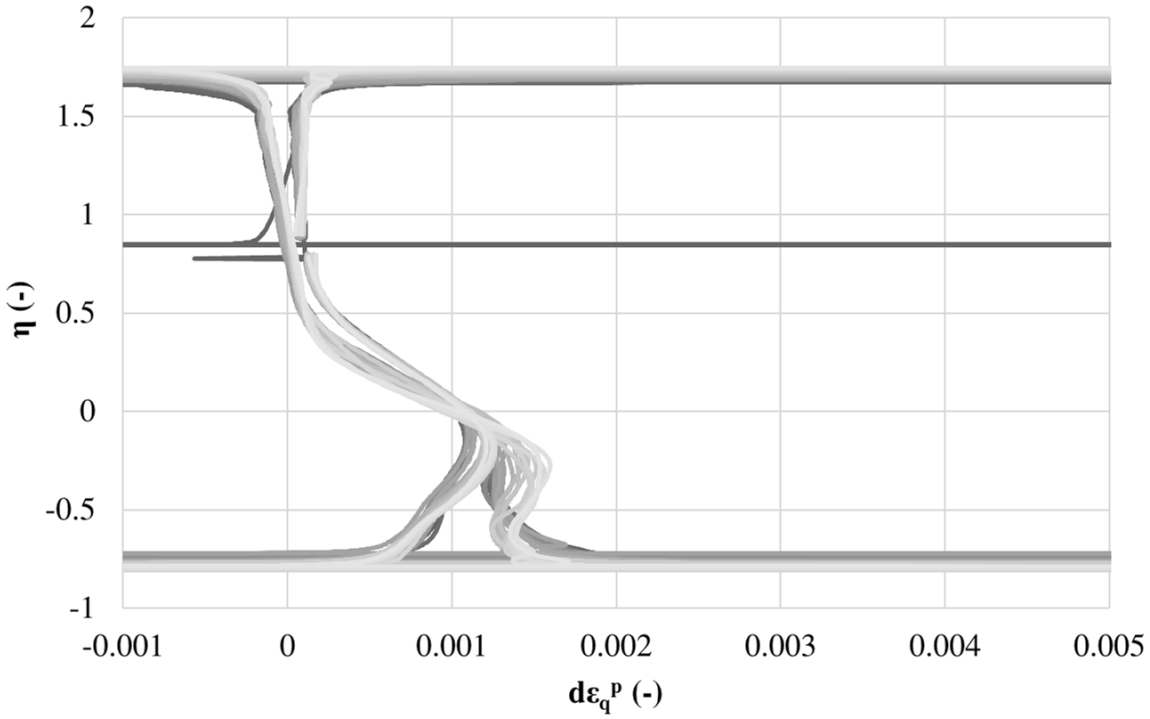

Figure B.40: $d\varepsilon_q^p - \eta$ plot

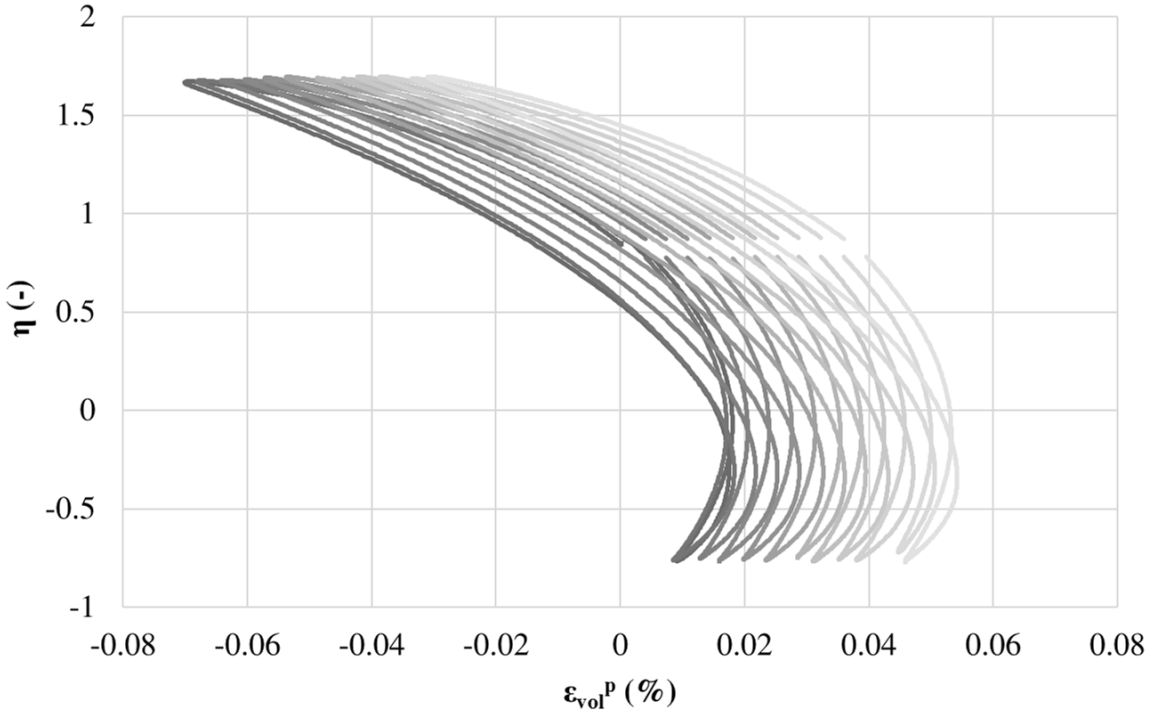

Figure B.41: $\varepsilon^p_{vol} - \eta$ plot

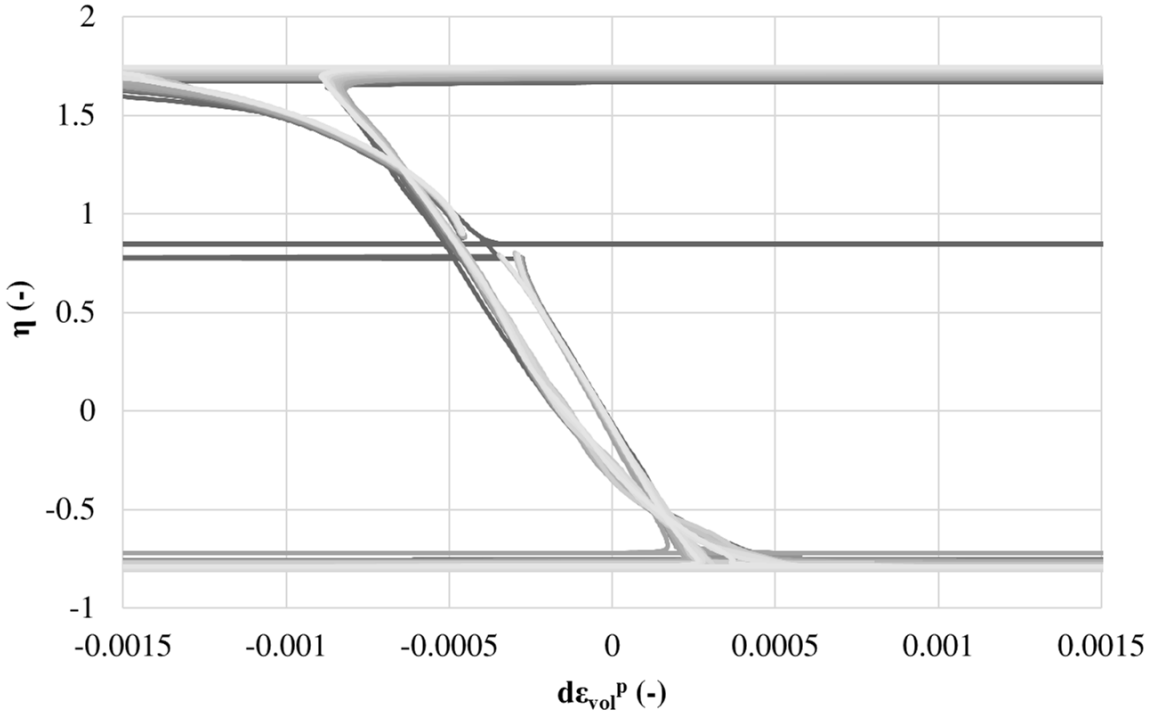

Figure B.42: $d\varepsilon^p_{vol} - \eta$ plot

B.7 Test 17

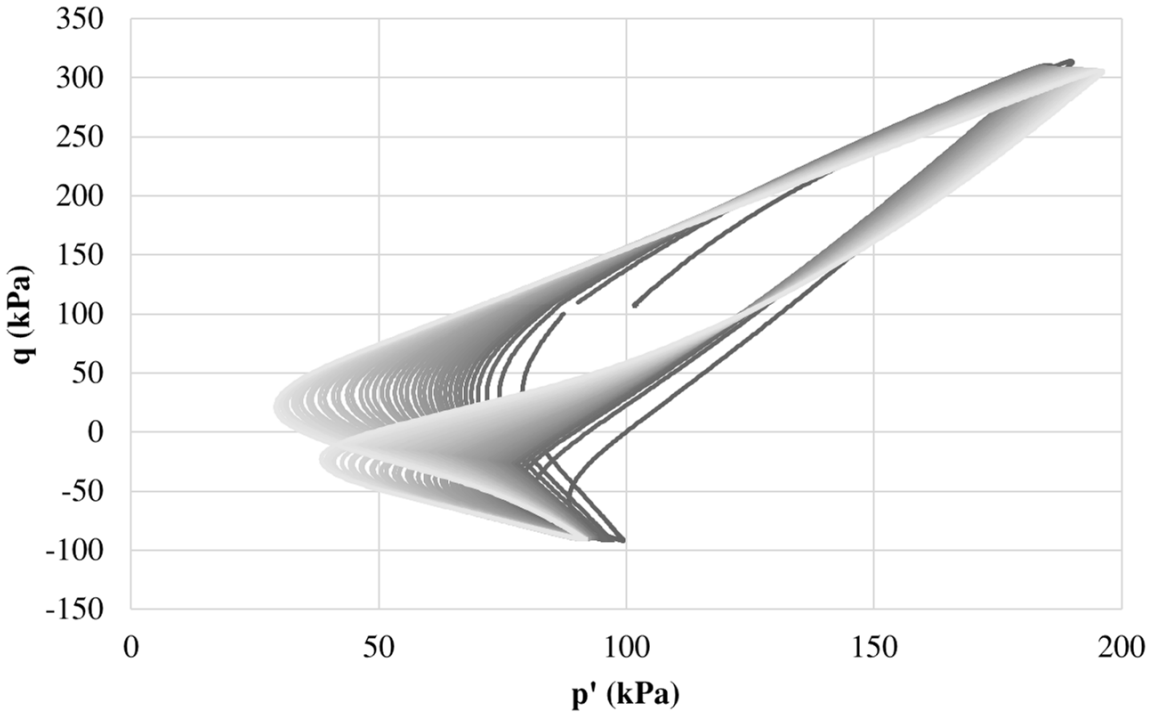

Figure B.43: $p' - q$ plot

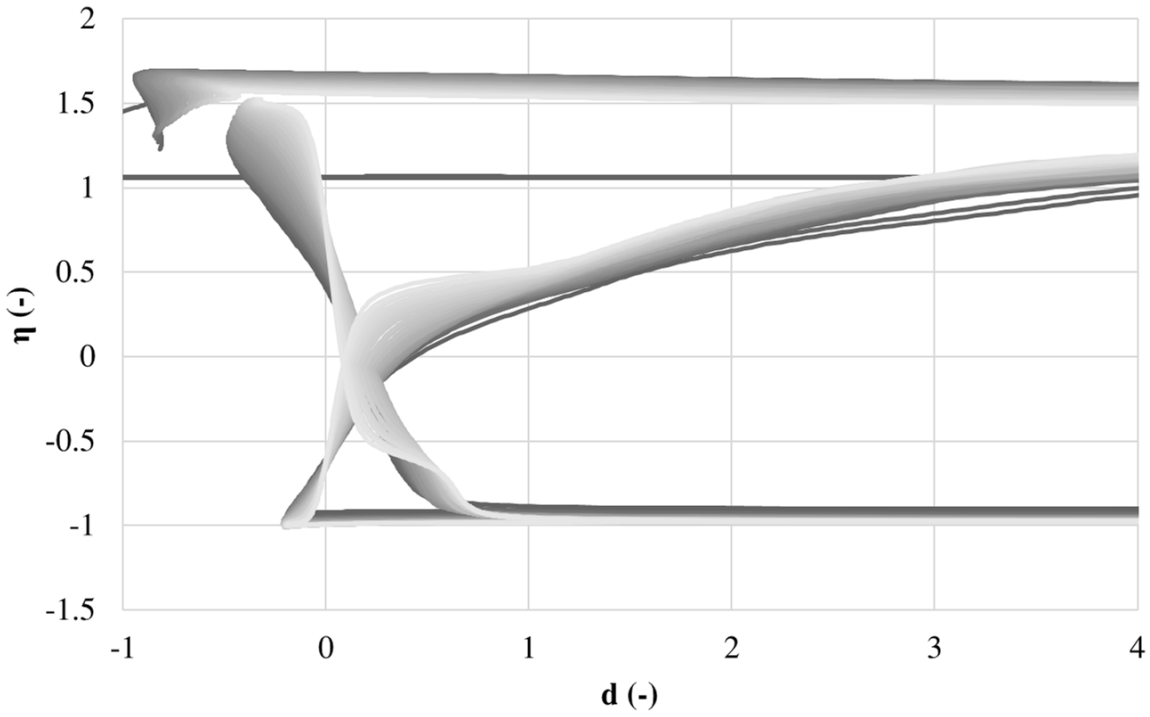

Figure B.44: $d - \eta$ plot

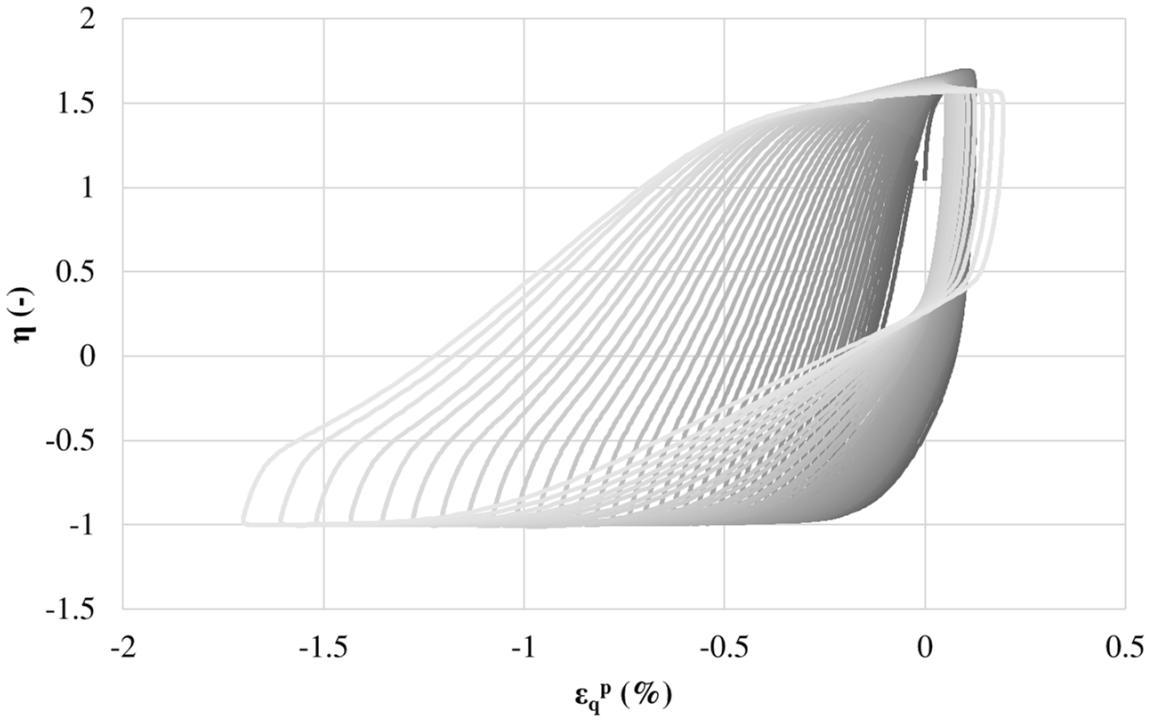

Figure B.45: $\varepsilon_q^p - \eta$ plot

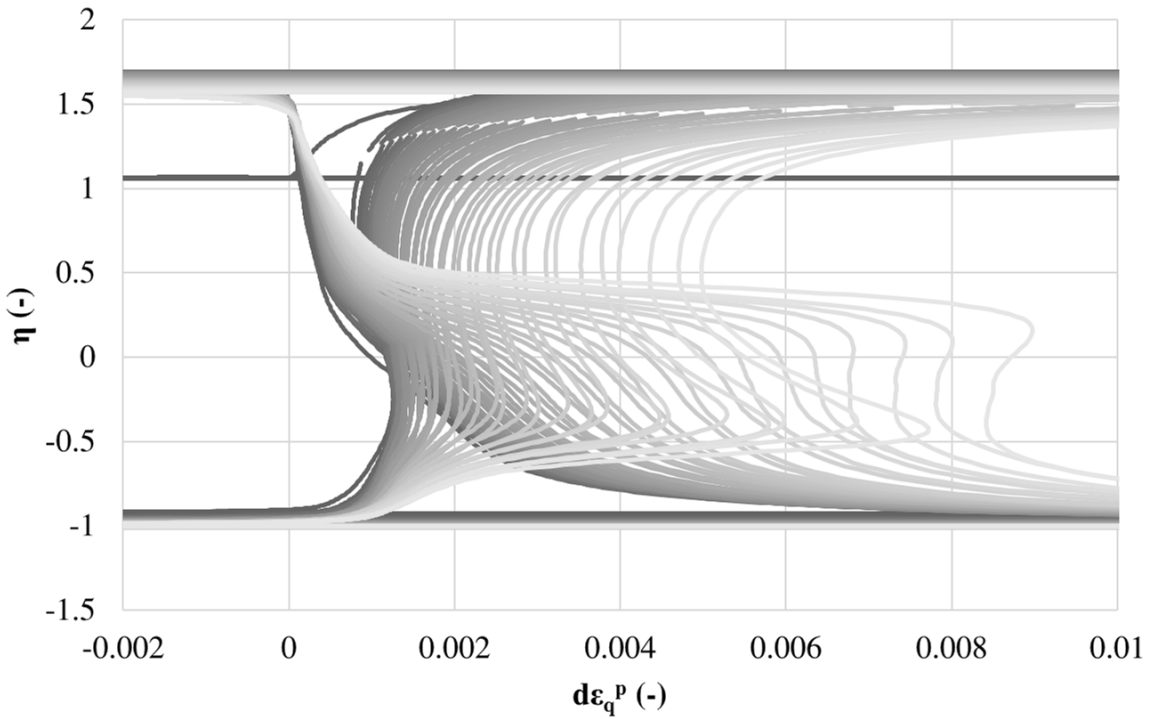

Figure B.46: $d\varepsilon_q^p - \eta$ plot

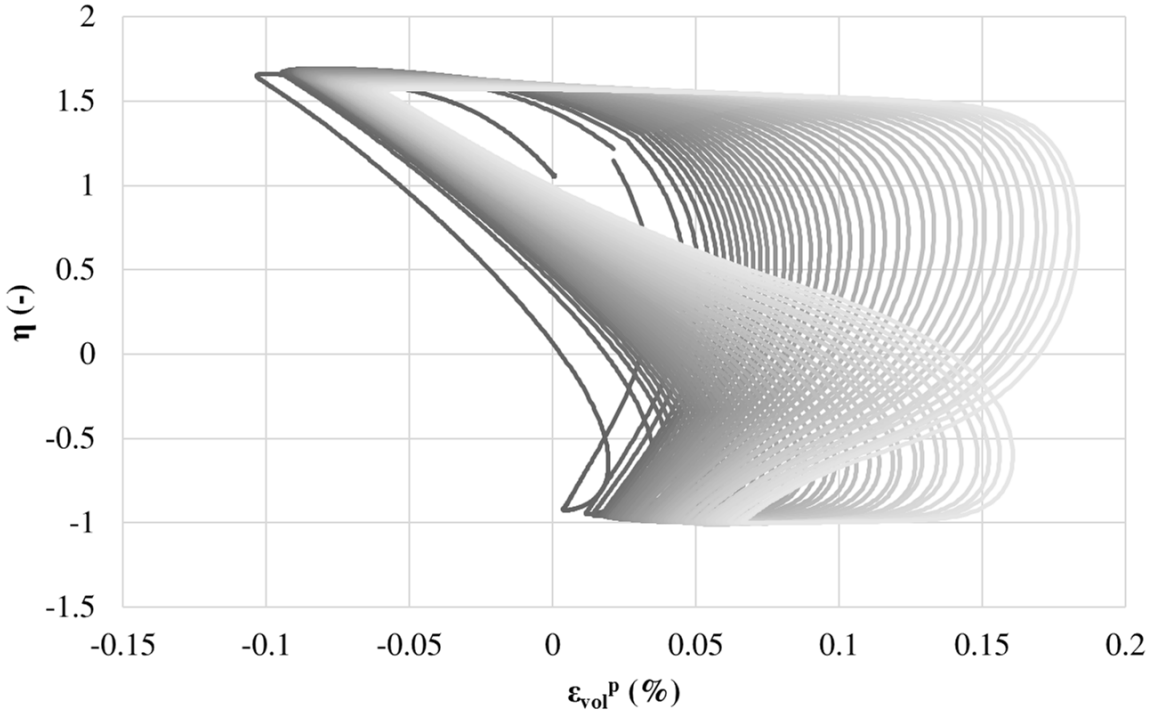

Figure B.47: $\varepsilon^p_{vol} - \eta$ plot

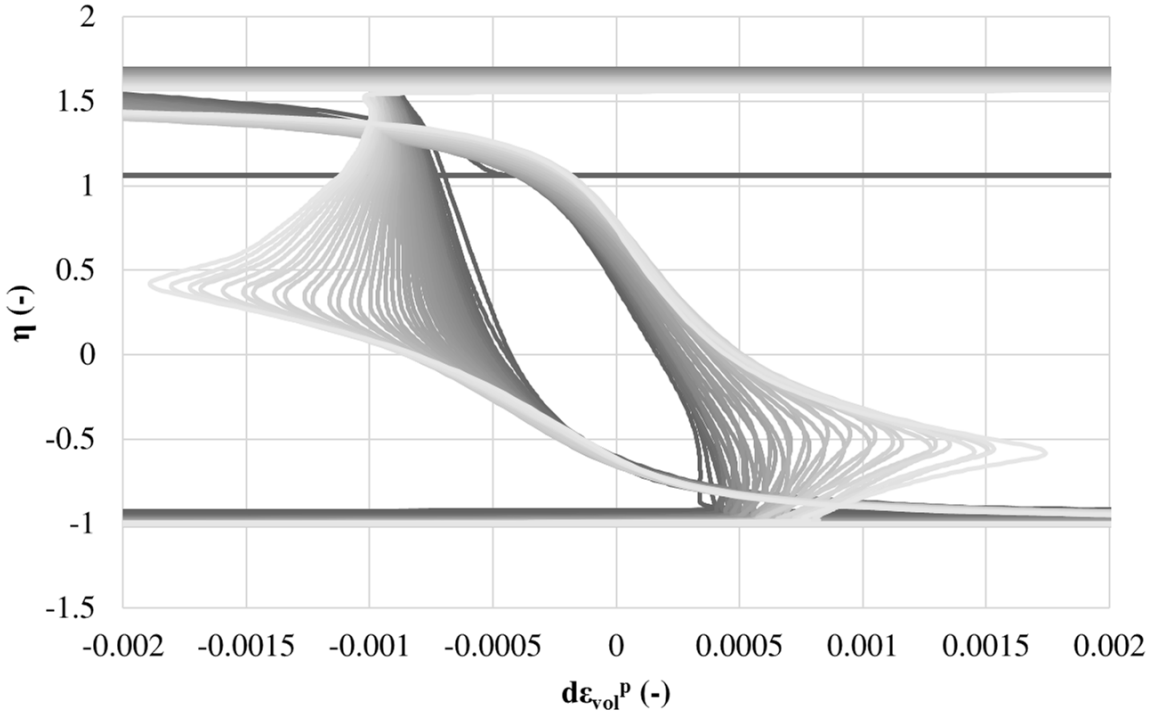

Figure B.48: $d\varepsilon^p_{vol} - \eta$ plot

B.8 Test 18

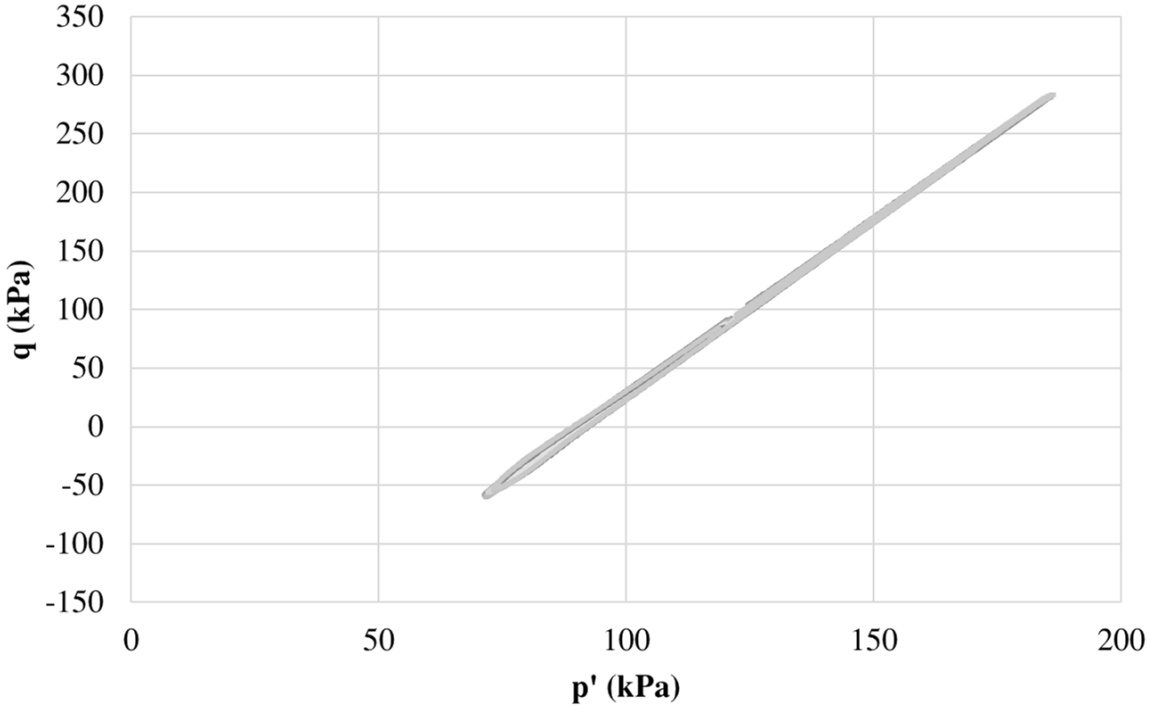

Figure B.49: $p' - q$ plot

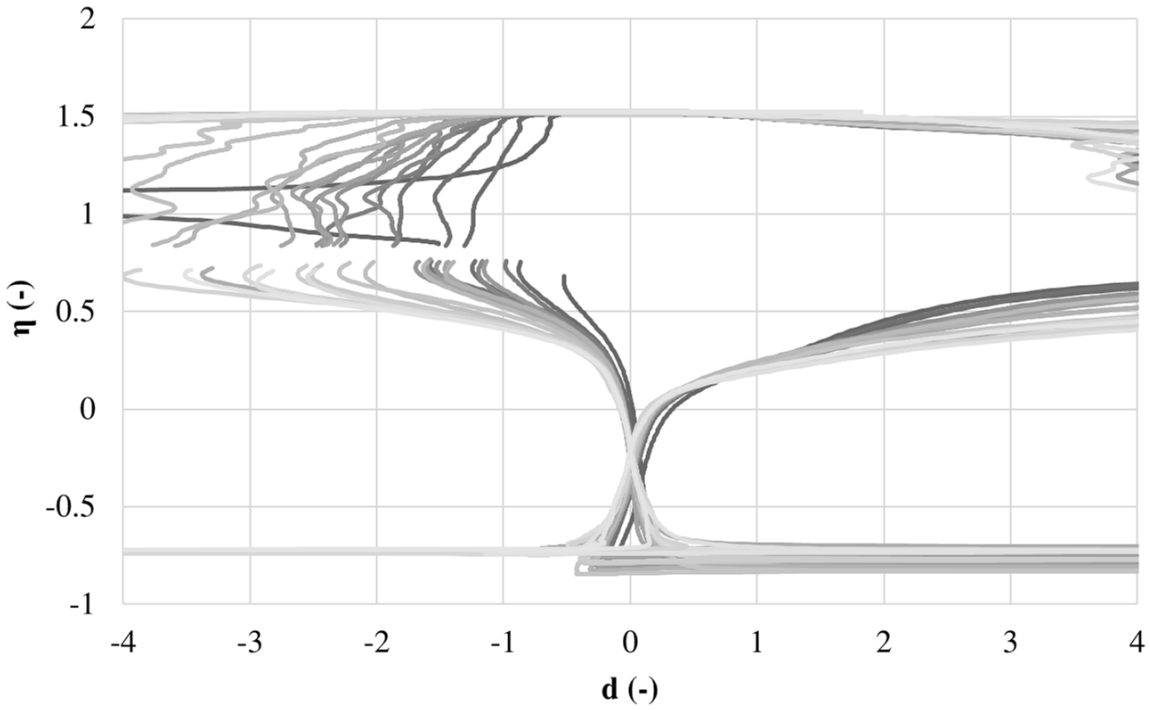

Figure B.50: $d - \eta$ plot

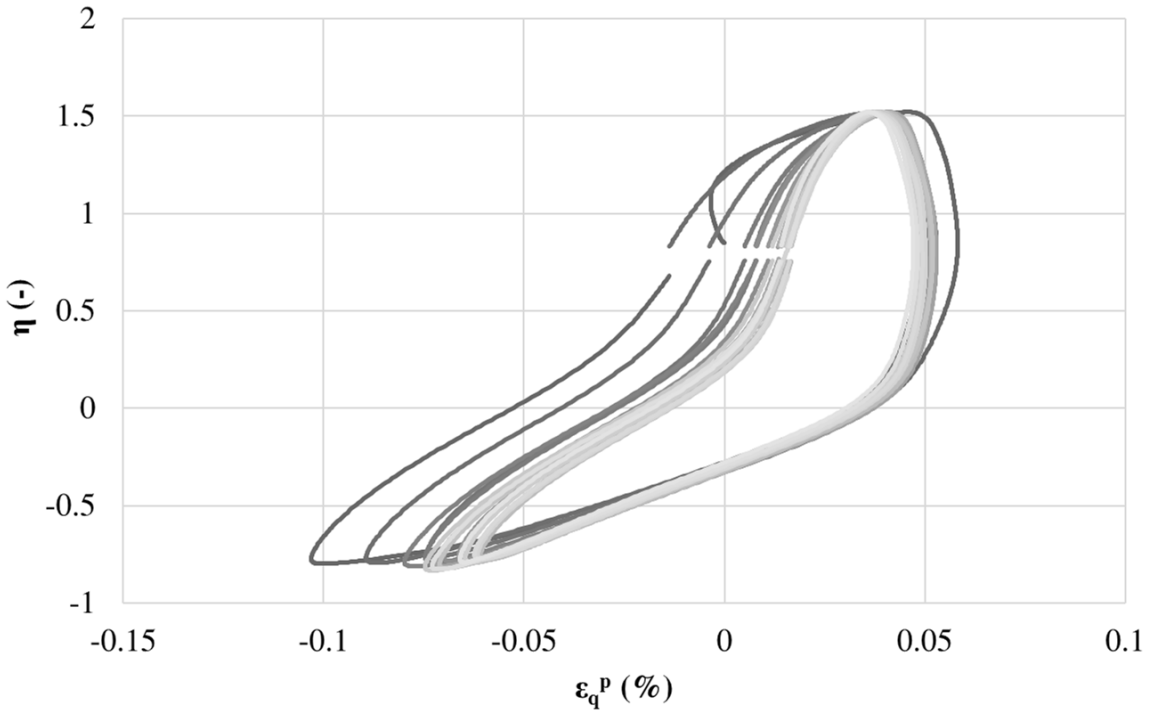

Figure B.51: $\varepsilon_q^p - \eta$ plot

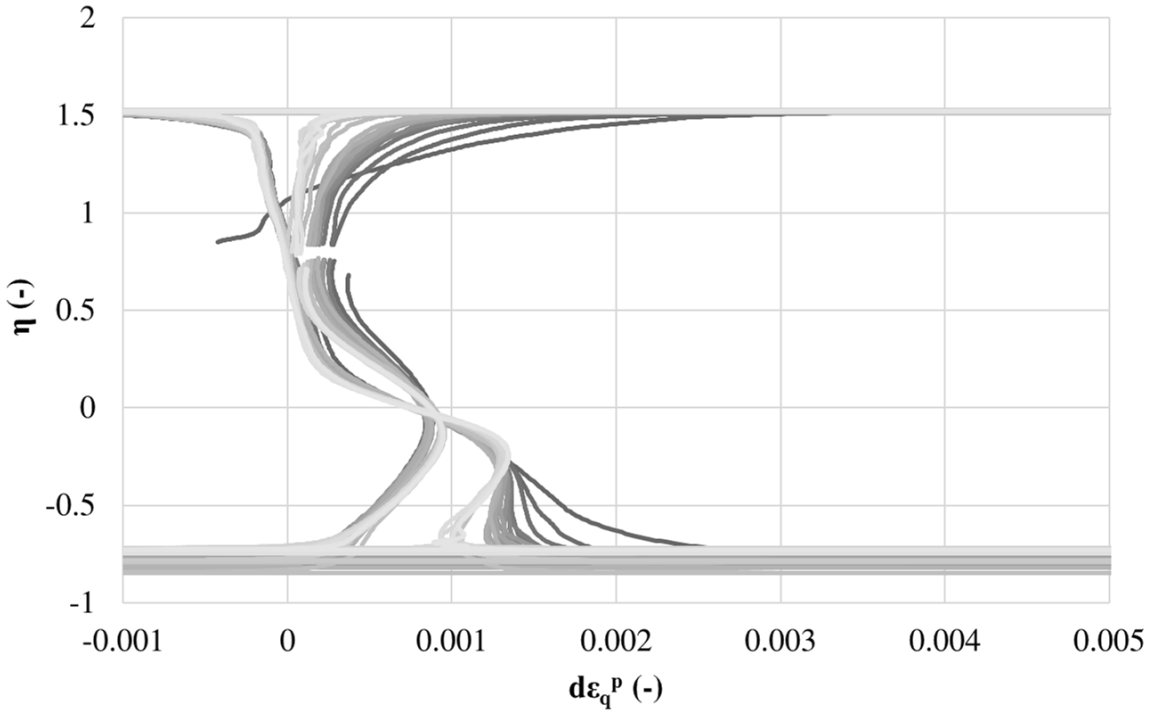

Figure B.52: $d\varepsilon_q^p - \eta$ plot

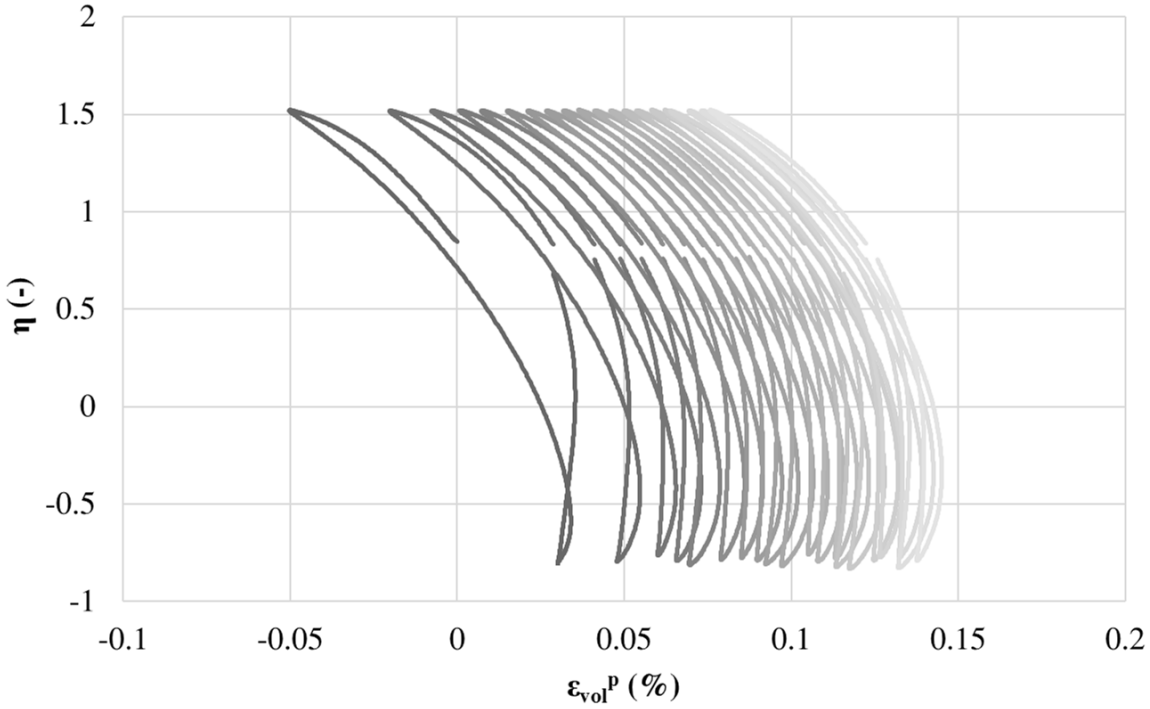

Figure B.53: $\varepsilon^p_{vol} - \eta$ plot

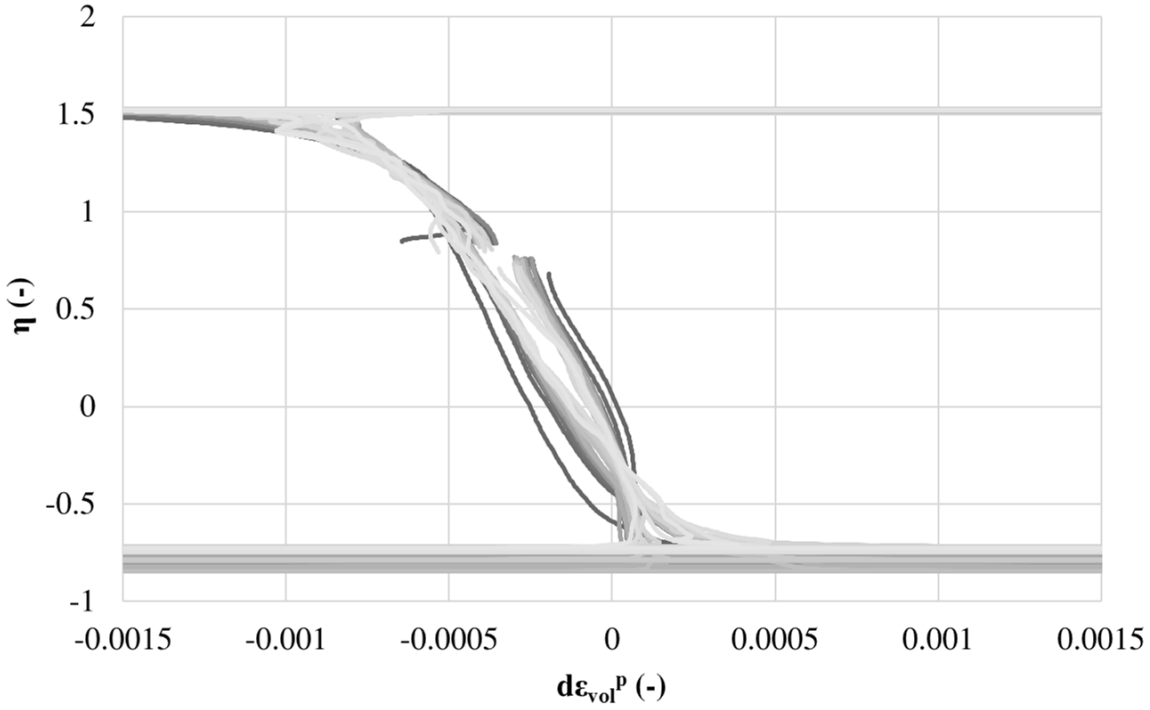

Figure B.54: $d\varepsilon^p_{vol} - \eta$ plot

Appendix C

Implementation of the Monotonic SANISAND Constitutive Model

Table C.1: Input parameters for the SANISAND material model, monotonic loading

Input parameters		**Compression** $D_r = 80$ **%**	**Extension** $D_r = 80$ **%**	**Compression** $D_r = 60$ **%**	**Extension** $D_r = 60$ **%**
Elasticity	G_0	250	250	250	250
	ν	0.05	0.05	0.05	0.05
Critical state	M	1.49	0.90	1.49	0.90
	c	-	-	-	-
	λ_c	0.013	0.013	0.013	0.013
	e_0	0.71	0.71	0.71	0.71
	ξ	0.67	0.67	0.67	0.67
Yield surface	m	0.0	0.0	0.0	0.0
Plastic modulus	h_0	5.0	8.0	4.0	8.0
	c_h	1.0	1.1	1.0	0.8
	n^b	1.3	2.0	1.3	0.2
Dilatancy	A_0	0.6	0.8	0.6	0.8
	n^d	5.0	7.0	15.0	7.0

C.1 Test 1, 2, 3, 4

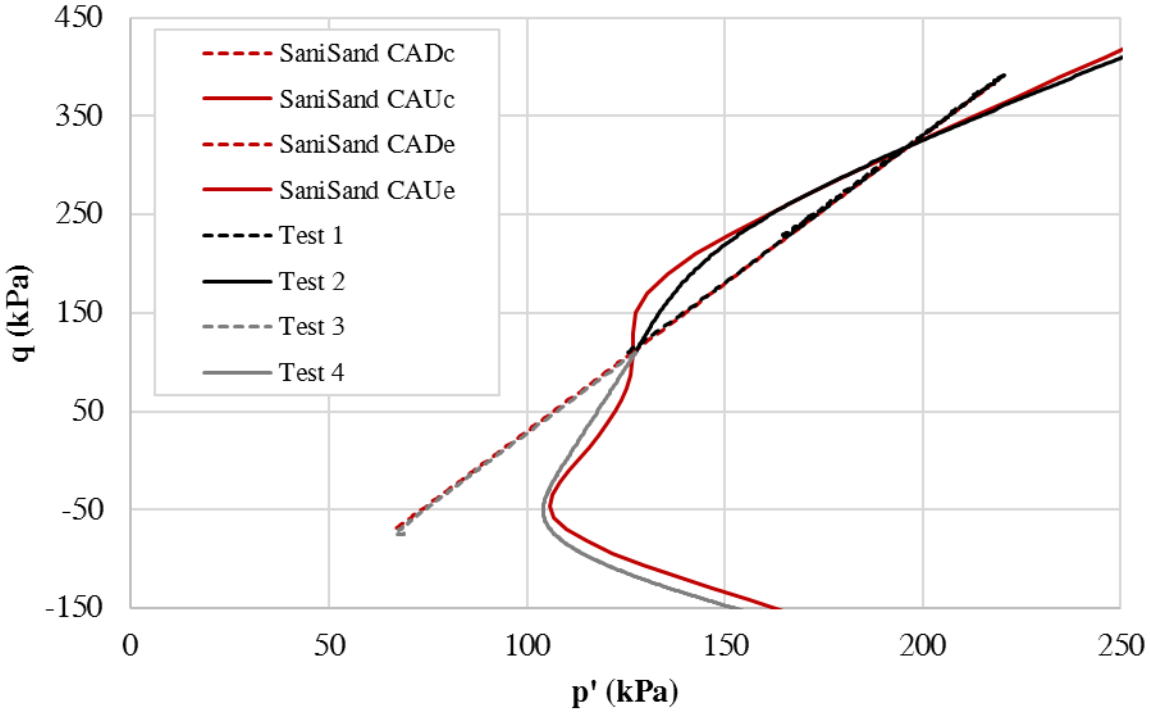

Figure C.1: $p' - q$ plot

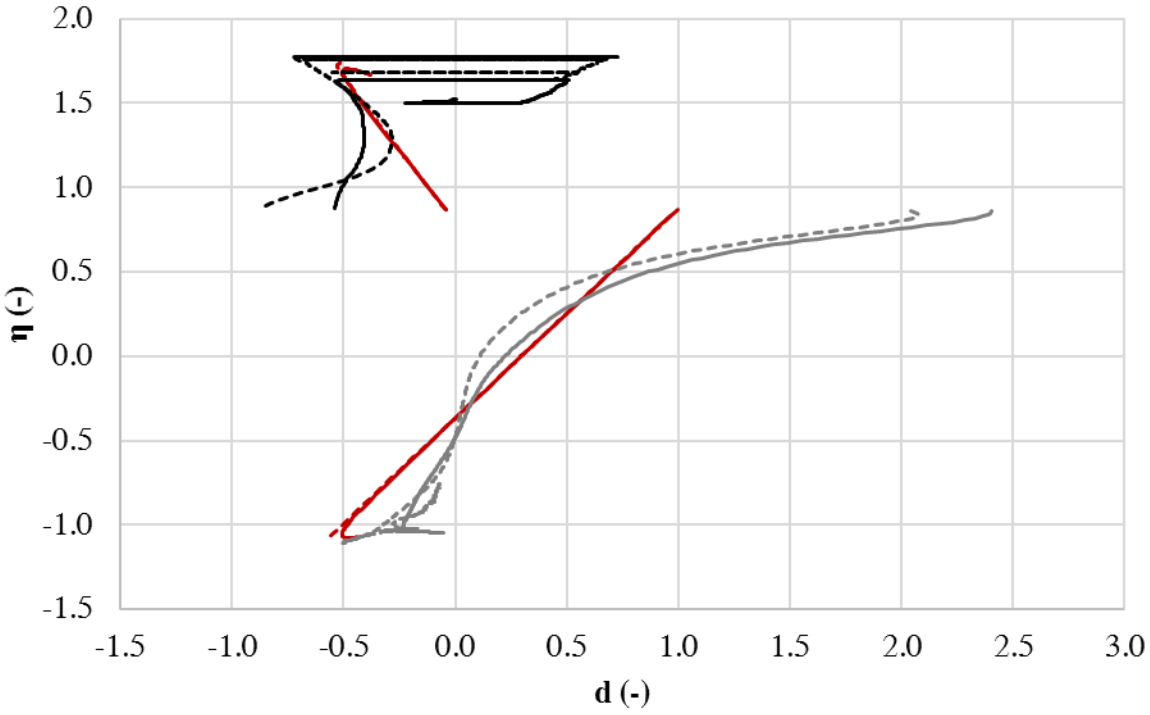

Figure C.2: $d - \eta$ plot

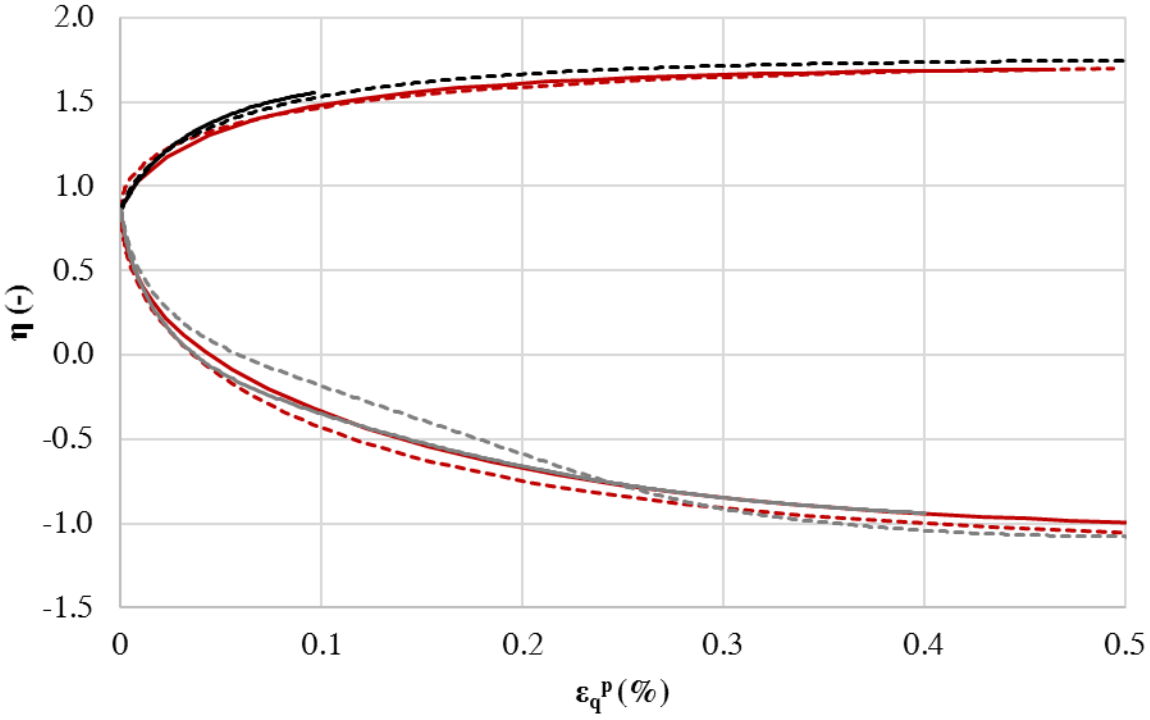

Figure C.3: $\varepsilon_q^p - \eta$ plot

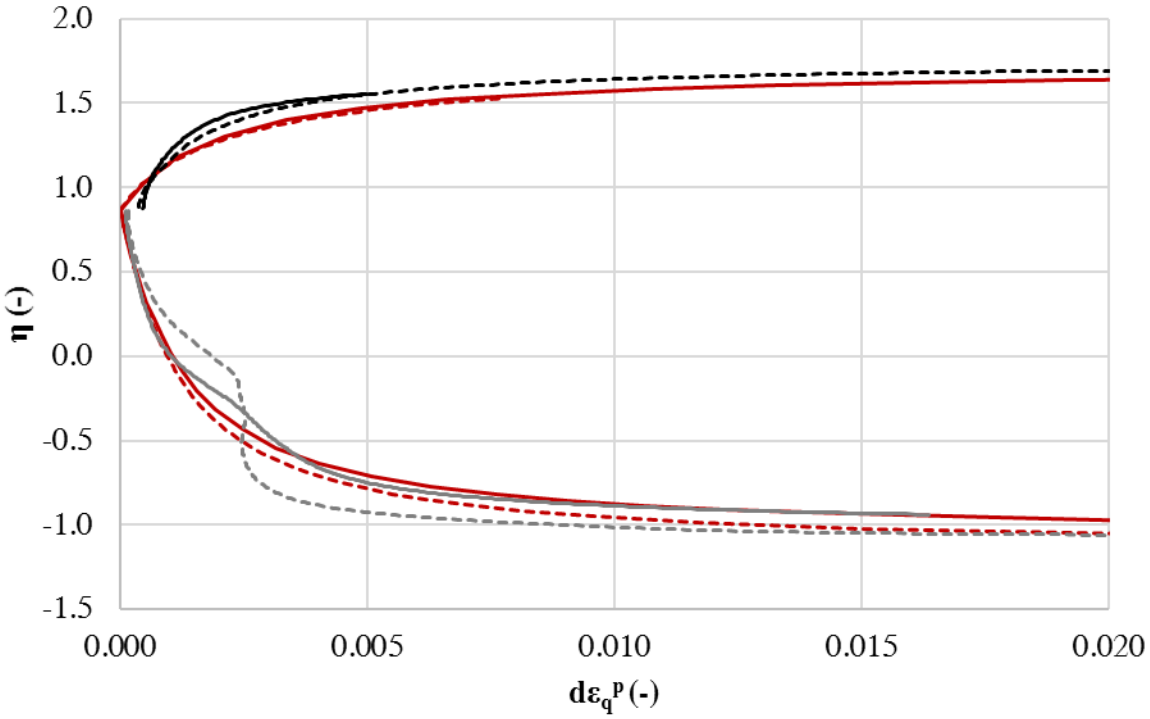

Figure C.4: $d\varepsilon_q^p - \eta$ plot

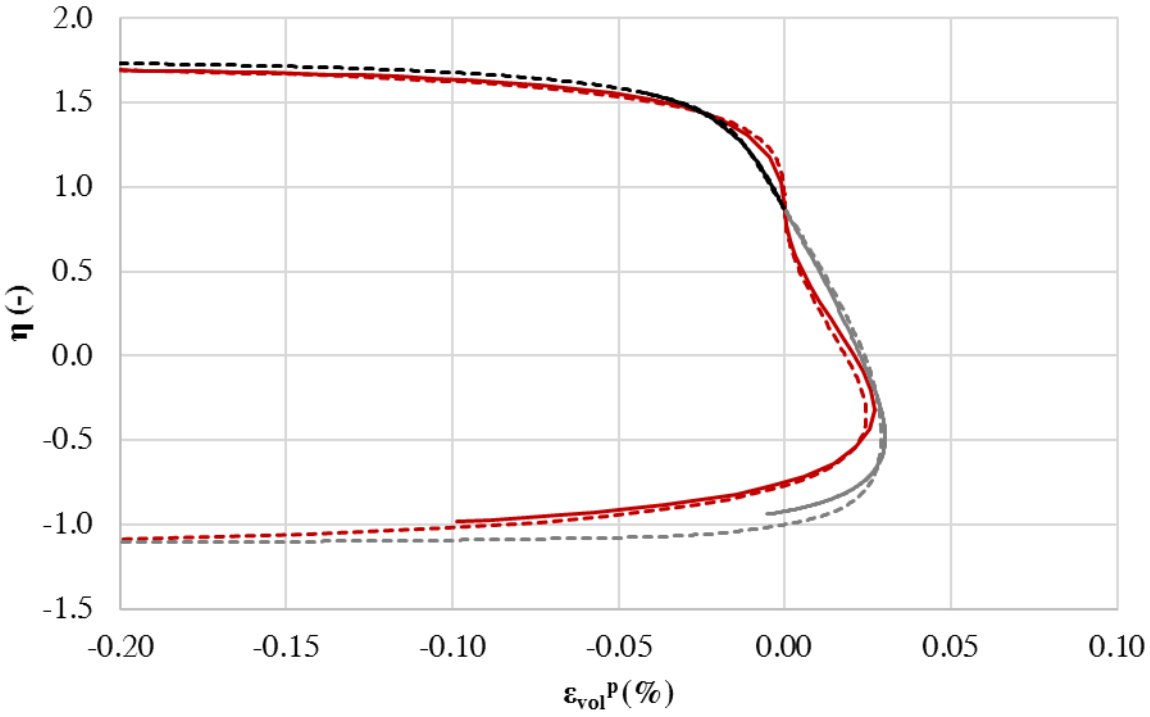

Figure C.5: $\varepsilon^{p}_{vol} - \eta$ plot

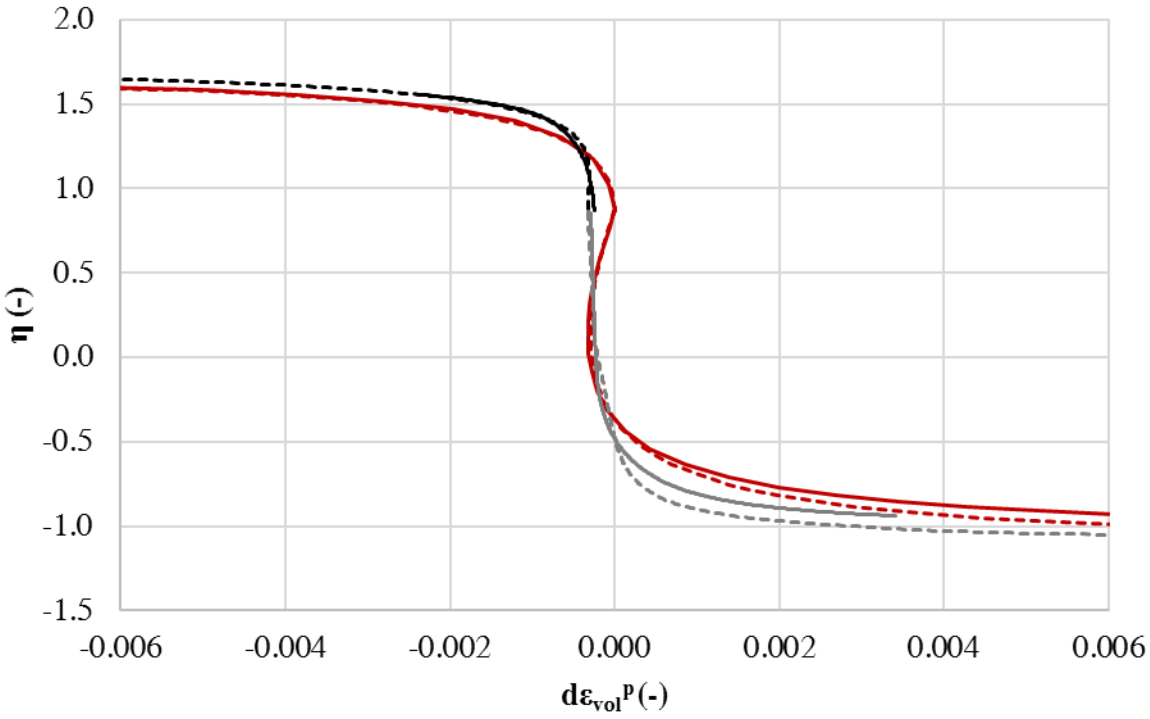

Figure C.6: $d\varepsilon^{p}_{vol} - \eta$ plot

C.2 Test 5, 6, 7, 8

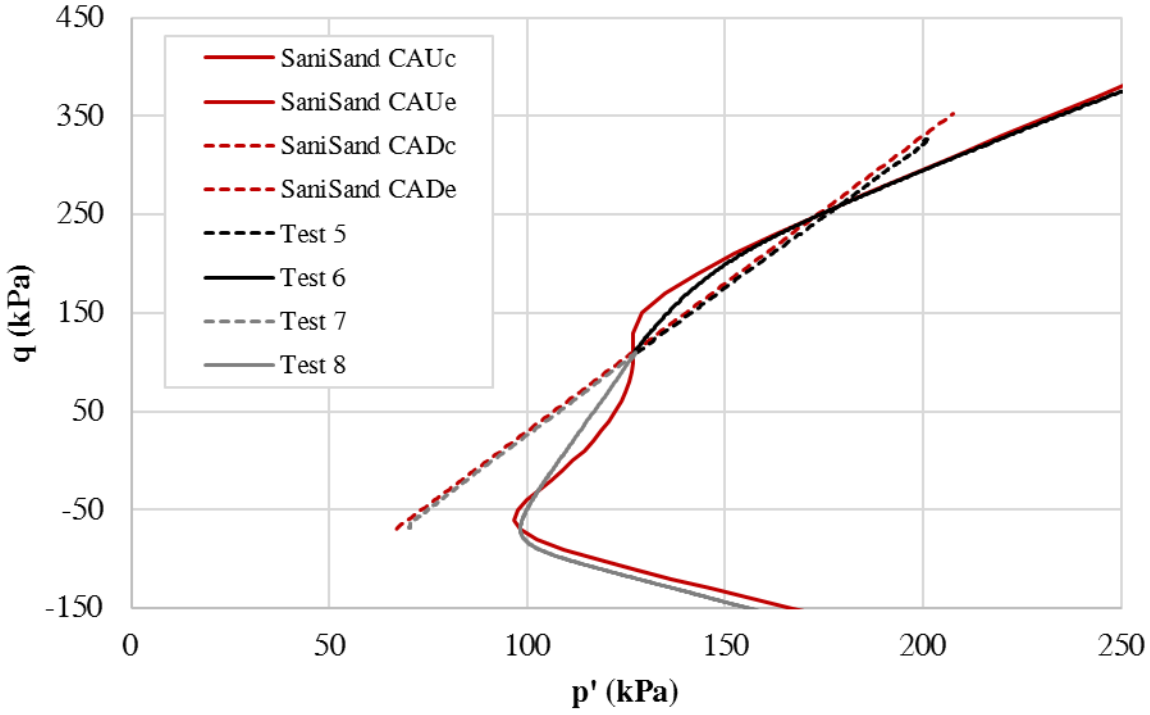

Figure C.7: $p' - q$ plot

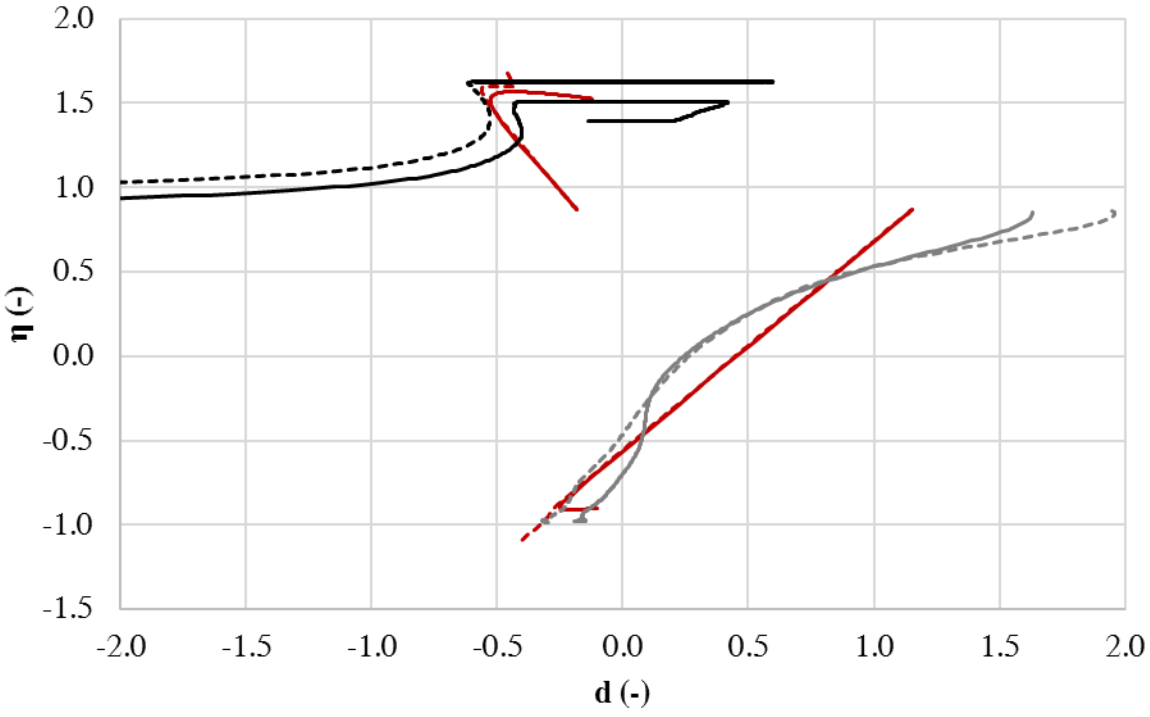

Figure C.8: $d - \eta$ plot

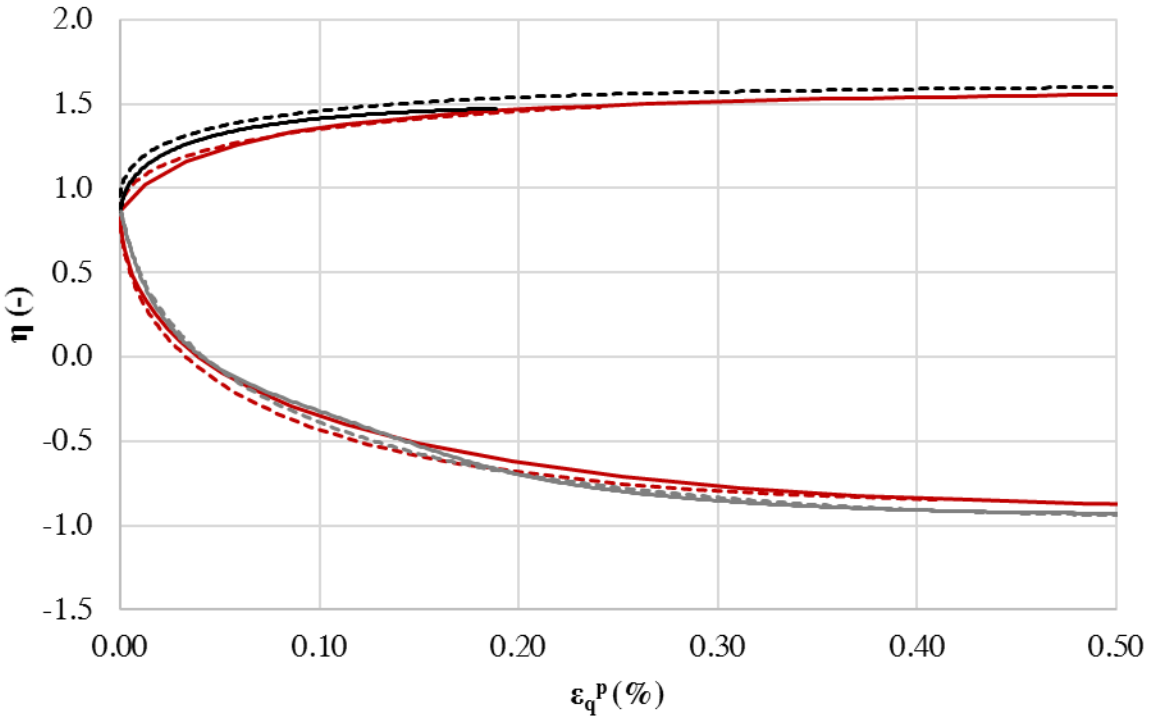

Figure C.9: $\varepsilon_q^p - \eta$ plot

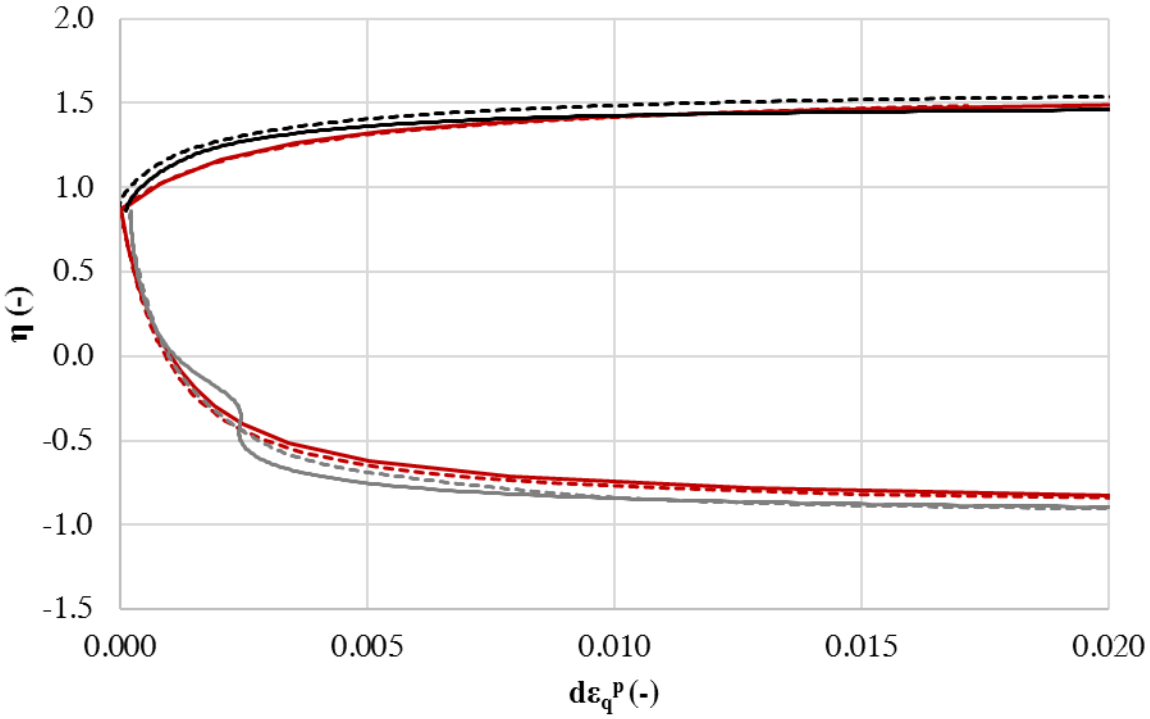

Figure C.10: $d\varepsilon_q^p - \eta$ plot

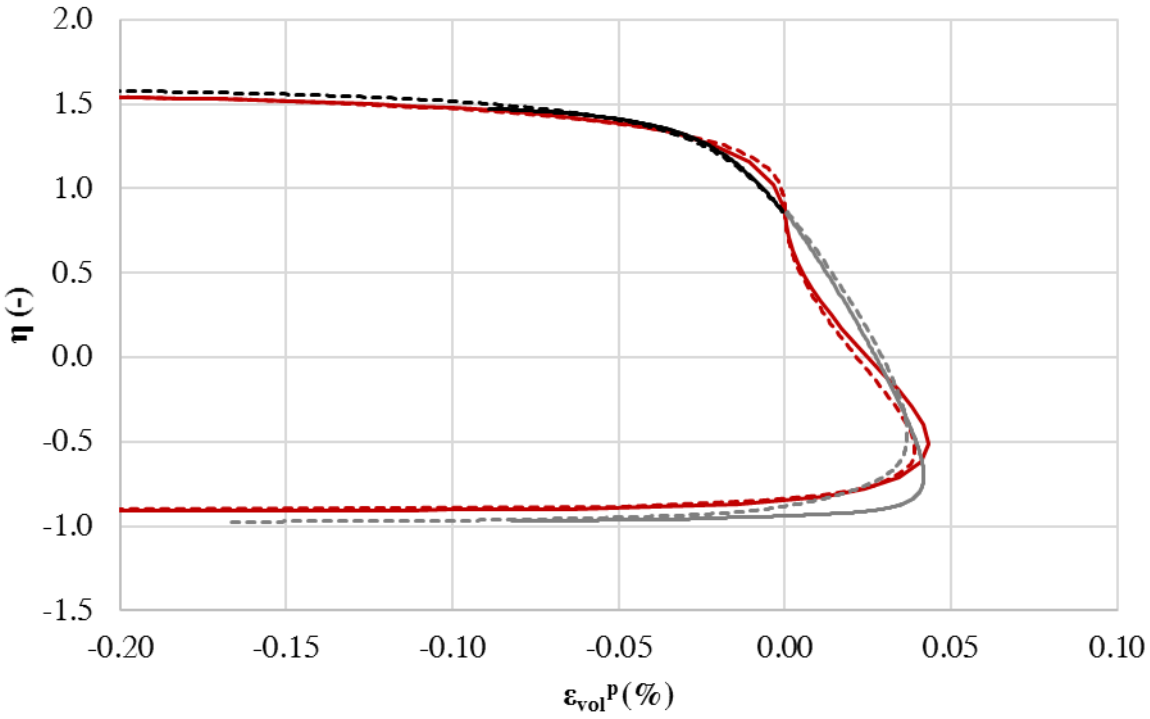

Figure C.11: $\varepsilon^p_{vol} - \eta$ plot

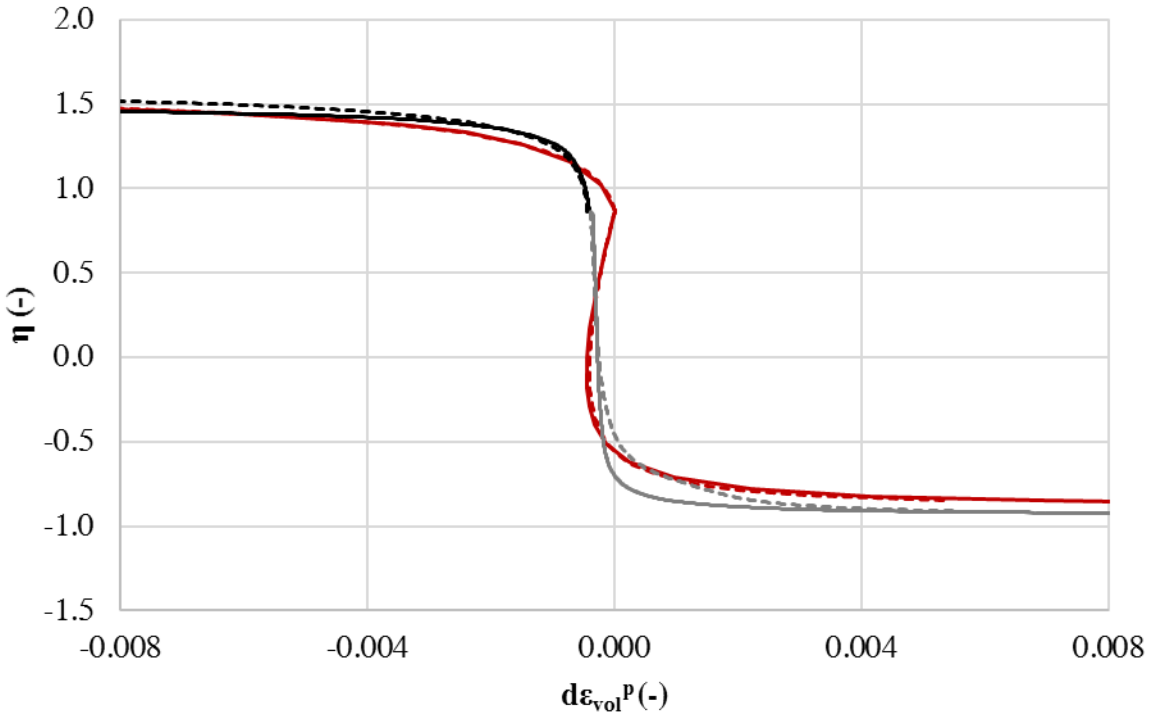

Figure C.12: $d\varepsilon^p_{vol} - \eta$ plot

C.3 Test 9, 10

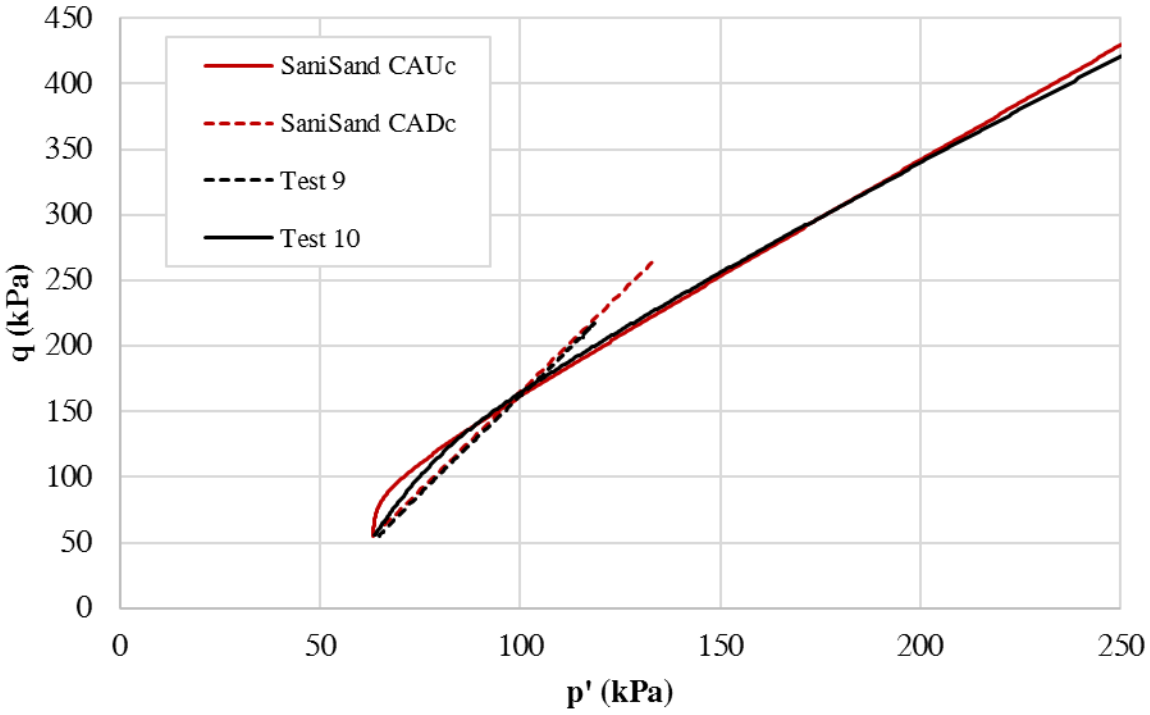

Figure C.13: $p' - q$ plot

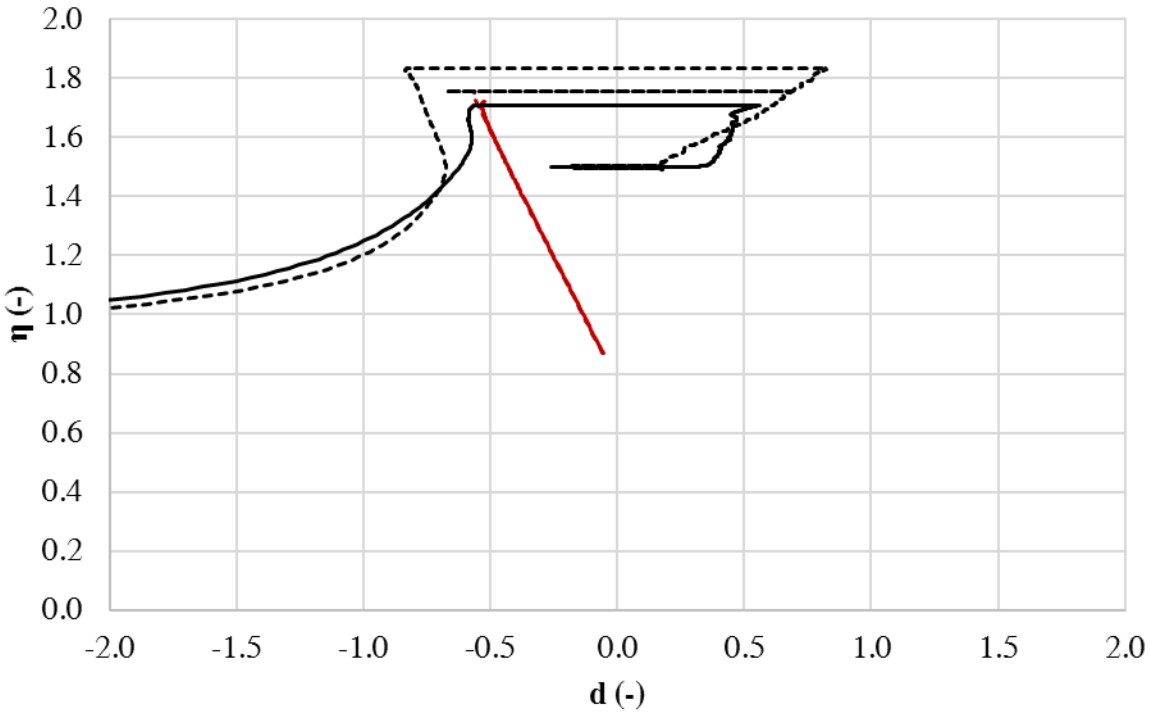

Figure C.14: $d - \eta$ plot

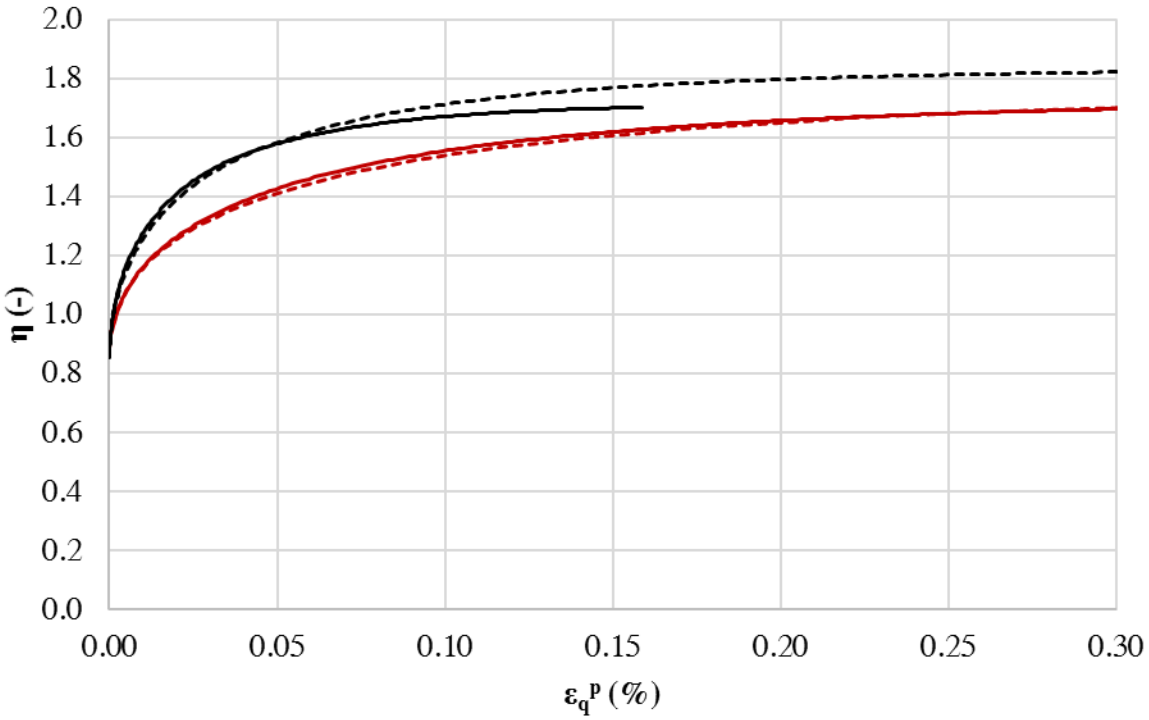

Figure C.15: $\varepsilon_q^p - \eta$ plot

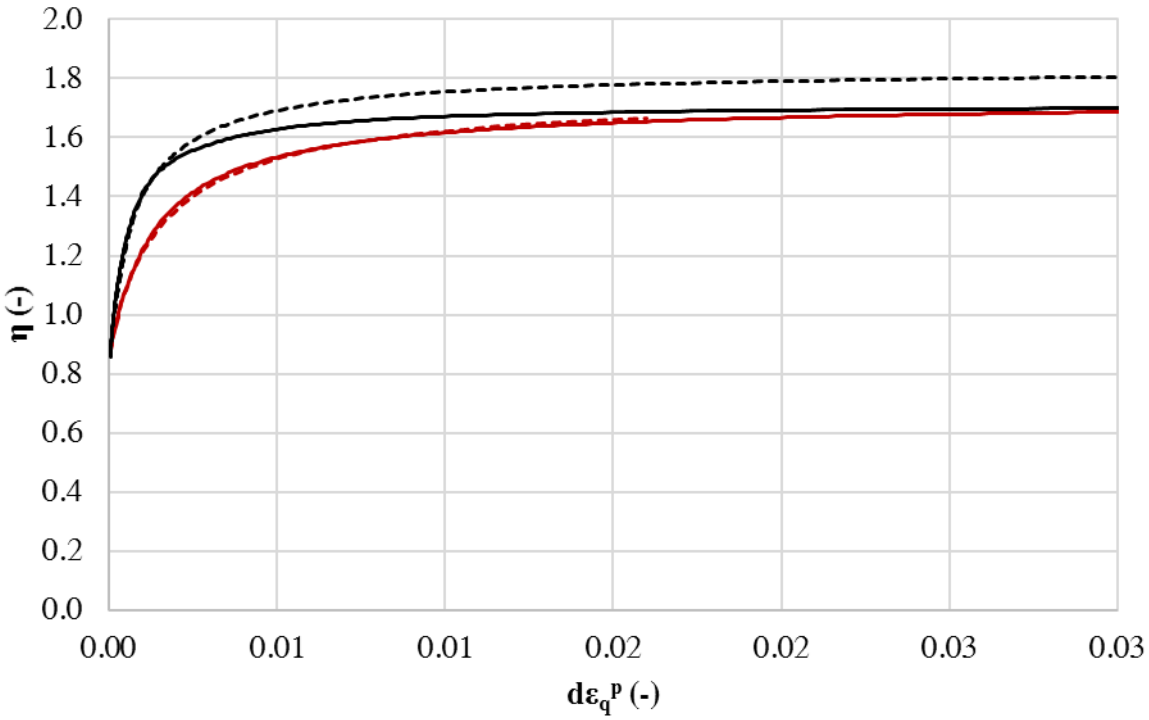

Figure C.16: $d\varepsilon_q^p - \eta$ plot

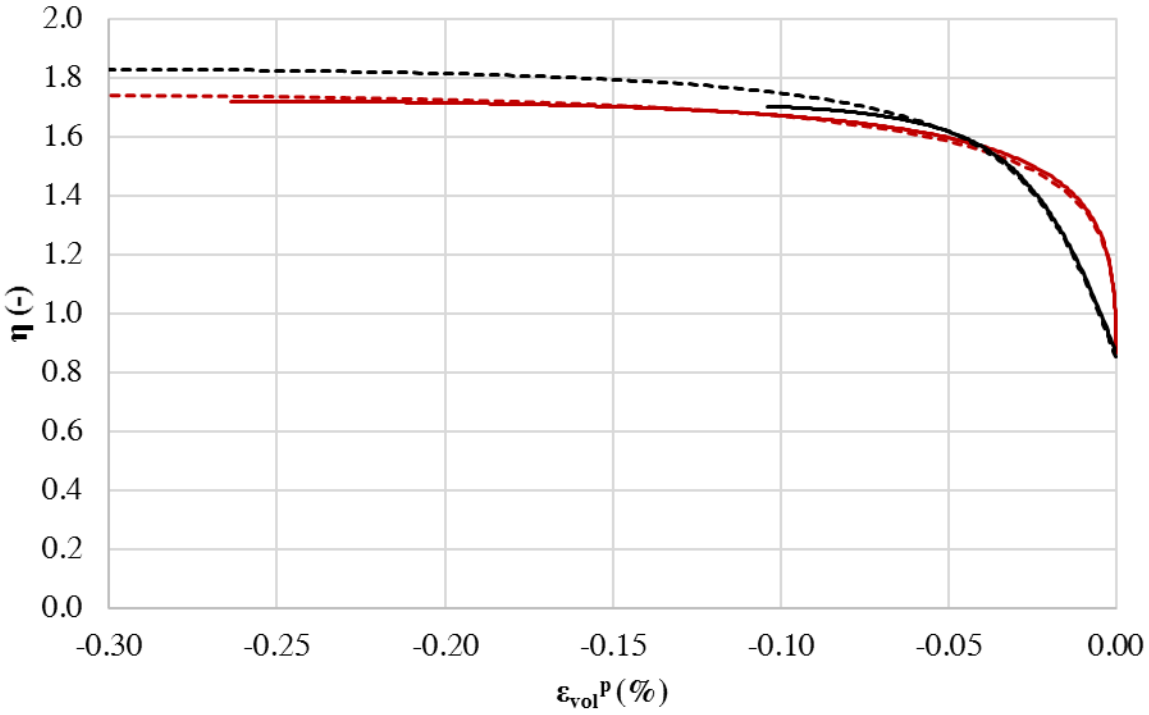

Figure C.17: $\varepsilon^p_{vol} - \eta$ plot

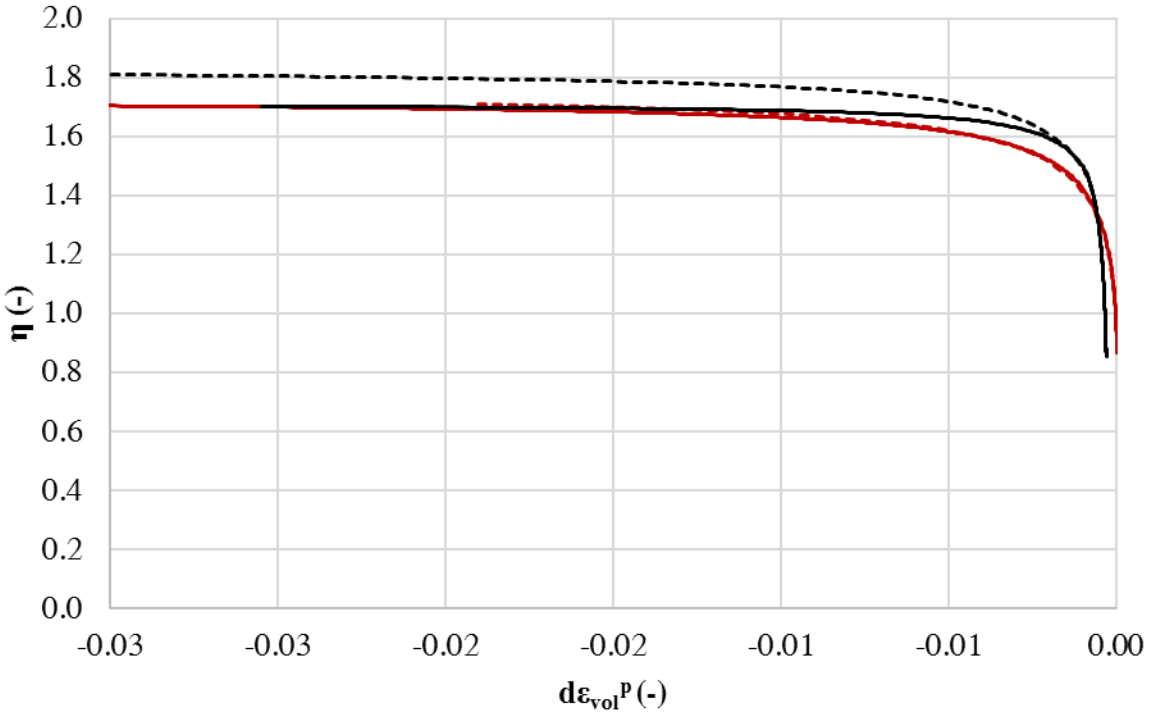

Figure C.18: $d\varepsilon^p_{vol} - \eta$ plot

Appendix D

Implementation of the Cyclic SANISAND Constitutive Model

D.1 Simulation of Undrained Cyclic Response

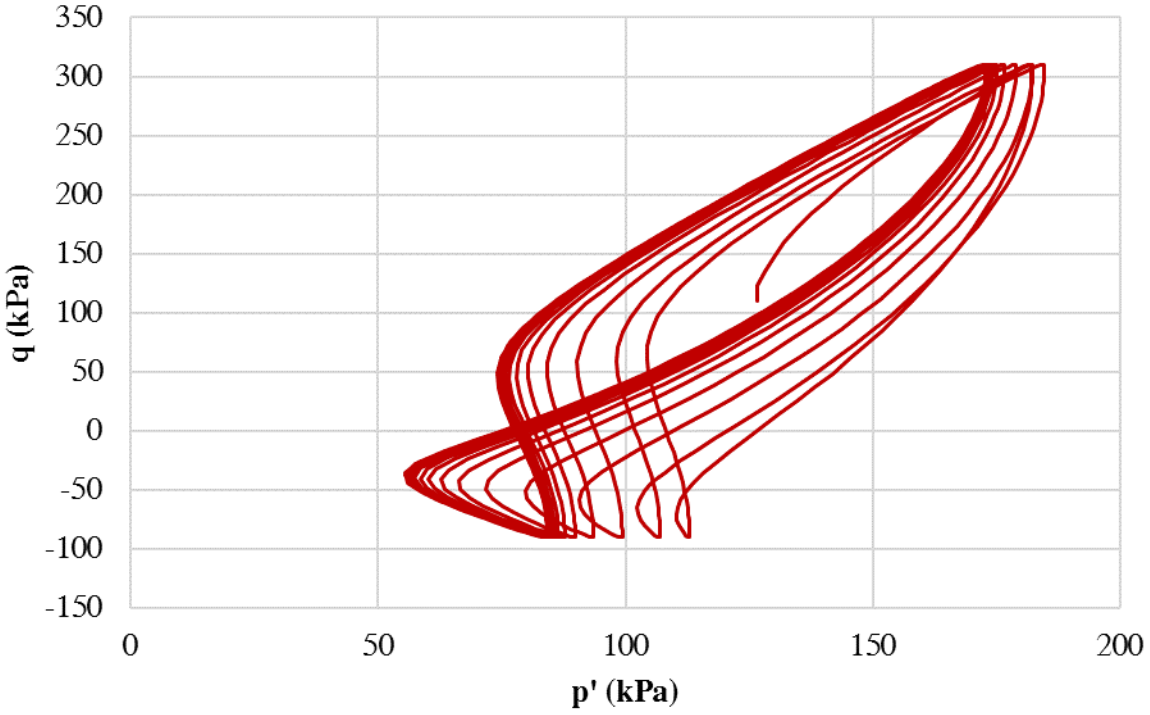

Figure D.1: $p' - q$ plot

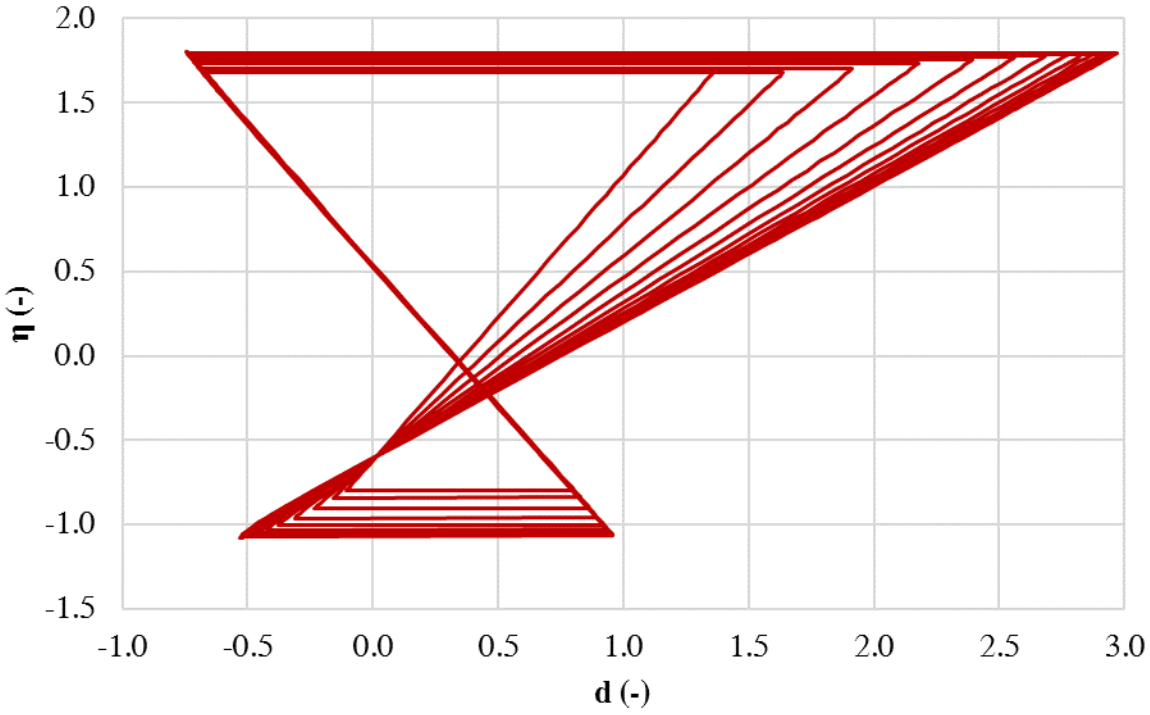

Figure D.2: $d - \eta$ plot

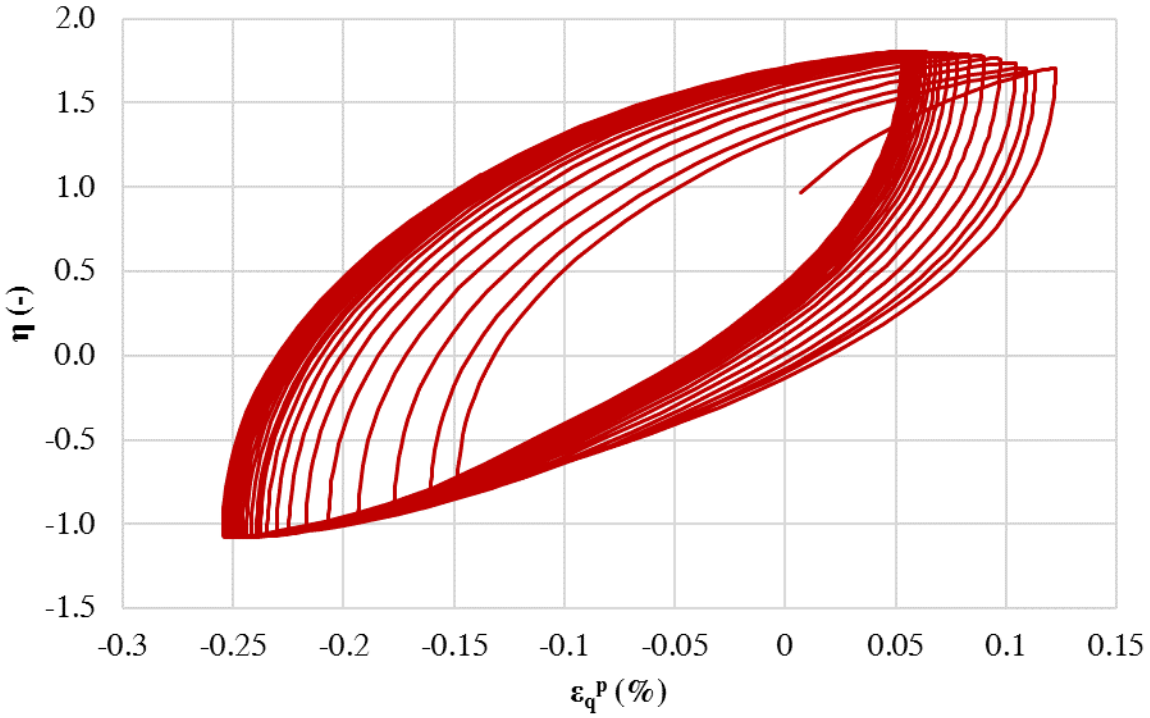

Figure D.3: $\varepsilon_q^p - \eta$ plot

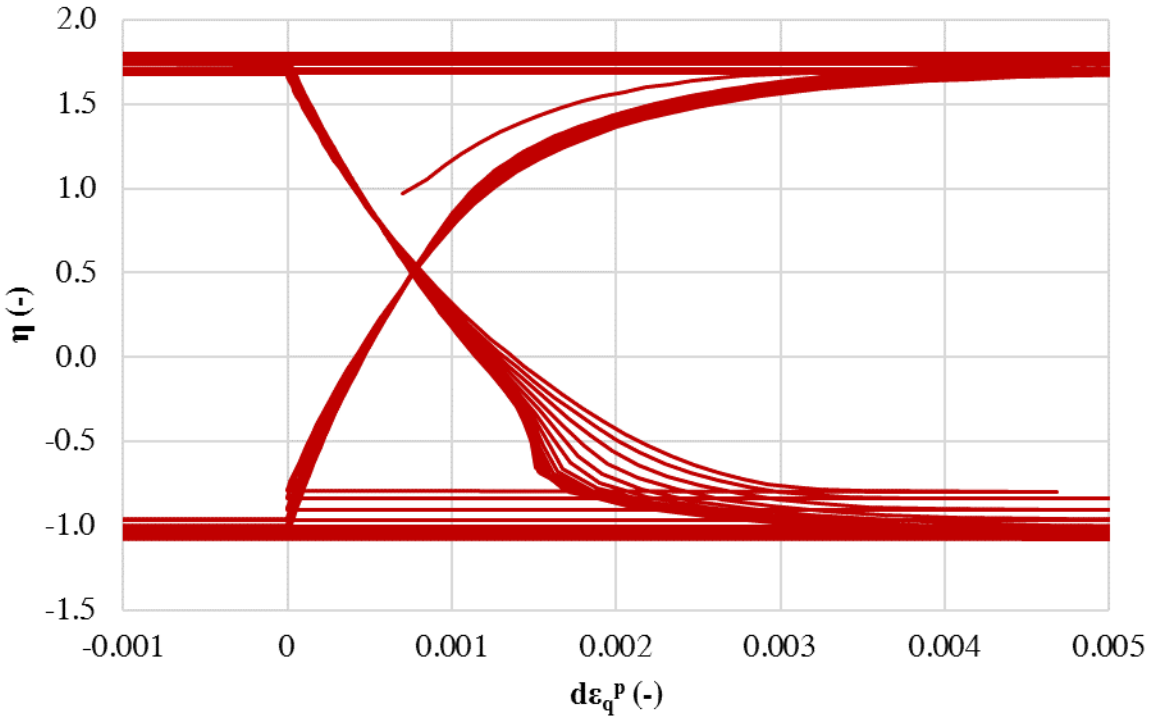

Figure D.4: $d\varepsilon_q^p - \eta$ plot

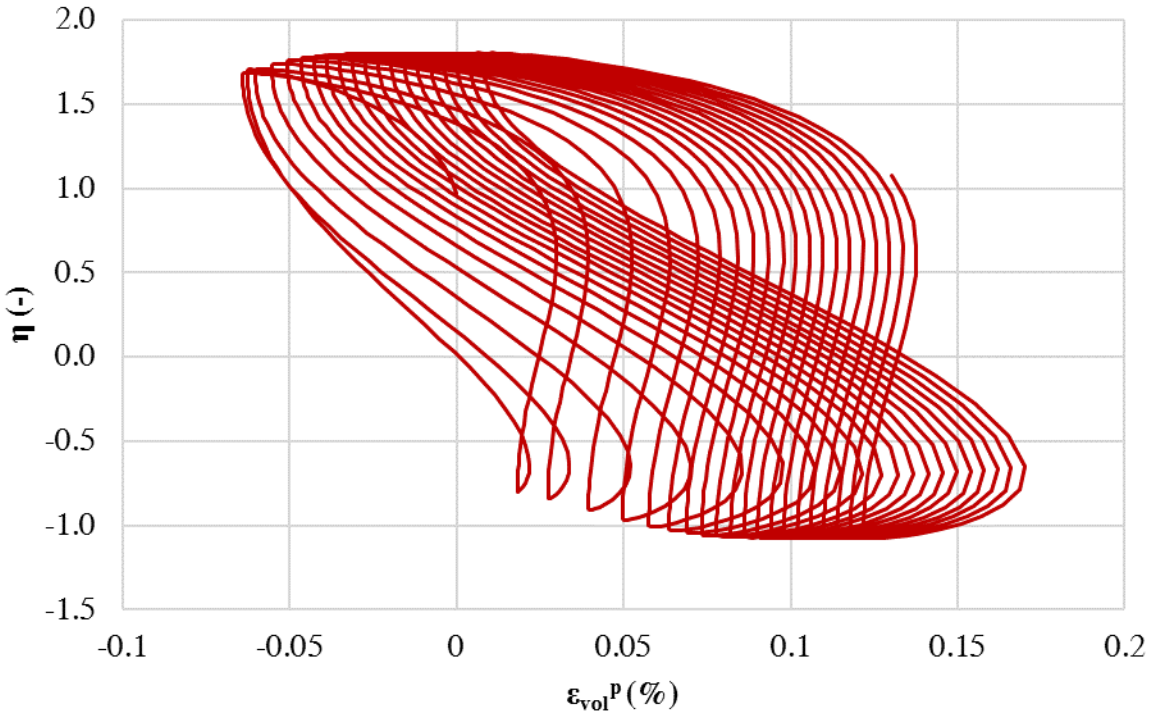

Figure D.5: $\varepsilon^p_{vol} - \eta$ plot

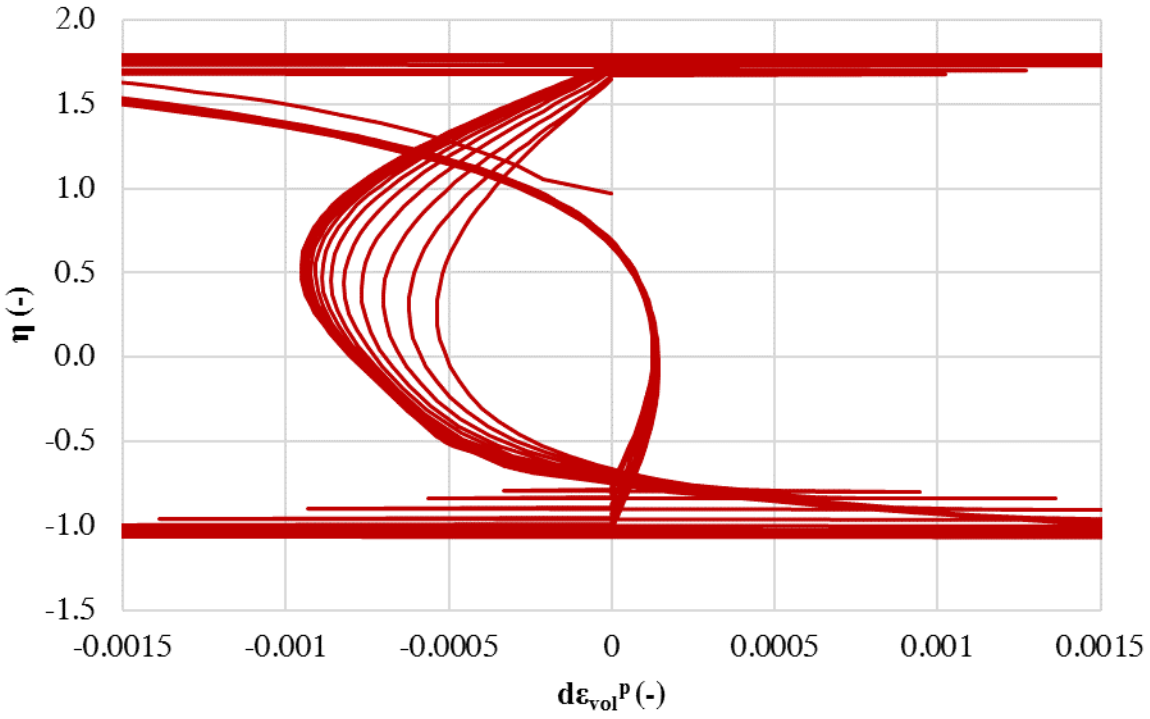

Figure D.6: $d\varepsilon^p_{vol} - \eta$ plot

D.2 Simulation of Drained Cyclic Response

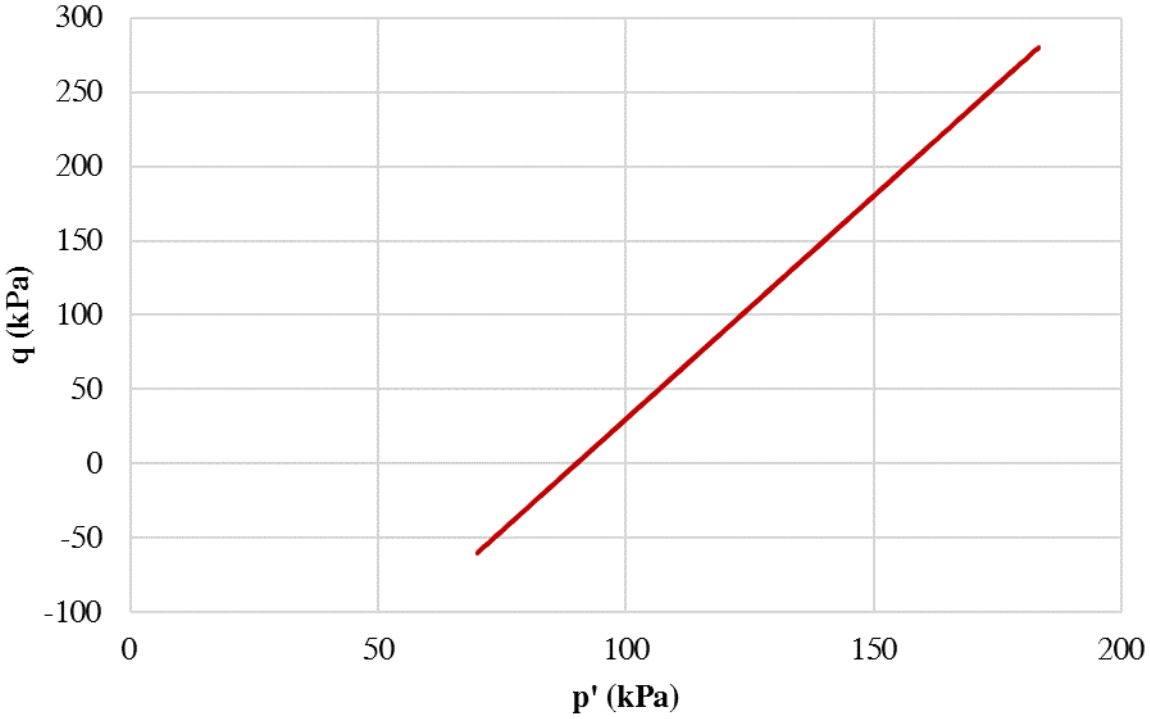

Figure D.7: $p' - q$ plot

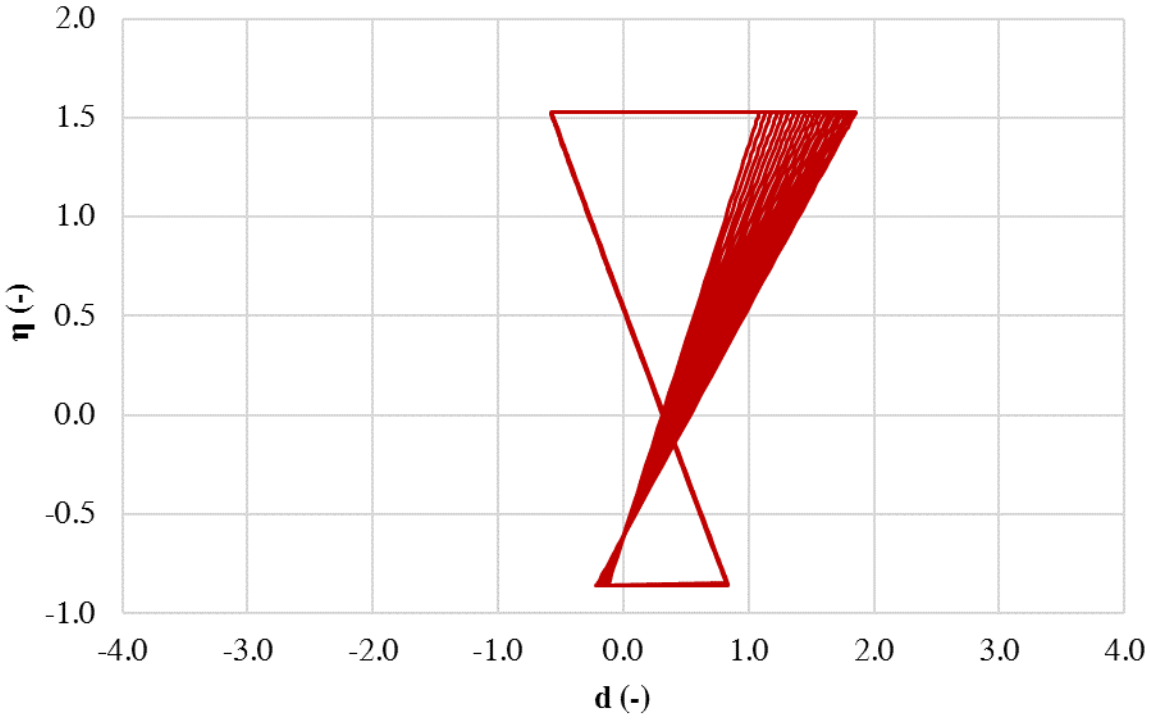

Figure D.8: $d - \eta$ plot

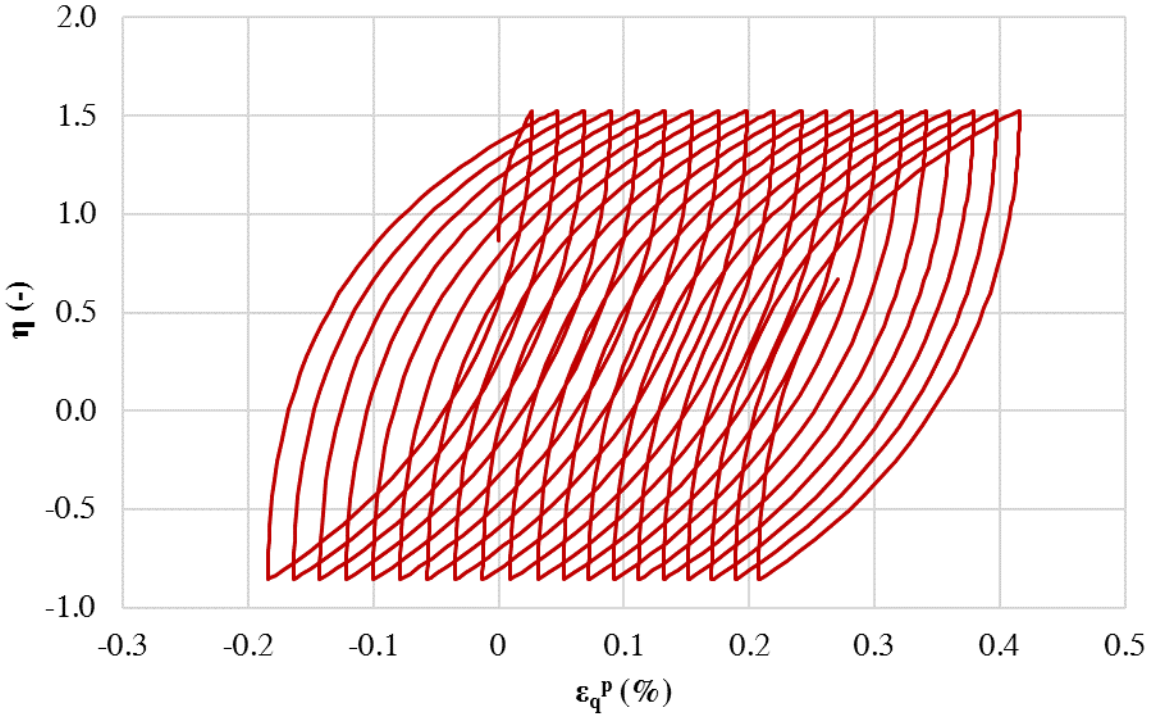

Figure D.9: $\varepsilon_q^p - \eta$ plot

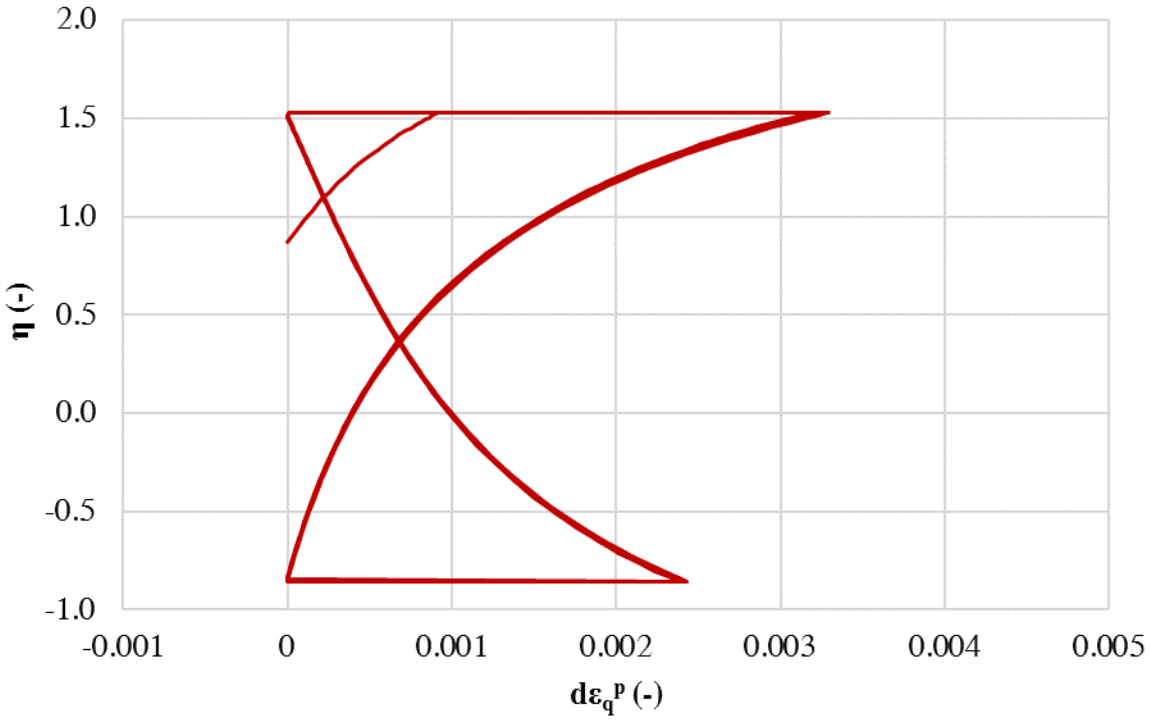

Figure D.10: $d\varepsilon_q^p - \eta$ plot

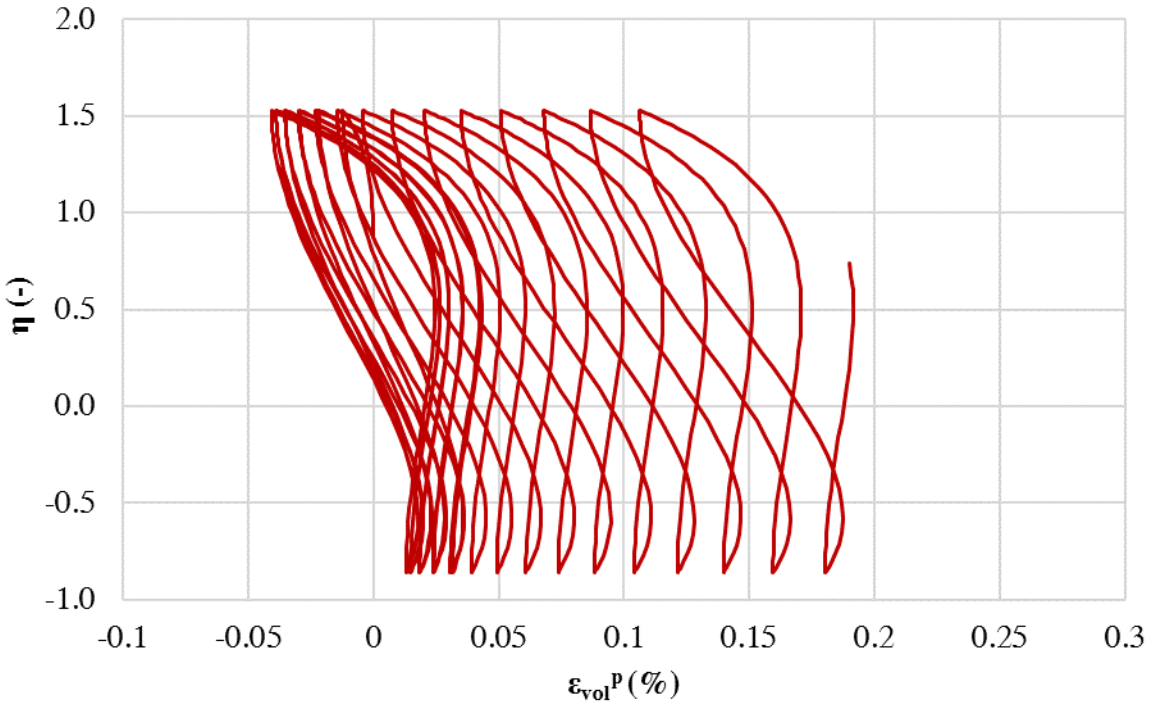

Figure D.11: $\varepsilon^p_{vol} - \eta$ plot

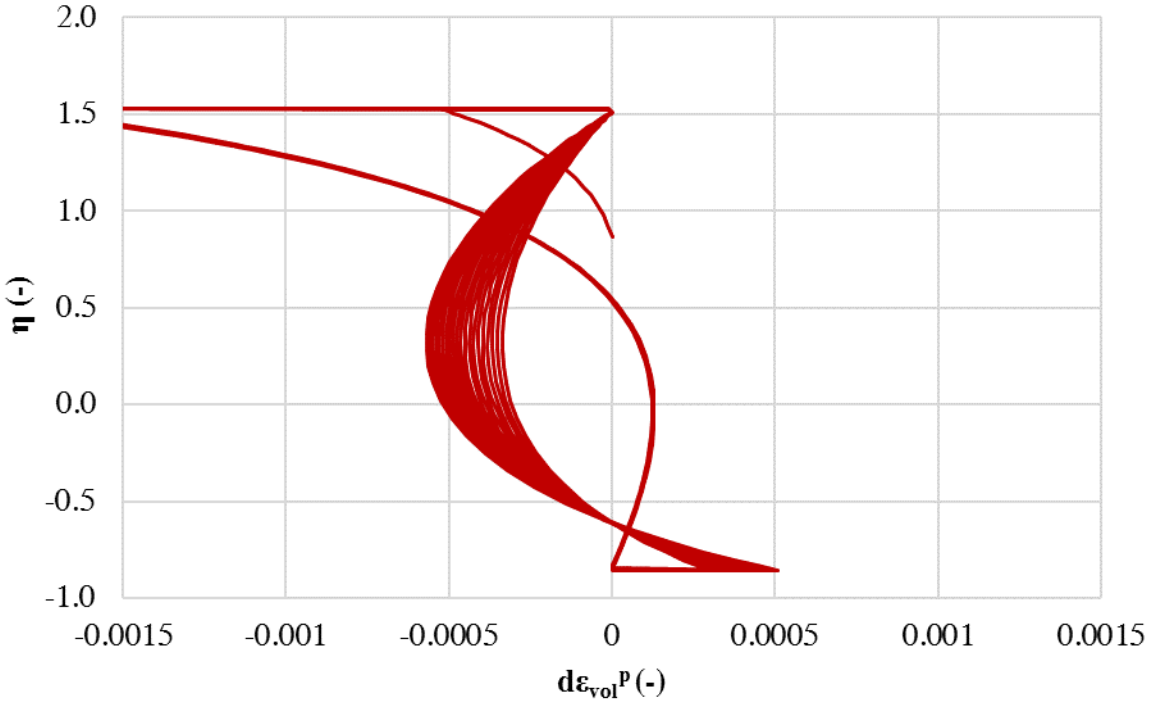

Figure D.12: $d\varepsilon^p_{vol} - \eta$ plot

Appendix E

MATLAB Script for Filtering Data

The raw-data from the triaxial tests have been filtered in MATLAB. The start of the code is presented below:

```
close all
clear all
format long eng

DataDirectory = ['D:\Master\'];
file = 'Filtrering.xlsx';
xlsfile = 'Results_Filt.xlsx';
Case = 'Raw';
fs = 1;
fsResamp = 10;
FiltFakt = 5;

cycle1 = xlsread([DataDirectory, file],Case,'E3:H114');
cycle2 = xlsread([DataDirectory, file],Case,'E10627:H10728');
cycle9 = xlsread([DataDirectory, file],Case,'AU11002:AX11103');
cycle10 = xlsread([DataDirectory, file],Case,'AU11104:AX11206');
cycle649 = xlsread([DataDirectory, file],Case,'AU21601:AX21817');
cycle650 = xlsread([DataDirectory, file],Case,'AU21818:AX21920');
cycles = [1,2,9,10,649,650];


for step = 1:length(cycles)
    eval(['ShearStrain = cycle',num2str(cycles(step)),'(:,1);']);
    eval(['ShearStress = cycle',num2str(cycles(step)),'(:,2);']);
    eval(['EffAxialStess = cycle',num2str(cycles(step)),'(:,3);']);
    eval(['EffMeanStress = cycle',num2str(cycles(step)),'(:,4);']);
    N = 2*floor(length(ShearStrain)/2);
    ShearStrain = ShearStrain(1:N);
```

Appendix F

SANISAND Model in Excel

F.1 Input Parameters and Simulations

Input parameters		Compression	Extension
Elasticity	G_0	125	125
	ν	0.050	0.050
Critical state	M	1.250	0.890
	c	0.712	0.712
	λ_c	0.019	0.019
	e_0	0.934	0.934
	ξ	0.700	0.700
Yield surface	m	0.010	0.010
Plastic moduli	h_0	7.050	7.050
	c_h	0.968	0.968
	n^b	1.100	1.100
Dilatancy	A_0	0.704	0.704
	n^d	3.500	3.500
Fabric-dilatan	z_{max}	5.000	5.000
	c_z	600.000	600.000
Stress state	p_{at}	100.000	
	σ_{a0}	252.000	
	σ_{h0}	251.000	
	e	0.735	

Load controll		
	dq_{tot}	114.20
	N	250.00
Calculated	q_{max} =	

Iterations	
Cycles	6.00
Iterations	500.00

Cycle Generator

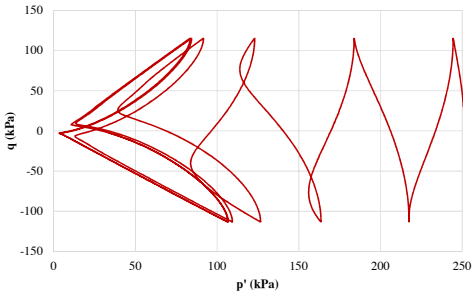

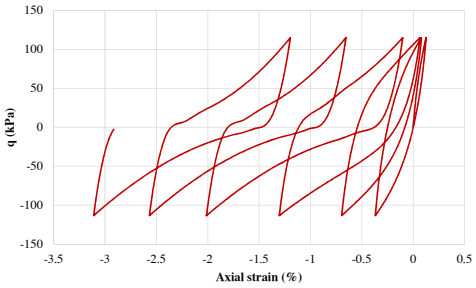

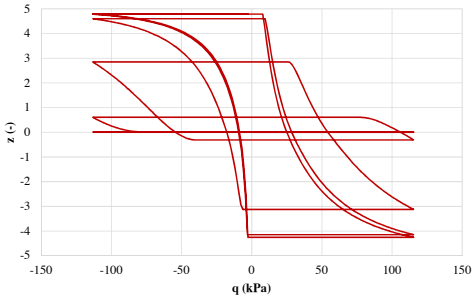

F.2 Excel Set Up

Half Cycle	Cycle	s	Steps	dq_{ass} (kPa)	dq (kPa)	σ_a (kPa)	σ_h (kPa)	e (-)	p (kPa)	q (kPa)	η (-)	$\eta_{initial}$ (-)	G (kPa)	K (kPa)	e_c (-)
1	1	1	0	0.00	0.00	252.00	251.00	0.735	251.333	1.000	0.004	0.004	57054.596	44375.797	0.898
1	1	1	1	1.43	1.43	253.43	251.00	0.735	251.333	2.434	0.010	0.004	57054.596	44375.797	0.898
1	1	1	2	2.87	1.43	254.87	251.00	0.735	251.333	3.868	0.015	0.004	57054.258	44375.534	0.898
1	1	1	3	4.30	1.43	256.30	251.00	0.735	251.333	5.302	0.021	0.004	57053.585	44375.010	0.898
1	1	1	4	5.73	1.43	257.73	251.00	0.735	251.333	6.735	0.027	0.004	57052.580	44374.229	0.898
1	1	1	5	7.17	1.43	259.17	251.00	0.735	251.333	8.167	0.032	0.004	57051.247	44373.192	0.898
1	1	1	6	8.60	1.43	260.60	251.00	0.735	251.333	9.598	0.038	0.004	57049.589	44371.903	0.898
1	1	1	7	10.03	1.43	262.03	251.00	0.735	251.333	11.028	0.044	0.004	57047.611	44370.364	0.898
1	1	1	8	11.46	1.43	263.46	251.00	0.735	251.333	12.456	0.050	0.004	57045.315	44368.579	0.898
1	1	1	9	12.88	1.43	264.88	251.00	0.735	251.333	13.882	0.055	0.004	57042.708	44366.550	0.898
1	1	1	10	14.31	1.42	266.31	251.00	0.735	251.333	15.306	0.061	0.004	57039.792	44364.283	0.898
1	1	1	11	15.73	1.42	267.73	251.00	0.735	251.333	16.728	0.067	0.004	57036.573	44361.779	0.898
1	1	1	12	17.15	1.42	269.15	251.00	0.735	251.333	18.147	0.072	0.004	57033.055	44359.043	0.898
1	1	1	13	18.56	1.42	270.56	251.00	0.735	251.333	19.564	0.078	0.004	57029.243	44356.078	0.898
1	1	1	14	19.98	1.41	271.98	251.00	0.735	251.333	20.978	0.083	0.004	57025.143	44352.889	0.898
1	1	1	15	21.39	1.41	273.39	251.00	0.735	251.333	22.388	0.089	0.004	57020.760	44349.480	0.898
1	1	1	16	22.80	1.41	274.80	251.00	0.735	251.333	23.795	0.095	0.004	57016.099	44345.854	0.898
1	1	1	17	24.20	1.40	276.20	251.00	0.735	251.333	25.199	0.100	0.004	57011.165	44342.017	0.898
1	1	1	18	25.60	1.40	277.60	251.00	0.735	251.333	26.599	0.106	0.004	57005.965	44337.973	0.898
1	1	1	19	26.99	1.40	278.99	251.00	0.735	251.333	27.995	0.111	0.004	57000.505	44333.726	0.898
1	1	1	20	28.39	1.39	280.39	251.00	0.735	251.333	29.386	0.117	0.004	56994.790	44329.281	0.898

ψ (-)	M_b (-)	M_d (-)	b_b (-)	h (-)	H (-)	dz (-)	z (-)	A_d (-)	d (-)	$d\varepsilon_q^p$ (-)	$d\varepsilon_q^e$ (-)	$d\varepsilon_{vol}^p$ (-)	$d\varepsilon_{vol}^e$ (-)	ε_q^{tot} (-)	dp (kPa)
-0.163	1.495	0.707	160.380	403088213312.958	601059578846.527	0	0	0.704	0.495	0.00E+00	0.00E+00	0.00E+00	0.00E+00	0.00E+00	0.000
-0.163	1.495	0.707	160.380	28103.198	41745.327	0	0	0.704	0.491	1.37E-07	8.38E-06	6.71E-08	-6.71E-08	8.52E-04	-0.003
-0.163	1.495	0.707	160.381	14052.567	20793.922	0	0	0.704	0.487	2.74E-07	8.38E-06	1.34E-07	-1.34E-07	1.72E-03	-0.006
-0.163	1.495	0.707	160.383	9369.461	13810.776	0	0	0.704	0.483	4.13E-07	8.38E-06	1.99E-07	-1.99E-07	2.60E-03	-0.009
-0.163	1.495	0.707	160.386	7028.237	10319.696	0	0	0.704	0.479	5.53E-07	8.37E-06	2.65E-07	-2.65E-07	3.49E-03	-0.012
-0.163	1.495	0.707	160.389	5623.766	8225.441	0	0	0.704	0.475	6.93E-07	8.37E-06	3.29E-07	-3.29E-07	4.39E-03	-0.015
-0.163	1.495	0.707	160.394	4687.673	6829.600	0	0	0.704	0.471	8.34E-07	8.36E-06	3.93E-07	-3.93E-07	5.31E-03	-0.017
-0.163	1.495	0.707	160.400	4019.224	5832.853	0	0	0.704	0.467	9.76E-07	8.35E-06	4.56E-07	-4.56E-07	6.25E-03	-0.020
-0.163	1.495	0.707	160.406	3518.053	5085.540	0	0	0.704	0.463	1.12E-06	8.34E-06	5.18E-07	-5.18E-07	7.19E-03	-0.023
-0.163	1.495	0.707	160.413	3128.402	4504.516	0	0	0.704	0.459	1.26E-06	8.33E-06	5.79E-07	-5.79E-07	8.15E-03	-0.026
-0.163	1.495	0.707	160.422	2816.815	4039.896	0	0	0.704	0.455	1.41E-06	8.32E-06	6.39E-07	-6.39E-07	9.13E-03	-0.028
-0.163	1.495	0.707	160.431	2562.002	3659.932	0	0	0.704	0.451	1.55E-06	8.31E-06	6.98E-07	-6.98E-07	1.01E-02	-0.031
-0.163	1.495	0.707	160.441	2349.771	3343.463	0	0	0.704	0.447	1.69E-06	8.30E-06	7.57E-07	-7.57E-07	1.11E-02	-0.034
-0.163	1.495	0.707	160.451	2170.294	3075.835	0	0	0.704	0.443	1.84E-06	8.28E-06	8.14E-07	-8.14E-07	1.21E-02	-0.036
-0.163	1.495	0.707	160.463	2016.555	2846.582	0	0	0.704	0.439	1.98E-06	8.26E-06	8.70E-07	-8.70E-07	1.31E-02	-0.039
-0.163	1.495	0.707	160.475	1883.405	2648.031	0	0	0.704	0.435	2.13E-06	8.25E-06	9.25E-07	-9.25E-07	1.42E-02	-0.041
-0.163	1.495	0.707	160.488	1766.984	2474.426	0	0	0.704	0.431	2.27E-06	8.23E-06	9.79E-07	-9.79E-07	1.52E-02	-0.043
-0.163	1.495	0.707	160.502	1664.341	2321.364	0	0	0.704	0.427	2.42E-06	8.21E-06	1.03E-06	-1.03E-06	1.63E-02	-0.046
-0.163	1.495	0.707	160.517	1573.181	2185.422	0	0	0.704	0.423	2.56E-06	8.19E-06	1.08E-06	-1.08E-06	1.74E-02	-0.048
-0.163	1.495	0.707	160.532	1491.689	2063.898	0	0	0.704	0.419	2.71E-06	8.16E-06	1.13E-06	-1.13E-06	1.85E-02	-0.050
-0.163	1.495	0.707	160.548	1418.417	1954.629	0	0	0.704	0.415	2.85E-06	8.14E-06	1.18E-06	-1.18E-06	1.96E-02	-0.052